NASA CONTRACTOR REPORT

NASA CR-2

WIND TUNNEL AND ANALYTICAL INVESTIGATION OF OVER-THE-WING PROPULSION/AIR FRAME INTERFERENCES FOR A SHORT-HAUL AIRCRAFT AT MACH NUMBERS FROM 0.6 TO 0.78

O. D. Wells, M. L. Lopez, H. R. Welge,
P. A. Henne, and A. E. Sewell

Prepared by
DOUGLAS AIRCRAFT COMPANY
Long Beach, Calif. 90846
for Lewis Research Center

NATIONAL AERONAUTICS AND SPACE ADMINISTRATION · WASHINGTON, D. C. · SEPTEMBER 1977

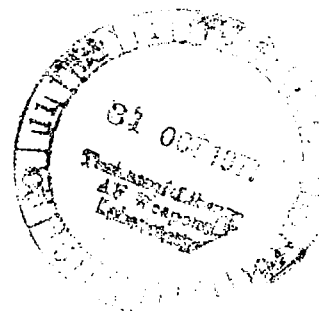| 1. Report No. NASA CR-2905	2. Government Accession No.	3. Recipient's Catalog No.
4. Title and Subtitle WIND TUNNEL AND ANALYTICAL INVESTIGATION OF OVER-THE-WING PROPULSION/AIRFRAME INTERFERENCES FOR A SHORT-HAUL AIRCRAFT AT MACH NUMBERS FROM 0.6 TO 0.78		5. Report Date September 1977
		6. Performing Organization Code
7. Author(s) O. D. Wells, M. L. Lopez, H. R. Welge, P. A. Henne, and A. E. Sewell		8. Performing Organization Report No. MDC J7601
		10. Work Unit No.
9. Performing Organization Name and Address Douglas Aircraft Company 3855 Lakewood Boulevard Long Beach, California 90846		11. Contract or Grant No. NAS3-18284
		13. Type of Report and Period Covered Contractor Report
12. Sponsoring Agency Name and Address National Aeronautics and Space Administration Washington, D.C. 20546		14. Sponsoring Agency Code

15. Supplementary Notes

Final report. Project Manager, Edward T. Meleason, Energy Conservative Engines Office, NASA Lewis Research Center, Cleveland, Ohio 44135

16. Abstract

Results of analytical calculations and wind tunnel tests at cruise speeds of a representative four-engine short-haul aircraft employing upper surface blowing (USB) with a supercritical wing are discussed. The wind tunnel tests were conducted in the NASA Lewis 8- by 6-foot tunnel and covered a range of Mach number M from 0.6 to 0.78. The design point for the study was M = 0.70. The test explored the use of three USB nozzle configurations: (1) a low-angle design with an 11° upper surface boattail angle; (2) a streamline contoured nacelle; and (3) a high-angle powered lift design with a 2.85° upper surface boattail angle. Results are shown for the isolated wing-body and for each of the three nozzle types installed. The experimental results indicate that the low-angle nacelle and the streamline contoured nacelle yielded the same interference drag at the design Mach number. The high-angle powered lift nacelle had higher interference drag primarily because of nacelle boattail low pressures and flow separation. Results of varying the spacing between the nacelles and the use of trailing edge flap deflections, wing upper surface contouring, and a convergent-divergent nozzle to reduce potential adverse jet effects are also discussed. Analytical comparisons with experimental data, made for selected cases, indicate favorable agreement.

17. Key Words (Suggested by Author(s)) STOL Aerodynamics Propulsion	18. Distribution Statement Unclassified - unlimited STAR Category 02

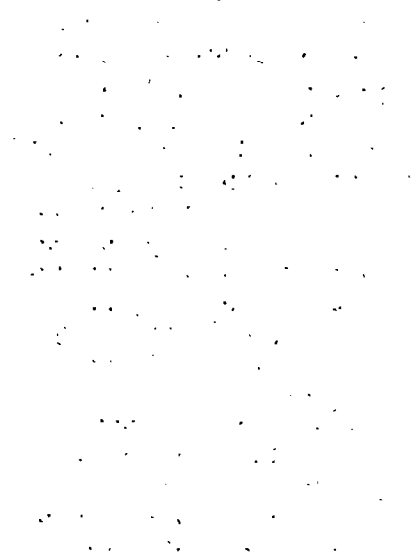| 19. Security Classif. (of this report) Unclassified	20. Security Classif. (of this page) Unclassified	21. No. of Pages 243	22. Price* A11

* For sale by the National Technical Information Service, Springfield, Virginia 22161

TABLE OF CONTENTS

1.0 ABSTRACT

Results of analytical calculations and wind tunnel tests at cruise speeds of a representative four engine short-haul aircraft employing upper surface blowing (USB) with a supercritical wing are discussed. The wind tunnel tests were conducted in the NASA Lewis 8x6-foot tunnel and covered a Mach number, M, range from 0.6 to 0.78. The design point for the study was M=0.70. The test explored the use of three USB nozzle configurations: 1) a low-angle design with an 11 degree upper surface boattail angle; 2) a streamline contoured nacelle; and 3) a high-angle powered lift design with a 28.5 degree upper surface boattail angle.

Turbine driven powered simulators were used to provide representation of the inlet and exhaust flows. Flow-through nacelles were also tested to represent the unpowered case so that the effects of the jet could be assessed separately from the effects of the nacelle installation. Nacelle afterbody, internal simulator, and wing surface pressures in and out of the jet were measured in addition to the model balance forces.

Results are shown for the isolated wing-body and for each of the three nozzle types installed. The experimental results indicate that the low angle nacelle and the streamline contoured nacelle yielded the same interference drag at the design Mach number. The high angle powered lift nacelle had higher interference drag due primarily to nacelle boattail low pressures and flow separation. Results of varying the spacing between the nacelles and the use of trailing edge flap deflections, wing upper surface contouring, and a convergent-divergent (C-D) nozzle to reduce potential adverse jet effects are also discussed. Analytical comparisons with experimental data made for selected cases, indicate favorable agreement.

1

2.0 SUMMARY

The design and wind tunnel test results of a four engine over-the-wing (OTW) short-haul transport aircraft are discussed. A general discussion is presented of STOL aircraft for short-haul transportation which indicates that one of the competitive concepts for the high lift system is an upper surface blowing (USB) flap. Two of the critical technology items identified for the USB flap concept, the nozzle design and nacelle/wing-fuselage integration at cruise conditions, are the subject of this investigation.

The baseline configuration resulting from previous systems studies is described. Several alternate configurations are discussed including alternate spanwise spacing of the nacelles, a streamline contoured nacelle, a high boattail angle nacelle, a convergent-divergent nozzle, and upper surface wing contouring. Jet deflection effects were evaluated by deflecting the trailing edge flaps within the region of the jet. The description of the experimental program covers the wind tunnel, wind tunnel model, test conditions and the powered simulator and their calibration. Discussion of the experimental procedures and installed simulator performance is followed by the experimental results.

The results of the test program indicate that, at the design condition of $M=0.70$ and $C_L=0.4$, the baseline, streamline contoured, and C-D nozzles all had similar low levels of nacelle interference drag at the design Mach number. The high boattail angle nacelle had a higher interference drag due primarily to low nacelle boattail pressures and flow separation.

3.0 INTRODUCTION

For many years the investigation of the aerodynamics of USB concepts placed emphasis on low-speed high-lift characteristics. That a compromise in low speed/cruise requirements would be necessary was noted. Due to a lack of powered high speed interference data in the 1973 time frame, the required design compromises for cruise and STOL operation were uncertain. Admittedly, high-speed tests had established that nacelle/wing interferences could be minimized with the correct contouring of the nacelle (Reference 1). Unfortunately, the majority of these experimental investigations were conducted with flow-through nacelles. There was also limited experimental and analytical evidence that engine jet exhaust interference effects might be of major consequence (Reference 2). Thus, this potential aerodynamic problem area needed further investigation by means of high-speed wind tunnel tests and analytical-experimental comparisons.

As a consequence of the above, the Douglas Aircraft Company and the NASA Lewis Research Center embarked on a collaborative exploratory, high-speed experimental investigation of the aerodynamic/propulsion interferences of OTW-propulsion system installations applicable to short-haul transport aircraft with emphasis being placed on the following:

o   An assessment of aerodynamic interferences.

o   The definition of flow conditions and mechanism of interference.

o   Establishing installation effects on internal engine characteristics.

o   An investigation of techniques for minimizing adverse interference effects.

The accomplishment of these objectives required the definition of a baseline STOL transport aircraft configuration, the development of suitable alternate configurations, the design and fabrication of a powered wind tunnel model that could be tested in the NASA Lewis Research Center 8x6-Foot Supersonic Wind Tunnel, the planning and conducting of a wind tunnel test and the analysis and interpretation of the experimental data so acquired.

3

4.0 SYMBOLS

A   area

AR   wing aspect ratio

C   local wing chord

C_d discharge coefficient

c_d section drag coefficient

C_D airplane drag coefficient

$C_{D_{ram}}$ ram drag coefficient $D_{ram}/q_0 S_w$

C_{GMX} gross thrust coefficient $F_g/q_0 S_w$

C_L airplane lift coefficient

C_l section or local lift coefficient

C_M pitching moment coefficient about the 25% C_{MAC} location

C_m section pitching moment coefficient

C_{m_L} section pitching moment about section leading edge

C_{MAC} (or C_{REF}) wing mean aerodynamic chord (21.88 cm)

cm   centimeters

C_n section normal force coefficient

C_P pressure coefficient $(P-P_0)/\frac{\gamma}{2} P_0 M_0^2$

C_T section chord force coefficient

C_v nozzle velocity coefficient

C_μ jet momentum coefficient referenced to freestream dynamic
                    pressure and wing area, $W_{aj} V_j/q_0 S_w$

D_{ram} ram drag

FPR   fan pressure ratio $\bar{P}_{T_3}/P_{T_0}$

F_g gross thrust

FT   feet

F.T.   flow-through nacelle

g   graviational acceleration constant

4

in	inches
$^\circ K$	degrees Kelvin (temperature)
kg	kilograms
km	kilometers
lbs	pounds
ℓ_{DIF}	diffuser length
L	inlet overall length
m	meters
M	Mach number
M_L	local Mach number
N_X	nacelle-configuration X

N_1 = baseline non-contoured nacelle

N_2 = streamline contoured nacelle

N_3 = high boattail angle nozzle nacelle

N_4 = C-D nozzle nacelle

N	Newtons
N	balance gage readings (section 10)
P	static pressure
P_t	total pressure
q_0	freestream dynamic pressure
R	radius
$^\circ R$	degrees Rankine (temperature)
S_w	wing reference area
T_t	total temperature

V	velocity
W_a	airflow
X	streamwise length
Y_L	wing defining section lower surface coordinate
Y_N	nacelle station
Y_U	wing defining section upper surface coordinate
α or ALPHA	configuration angle of attack-fuselage reference line relative to freestream
Γ	referred airflow $\dfrac{W_a\sqrt{\theta_t}}{\delta_t}$
η	percent wing span
θ_t	relative absolute or total temperature, $\dfrac{T_t(^\circ K)}{288}$ or $\dfrac{T_t(^\circ R)}{519}$
δ_t	relative absolute or total pressure, $\dfrac{P_t(N/m^2)}{101,314}$ or $\dfrac{P_t(lbs/ft^2)}{2116}$

SUBSCRIPTS

A	outboard nacelle location
B	inboard nacelle location
f	fan conditions
i	inlet throat
j	conditions within the jet
HL	inlet highlight
L	local conditions
max	maximum
o	freestream ambient

6

1,2, etc.   simulator station locations for pressures and temperatures, see Figure 9.1, also, nacelle configuration.

SUPERSCRIPT

-        average value

5.0 STOL AIRCRAFT FOR SHORT HAUL TRANSPORTATION

The prime objective of a short-haul transportation system is community acceptance. At the present time this can, to a large extent, be equated to the achievement of noise levels compatible with existing community levels. In addition to noise, other factors associated with community acceptance which must also be considered include, for example, emissions, congestion, safety, and land use. Other stated objectives include economic viability, passenger acceptance, growth potential, and compatibility with existing transportation systems. It has been suggested that these broad objectives might be achieved through the utilization of STOL aircraft. It is pertinent, therefore, to consider some of the conclusions derived from a recent study (Reference 3) performed for NASA, "Study of Quiet Turbofan STOL Aircraft for Short-Haul Transportation (NASA STOL Systems Study)" by the Douglas Aircraft Company.

The NASA STOL Systems Study was based on a comprehensive interdisciplinary systems evluation approach which considered the complex interaction between markets, aircraft, airport, economics, and systems operations and on technology and environmental considerations consistent with 1980-1990 commercial operating systems. A major conclusion of this study is that STOL short-haul transportation systems appear to be economically viable. Further, that a major benefit of a short-haul STOL aircraft would be the relief in the noise environmental impact in the vicinity of the airport resulting partially from its STOL performance and partially from its utilization of a high-bypass ratio "quiet" turbofan engine.

In considering the first generation STOL/short haul aircraft, the work reported in Reference 3 indicates that it should be designed to no less than 914 meter (3000 ft) field length, a payload of approximately 150 passengers, and to a short-haul range requirement of 926 kilometers (500 n.mi.). In relation to noise level, a study design goal of 95 EPNdB on a 152 meter (500 ft) sideline was considered appropriate. It was concluded that the economic penalties for designing to 457 to 610 meter (1500 to 2000 ft) field lengths are large and that a requirement for this type of performance is not well substantiated. The passenger size is primarily a tradeoff between frequency of service and operating economics. The 926 kilometer (500 n.mi.) range requirement appears to have been somewhat arbitrarily selected. It was noted, however, that a STOL/short-haul aircraft could be designed to fly extended ranges with no significant penalty to its basic short range economics. The design noise level was found to have a critical impact on aircraft sizing and economics. Of the high lift concepts considered appropriate for STOL transport aircraft applications, it was concluded that the externally blown flap (EBF), upper surface blowing (USB) flap, and a mechanical high lift system are, in relation to the design requirements, competitive and could meet the study noise goal through the utilization of a new, quiet, clean high bypass ratio engine. It was noted, however, that a mechanical high-lift system/STOL aircraft has a relatively low wing loading and would require ride quality improvement.

The critical impact relative to engine treatment level and engine cycle characteristics of the design noise level on aircraft sizing and economics referred to earlier has been the subject of several studies (References 3 and 4). In these studies fan pressure ratio was the primary independent variable since noise, thrust lapse, and cruise performance are strongly dependent on this parameter. Bypass ratio was established at a value which resulted in a primary jet exhaust velocity at takeoff sufficiently low that the primary jet is not the dominant source. Considering the takeoff fan pressure ratio range studied (i.e., 1.25 to 1.57) several general trends were noted. The highest fan pressure ratio engine have the highest cruise speed capability and lowest direct operating cost. On the other hand, due to the higher fuel consumption of the high fan pressure ratio engines, any significant increase in fuel prices will reduce the direct operating cost advantages. The propulsive lift noise for EBF and USB designs constitute a noise floor beyond which it is not economically feasible to suppress the engine noise source. Thus the sideline noise levels for an economically viable aircraft with the highest fan pressure ratio engines are slightly higher than the noise goal.

The NASA STOL Systems Study was not intended to define actual transport airplanes nor dictate the selection of specific concepts. Rather, the design studies were conducted to provide a realistic basis for the system analysis and in assessing technology development requirements. In relation to the latter it is pertinent to note that to quote Reference 3, "The greatest STOL technology gaps are for the development of the aerodynamic and acoustic characteristics of the upper surface blowing concepts and for the reduction of flap interaction noise for the externally blown flap concept." The aerodynamics of the upper surface blowing concept, in particular the aerodynamic/propulsion interferences in cruise, was the subject of the investigation reported herein.

6.0 AERODYNAMICS OF OTW PROPULSION INSTALLATIONS

The potential acoustic advantages of over-the-wing (OTW) propulsion system installations have been partly responsible for the interest in the upper surface blowing (USB) concept for application to STOL transport aircraft. Upper surface blowing is conceptually accomplished by the selection of an over-the-wing engine exhaust installation, the engines being mounted high and forward of the wing. The lift required for takeoff and landing is achieved through the deflection of the engine exhaust to produce a substantial increase in wing circulation. The deflection of the engine exhaust is achieved by exhausting all of the engine efflux in such a manner that it becomes attached to the wing so that it can be subsequently turned by a curved wing/flap arrangement, the turning occurring as a result of the Coanda effect. The mechanism for the noise advantage appear to be a combination of shielding by the wing and flap surfaces of the engine noise sources and an alleviation of the noise associated with spreading of the jet itself.

As a consequence of recent technology development efforts, the STOL technology base in relation to USB concepts has been greatly enhanced from that which existed in 1973, the year when the plans for the investigation reported herein were initiated. Therefore, to retain a historical perspective a brief review of the features and characteristics of USB concepts in the context of the technology base that existed at that time is presented below.

6.1 Powered Lift

In many aerodynamic aspects USB high lift systems are, as are EBF systems, generic classes of the jet flap. In other words, as a consequence of having deflected the jet additional circulation is generated. This contributes appreciably to the total lift which includes the direct lift associated with the vertical component of the jet momentum while the propulsive thrust lies between the corresponding horizontal component and the full jet momentum. As mentioned earlier, the turning of the engine exhaust is the result of the Coanda effect. Thus, turning effectiveness will be dependent on those parameters (e.g., jet pressure ratio, jet thickness to turning radius ratio, and engine nozzle aspect ratio) which are normally associated with it. For example, if the jet pressure ratio is too high or the ratio of the jet thickness to flap turning radius too large, the turning effectiveness will be poor. Also, in view of the finite aspect ratio of the nozzle, the pressure decrease as the flow turns will cause the jet to coalesce along its center line. As a consequence, if the aspect ratio of the nozzle is too small the turning effectiveness will also be poor. In other words, for a given exhaust nozzle area a relatively thin jet prior to turning is required for effective flow turning.

Early low-speed wind tunnel data (References 5 to 11) confirmed the importance of achieving high turning effectiveness and the results of experimental and analytical studies (e.g., References 12 to 16) of jet flaps provided a basis for identifying the relative importance of effective flow turning and spreading in order to obtain good powered lift characteristics. In other words, high-turning effectiveness provides a high jet reaction contribution to total

lift while it was anticipated that a combination of high-turning effectiveness and extensive spreading of the engine exhaust would provide both "boundary layer control" over the USB flap and "supercirculation" as a consequence of the "jet-flap" action.

As mentioned in Section 5.0, a major benefit of a short-haul STOL aircraft would be the relief in the noise environmental impact in the vicinity of the airport, a reduction in noise resulting, in part, from its utilization of a high-bypass-ratio engine. Unfortunately, despite the reduction in exhaust jet pressure ratio with increasing bypass ratio, the installation of a high bypass ratio engine in a more or less conventionally shaped nacelle results in a ratio of exhaust-jet thickness to USB flap turning radius that is still too high for good turning performance. Thus, low speed studies centered on the investigation of several suggested techniques for improving turning efficiency. Some of these techniques are briefly discussed below.

The most obvious technique is to simply adopt a high aspect ratio "fishtail" nozzle, a nozzle designed to have the proper height for effective turning. However, not only are nozzle losses likely to be high but the cruise drag penalties inherent with the adoption of such a nozzle are likely to be unacceptable. Two viable alternative techniques producing the equivalent to a high aspect ratio nozzle were, therefore, conceived. The first of these techniques (References 7 to 9) involves the use of an exhaust-flow deflector attached to the top of the nacelle exit in such a way that it can be mechanically articulated to direct the exhaust flow down toward the wing surface. The exhaust flow, being free to expand and spread spanwise, is effectively thinned enough to.provide good turning performance. The second technique (References 10 and 17) involves the selection of an internal nozzle wall shape that will essentially accomplish the desired change in exhaust flow, a change similar to that acquired with the use of a deflector. In other words, the upper internal boattail angles (often referred to as kick-down angle) are selected to provide the required spreading and thinning of the jet. Other alternatives include the use of boundary layer control on the USB flap, a turning vane located above the flap knee, vortex generators, or a suitable combination of any of the above.

6.2 Cruise Performance

The incompatibility in the aerodynamic requirements associated with a short-field operational capability and those associated with efficient cruise at moderate Mach numbers are well understood. Consider, therefore, whether the features of the selected high lift system, in this instance the USB flap, will introduce any significant penalties in cruise performance.

The influence of over-the-wing (OTW) nacelle installations on the wing flow field is the principal concern when considering the possible problems of high speed flight. Advanced wings are normally designed to operate with extensive regions of supercritical flow on the upper surface with deceleration to subcritical velocities being accomplished with minimum shock drag. The guiding rationale in the design of conventional engine nacelle installations is to locate them so as to minimize any disturbance, in particular any disturbances to the wing upper surface leading-edge region.

11

The requirement, in this instance, to place the engine nacelles in this critical region could cause unacceptable interference drag penalties. Further, such penalties would be in addition to any that might be attributed directly to the nacelle. For example, one of the techniques mentioned in Section 6.1 for obtaining good low-speed turning of the engine exhaust utilizes high internal boattail angles on the top of the nozzle. The external shape of such a nozzle might well introduce unacceptable drag penalties.

Consider in more detail the nature of OTW high-speed nacelle-jet-wing interferences. The installation of the nacelles on the wing upper surface can be expected to adversely affect both the induced drag and compressibility drag characteristics, as well as creating an excess drag penalty due to the "scrubbing" of the engine exhaust on the surface.

The induced drag is affected not only by having closely coupled the nacelle and wing but also as a consequence of the fact that engine exhaust adheres to the wing upper surface, leaving the trailing edge at some angle to the free-stream. Both contribute to a change in spanwise loading. For example, the deflected engine exhaust will induce a change in wing circulation, a change expected to be concentrated in the area of the nacelles. The resulting distorted span load distribution is a source of a possible increase in induced drag. An additional adverse effect on the deflected engine exhaust can be attributed to the inclination of the jet far downstream which will result in a loss of thrust recovery. In other words, the engine exhaust is imbedded in the wake of the wing requiring the induced drag to be evaluated according to the procedures developed for jet-flap wings (See Reference 15).

The local increase in span load caused by the jet could possibly be eliminated by some appropriate selection of wing twist and/or local camber or possibly by a trailing edge control device. In either case, the intention would be to counteract the jet-induced circulation. However, any such device might well introduce a parasite drag penalty that would have to be balanced against the induced drag reduction. Alternatively, with the appropriate selection of spanwise spreading of the engine exhaust (i.e., distribution of jet momentum at the wing trailing edge) a favorable affect on induced drag might be obtained, it being noted that the induced drag of a jet-flap wing, in principle, is less than that of a conventional wing. Again, however, such favorable effects must be balanced, in part, with an increase in scrubbing drag.

The wing compressibility drag can be affected by the OTW nacelle installation because, as mentioned earlier, the nacelle flow field can interfere with the wing flow field to substantially alter the wing shock system and thus lower the drag divergence Mach number. The flow through nacelle wind tunnel results presented in Reference 1 have substantiated the existence of this interference in tests conducted without any simulation of the engine exhaust. The presence of the jet is expected to further complicate this problem.

Consider the interference of the nacelle without the jet on the wing flow field. Any disturbance should be in a favorable direction. Specifically, the nacelle must not cause any isobar unsweeping, but may be allowed to cause increased

isobar sweep. In principle, if the nacelle contours were to match a sheet of the wing-fuselage streamlines then the disturbances would be a minimum (Reference 18). As will be shown later (see Section 8.0), there are practical considerations that prevent this from being completely accomplished. Nevertheless, some promising results (Reference 1) have been demonstrated using unpowered wind tunnel models.

The effect of the jet on the wing flow field is of considerable concern due to the nature of the jet flow field. The concern is that the jet flow will interact with the wing shock system causing excess compressibility drag. This "power" effect cannot be simulated experimentally by a flow through nacelle of the type used in Reference 1 , proper simulation of the jet including the effects of shock expansion and entrainment being required. Experimental verification of some adverse effects can be implied from the results of Reference 2 . In this reference a straight wing panel was tested in the presence of a simulated OTW nacelle with a jet. The results showed a large increment in drag-due-to-lift associated with the nacelle and jet. There were several possible mechanisms involved. The pressure distribution on the jet centerline showed the effects of repeated jet expansion and compression cells which appeared to cause a pressure drag increase. The integrated span loading also showing very large increments between the jet-on condition and the simulated flow through case. In addition, traverses of the jet downstream of the wing showed the downward deflection of the jet taking the form of a relatively thin jet sheet with a rolled up vortex like structure at the edges of the jet.

The flight envelope of a STOL transport aircraft will result in engine operation at jet pressure ratios that can be either less than or greater than critical. In either case, the jet of an OTW engine installation enters an environment dependent not only on its location but also the speed and angle of attack of the aircraft. In cruise, if the jet is underexpanded, then one of the following two techniques might alleviate the compressibility drag problem. In the first technique, the high expansion velocities could be reduced by expanding to the local wing static pressure with a convergent-divergent nozzle. In the second a controlled-expansion arrangement where the wing is contoured aft of the nozzle could be used to control the expansion such that the familiar expansion-compression cyclic or "shock-diamond" variations and attendant shock waves are eliminated. With reference to those conditions during which the jet pressure ratio is less than critical, it should be noted that the external pressures in the area local to the nozzle exit can alter flow characteristics upstream of the nozzle itself. Undoubtedly, greater changes in propulsion system performance can be affected with an OTW installation than might be expected with a conventional under-the-wing arrangement, but whether such influences are important in the context of engine performance is still conjecture.

To conclude, the induced drag and compressibility drag effects as discussed above are clearly not independent of one another. While the jet locally increases wing loading it does offload the remaining portion of the wing at a constant total lift coefficient. Since this portion of the wing is carrying less lift, the compressibility drag associated with it will be lower than that of a wing with no jet (especially near the drag divergence

Mach number). This favorable change in compressibility drag is offset, however, by the added jet induced drag, the effect of the OTW installation on the wing-fuselage shock system, the jet scrubbing drag, and nacelle drag.

7.0 BASELINE SHORT-HAUL TRANSPORT AIRCRAFT

To assure that this technology development effort was grounded in realism, a baseline short-haul transport aircraft was developed to the extent necessary to define those parameters pertinent to this exploratory, high-speed investigation. Based, in part on the results of the system studies of Reference 3, the baseline aircraft was intended to be representative of a first generation STOL passenger aircraft. In other words, the aircraft should, as noted earlier, be approximately 150 passenger size and have a primary short-haul range requirement of 926 kilometers (500 n.mi.). In addition, the minimum field length performance of the aircraft should be in the neighborhood of 914 meters (3000 ft). Specified study ground rules required the baseline to be a four-engine high-wing aircraft with a cruise Mach number of approximately 0.7. The noise requirement described earlier was to be met through the utilization of a QCSEE (Quiet, Clean, Short-Haul Experimental Engine) type engine. This implied the selection of an engine cycle that would provide a fan pressure ratio at takeoff of 1.34 (Reference 17) and a fan pressure ratio in cruise in the range of 1.35 to 1.40. The noise shielding benefits of the OTW propulsion system installation permits the selection of a higher fan pressure ratio than would be appropriate for an EBF design. As a consequence, better engine propulsive performance and the potential for improved economics can result from the OTW location.

The ground rules and methods used in the aircraft sizing process performed in deriving the baseline aircraft are described in Reference 3. The procedure involves calculating takeoff and landing performance to determine wing loading (W/S) and thrust-to-weight ratio (T/W) combinations that produce a 914 meter (3000 ft) field length. These W/S and T/W combinations together with parametric weight, drag, engine performance and tail sizing data are combined with the mission requirements to define the aircraft characteristics such as takeoff gross weight (TOGW), wing area, and engine size. The derived aircraft characteristics presented below are considered to satisfy the study requirements discussed earlier.

Takeoff Gross Weight	kg	70,398
	(lb)	(155,200)
Wing Area, S_w	m^2	153
	(ft^2)	(1,651)
Engines (4)		
Static Uninstalled Thrust/Eng	N	76,954
	(lb)	(17,300)
Fan Pressure Ratio in Cruise		1.4
Bypass Ratio		10.5
Mixed Nozzle Area, A_{exit}/Eng	m^2	1.39
	(ft^2)	(14.8)

15

Performance
    Field Length   m   914
                                            (ft)   (3,000)

    Cruise Altitude   m   2,925
                                            (ft)   (26,000)

    Cruise Mach Number   0.715

    Radius   km   926
                                            (n.mi.)   (500)

    S_w/A_{exit} 28

The selected baseline aircraft is shown in Figure 7.1 and will henceforth be designated as U-150-3000 where U designates USB, the passenger payload is 150 and the field length is 914 meters (3000 ft). The selected baseline is a four engine high-wing aircraft with a wing aspect ratio, AR, of 7, taper ratio, λ, of 0.3, and a sweep angle, $\Lambda_{c/4}$, of approximately six degrees. The wing is a supercritical design with an average thickness/chord ratio of 0.14. The engine fan pressure ratio at cruise is 1.4 and wing area to engine mixed nozzle exhaust area ratio is 28.4. The choice of wing aspect ratio is based on a tradeoff between increased aerodynamic efficiency and increased wing structural weight associated with an increase in aspect ratio. The influence of aspect ratio on the sizing of a 150 passenger, 914 meter (3000 ft) field length externally blown flap STOL aircraft was evaluated in the NASA STOL Systems Study (Reference 3). The primary effect of increasing aspect ratio on aircraft drag is to decrease induced drag. Wing flutter penalties, which are a function of aspect ratio, wing loading, and wing area, are reflected in an increase in wing box weight needed to satisfy stiffness requirements. Results indicated that the variation of direct operating cost with aspect ratio is very small, being less than 0.5 percent for a variation in aspect ratio from 7 to 9 with a minimum occurring at an aspect ratio of 8. A similar aspect ratio trend for USB aircraft is expected. Considering today the increasing cost of fuel in relation to total direct operating costs combined with fuel economy considerations (passenger miles-per-gallon of fuel) the appropriate design compromise between wing weight, thrust requirements, and airport compatibility would be a wing with an aspect ratio in the order of 9. To conclude, it should be noted that engine size was selected for the field length and side line noise requirement rather than for the cruise speed requirment.

CHARACTERISTICS DATA

ITEM	WING	HORIZONTAL STABILIZER	VERTICAL STABILIZER
AREA (m^3)	153.38	53.33	38.83
(FT^3)	(1651)	(574)	(418)
ASPECT RATIO, AR	7.0	5.0	0.8
TAPER RATIO	0.3	0.45	0.8
SWEEP, $\Lambda_{c/4}$	$6^o15'$	$5^o15'$	40°
DIHEDRAL	0°	-3°	~
TAIL VOLUME	~	1.2	0.11

o   PAYLOAD CAPACITY
     ALL-TOURIST CLASS
        7 ABREAST (DC-9 SEATS) AT 0.86m (34 IN.) PITCH = 153 SEATS
o   CONVENTIONAL GALLEY
o   LOWER COMPARTMENT
  FORWARD BAY = 5 CONTAINERS (LD-3) AT 4.47 m^3 (158 FT^3) = 22.37 m^3 (790 FT^3)
  AFT BAY   = 2 CONTAINERS (LD-3) AT 4.47 m^3 (158 FT^3) = 8.95 m^3 (316 FT^3)
      TOTAL   = 31.32 m^3 (1106 FT^3)

38.56m (126.50 FT)

16.33m (53.57 FT)

32.77m (107.50 FT)

12.78m (41.92 FT)

.25 MAC
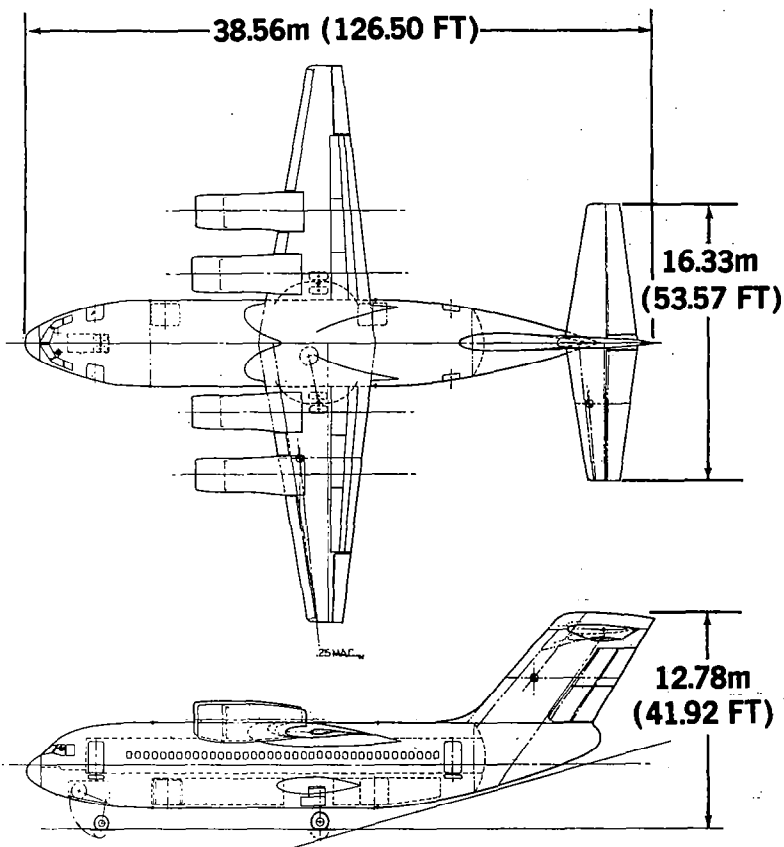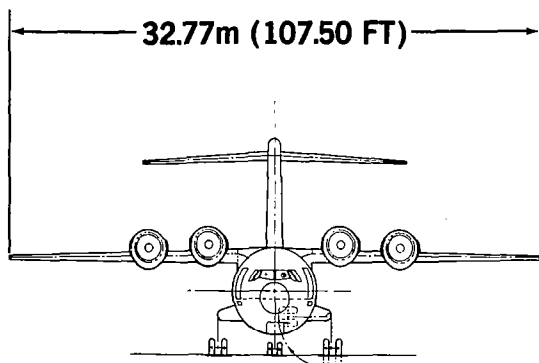
Figure 7.1.   Baseline Short-Haul Transport Aircraft -
Four Engine High-Wing and USB Flap (U-150-3000)

17

8.0 WIND TUNNEL MODEL CONFIGURATION DEFINITION

The configurations selected for the wind tunnel test are representative of components of the baseline short-haul transport aircraft (i.e. U-150-3000) described in Section 7.0. The array of configurations consists of a baseline wing + body + powered nacelles and several nacelle related alternate configurations.

8.1 Baseline Configuration

The baseline configuration consists of a wing + body and two nacelles on a semispan model utilizing low-angle nozzles that would require external flow deflectors to provide satisfactory low speed powered lift performance. The nacelles are referred to as "non-contoured" in that the nacelle designs do not reflect sophisticated or unusual external curvature intended specifically to match the wing-body flow field other than aligning the engine centerline and inlet with the mean local flow direction in the presence of the wing-body. During the test program, the baseline configuration was identified as N_1.

8.1.1 Wing-Body Configuration

The wing-body configuration is representative of the baseline short haul transport aircraft discussed in Section 7.0 and designated as the U-150-3000 with the exception that the fuselage design selected for the model is simplified relative to the U-150-3000 configuration in order to minimize the possibilities of masking or obscuring the nacelle interference results with fuselage upsweep or compressibility drag effects. The significant contribution of the fuselage to the nacelle interference study is judged to be in the area of wing span-load or induced drag, so the fuselage diameter-to-wing span ratio was set to match the U-150-3000 value, and the wing-to-fuselage height relationship and fillet arrangement is consistent with the U-150-3000.

The fuselage fineness ratio is higher than would be used in an aircraft design to ensure that no fuselage compressibility drag will be experienced prior to the wing drag rise Mach number.

The wing configuration is based on one of the wings tested during the development of the Douglas/Air Force AMST Prototype (i.e. YC-15). This design evolved from Douglas analytical and experimental technology development activities, the aerodynamic characteristics of which have been verified through wind tunnel tests. The aerodynamic characteristics of this wing, including surface pressure distributions, were available and deemed to be well suited to this investigation. The use of this proven wing design ensured that the baseline wing-body aerodynamic characteristics would be appropriate for the intended investigation. The margin between the predicted model drag rise Mach number and the typical cruise Mach number of the U-150-3000 configuration ($\Delta M=0.04$) is particularly appropriate relative to fixing boundary layer transition of the wing as will be explained in Sections 10 and 11.

The characteristics of the wing-body are shown in Figure 8.1, the wing twist is plotted in Figure 8.2, and the defining airfoil shapes and ordinates are shown in Figures 8.3, 8.4, and 8.5. The wing is a straight taper wing of aspect ratio 7 and taper ratio 0.3. The sweep back of the quarter chord line is 5.62 degrees. The fuselage has a fineness ratio of 9.8 and is a streamline body of revolution having no upsweep or windshield represented. Other significant model parameters are also listed in Figure 8.1.

8.1.2 Location of Nacelles

The selection of the spanwise location of the nacelles (23 and 48 percent of the wing semispan) was based on STOL technology development and design activities conducted by Douglas and reported in Reference 3. The dominant factors in the selection problem relate to low speed high-lift performance and to lateral-directional stability and control requirements under conditions of a single engine failure in the most critical low-speed high-lift condition.

One alternate (28 percent of wing semispan) location of the inboard nacelle provides the capability of evaluating nacelle to body and nacelle to nacelle spacing effects on nacelle interference drag. The three possible nacelle locations also provide the capability of evaluating the effect of nacelle spanwise location on configuration drag due to lift.

The nacelle nozzle exit plane is located at 35 percent of local wing chord. This position was selected after considering several factors:

1. The wing pressure distributions (Figure 8.6) show that the local flow is subsonic with moderate chordwise pressure gradients in the vicinity of this location at the design conditions of $M = .70$ and $C_L = .38$. The nozzle exit is trimmed normal to the fuselage (and nozzle) centerline, resulting in an exit plane that does not lie along the isobars of the wing. Also a modest pressure gradient exists in the vertical direction in the basic wing-body flow field. It was considered desirable to locate the nozzle such that these pressure gradients would be minimized to avoid undue distortion of the nozzle sonic sheet.

2. An external deflector located aft of the nozzle would be required to deflect the exhaust flow toward the wing surface. The resulting impingement of the flow on the wing, and attendant spreading of the flow to accomplish the desired thinning of the plume prior to reaching the flap knee would require a significant portion of the wing chord.

3. The acoustic shielding provided by the USB type of nacelle installation is enhanced by extending the run of the exhaust over the wing surface, i.e., the acoustic advantages of the configuration are maximized with forward exit plane locations.

4. Practical considerations relating to structural arrangements, internal duct shapes, and the desire to keep the engine completely forward of the front spar (to permit lowering the engine straight down during engine change) led to relatively forward nozzle exit locations.

19

.The selected location of the nozzle exit plane is considered to be satisfactory for the purpose of this investigation, but a more comprehensive investigation might well include alternate chordwise locations as a configuration variable. The nacelle locations on the wing are shown in Figure 8.7.

8.1.3 Simulator Cycle Analysis

The major objectives of the nacelle internal design were:

1. To provide an exhaust flow with an essentially uniform total pressure distribution over a range of fan pressure ratio (FPR) of 1.2 to 1.5, optimized at FPR = 1.38.

2. To ensure that the simulator fan will be unstalled throughout the desired operational envelope.

A cycle analysis was conducted for the Tech Development Inc. model TD-800 turbo simulator (described in more detail in Section 9) based on an experimentally determined fan performance map, estimated turbine characteristics, and estimated duct losses. With the objective of providing uniform exit total pressure, the areas at the turbine and fan discharge stations were determined. The fan and turbine discharge Mach numbers were predicted to be essentially equal, indicating that a forced mixer turbine discharge nozzle would not be required. The required duct areas entering the mixed region and the final exit area as well as nominal flow properties through the internal flow system were predicted. Comparisons of the nominal predicted flow properties with measured quantities during the subsequent nacelle calibrations established the validity of the cycle analysis, and no rematching of the simulator was required.

8.1.4 Nozzle Design

Analysis of published data relating to static turning effectiveness of USB systems utilizing external deflectors (References 8, 19, and 20) indicates that the system effectiveness is relatively insensitive to nozzle aspect ratio, (width)^2/area, over the range of two to five with reasonable deflector sizes and deflections. A nozzle aspect ratio of 2.5 was selected for the baseline nozzles to provide nearly constant width nacelles, i.e., to avoid severe boattailing or fishtailing in the plan view. A relatively soft "cornered" D shape was selected at the exit plane to avoid severe suction peaks due to crossflow over the "corners".

Approximately equal upper and lower boattail angles (11°) were selected in conjunction with a relatively mild internal duct offset in the mixing section between the nozzle exit station and the forward end of the nozzle, approximately 13.2 cm (5.2 inches) forward of the exit station. A drawing of the N_1 nozzle geometry is shown on Figure 8.8. Geometric details and the internal area distribution are presented in Section 8.3.

The objectives of this program are primarily related to nacelle interference studies involving external flows; so the internal design of the nacelles was deliberately conservative. The resulting compromise in nacelle overall length, partly attributable to the conservative nozzle design should not significantly influence the results of the current investigation. It is

recognized however that a comprehensive configuration development program would necessarily involve extensive coordinated internal and external development work.

8.1.5 Inlet Design

The nacelle inlet was designed to pass the maximum airflow that would be required under any planned test condition at a throat Mach number of .75. The diffuser was conservatively designed with a length equal to one fan diameter.

The inlet, cowl, and diffuser geometric parameters are:
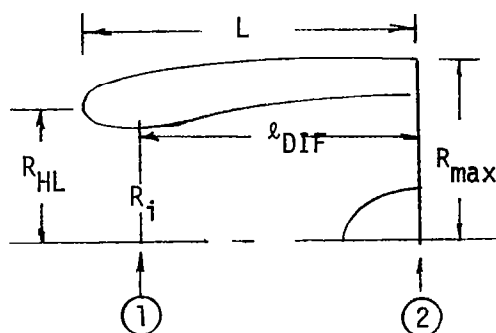
$$\left(R_{HL}/R_{max}\right)_{TOP,SIDE} = .798$$

$$\left(R_{HL}/R_{max}\right)_{BOTTOM} = .641$$

$$\left(\frac{R_{HL}-R_i}{R_{HL}}\right)_{TOP,SIDE} = 0.11$$

$$\left(\frac{R_{HL}-R_i}{R_{HL}}\right)_{BOTTOM} = 0.20$$

$$\left(A_2/A_i\right)_{DIFFUSER} = 1.23$$

$$\ell_{DIF}/R_i = 2.426$$

$$L = 8.58 \text{ cm (3.377 IN)}$$

CONSISTENT WITH
DOUGLAS EBF QCSEE
EXPERIENCE (REF 21).

21

The external cowl shape is a modified NASA Series 1 inlet cowl.

The inlet (internal) lips are elliptic.

The external inlet cowl was designed to ensure freedom from inlet spillage drag over the range of fan pressure ratios planned for the test, and for the flow-through versions of the nacelles. A drawing describing the inlet which forms a part of the N_1 nacelle is shown on Figure 8.8.

8.1.6 Flow-Through Nacelles

A reason for including flow-through type nacelles in this program was to provide an unpowered nacelle reference level for the studies related to the effects of fan pressure ratio on interferences due to the exhaust plume. Also, the flow-through nacelle was needed to better identify the mechanisms of aerodynamic propulsion interferences and to establish the limitations of methodology which can only approximate multi-energy flows. Consideration was given to the possibility of utilizing the powered nacelles at an engine pressure ratio of 1.0 for this purpose, but two factors precluded this possibility.

1. At a fan pressure ratio of 1.0 elements of the fan blades would be operating at relatively high negative blade sectional lift coefficients, and could be subjected to unsteady blade loading.

2. Uncertainties related to the residual swirl, turbulence and possible distortions of the exhaust total pressure distribution within the plume of the powered nacelles operating at a fan pressure ratio of 1.0 might introduce extraneous interferences that would obscure the results of the investigation.

It is of some interest to note that late in the experimental program, a single direct comparison of flow-through and powered nacelles was obtained at comparable FPR. Excellent agreement was observed when comparing the resulting drag polars.

The flow-through nacelle configurations utilized in this program, as implied above, were required to utilize the same outer shape as the powered nacelles, as that shape influence the interference drag at any level of fan pressure ratio. Fortuitously, the powered nacelle airflow requirements are approximately equal to the flow-through nacelle airflow requirements, so that the powered nacelle inlet is well suited for use as the flow-through inlet.

The flow-through nacelles were obtained by removing the powered simulators and installing a simple fairing ring in their place.

8.2 Alternate Configurations

Several alternate model configurations were provided, including an alternate inboard nacelle location and inboard or outboard nacelle alone, streamline contoured nacelles, a convergent-divergent nozzle version of the baseline nacelle, a controlled expansion panel inset into the wing aft of the nacelle, trimmer flaps aft of the baseline nacelle locations, and a high boattail

22

angle nozzle of the type that would not require an external flow deflector to achieve satisfactory low-speed high lift performance.

8.2.1 Alternate Spanwise Location of Nacelles

The inboard nacelle locations were at 23 or 28 percent of wing semispan. Each nacelle location was provided with a plain wing insert so that the model may be configured without nacelles, with one nacelle at three different spanwise stations, with the baseline spacing or with the baseline outboard and 28 percent semispan inboard location. As previously stated, this permits evaluation of nacelle to body and nacelle to nacelle interference effects, and nacelle spanwise location effects on drag due to lift.

8.2.2 Streamline Contoured Nacelles

The interferences of the nacelles with the wing body flow field may be grouped into two broad categories:

1. Those effects resulting from shape differences between the actual nacelle (referred to here as solid body interference) and the local wing-body flow field stream sheets (formed by streamlines) in the vicinity of the nacelle.

2. The effects of the propulsive stream tube on the wing-body flow field. In this case the exhaust plume portion of this propulsive stream tube is the significant contributor to the interferences.

8.2.2.1 Streamline Contouring to Minimize Solid Body Interference - The wing-body flow field was established for the design conditions of $M_0 = .7$ and $C_L = .38$ using the Douglas Neumann three-dimensional lifting potential flow program (Reference 22), which includes a Goethert correction for compressibility effects. Inasmuch as the wing design provided a small margin between the design point and the drag divergence Mach number at $C_L = .38$, the shock system is very weak at the design point. The validity of this approach is substantiated by the agreement between the calculated and experimentally measured surface pressure distribution (Figure 8.6).

To further establish the credibility of the approach, a very high aspect ratio constant section wing (AR = 30) was used in a trial case. The flow field was established using the three-dimensional potential flow method and the results were compared to a direct Garabedian transonic two-dimensional flow field solution (Reference 23) for the same airfoil. Off-body stream-lines were traced through each of the flow fields. An approximate correction was applied to the mean downwash angle at the three-dimensional wing. The observed differences in the two sets of streamlines were negligible.

The effects of the boundary layer on calculated supercritical airfoil aerodynamic characteristics have for some time been recognized as being significant, particularly with respect to the effectiveness of the aft camber of the air-foil. To approximately account for these effects, the displacement thickness of the boundary layer assuming natural transition was calculated using the methods of Reference 24 at each of the three design airfoil stations at

appropriate values of section lift coefficient and at the expected test values of Mach number and Reynolds number.

The calculated boundary layer displacement thickness distribution was slightly modified near the wing trailing edge. These modifications are based on recent Douglas experience acquired in the correlation of two-dimensional test data with analytical predictions. The resulting estimated displacement thickness distributions were added to the geometric airfoil shapes at the design airfoil stations to define the mathematical model of the wing to be used in the flow field soltuions.

Off-body streamlines were traced through the wing-body flow field solution in the vicinity of the nacelle locations. The results indicated that the most pronounced streamline curvatures in the vicinity of the nacelles exist in the profile view. The straight wing selected for this model, as would be expected, does not produce extreme streamline curvatures in the plan view, except in the region very close to the leading edge.

The off-body wing-body streamlines in the profile view at design conditions are shown in Figure 8.9 with the contoured nacelle superimposed in the flow field. The general approach taken to minimize the solid body interference of the nacelle with the wing-body flow field was to establish a "design" stream tube coincident with the nacelle surfaces well forward of the wing, traced back over and under the wing, and to force the nacelle to conform to the design stream tube where practical. The design stream tube was treated in two pieces: an upper and a lower stream tube separated forward of the wing by the quasi-stagnation sheet. The upper wing surface was considered to be more sensitive to the solid body interference in this case; so the portion of the nacelle located above the quasi-stagnation sheet was forced to closely conform to the upper stream tube shape. The remainder of the nacelle was permitted to violate the lower design stream tube shape, particularly in regions of favorable pressure gradient.

The essence of the lower stream tube design problem is to reduce the nacelle cross-sectional area (i.e., to terminate the lower surface of the nacelle contrary to the requirements of the design stream tube) in a manner that does not unreasonably affect the configuration lift or drag.

The undersurface fairing, as designed, represents a first cycle result. The flow field analysis of the configuration utilizing this fairing strongly suggested that the fairing could, contrary to intuition, be terminated in the vicinity of the lower 35-percent chord station. The high local boattail angles of such a truncated fairing are, in this case, acceptable even in this favorable pressure gradient. The word acceptable in this case is used primarily with respect to the likelihood of inducing local flow separation. The effects of the local downward lift forces generated by these fairings and the attendant distortions of the spanload distributions are calculable using this methodology, but the credibility of such calculations must be established through correlations with experimental results before the methods may be used for direct design work.

Schedule limitations precluded recycling the first fairing shape, but the

calculated and experimental results suggest that further development work in this area may be justified.

The nacelle also conformed closely to the streamlines in the plan view. The plan view contouring was accomplished by shearing spanwise the nozzle cross-sectional cuts so that the centerline of the nacelle in the plan view followed a selected streamline as illustrated in Figure 8.10. The selected streamline is shown in the profile view in Figure 8.9.

The resulting nozzle is shown on Figure 8.11 and is identified as the N_2 nacelle. The internal duct has a large curvature just upstream of the nozzle exit. Internal flow analyses were used to verify that flow choking or large losses did not occur in this region.

8.2.2.2 <u>Internal Nozzle Design to Minimize Plume Interferences</u> - To compliment the contoured nacelle which was designed to minimize the solid body interferences of the nacelle with the critical wing upper surface flow field, a convergent-divergent (C-D) nozzle was designed for inclusion in the contoured nacelle to deliver the exhaust plume to the flow field aft of the nozzle in a fully expanded condition. Such a plume would more closely represent a smooth extension of the contoured nacelle nozzle by eliminating a rapidly expanding plume aft of the nozzle. In addition, the C-D nozzle will eliminate or reduce the cyclic pattern of the jet thereby reducing the probability of jet effects on the wing flow structure.

The shortening of the subsonic portion of the internal ducting resulting from incorporating the C-D nozzle in the N_2 nacelle produced an "S bend" that was considered to be unacceptable. The apparent options of lengthening the nacelle to relieve this problem, or separately evaluating the C-D nozzle in the baseline nacelle shape (N_1) (with a less severe internal duct offset) were considered. The latter option was selected and a C-D nozzle was incorporated into a set of nacelles having the same basic shape as the baseline nacelles except that the exit nozzle area is enlarged appropriately to accommodate the C-D nozzle.

The convergent-divergent nozzle design was based on a Method of Characteristics (MOC) analysis (Reference 25) and a FPR of 1.54*. A nozzle lower surface was chosen which faired smoothly into the wing upper surface. A pressure distribution was chosen on this lower surface which faired smoothly into the predicted C_p's of the wing upper surface aft of the nozzle exit. The flow field in the region shown in Figure 8.12 was defined using the 2-D MOC solution and streamlines were traced in this flow field at various heights. The 3-D nozzle was designed as illustrated in Figure 8.13 by tracing streamlines forward from the desired exit shape to the throat. The exit was sized to provide the throat area required for simulator cycle matching.

The resulting nozzle design is shown in Figure 8.14 and is identified as the N_4 nacelle.

---

*This value of FPR was selected prior to the final definition used for the program of 1.38.

8.2.3 Controlled Expansion Panel

Another way of reducing the plume expansion into the wing flowfield and improving the engine thrust is to contour the wing surface downstream of the nozzle exit. Proper contouring can reduce or eliminate the cyclic shock pattern of the jet boundary, as described in Reference 25. To design the controlled expansion (C-E) panel, the shape of the jet upper surface was assumed and the pressure distribution along this surface computed using the previous wing-body 3-D Neumann streamline solution. 2-D corrections were applied to the C_p's to correct for the small differences in the wing-body streamline and the prescribed jet surface. The 2-D MOC solution at a FPR of 1.54* was then used to solve for the flow from the jet surface downward through the wing surface as shown in Figure 8.15. A streamline was then traced from the lower surface of the nozzle exit. The jet free surface was modified as required to ensure shock free jet flow and a streamline which fairs smoothly from the nozzle exit to the wing trailing edge. As shown in Figure 8.15 the jet flow does not exhibit the typical sonic nozzle cyclic flow pattern and does not contain any shock waves. These two effects should reduce the effect of the jet on the wing and improve the thrust performance.

The design of the C-E panel is based on the assumption of 2-D supersonic flow. Such a condition will not exist at the sides of the jet since it will expand laterally into the wing flow field. Side plates to control this lateral expansion were not included in the test program.

8.2.4 Jet Deflection Effects

As described in Section 6 , the effects of the downward deflection of the exhaust plume by the upper aft surface of the wing, if such deflection is of the order of ten degrees or more, may be expected to produce significant effects on both lift and drag. The lift will be increased through the familiar part-span jet flap mechanisms involving both reaction and induced circulation effects. The drag will be adversely affected by the resulting distortions of the wing span loading in addition to the thrust vectoring losses associated with thrust deflection angles greater than optimum (normally in the range of 2-4 degrees).

The effective thrust deflection angle under "wind on" test conditions can be directly determined only through extensive wake survey techniques that were beyond the scope of this program. Assumed values of effective exhaust turning based, in part, on static (wind off) turning values are customarily used to predict the jet deflection effects.

What is needed is an analytical method which will account for the magnitude and direction of the jet as it leaves the trailing edge of the wing. The jet momentum, C_μ, is not necessarily that of the jet as it leaves the nozzle, but rather some factor times C_μ determined by the geometry of the wing and the effects of the external flow.

To provide a basis for establishing a correlation between the theoretical and experimental sensitivities of lift and drag to thrust deflection angle, plain flaps were located at the wing trailing edge directly aft of the baseline nozzle locations. The pressure distributions within the plume would provide

----

* See note previous page.

a basis for estimating the turning losses (due to flap deflection) and permit
a basis for correlating the remaining drag change with the Douglas Elementary
Vortex Distribution (EVD) (Reference 15) predicted results.

The trimmer flaps are not regarded as a means of improving performance, but
rather as a means of establishing a correlation between the existing analyti-
cal modeling techniques and experimental data relating to jet deflection
effects. Also, the trimmer flaps will provide an indication of the effect
of the turning of the jet on the induced drag.

The results of the analysis are compared to the test data in the Results
Section (Section 11.0).

8.2.5 High Boattail Angle Nacelle

The high boattail angle nozzle design for this model was furnished by NASA.
This nozzle, with an external crown-line terminal boattail angle of 28.5
degrees, was developed for the NASA QCSEE (Quiet Clean Short-Haul Experimental
Engine) program (Reference 26) and is representative of the type of USB nozzle
that is capable of providing satisfactory low-speed high-lift performance
without the use of external flow deflectors. The objectives in including
this configuration were to evaluate the nozzle design at cruise and to compare
cruise performance for this type of installation to that of the low angle
nozzles (N_1, N_2, and N_4) which would require flow deflectors for satisfactory
powered lift. It should be noted that related low-speed tests were conducted
at NASA Langley (Reference 27) using a low-speed version of this nozzle design
as part of a more comprehensive design development program under the manage-
ment of the NASA QCSEE Project Office.

Several modifications to this nozzle were evaluated at cruise speeds by NASA-
Lewis following the completion of the joint Douglas-NASA program. These
results were reported in Reference 28 and are not presented here.

The nozzle design used for this program is identified as the N_3 configu-
ration and a description of the nozzle is shown in Figure 8.16.

8.3 Summary of Nozzle Designs

8.3.1 Nozzle Geometric Parameters

Significant geometric parameters for the four experimental nozzle configu-
rations are defined in Figure 8.17. All of the nozzles had similar D-shaped
exit geometries.

8.3.2 Nozzle Internal Area Distributions

The internal area distribution of each of the nozzles previously described
is shown on Figure 8.18.

MODEL DIMENSIONS

WING   FUSELAGE

Wing Area   0.279 m² (3.0 FT²)   Length   1.803 m   (5.917 FT)
           (0.139 m² For Half Model)   Diameter 0.182 m   (0.596 FT)

Aspect Ratio 7

Semi-Span   0.698 m (2.29 FT)

Quarter Chord Sweep   5.6°

Taper Ratio   0.3

$C_{MAC} = C_{REF} = 21.88$ cm (8.616 IN)

10 cm
10 in
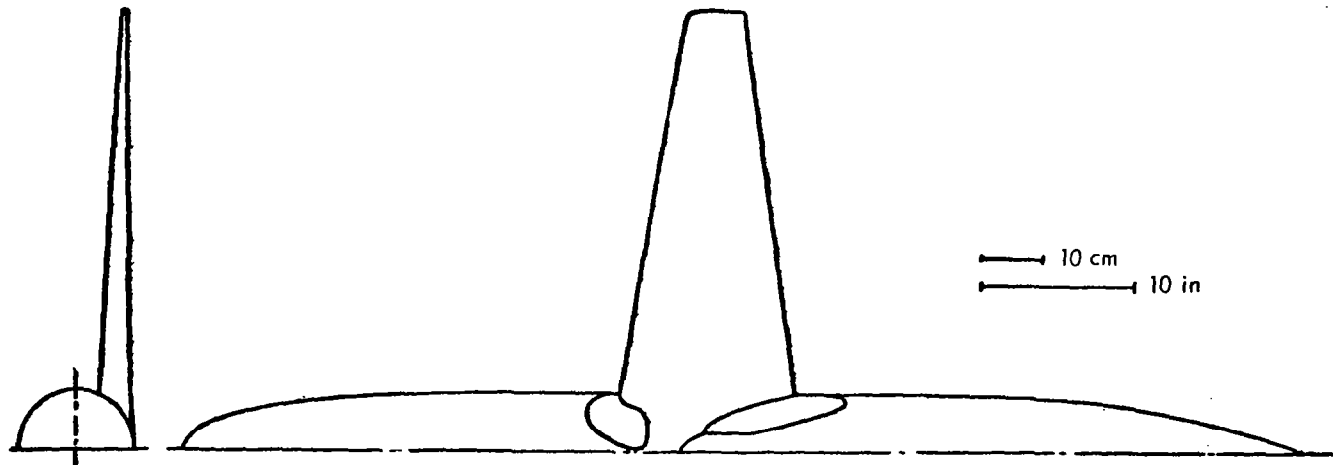
Figure 8.1. Drawing of Wing-Body
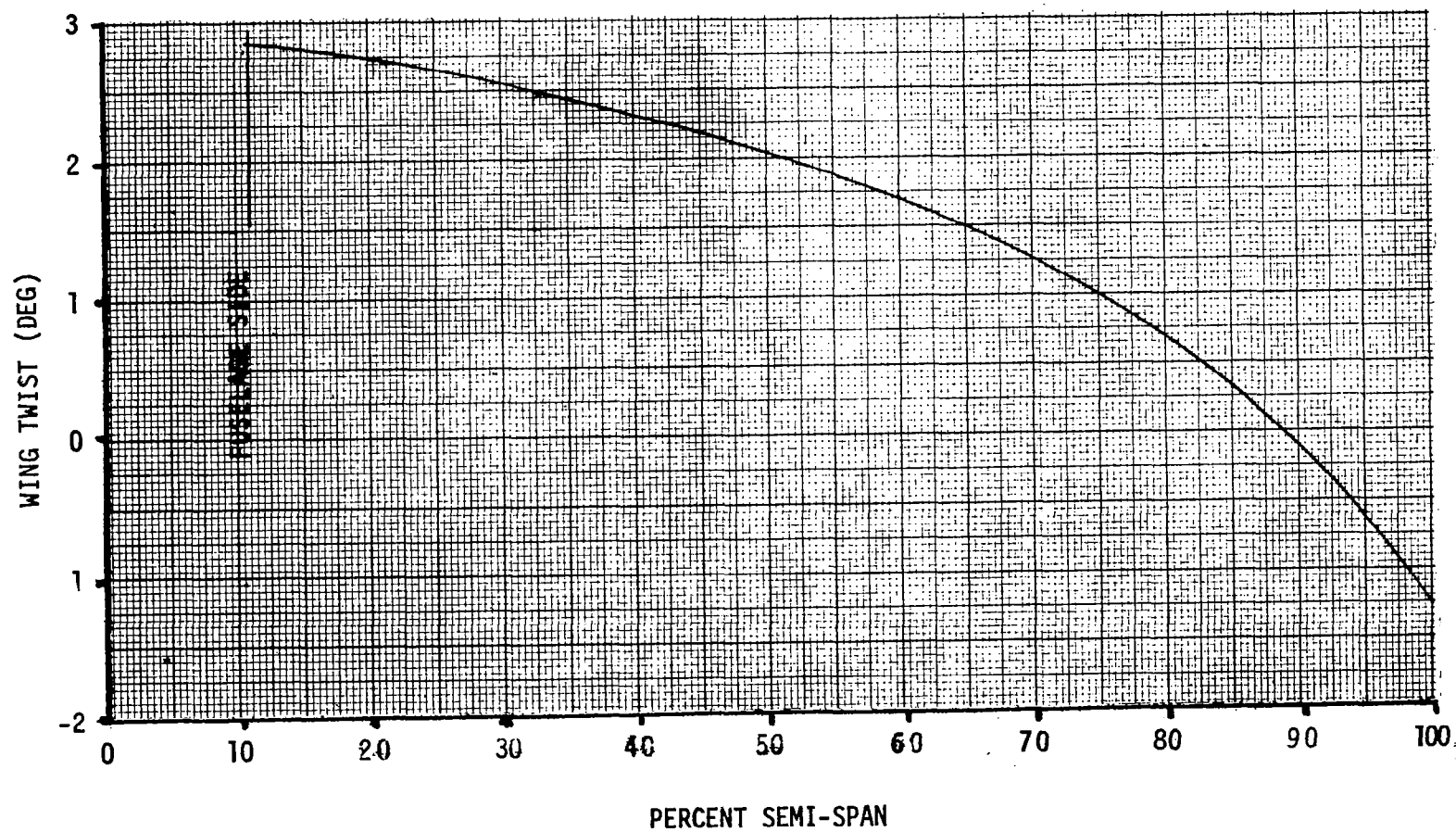
Figure 8.2. Wing Geometric Twist

11 PERCENT SEMI-SPAN AIRFOIL

X/C	Y_U/C	Y_L/C
0.0	0.0	0.0
.0008	.00712	-.00503
.0050	.01648	-.01419
.0152	.02727	-.02519
.0295	.03666	-.03485
.0475	.04513	-.04349
.0740	.05380	-.05277
.1086	.06173	-.06149
.1575	.06948	-.07022
.2200	.07564	-.07684
.2991	.07897	-.07931

X/C	Y_U/C	Y_L/C
.3920	.07746	-.07619
.4867	.07133	-.06856
.5725	.06299	-.05747
.6553	.05327	-.04384
.7351	.04249	-.02956
.8060	.03181	-.01727
.8640	.02264	-.00857
.9111	.01519	-.00341
.9480	.00948	-.00114
.9770	.00515	-.00086
1.0	.00187	-.00187

Figure 8.3.   Airfoil Definition at 11% Semispan

32.6 PERCENT SEMI-SPAN AIRFOIL

X/C	Y_U/C	Y_L/C
0.0	0.0	0.0
.0008	.00531	-.00419
.0050	.01270	-.01162
.0152	.02116	-.02040
.0295	.02864	-.02822
.0475	.03543	-.03537
.0740	.04257	-.04320
.1086	.04939	-.05075
.1575	.05648	-.05866
.2200	.06270	-.06538
.2991	.06744	-.06962

X/C	Y_U/C	Y_L/C
.3920	.06953	-.06938
.4867	.06817	-.06411
.5725	.06421	-.05415
.6553	.05804	-.04006
.7351	.04963	-.02377
.8060	.03983	-.00932
.8640	.03013	-.00022
.9111	.02119	.00341
.9480	.01360	.00321
.9770	.00734	.00094
1.0	.00225	-.00225

Figure 8.4. Airfoil Definition, 32.6% Semispan

95 PERCENT SEMI-SPAN AIRFOIL

X/C	Y_U/C	Y_L/C	X/C	Y_U/C	Y_L/C
0.0	0.0	0.0	.3920	.05953	-.06353
.0008	.00427	-.00427	.4867	.05846	-.05893
.0050	.01087	-.01090	.5720	.05584	-.04948
.0152	.01783	-.01808	.6553	.05149	-.03613
.0295	.02373	-.02432	.7351	.04513	-.02091
.0475	.02905	-.03004	.8060	.03728	-.00771
.0740	.03493	-.03664	.8640	.02916	.00018
.1084	.04097	-.04354	.9111	.02145	.00270
.1575	.04748	-.05118	.9480	.01478	.00160
.2200	.05326	-.05788	.9770	.00928	-.00137
.2991	.05773	-.06257	1.00	.00515	-.00514

Figure 8.5. Airfoil Definition, 95% Semispan
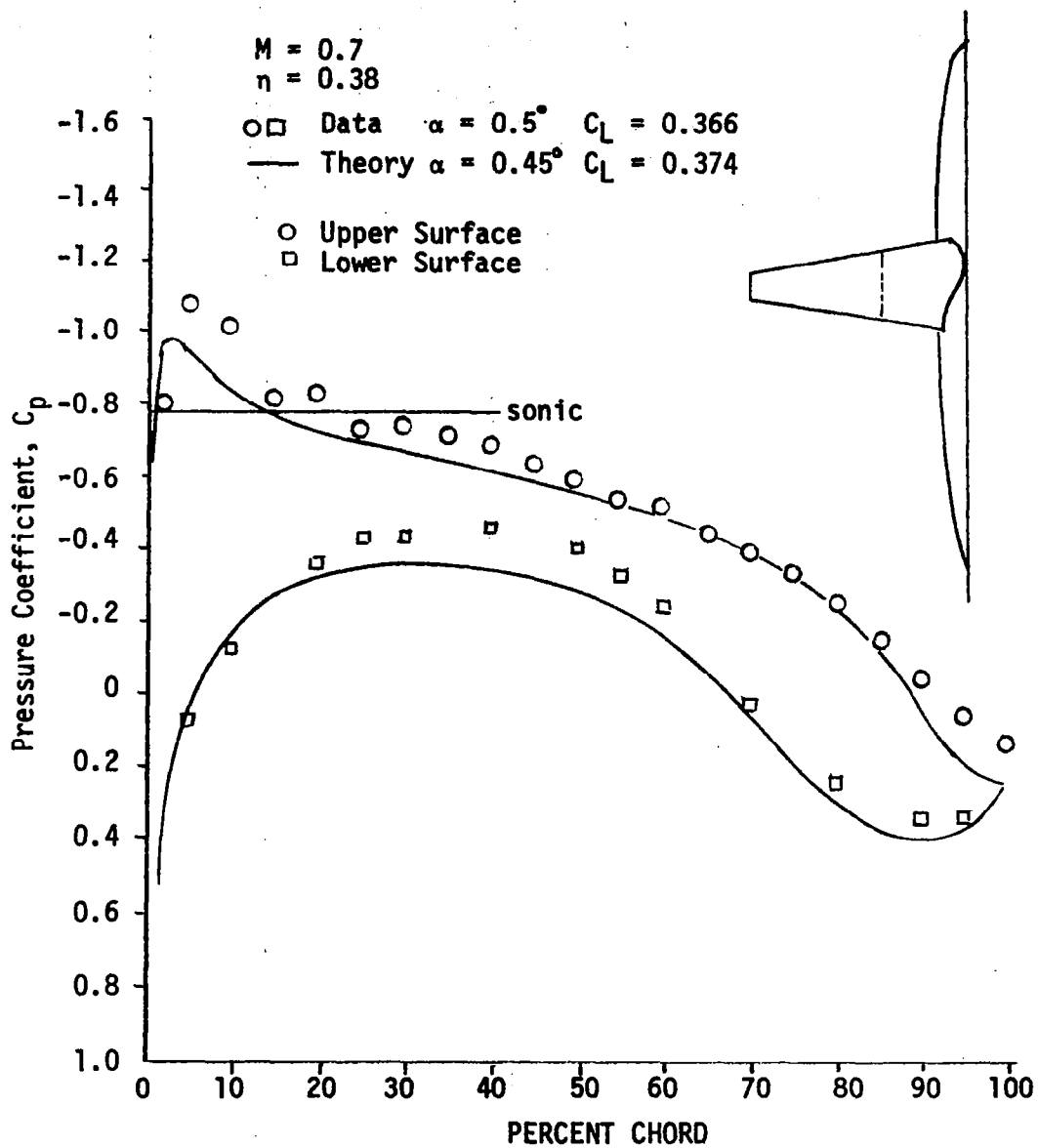
Figure 8.6. Theory-Data Comparison for Wing-Body at 38% Semispan
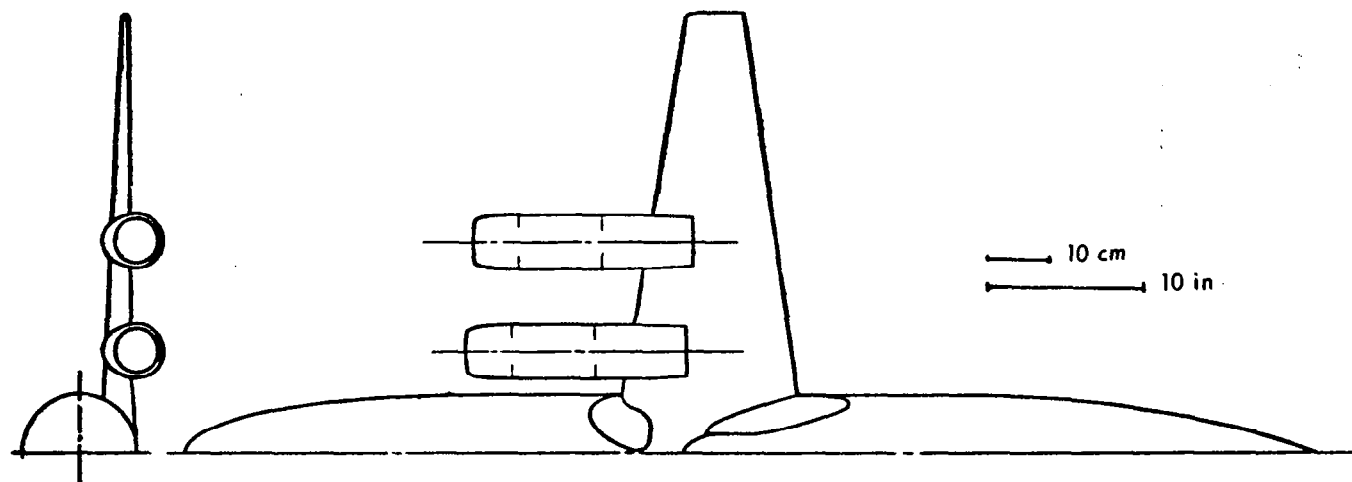
Figure 8.7.   Wing Body with Nacelles Installed
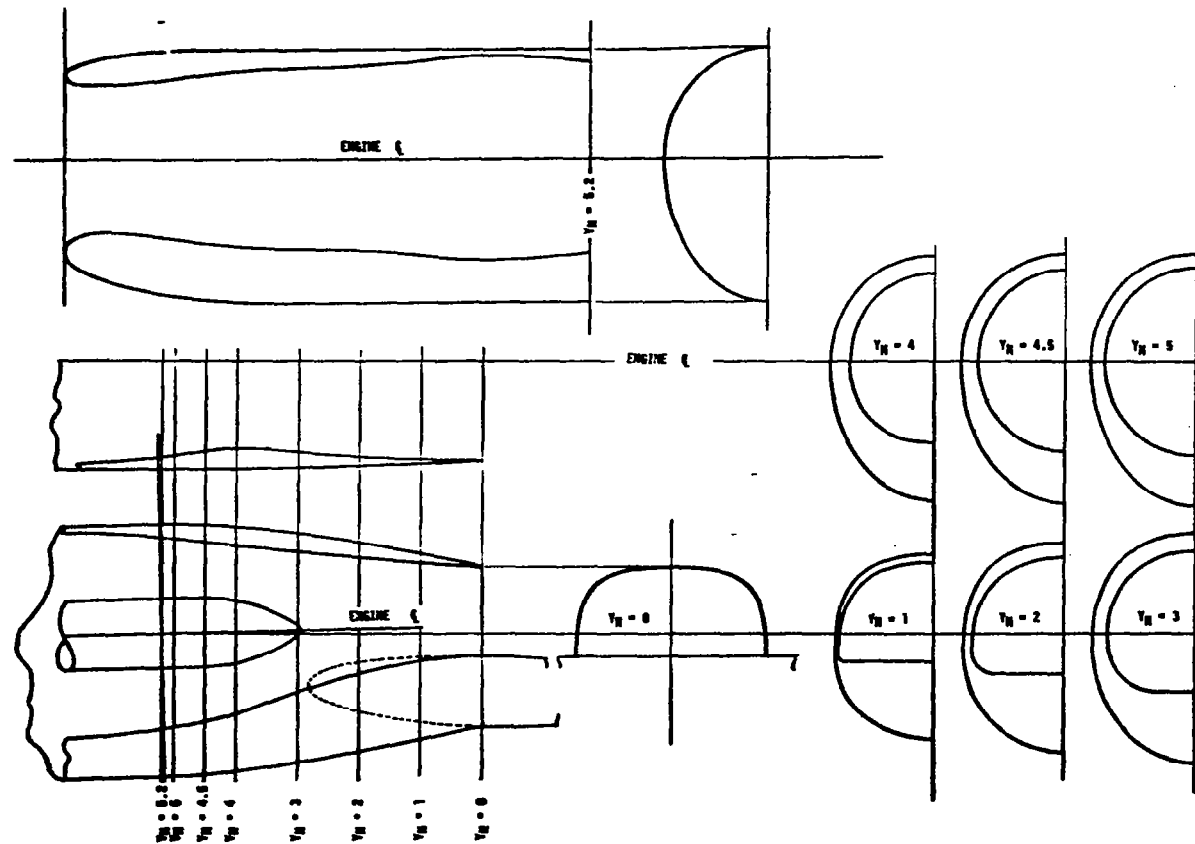
Figure 8.8. Description of Baseline Non-Contoured Nacelle N_1

Streamline used for
spanwise contouring
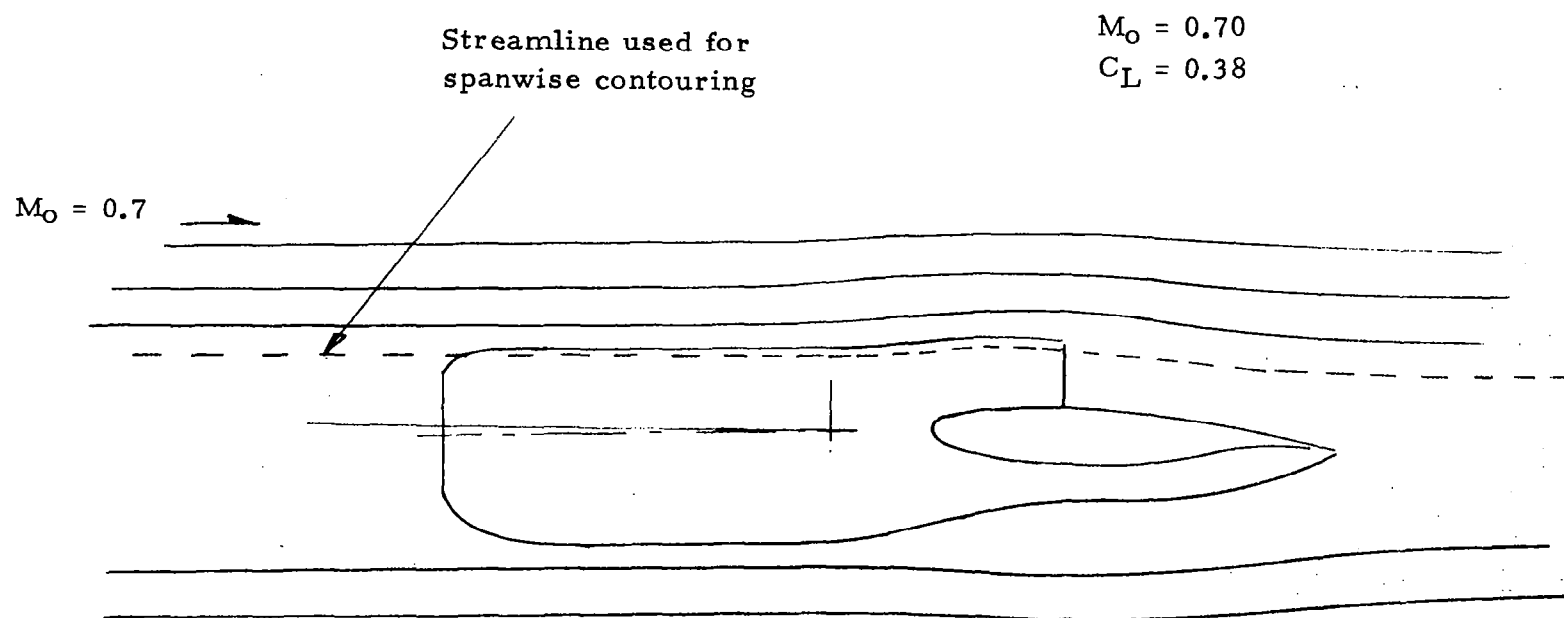
$M_O = 0.70$
$C_L = 0.38$

$M_O = 0.7$

Figure 8.9. Profile View of Wing-Body Streamlines and Contoured Nacelle

$M_O = 0.70$
$C_L = 0.38$

Spanwise Variation of Nacelle Centerline
(Coincident with Streamline)
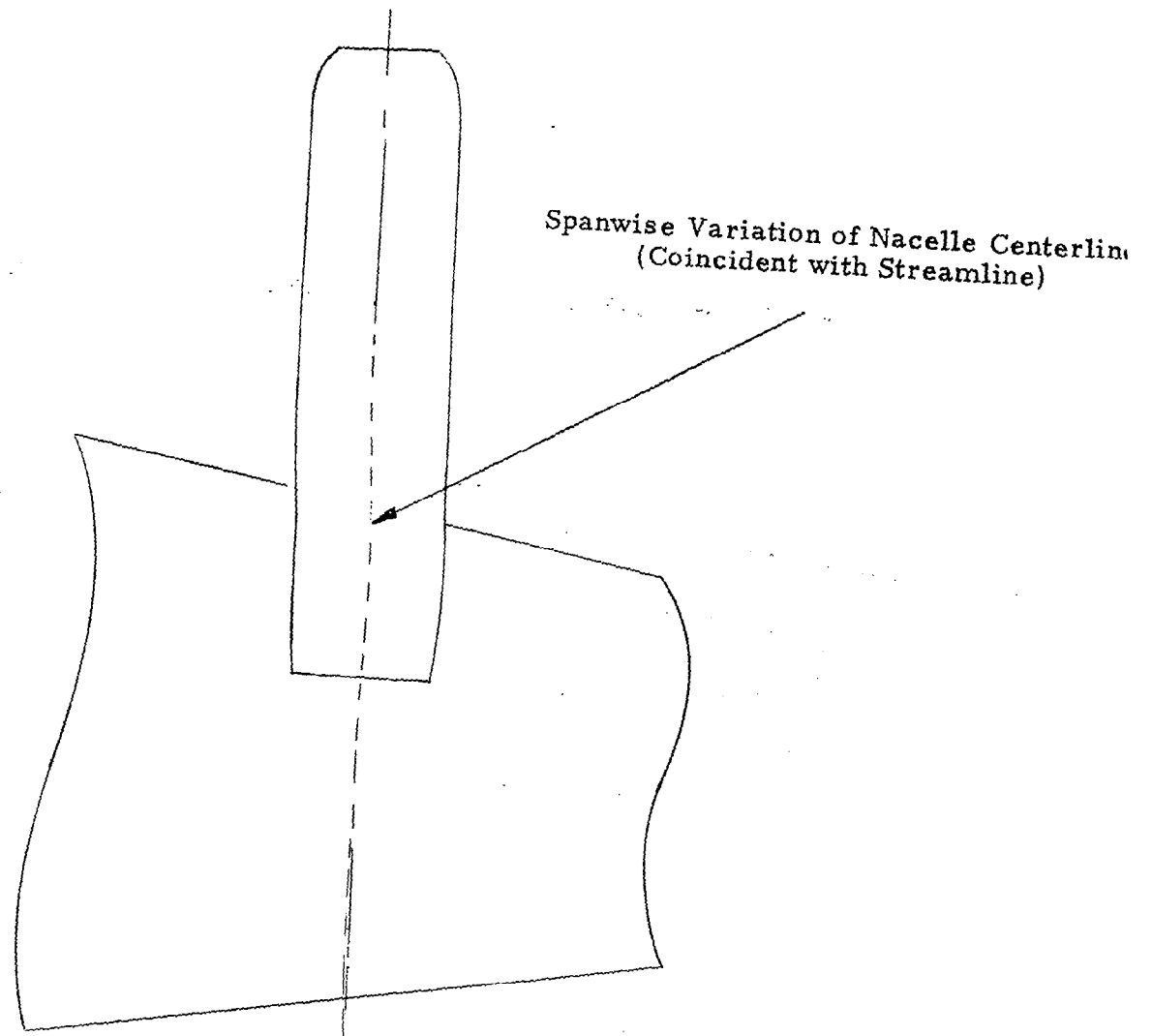
Figure 8.10. Planview of Contoured Nacelle

REF. RIGGING LINE

ENGINE $\mathcal{G}$

ENGINE $\mathcal{G}$

$Y_N = 3$

$Y_N = 4$

$Y_N = 5$

$Y_N = 0$

$Y_N = 1$

$Y_N = 2$

$Y_N = 5.2$
$Y_N = 5$

$Y_N = 4$

$Y_N = 3$

$Y_N = 2$

$Y_N = 1$

$Y_N = 0$
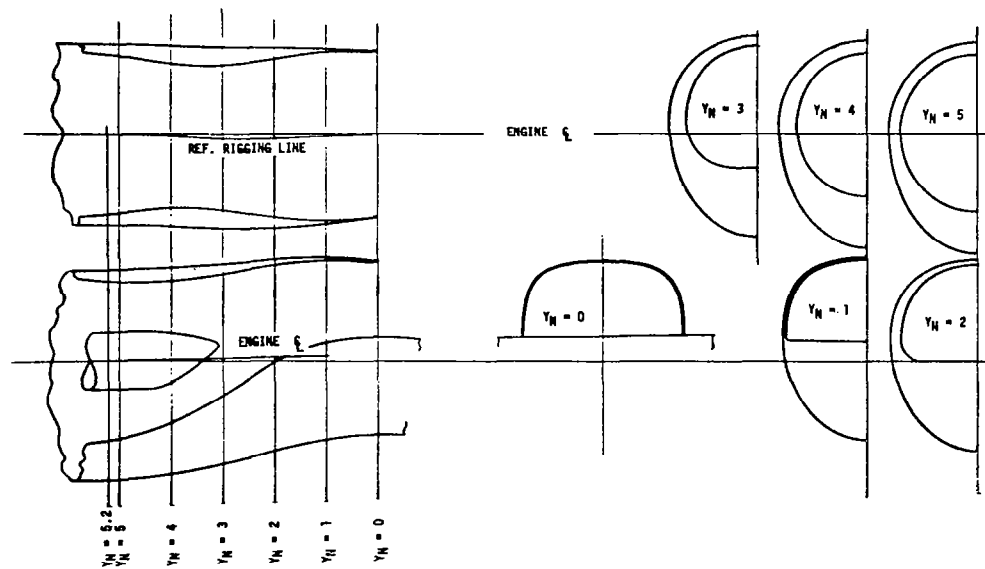
Figure 8.11. Description of Streamline Contoured Nacelle N_2
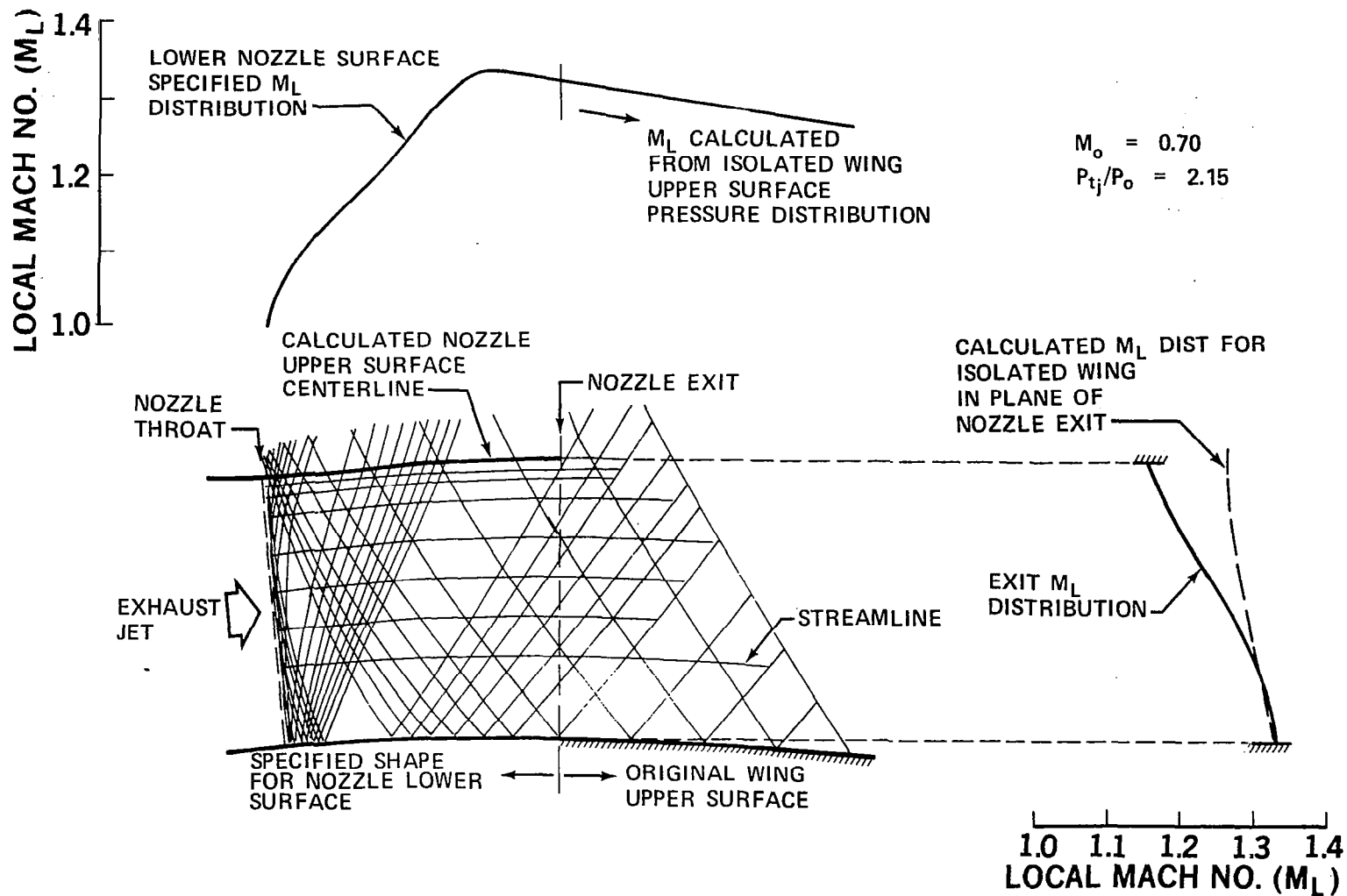
Figure 8.12. 2-D Inverse Method of Characteristics Solution for C-D Nozzle

STREAMLINES
IN 2-D FLOW

SPECIFIED CURVE
SHAPE ENCLOSING
SPECIFIED MASS FLOW

LOCUS OF STREAMLINES
PASSING THROUGH
SPECIFIED CURVE

3-D STREAM TUBE CONTOUR
FOR C-D NOZZLE
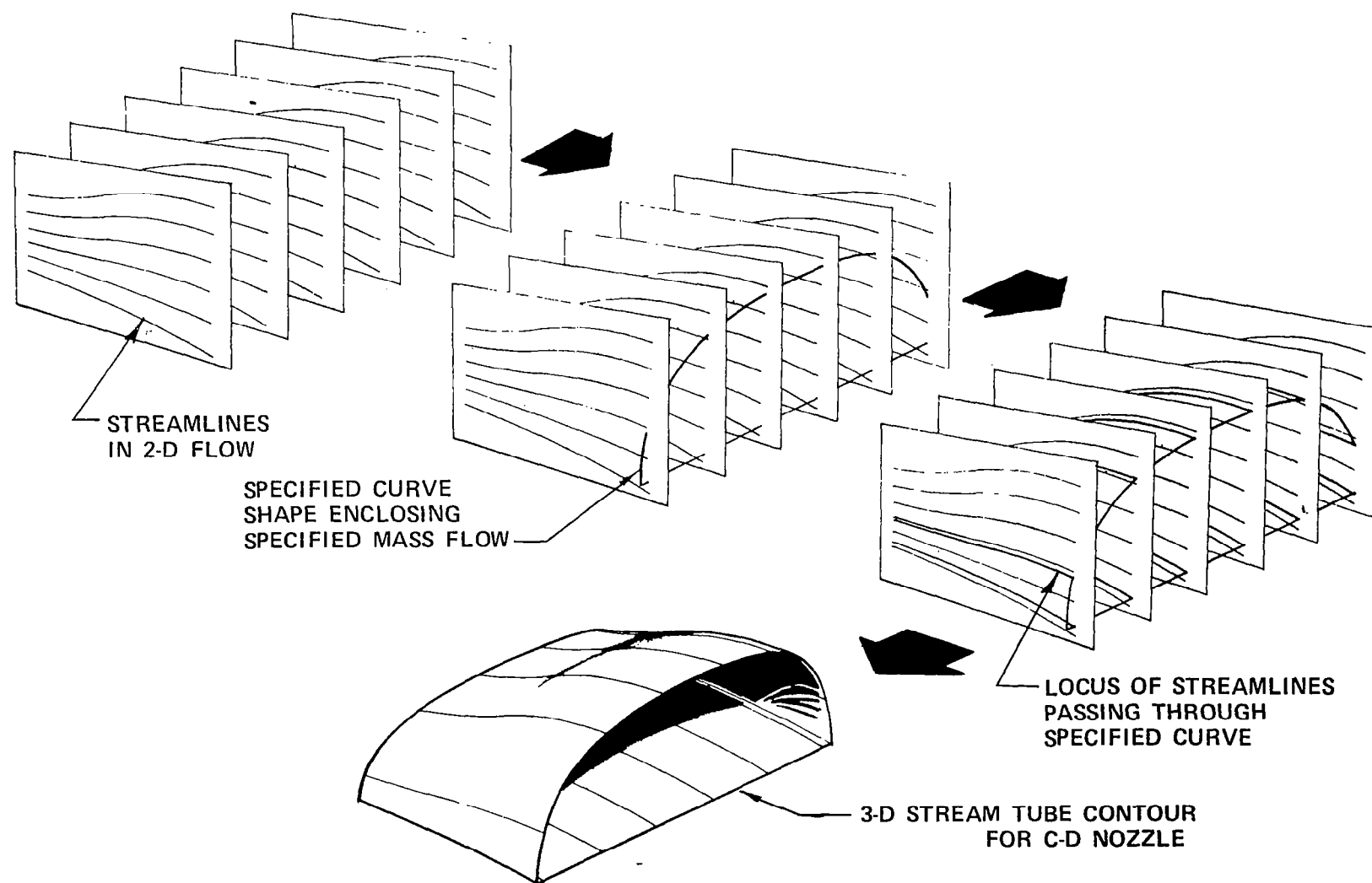
Figure 8.13. Steps used to Define 3-D C-D Nozzle Contour from 2-D Flow Solution
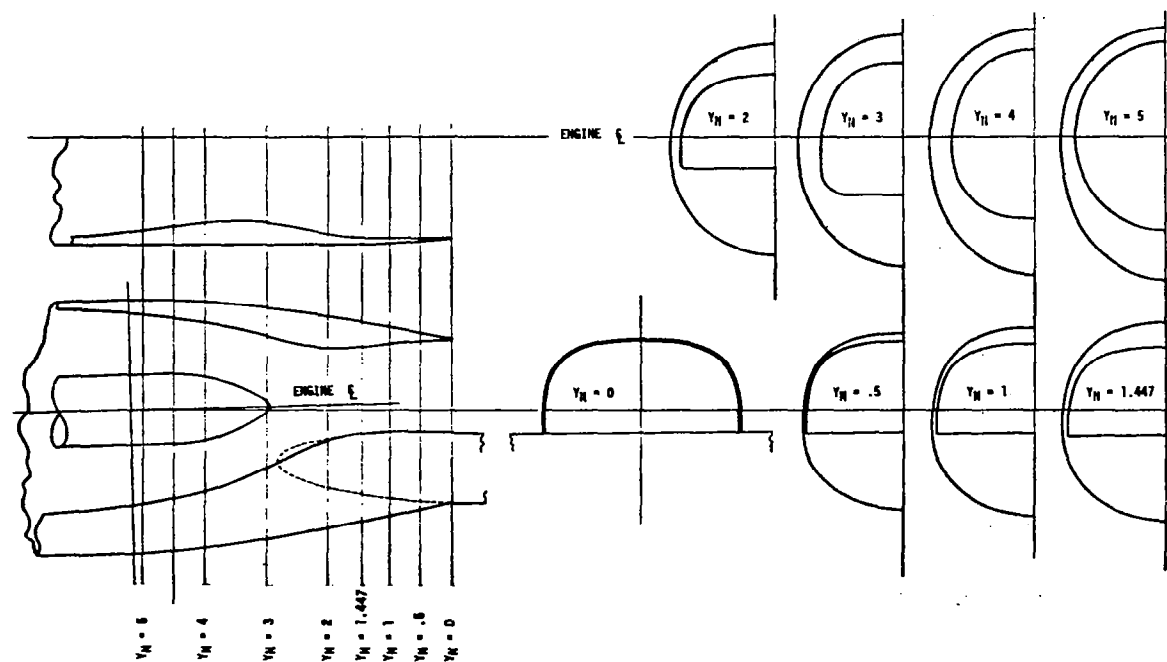
Figure 8.14. Description of C-D Nozzle Nacelle N_4

LOCAL MACH NO. (M_L)

SKIN FRICTION COEFF (C_f)

C-E CONTOUR M_L

C-E CONTOUR C_f

INBOARD NACELLE
M_o = 0.70
P_{t_j}/P_o = 2.15
R/FT = 8 x 10⁶

NOZZLE AFTERBODY

CONVERGENT EXIT

DIVIDING STREAMLINE

ORIGINAL WING SURFACE

C-E CONTOUR

35% CHORD

70% CHORD
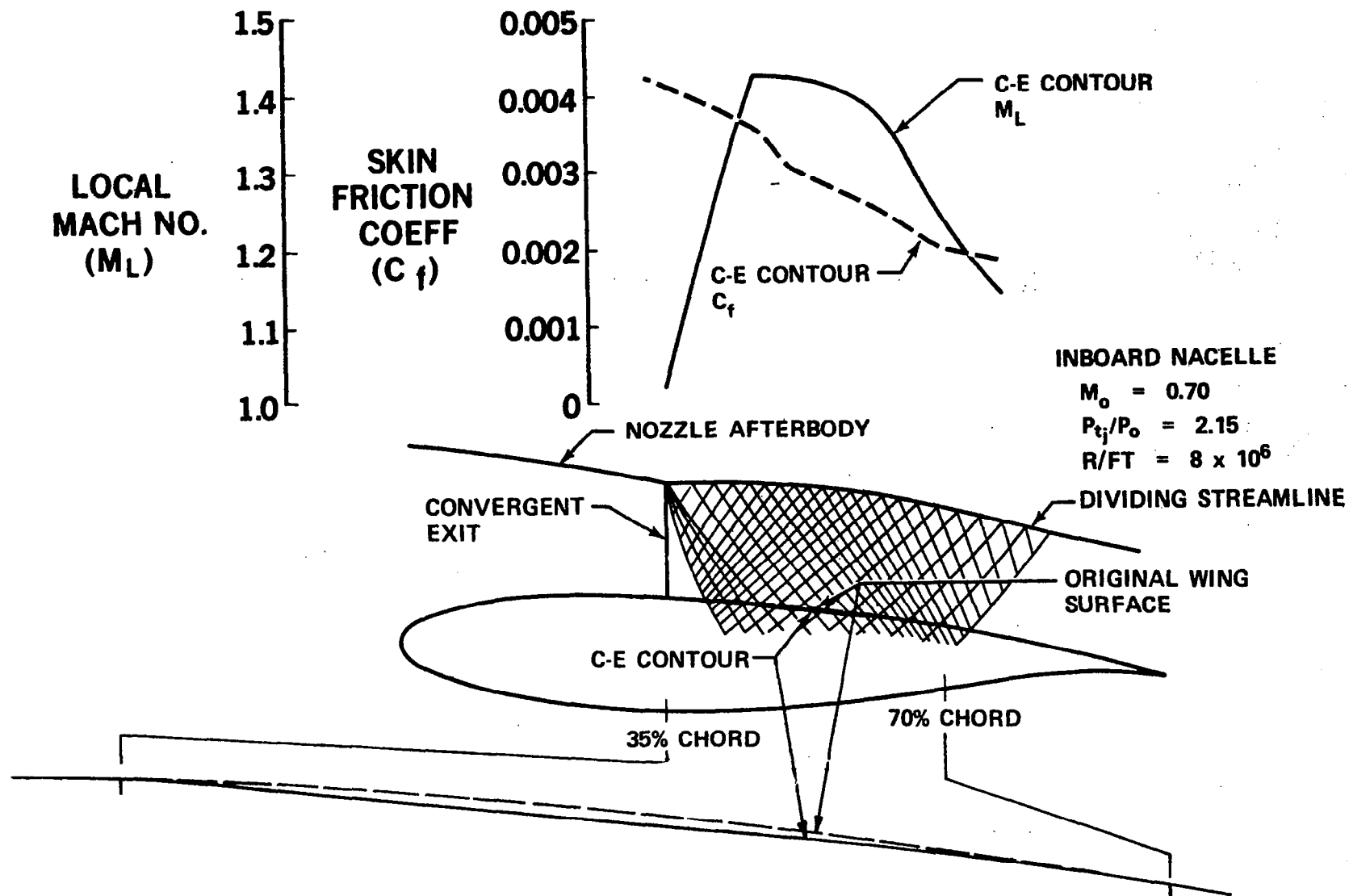
Figure 8.15. 2-D Inverse Method of Characteristics Solution for C-E Contour
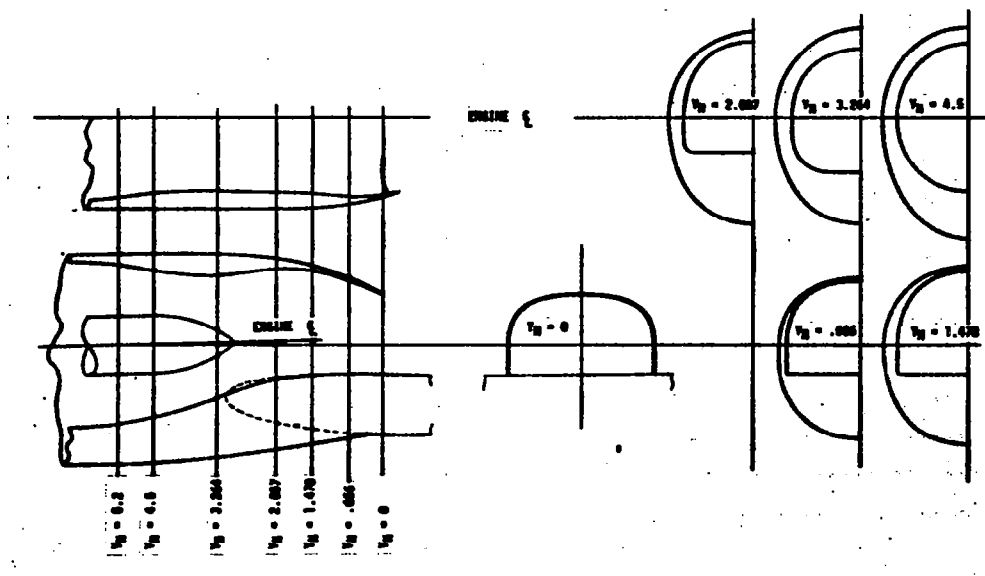
Figure 8.16. Description of High Boattail Angle Nozzle Nacelle N₃

β_{TOP} = top ₵ boattail angle (external)

δ_{TOP} = top ₵ deflection angle (internal)

ϕ = sidewall extension angle

β_{SIDE} = side boattail angle (external)

δ_{SIDE} = side boattail angle (internal)

w = nozzle exit width

h = nozzle exit height
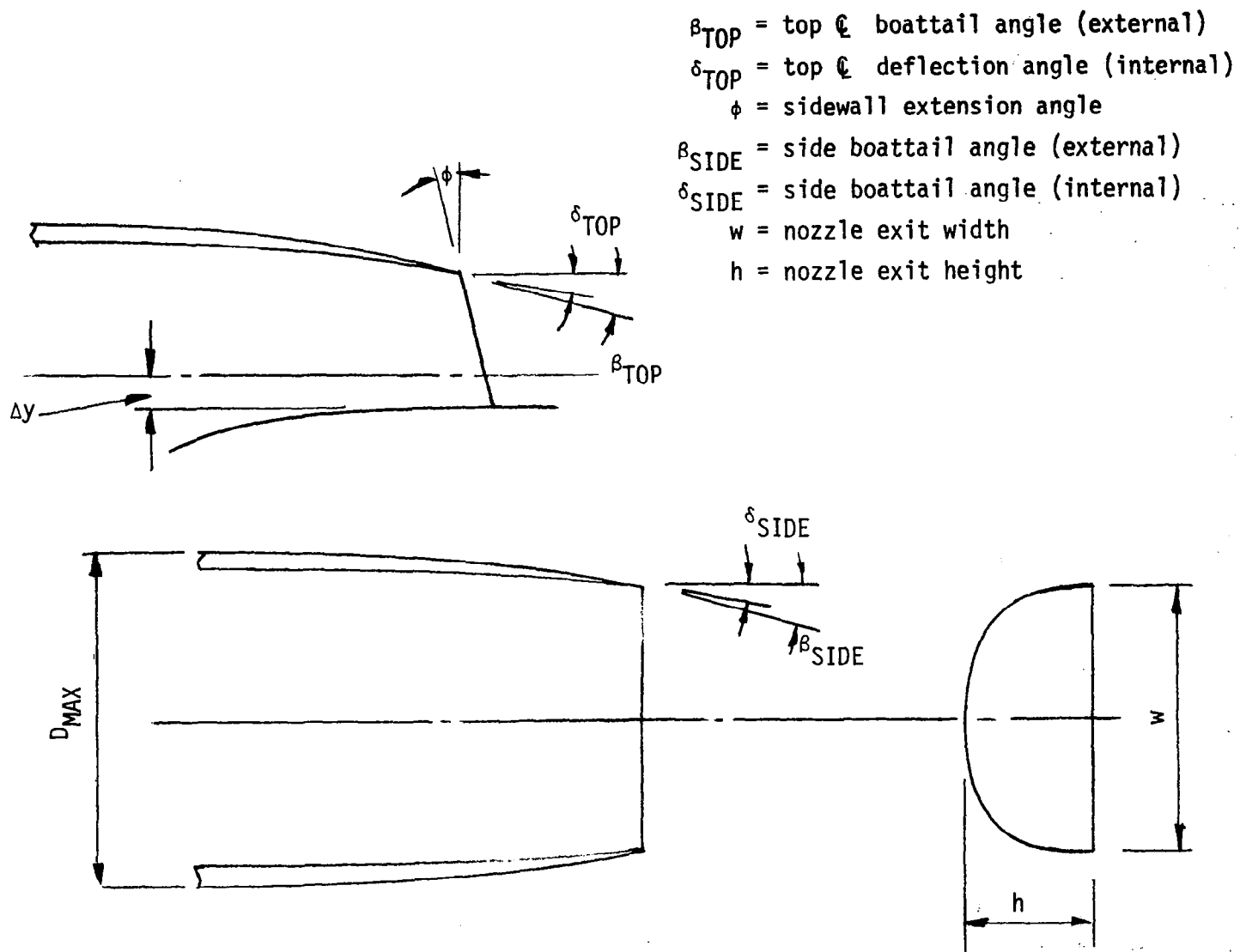
Figure 8.17. Definition of Nacelle Parameters

CONFIGURATION	β_{TOP}(DEG)	δ_{TOP}(DEG)	β_{SIDE}(DEG)	δ_{SIDE}(DEG)	ϕ (DEG)	w/h	$\Delta Y/D_{MAX}$
N_1 (BASELINE)	11.0	4.0	2.0	0.0	0.0	2.17	0.105
N_2 (STREAMLINE CONTOURED)	6.0	1.0	2.5 I/B 7.5 O/B	-0.5 I/B 4.5 O/B	0.0	2.17	-0.139
N_3 (HIGH ANGLE)	28.5	21.5	17.0	10.0	15.0	1.90	0.161
N_4 (CONVERGENT -DIVERGENT)	11.0	-2.5	2.0	0.0	0.0	2.17	0.105

Figure 8-17. (Cont)
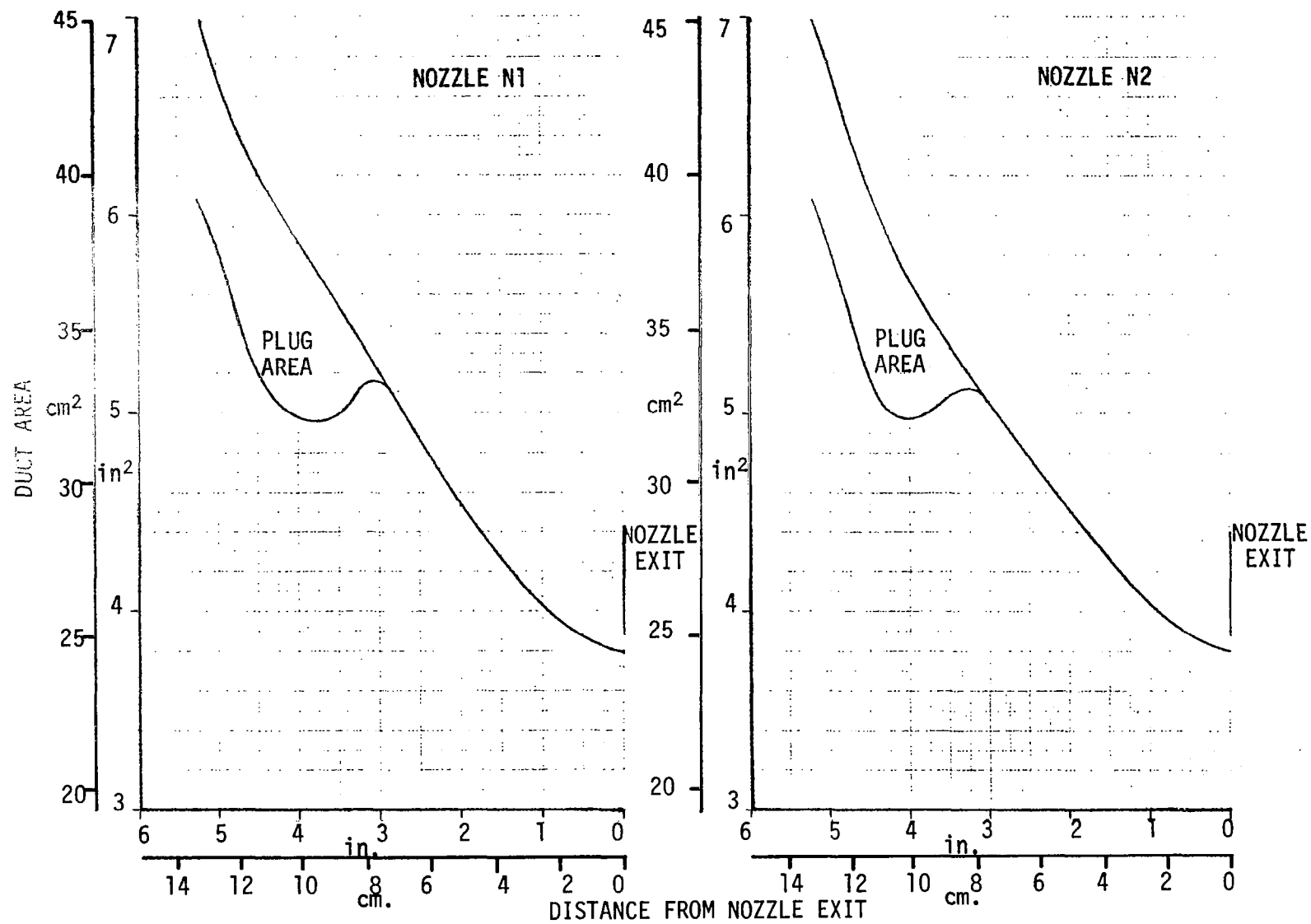
Figure 8.18. Nozzle Internal Duct Area Distribution
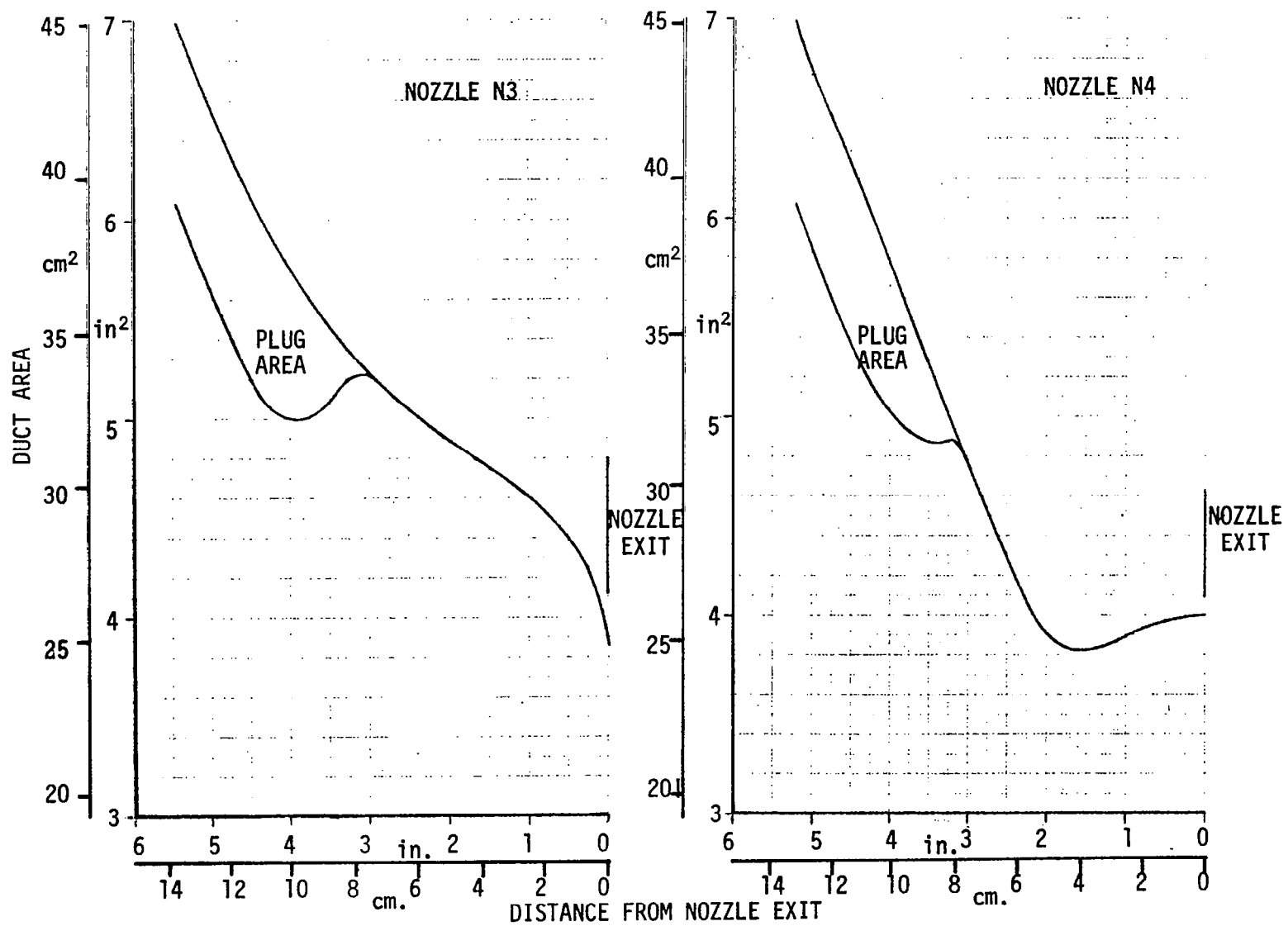
Figure 8.18. (Continued)

9.0 EXPERIMENTAL PROGRAM

9.1 Wind Tunnel and Test Conditions

The wind tunnel used for this test was the NASA Lewis 8-ft x 6-ft supersonic tunnel (Reference 29). The tunnel was operated in the aerodynamic cycle which is a closed return cycle. The air passing through the working section is returned after passing through air cooling and drying systems. The working section of the tunnel is perforated on all four walls, with an open porosity ratio of 3.1 percent.

For this test, the tunnel was only operated subsonically over the Mach number range from 0.6 to 0.78. Over this Mach number range the Reynolds number varied from 2.6 to 3.0 million, based on the mean chord of the model wing. For most of the test, the angle of attack range was from -3 degrees to +3 degrees.

9.2 Powered Simulator

The NASA LeRC TD-800 powered simulators which were used for this program are 3.25-percent scale air-driven simulators of the General Electric CF6 turbofan engine. An air-driven, dual-stage turbine powers the dual-stage fan. The fan and turbine assembly is supported on two ball bearings which are lubricated by an automatic oiling system that pulses oil to the bearings at prescribed intervals from a remote oil reservoir source. The simulator has an overall diameter of 8.00 cm (3.15 inches), is 16.002 cm (6.3 inches) in length and has a fan diameter of 7.14 cm (2.81 inch). The simulator is shown installed in the N_1 nacelle in Figure 9.1. This figure also defines the nacelle stations and instrumentation to be referred to later.

The nacelles were designed to simulate the QCSEE (upper surface blowing) engine cycle with a fan pressure ratio of 1.38.

Figure 9.2 illustrates typical fan characteristics for these simulators in the nacelle installation for this test. The characteristics were obtained in the static calibration phase described in Section 10.0. The fan map in Figure 9.2 indicates that at a fan pressure ratio of 1.4 the fan referred airflow is approximately 0.581 kg/sec (1.28 lb/sec).

9.3 Description of Wind Tunnel Model

The model was sized to reflect the installed thrust to weight ratio and wing loading of the U-150-3000 configuration. For a given fan pressure ratio, consistent with the NASA QCSEE USB design (FPR = 1.38), the ratio of nozzle exit area to wing area of the U-150-3000 configuration of A_E/S_W = .036 was used to size the wind tunnel model. The nozzle exit area was established at 24.52 cm^2 (3.8 square inches) as part of the cycle analysis task described in Section 8.0. This sizing was consistent with wind tunnel test section blockage considerations and yielded a semispan to tunnel width ratio of 0.43. It was understood at the outset of the program that existing simulators would be utilized and that the experimental program would be conducted in the NASA Lewis Research Center 8-ft x 6-ft supersonic wind tunnel, thereby, essentially precluding the use of a full-span model due to both span and blockage considerations. In addition to these factors, complex operational problems

related to the simulators were considerably relieved by the adoption of the reflection plane semispan type model, as will be implied by the descriptions of the model support and drive air supply systems.

The half model, shown in Figure 9.3, was mounted, via a six component balance onto a rectangular splitter plate, which was mounted eight inches from one of the tunnel side walls. This plate allowed the tunnel boundary layer to pass under the plate, minimizing the half model interference effects. To change the incidence of the model, a circular section of the splitter plate was rotated within the main plate. The model and balance were mounted on this circular section.

The half fuselage was metric with the wing and designed to stand a small distance from the splitter plate. A seal was provided around this space.

Each of the nozzles described previously were interchangeable with a common nacelle body forward of nacelle station 5.2 (shown on the figures describing the nozzles). The nacelle body housed the simulator and instrumentation forward of station 5.2. Each nozzle contained its own instrumentation.

The semispan model designed and fabricated by Douglas for this investigation is illustrated in Figures 9.4 through 9.7.

9.3.1 Force Balance Arrangement - A six component 3.5-inch Task Mark IC balance was utilized within the model. The balance was mounted within an electrically heated sleeve, located near the middle of the fuselage.

9.3.2 Metric to Non-metric Crossover Systems - In addition to the seal, turbine drive air lines, engine and flow visualization oil lines, reference pressure lines, and electrical leads bridged the metric and non-metric systems.

The drive air lines were 0.874 cm (0.344 inches) OD thin wall steel tubes routed through the tunnel wall into a non-metric windshield behind the splitter plate and onto the metric model. To reduce the drive air line size, a choke plate, or baffle, was installed at the entrance to the simulator to reduce the line pressure by about a factor of two. Outside the tunnel, these lines were arranged to provide minimum tares on the metric system with variations of pressure and angle of attack. The effects of pressure and angle of attack on the drive air lines were demonstated to be negligible during the pre-test calibrations. There are no momentum corrections required for this type of crossover system.

The electrical and oil crossover systems consisted of a metric tray extending through the non-metric windshield to the area outside the test section to provide support for the leads. A simple deep loop between the leads and the non-metric structure completed the system.

9.3.3 Model Instrumentation - The model was equipped with wing and nacelle surface static pressure orifices, nacelle internal static and total pressure orifices, turbine and fan duct total temperature sensors, and internal turbo-simulator instrumentation including turbine drive pressure, RPM, bearing temperature, and accelerometers.

9.3.3.1 <u>Wing Surface Static Pressure Instrumentation</u> - The wing contained six full rows of static pressure orifices located at the stations indicated in Figure 9.8. Partial rows were located at 23 and 48 percent of the wing semi-span, aft of the baseline nozzle positions on the upper surface of the wing.

9.3.3.2 <u>Nacelle External Surface Static Pressure Instrumentation</u> - Each nozzle contained selected trailing edge reference static pressure orifices for calibration purposes and each nozzle, except the convergent-divergent nozzle, contained static pressure orifices as indicated in Figure 9.9.

9.3.3.3 <u>Inlet Static Pressure Instrumentation</u> - Two independent airflow reference static pressure rings were installed in the inlets as indicated at Stations 1 and 2 in Figure 9.1.

The inherently more sensitive throat ring proved to be relatively sensitive to angle of attack effects, and the station within the diffuser was selected as the reference for measuring inlet airflow during the wind tunnel test.

9.3.3.4 <u>Fan Duct Instrumentation</u> - The fan duct instrumentation, located at Station 3 (Figure 9.1), is shown in detail on Figure 9.10. Seven blade type rakes were installed at the fan discharge station. Each rake contained five instrumentation stations. Three blades contained one thermocouple and four total pressure tubes, and the remaining four blades contained five total pressure tubes. The blades were designed to provide a high degree of flow straightening to minimize fan stream residual swirl at low values of fan pressure ratio. Relatively short total pressure tubes were used to minimize the risks of damage (due to handling during model assembly operations) to the tubes in the interval between the calibrations of the nacelles and the wind tunnel test. Seven outer fan duct wall static orifices were installed as indicated in Figure 9.10.

9.3.3.5 <u>Turbine Duct Instrumentation</u> - The turbine duct instrumentation, located at Station 6 (Figure 9.1), is shown in detail on Figure 9.11. Three rakes containing three total pressure tubes each were located in the turbine discharage duct as indicated in the figure. Three thermocouples were installed; one between each of the rakes.

9.3.3.6 <u>Nozzle Exit Instrumentation</u> - The nozzle had six station pressures just upstream of the exit (Station 8, Figure 9.1) as shown on Figure 9.12. These pressures were located inside the duct.

9.3.3.7 <u>Turbo Simulator Internal Instrumentation</u> - Two pressure orifice and two thermocouples were located within the plenum of the TD-800 turbo simulator. These were considered to be sensing total conditions. A mechanical RPM sensor and two bearing thermocouple sensors were also located within the simulators to provide operational information. Internal accelerometers were installed to provide information related to unbalance or unsteady blade loading conditions that might lead to simulator failure.

9.3.3.8 <u>Scanivalve Installation</u> - Two modules of six scanivalve barrels each were mounted within the metric portion of the model, as shown in Figure 9.13. All of the pressure data except those of the turbine drive system were acquired through the scanivalve system.

Flow Station	Location
0	upstream = (plenum)
1	inlet
2	compressor face
3	fan rake station
4	fan mixing plane
5	turbine plenum
6	turbine rake station
7	turbine mixing plane
8	nozzle exit
9	downstream =
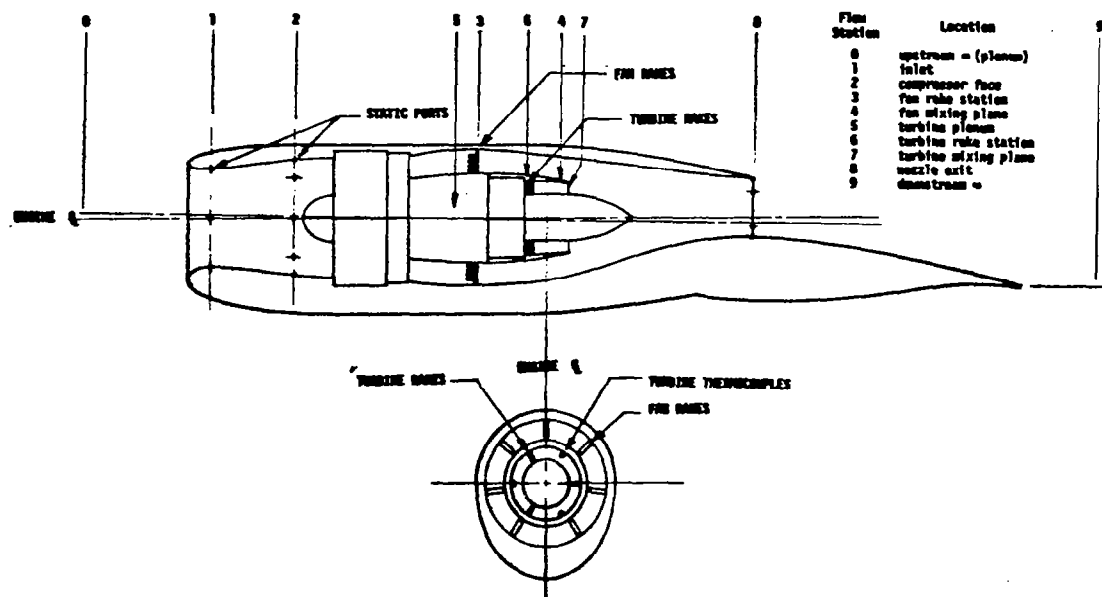
Figure 9.1. Description of Engine Simulator
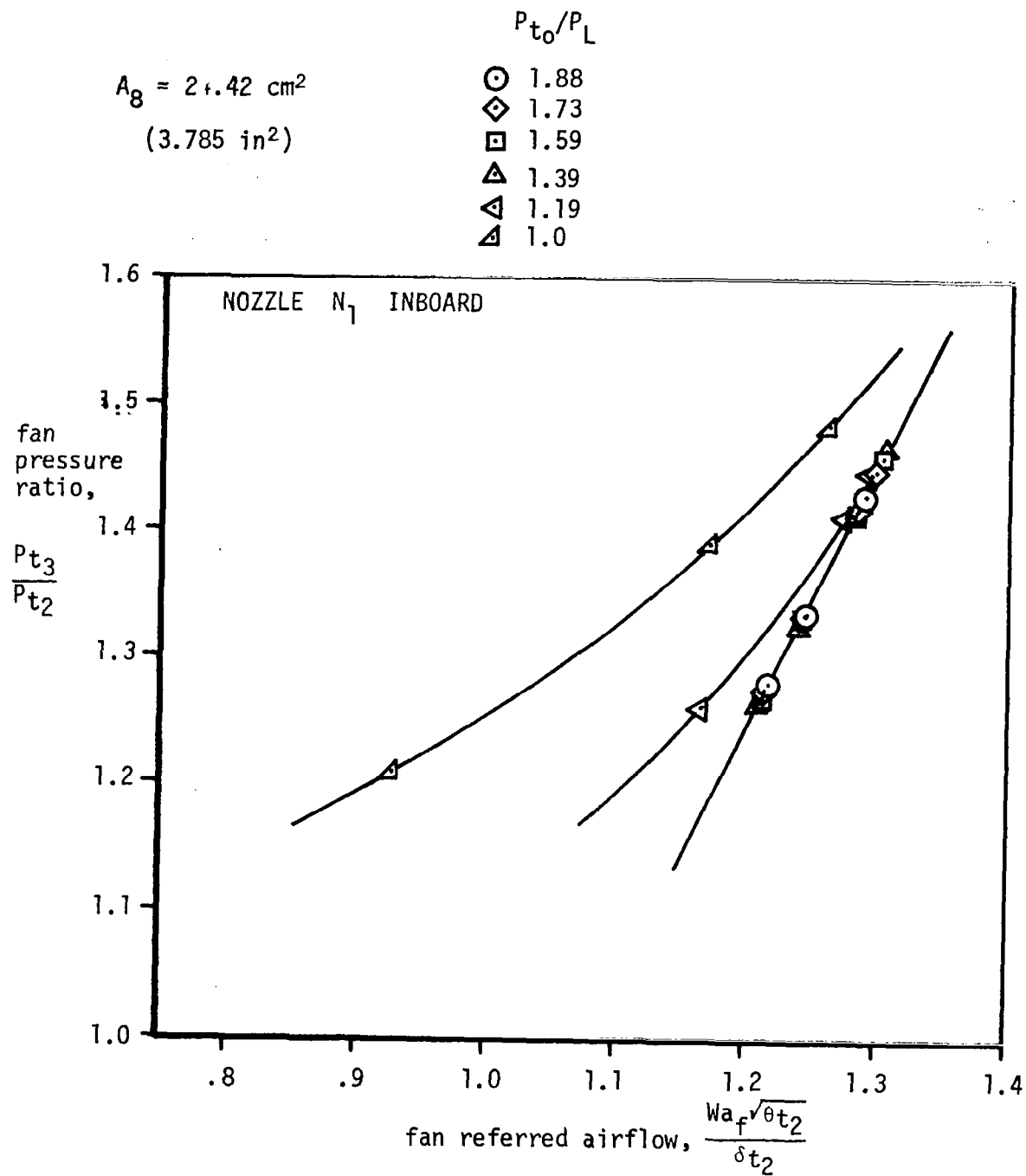
Figure 9.2. Typical Fan Map Data Obtained from Static Calibration of TD-800 Simulators.
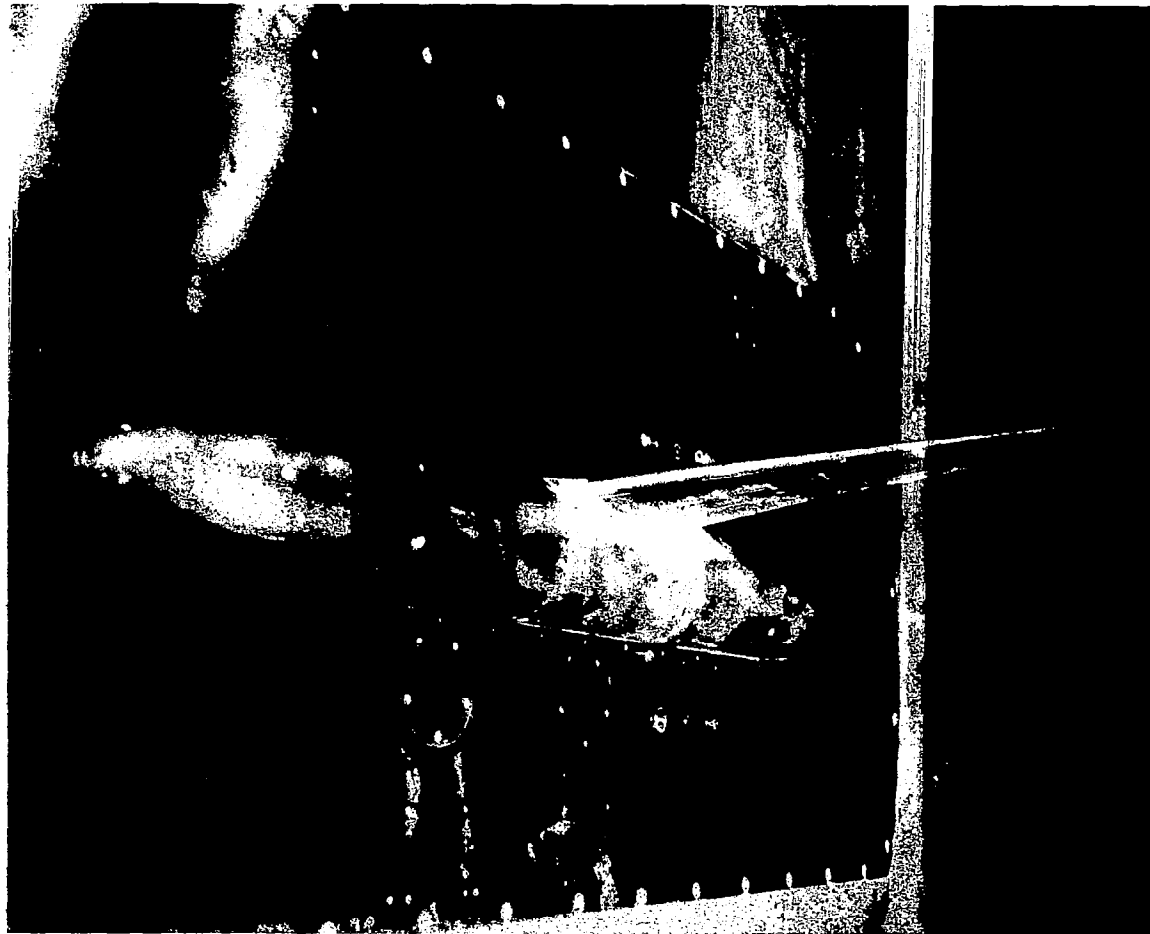
Figure 9.3. Photograph of the Wing-Body

NON METRIC COVER

SPLITTER PLATE

SEALED
GAP BETWEEN
METRIC FUSELAGE
& NON-METRIC
SPLITTER PLATE

STING BALANCE

METRIC FUSELAGE
SHELL

SCANIVALVES

REMOVABLE
INLETS

TRIMMER FLAPS

ENGINE SIMULATOR
INSTALLATION

SIMULATOR AIRLINES

INTERCHANGEABLE
NOZZLES

54
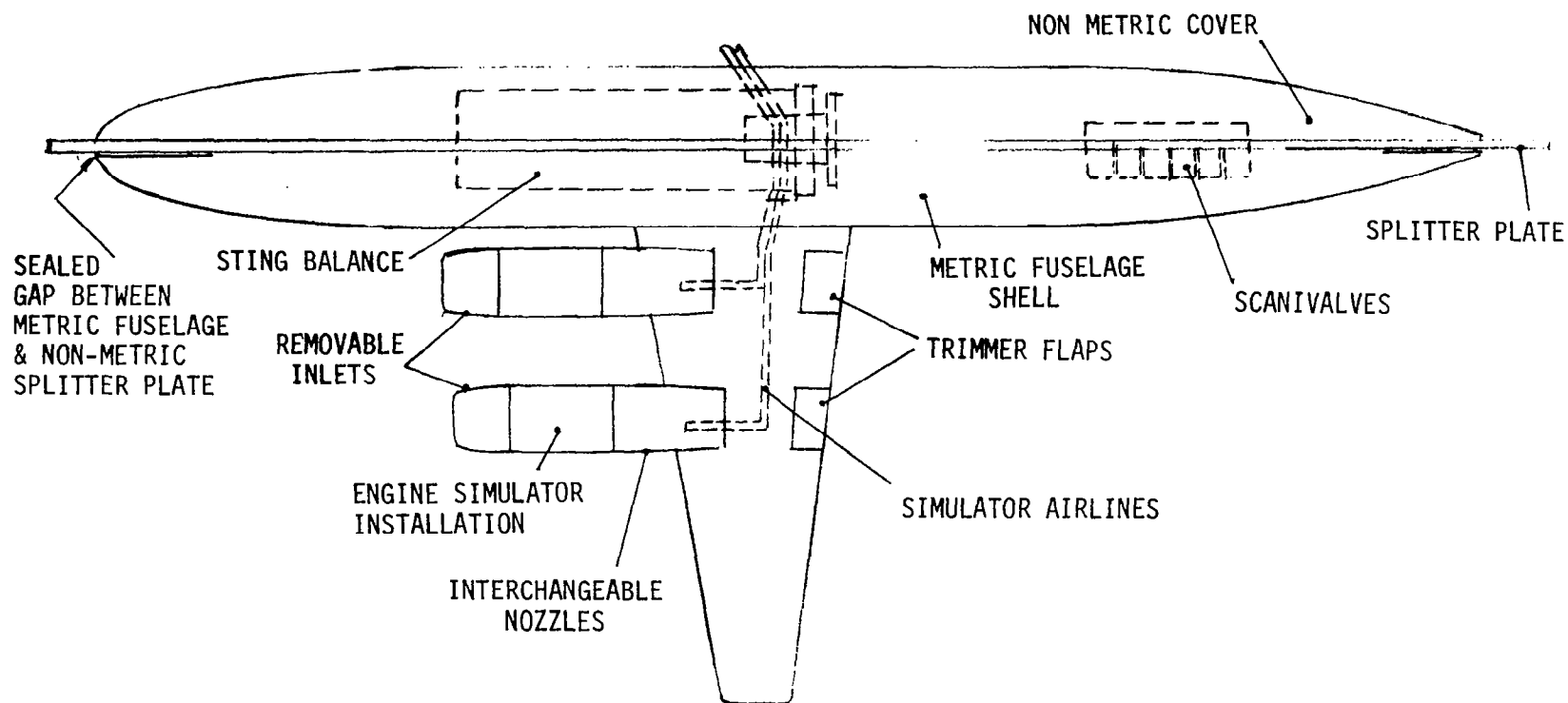
Figure 9.4. Model General Arrangement
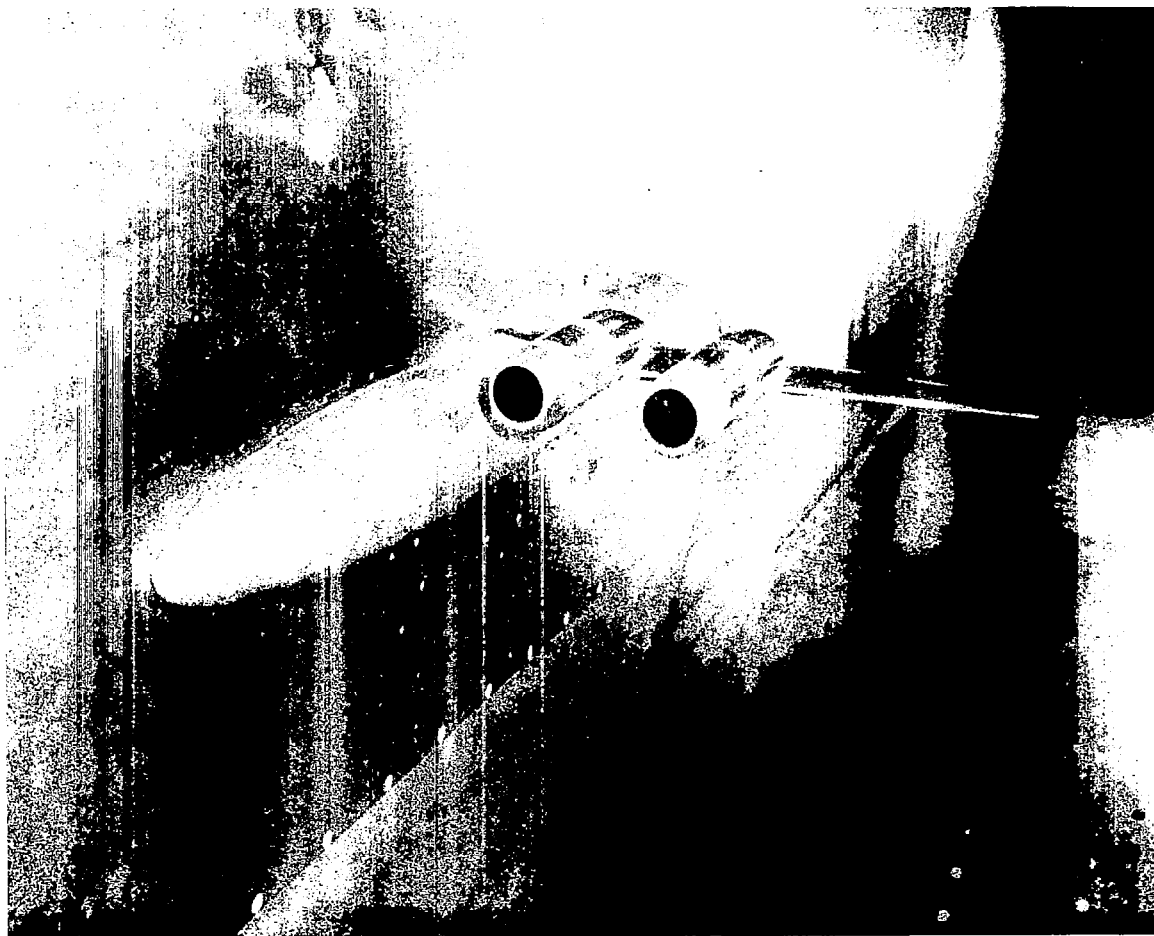
Figure 9.5. Front View Photograph of the Model with N_3 Nacelles

56

Figure 9.6. Aft View Photograph of the Model with N_1 Nacelles.
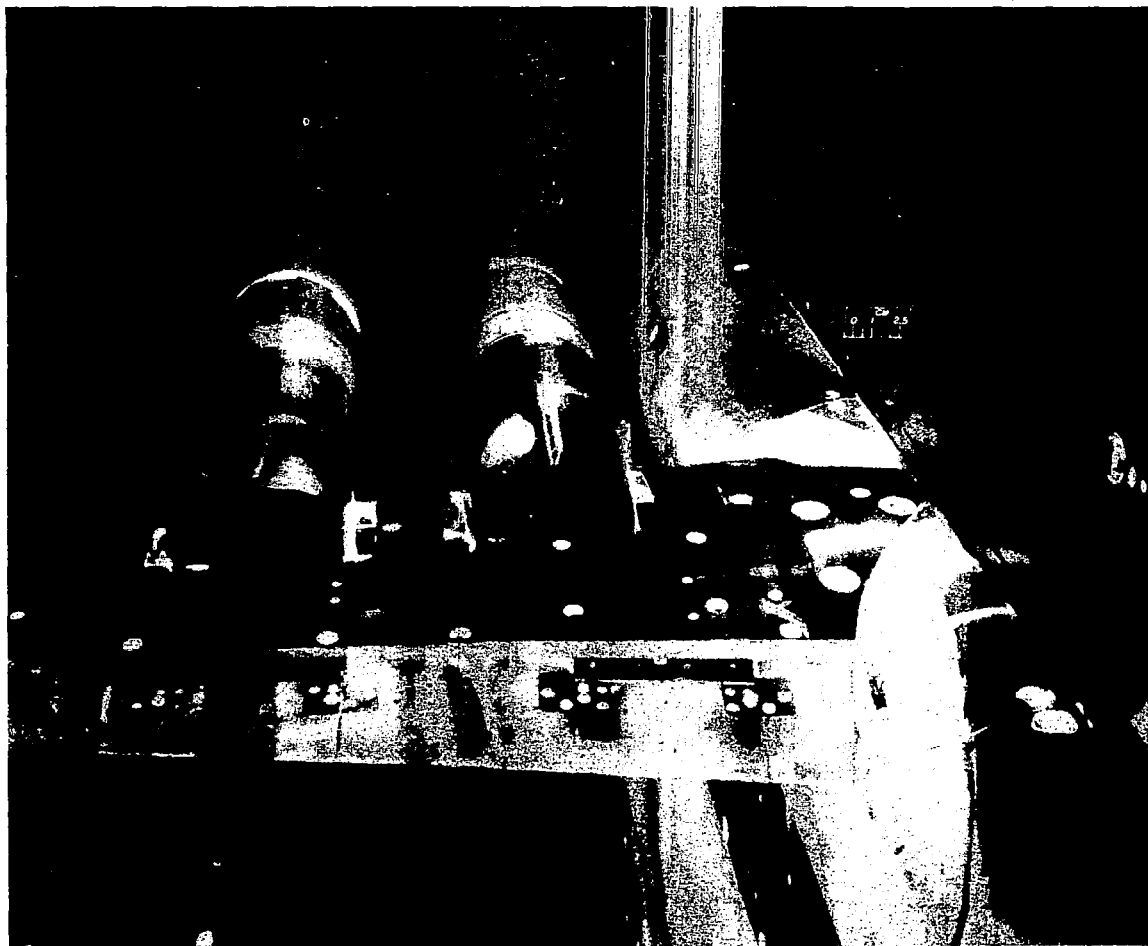
Figure 9.7. Close-up Aft View Photograph of the N_1 Nozzles with the Alternate Spanwise Spaci

% SEMISPAN =

13

23

33
38

48

58

70

90
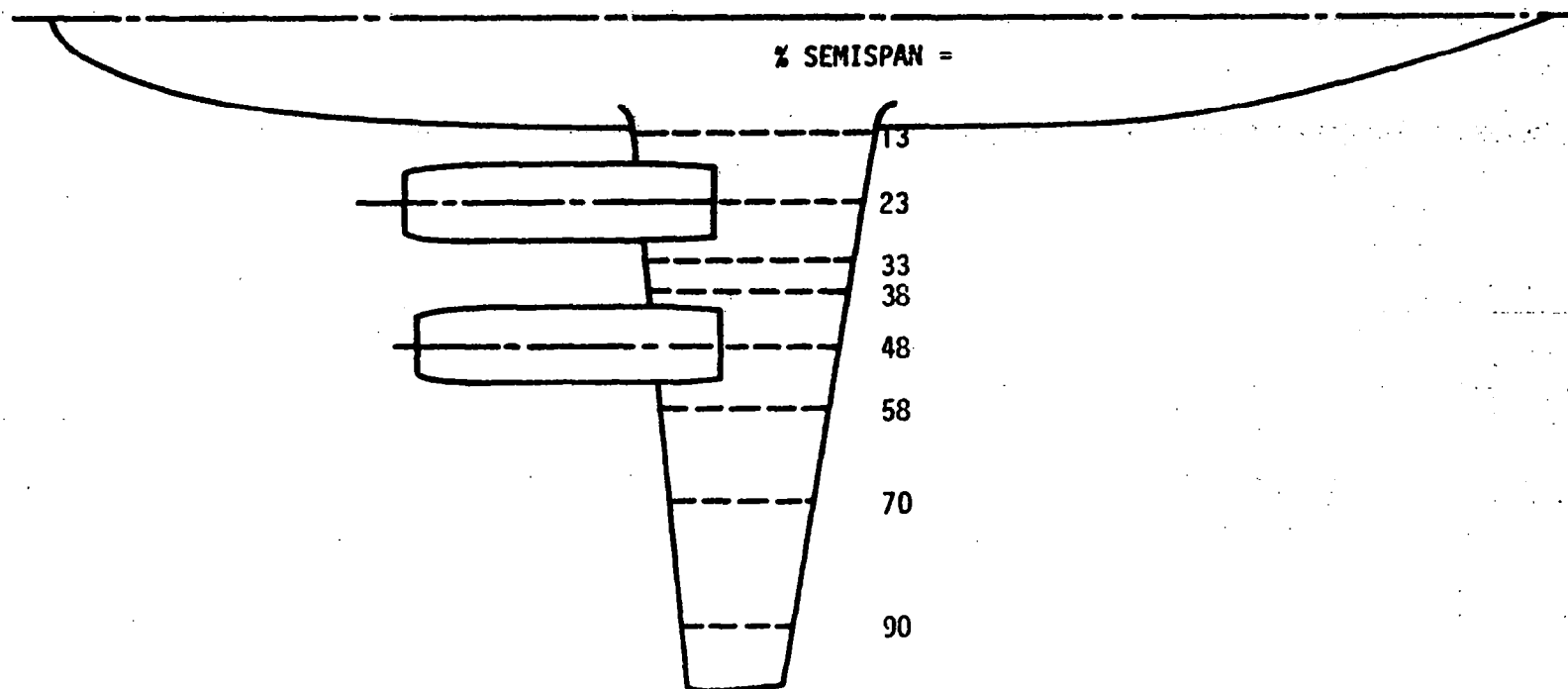
Figure 9.8. Spanwise Location of Wing Pressure Stations

58

8 pressure taps along each
side of nozzle

8 pressure taps along top
center line of nozzle

6 pressure taps
each side of
fairing

15 pressure taps along
bottom center line of fairing
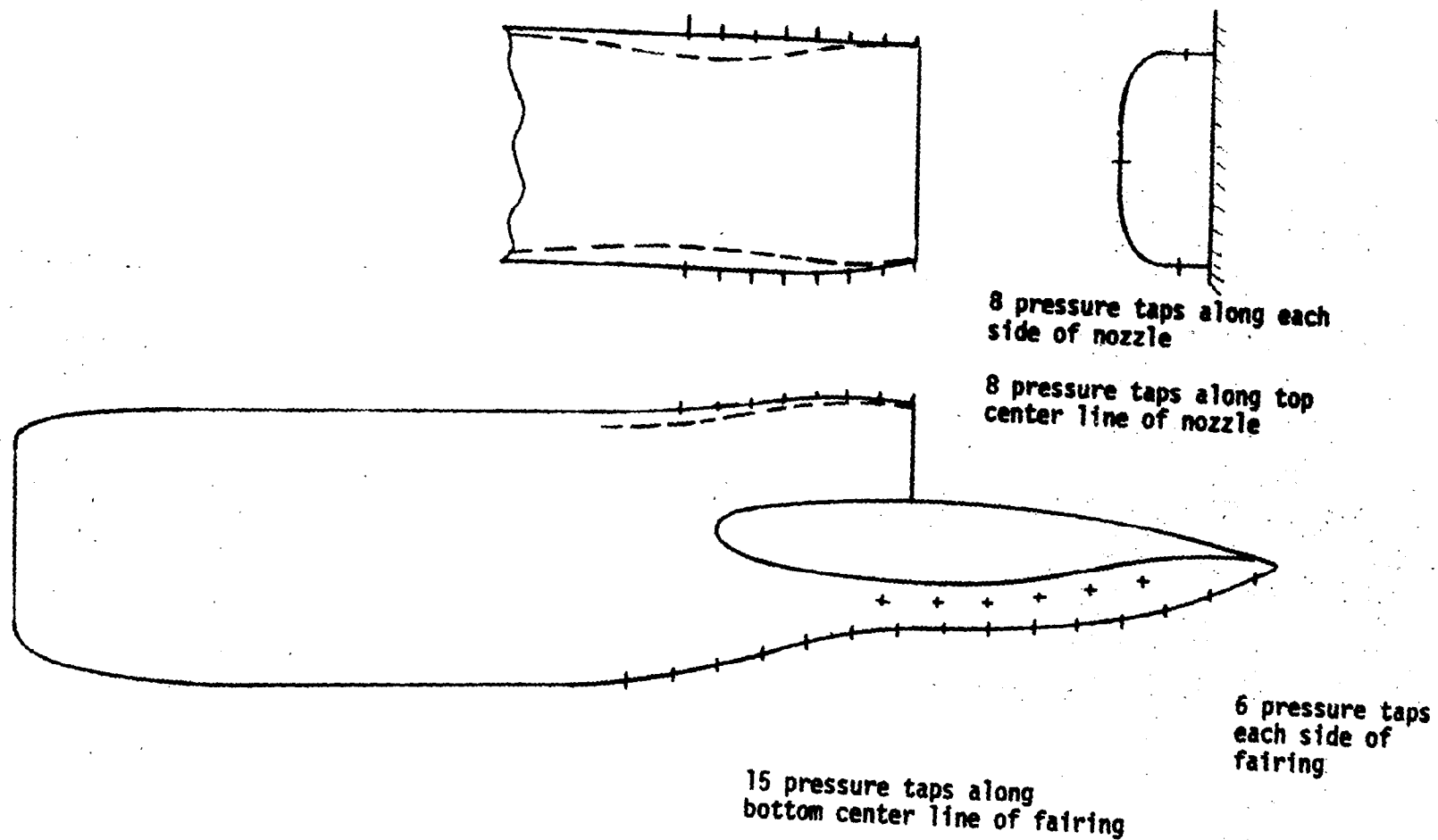
Figure 9.9. Typical Nozzle External Instrumentation and Instrumentation on Lower Surface Fairing of N_2.

r	Centimeters
1	2.558
2	2.609
3	3.060
4	3.353
5	3.622
6	3.874
7	3.993

○ static pressure orifices

● total pressure probes

✖ total temperature probes
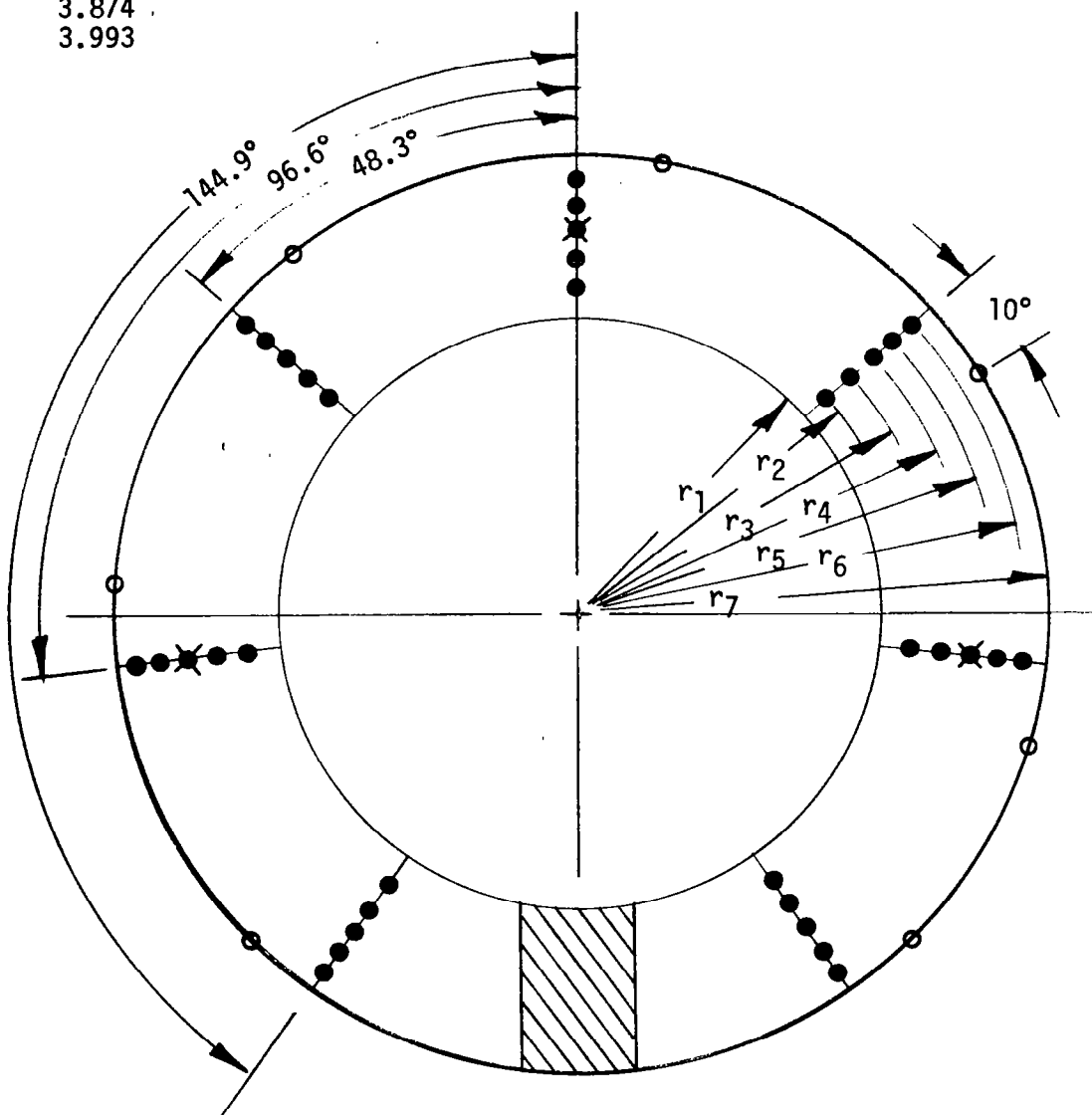
Figure 9.10. Fan Discharge Station Instrumentation

o static pressure orifices

● total pressure probes

✖ total temperature probes

r	Centimeters
1	1.374
2	1.542
3	1.832
4	2.083
5	2.197

30°

r_1 r_2 r_3

r_4 r_5

15°

r_3

30°
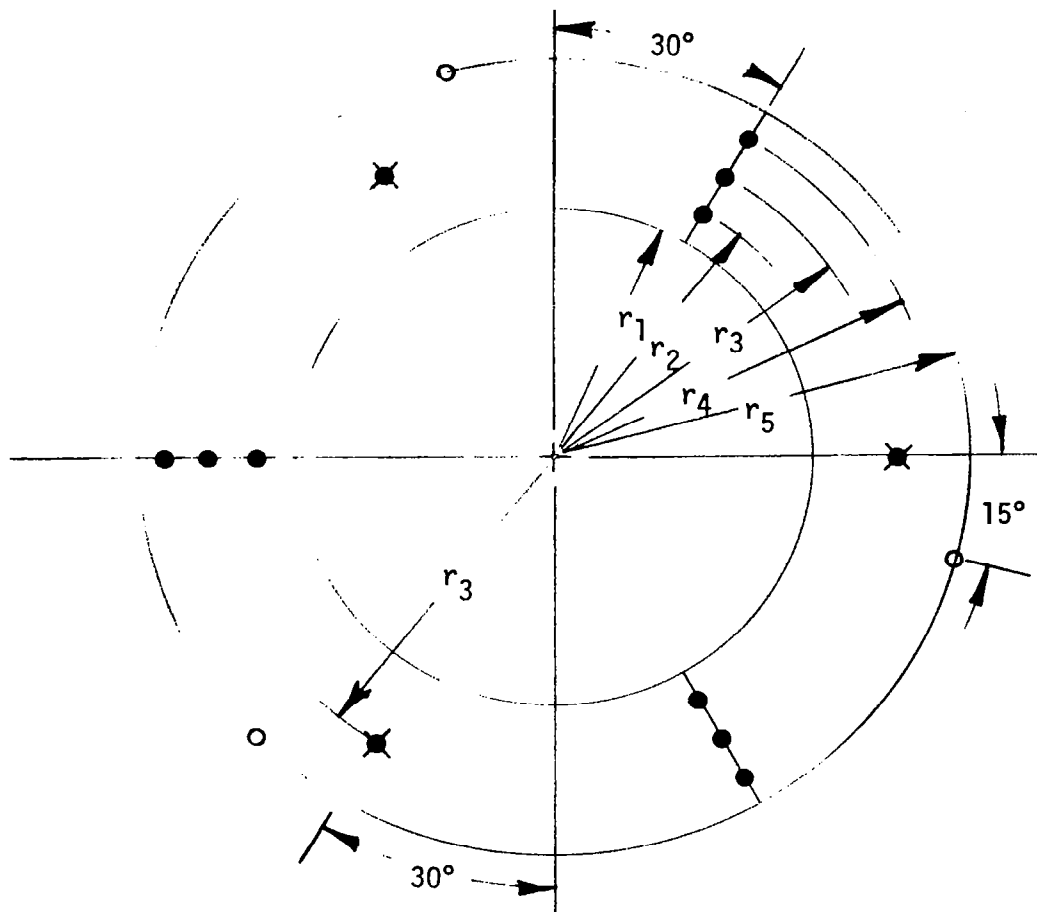
Figure 9.11. Turbine Discharge Station Instrumentation
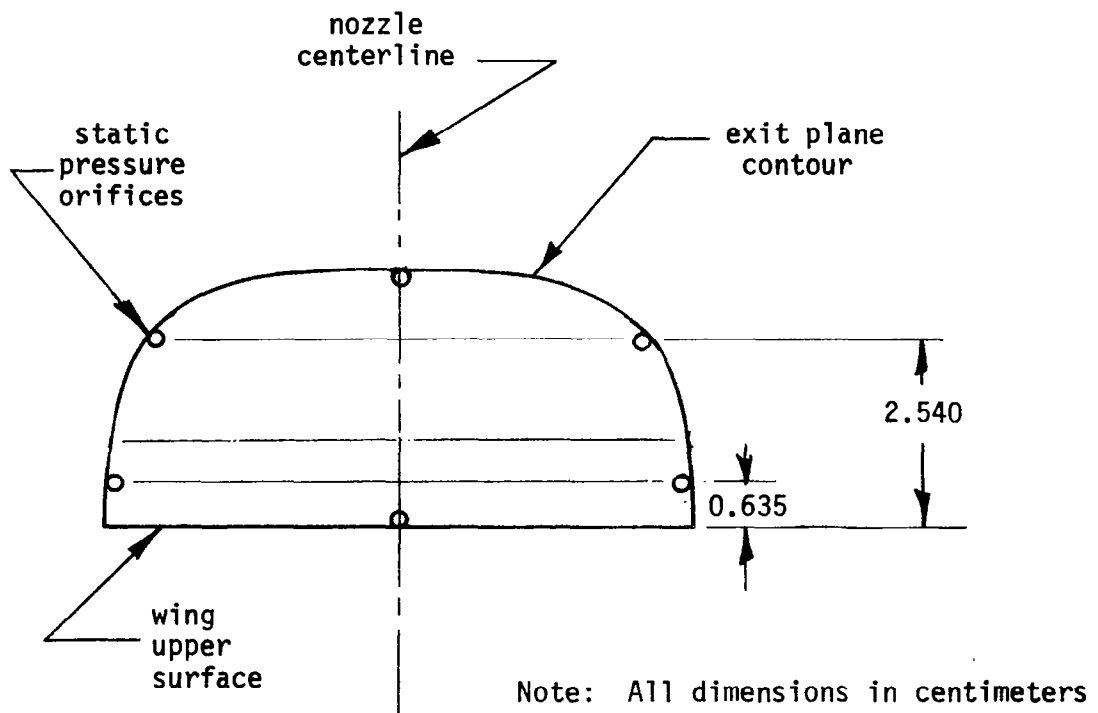
Figure 9.12. Nozzle Exit Plane Static Pressure Orifice Locations

Figure 9.13.   Photograph of Instrumentation and Scanivalves Installed in the Model

10.0 EXPERIMENTAL PROCEDURES, TECHNIQUES, AND DATA REDUCTION

10.1 Balance Data

The isolated balance was calibrated by the NASA Ames Research Center prior to the wind tunnel test. This calibration determined the primary and interaction load coefficients. The equations relating the balance gage readings to the applied loads were assumed to take the form of a quadratic equation:

$$N = p\,N_R + q\,N_R{}^2$$

where N_R is the balance gage reading. This equation was also assumed to hold for the interaction components. However, the second order interaction coefficients were, in general, small enough to be ignored.

The full equations will not be presented here, but for one of the loads N_1, the balance data reduction equation would be:

$$N_1\left(1 - \frac{\Delta N_1}{N_1}\right) = p_1\,N_{1_R} + q_1(N_{1_R})^2 - \left[\frac{\partial N_1}{\partial N_2}\,N_2 + \frac{\partial N_1}{\partial A}\cdot A\right.$$
$$\left. + \frac{\partial N_1}{\partial S_1}\,S_1 + \frac{\partial N_1}{\partial S_2}\cdot S_2 + \frac{\partial N_1}{\partial R_M}\cdot R_M\right]$$
$$+ \frac{\partial N_1}{\partial \alpha}\cdot \alpha + \frac{\partial N_1}{\partial P}\cdot P$$

where

N_1 is forward normal force load

N_2 is aft normal force load

A is axial load

S_1 is forward side force load

S_2 is aft side force load

R_M is the rolling moment

The first two terms on the right hand side of this equation are the primary balance loads calculated from the gage readings. The terms contained in the square parenthesis contain the first order balance interaction terms, and the last two terms have been included to allow for angle of attack and air line pressure corrections. The term $1 - \Delta N_1/N_1$ was introduced to take into account any apparent reduction in balance stiffness due to the crossover lines. Both this correction and the air line pressure correction were found to be negligible during check calibrations of the assembled model and were subsequently ignored.

The location of the moment reference center for the pitching moments was 25 percent of the wing mean aerodynamic chord.

10.2 Pressure Data

The following equations were used to reduce the wing, external nacelle and external fairing pressure data

$$C_P = \frac{p - p_0}{q_0}$$

$$M = \left\{ \frac{2}{\gamma-1} \left[\left[\frac{p_{t_0}}{p} \right]^{\frac{\gamma-1}{\gamma}} - 1.0 \right] \right\}^{1/2}$$

$$q_0 = \frac{\gamma}{2} p_0 M_0^2$$

The equations used to integrate the wing pressure distributions to obtain sectional aerodynamic coefficients, are as follows. The various functions are integrated with respect to the square root of the distance from the leading edge in order to improve the integration in the leading edge region.

$$C_\ell = C_n \cos\alpha + C_T \sin\alpha$$

$$C_m = C_{m_L} + 0.25\, C_n$$

$$c_d = C_n \sin\alpha + C_T \cos\alpha$$

where α is the local section incidence ($\alpha = \alpha_{model} + \alpha_{twist}$)

$$C_n = 2 \int_0^1 (C_p \sqrt{x})_{LS}\, d\sqrt{x} - 2 \int_0^1 (C_p \sqrt{x})_{US}\, d\sqrt{x}$$

$$C_T = 2 \int_0^1 (C_p \frac{dz}{dx} \sqrt{x})_{LS}\, d\sqrt{x} - 2 \int_0^1 (C_p \frac{dz}{dx} \sqrt{x})_{US}\, d\sqrt{x}$$

$$C_{m_L} = 2 \int_0^1 (C_p x \sqrt{x})_{US}\, d\sqrt{x} - 2 \int_0^1 (C_p x \sqrt{x})_{LS}\, d\sqrt{x}$$

$$+ 2 \int_0^1 (C_p z \frac{dz}{dx} \sqrt{x})_{US}\, d\sqrt{x} - 2 \int_0^1 (C_p z \frac{dz}{dx} \sqrt{x})_{LS}\, d\sqrt{x}$$

65

The average pressure in the fan and turbine duct of the simulator used for calibrating and thrust calculation were obtained by adding the readings of the individual probes together and dividing by the total number of probes. Since the probes were located in segments of equal area, this procedure produced an area averaged total pressure.

For the presentation of the data in Section 11.0 the parameter used to indicate the level of power, or thrust, was the fan pressure ratio, FPR. This value was obtained by using the instrumentation in the fan duct (Station 3) to obtain the average fan exit total pressure, $\bar{P}t_3$, and dividing by the freestream total pressure, Pt_o, to form the ratio, $\bar{P}t_3/Pt_o$.

10.3 Installed Simulator Performance

10.3.1 Thrust-Drag Accounting

- Powered model simulation of propulsion system interaction effects introduces extra complexity to wind tunnel testing. Part of this complexity involves properly accounting for the aerodynamic forces acting on the powered model. Since these forces include both thrust and drag, the model force balance measures the difference between thrust and drag. When thrust equals drag, the balance measures no longitudinal forces, and the model is essentially self-propelled in the tunnel. To obtain useful drag measurements from the force balance readings, the model propulsion system thrust must be known separately. Known thrust characteristics as a function of propulsion system operating conditions provide a method of determining drag by using the following relation

$$D_{balance} = D - F_n + D_{ESF} \qquad (10-1)$$

where $D_{balance}$ is the measured balance force in the drag direction, F_n is the known net thrust, D_{ESF} is the calculated external nacelle skin friction and form drag accounting for that part of the wing which the nacelle covers and D is the unknown aircraft drag. By rearranging and substituting the definition of net thrust, equation (10-1) becomes

$$D = D_{balance} + F_g - D_{ram} - D_{ESF} \qquad (10-2)$$

where F_g is the gross thrust in the freestream direction and D_{ram} is the ram drag. For the powered simulators, F_g and D_{ram} are determined from measured pressures and temperatures in conjunction with nozzle velocity and inlet discharge coefficients obtained by static calibration of the powered simulator nacelles as described below. For the flow-through nacelles the difference between F and D_{ram} is equal to the calculated internal skin friction and form drag.

The over-the-wing nacelle design used in this study introduces a further complexity in thrust-drag accounting. The nacelle is designed with a nozzle that discharges the exhaust stream into the wing upper surface flowfield. With such a design the propulsion system and wing flowfield are closely coupled. The static pressure at the nozzle exit is dependent on not only freestream Mach number but also wing lift coefficient. Since the nozzle exit static pressure controls the engine operation, a change in aircraft attitude or Mach number can affect the engine operating point or thrust. This coupling effect must be included in the thrust-drag accounting system to properly

identify the thrust and drag components.

These effects can be included by using the following relation for gross thrust

$$F_g = F_{g_S} + (P_L - P_0) A_8 \qquad (10\text{-}3)$$

where F_{g_S} is the gross thrust determined from measured pressures and temperatures in conjunction with a nozzle velocity coefficient obtained from the static calibration. F_{g_S} assumes expansion to the local external static pressure, P_L. $(P_L - P_0)$ is the difference between the local and freestream static pressure, obtained from the external instrumentation at the nozzle exit shown on Figure 9.9, and A_8 is the nozzle exit area. The second term of this equation is the result of the close coupled nacelle-airframe configuration and is essential in a meaningful thrust-drag accounting system. It is important to remember that, statically, the local pressure, P_L, is assumed to be equal to the ambient pressure, P_0, while with freestream flow, P_L and P_0 can be significantly different for this nacelle installation.

The engine ram drag is found using the following relation

$$D_{ram} = \frac{W_{a_f} V_0}{g} \qquad (10\text{-}4)$$

where the fan weight flow, W_{a_f}, is found from measured inlet flow quantities and a calibration of the inlet discharge coefficient.

In summary the fundamental relations used in the thrust drag accounting system are equations 10-2, 10-3, and 10-4. To use these relations, two parameters, F_{g_S} and W_{a_f}, must be derived using measured quantities and empirical factors or coefficients which by definition are derived from a static calibration of the simulators under specified conditions (conditions described under 10.3.2).

10.3.2 Static Calibration

10.3.2.1 Powered Model Test Stand - The powered nacelle installations were statically calibrated on the Powered Model Test Stand at the Douglas Aerophycis Laboratory in El Segundo, California. The thrust stand, shown in Figures 10.1 and 10.2, allows direct reading of two force components and the moment in the nozzle plane of symmetry. The apparatus consists of a metric platform supported by four pads floating in mercury. The platform is restrained by load cells which provide the force and moment measurements. Each of the load cells can be loaded for calibrations with a special screw jack and reference load cell. High pressure air is supplied to the platform through a flexible hose cross-over system. The cross-over hoses terminate in the plenum chamber. The models attach to the apparatus at this point.

Proper simulation of the nozzle pressure ratios $(\bar{P}_{t_3}/P_L)$ encountered in the wind tunnel was accomplished by pressurizing the fan airflow to a total pressure of nearly 1.9 atmospheres. At the highest pressure ratio setting $(\bar{P}_{t_3}/P_{t_0})$ and highest inlet total pressure setting, nozzle pressure ratios $(\bar{P}_{t_3}/P_L)$ were on the order of 2.7.

The nozzle exit flowfield included simulation of the wing upper surface

geometry effects. This simulation was accomplished using a curved plate to represent the wing upper surface. The plate was mounted to the nacelle installation through a force balance. The forces and moment measured by this balance were removed from the total forces and moment measured by the thrust stand system. The resulting forces and moment represent the values exerted by the powered simulator nacelle only, i.e., the nozzle stream thrust minus the term P_0A_8. Hence, the turning effect of the wing upper surface is not included in the calibrated thrust, while the effect of the downstream geometry on the nozzle exit conditions is simulated except for the effects of forward speed.

10.3.2.2 <u>Calibration Analysis and Results</u> - During the static calibration the following items were measured and recorded:

a.   fan flow rate
b.   turbine flow rate
c.   total pressure and temperature upstream of fan
d.   static pressure around inlet duct (stations 1 and 2)
e.   total pressure and temperature in fan exhaust duct (station 3)
f.   static pressure around fan exhaust duct (station 3)
g.   total pressure and temperature in turbine exhaust duct (station 6)
h.   static pressure around turbine exhaust duct (station 6)
i.   static pressure around nozzle exit (internal station 8)
j.   static pressure around nozzle exit (external station 8)
k.   thrust of simulator/nacelle/nozzle assembly

(the simulator stations have been defined in Section 9.3.3 and Figure 9.1)

Both the fan flow rate and turbine flow rate were measured using standard flow meters. These flow meters were installed in the air supply lines upstream of the thrust stand.

The fundamental parameters calibrated were the following:

- fan weight flow, Wa_f
- nozzle gross thrust, Fg_s

The fan weight flow calibration is based upon measured inlet flow conditions. The gross thrust calibration is determined from measured fan and turbine discharge characteristics and from local flow conditions external to the nozzle exit. The pressure data were recorded using the instrumentation described in Section 9. The thrust was measured by the powered model test stand.

The instrumentation used in the powered nacelles was sufficiently redundant to provide different methods of calibration for both weight flow and thrust. The following discussion describes the version of fan weight flow and gross thrust calibrations that were used for the wind tunnel testing. The selected methods of calibration provide the most accurate and straightforward results.

10.3.2.2.1 <u>Fan Weight Flow Calibration</u> - The fan referred airflow is defined as

$$\Gamma_2 = \frac{Wa_f \sqrt{\theta t_2}}{\delta t_2} \qquad (10-5)$$

68

where

$$W_{a_f} = \text{fan weight flow (kg/sec)}$$

$$\sqrt{\theta_{t_2}} = (T_{t_2}/288)^{1/2}$$

$$\delta_{t_2} = P_{t_2}/101,314$$

$$T_{t_2} = \text{inlet total temperature (°K)}$$

$$P_{t_2} = \text{inlet total pressure (N/m}^2\text{)}$$

Since the inlet flow is adiabatic, T_{t_2} is assumed equal to T_{t_0}.

The fan referred airflow can be represented as

$$\Gamma_2 = \frac{101,314}{340} \gamma \; A_2 \; h\left(\frac{P_2}{P_{t_2}}\right) \tag{10-6}$$

where the h function is

$$h(P_2/P_{t_2}) = \left(\frac{P_2}{P_{t_2}}\right)^{\frac{\gamma+1}{2\gamma}} \left\{\frac{2}{\gamma-1}\left[\left(\frac{P_2}{P_{t_2}}\right)^{\frac{1-\gamma}{\gamma}} -1\right]\right\}^{1/2} \tag{10-7}$$

The above relations assume uniform static and total pressure distributions at station 2. However, due to the inlet profile and boundary layer effects, the flow at station 2 had some distribution both in static and total pressure. Hence, these equations must be used in conjunction with a calibration constant to provide a meaningful evaluation of fan referred airflow. The static pressure used as P_2 was the average static pressure, $\bar{P}_2$, measured around the inlet wall at station 2. The calibration was accomplished using a bellmouth upstream of the inlet throat so that the inlet boundary layer and local static pressure at station 2 was simulated for cruise mass-flow-ratios. Since the $(P_{t_2}/P_{t_0}>0.99)$ P_{t_0} can be used as P_{t_2} with no loss in calibration accuracy. Making these substitutions into Equation (10-7) and introducing a calibration discharge coefficient, C_{d_2}, leads to

$$\Gamma_2 = C_{d_2} \; \frac{101,314}{340} \gamma \; A_2 \; h\left(\frac{\bar{P}_2}{P_{t_0}}\right) \tag{10-8}$$

During the calibration test, Equation (10-8) was used to solve for C_{d_2} versus $\bar{P}_2/P_{t_0}$ with measured values of $\bar{P}_2$, P_{t_0}, T_{t_0}, and W_{a_f}. During the wind tunnel testing, the same relation was used to evaluate Γ_2 and, hence W_{a_f} for measured values of $\bar{P}_2$, P_{t_0}, and T_{t_0}, and a value of C_{d_2} from the calibration curve.

Figure 10.3 illustrates the calibration curves for both the inboard and outboard inlets.

10.3.2.2.2 Gross Thrust Calibration - The nacelle design used in this study includes a nozzle which combines both the fan and turbine exhaust streams before the nozzle exit. Although only one combined stream is exhausted, different methods of calibration indicated the performance is best represented by using a procedure assuming two independent streams. These considerations

69

lead to the following definition for nozzle velocity coefficient:

$$C_V = \frac{F_{g_S}}{F_{g_{iv}}} \qquad (10\text{-}9)$$

where

F_{g_S} is the measured static gross thrust

$F_{g_{iv}}$ is the ideal gross thrust

$F_{g_{iv}}$ is defined as:

$$F_{g_{iv}} = \frac{W_{af}}{g} V_{9_{if}} + \frac{W_{at}}{g} V_{9_{it}} \qquad (10\text{-}10)$$

In this equation the f subscript indicates fan stream quantities, and the t subscript indicates turbine stream quantities. In Equation (10-10), W_{af}/g and W_{at}/g are the actual fan and turbine mass flows, respectively. V_{9_i} is the ideal flow velocity assuming expansion to the local static pressure for the fan and turbine streams, respectively. These velocities are given by:

$$V_{9_i} = 1116 \sqrt{\theta_t} \left\{ \frac{2}{\gamma-1} \left[\left(\frac{P_L}{\bar{P}_t}\right)^{\frac{1-\gamma}{\gamma}} - 1 \right] \right\}^{1/2} \left(\frac{P_L}{\bar{P}_t}\right)^{\frac{\gamma-1}{\gamma2}} \qquad (10\text{-}11)$$

where

$$\sqrt{\theta_t} = \sqrt{\bar{T}_t/288\,^\circ R} \qquad (10\text{-}12)$$

and $\bar{T}_t$ and $\bar{P}_t$ are the average measured total temperature and total pressure in either the fan or turbine streams.

Figure 10.4 illustrates the calibrated C_V results for the four inboard and four outboard nozzle configurations. The curves are plotted versus the local nozzle pressure ratio, $\bar{P}_{t_3}/P_L$. $\bar{P}_{t_3}$ is used as the correlating total pressure for two reasons. First, the fan stream is the more dominant stream in the total exhaust. Depending on the operating point, the fan weight flow is two to three times the turbine weight flow. Secondly, the turbine total pressure, $\bar{P}_{t_6}$, is never greatly different from $\bar{P}_{t_3}$, as shown in Figure 10.5. Some differences in C_V are noted between inboard and outboard nozzles of the same configuration. These differences are attributed to differences in the model hardware. The repeatability of the data appears to be on the order of ±.005 in C_V.

During wind-on testing, the C_V calibration and simulator instrumentation were used to obtain F_{g_S} using Equation (10-9). F_{g_S} was then used with Equation (10-3) to get the quantity F_g used to correct the balance as shown by Equation (10-2).

Figure 10.6 illustrates the nozzle discharge coefficient, C_d, for the four inboard and the four outboard nozzle configurations. The curves for N_1 and

N_2 are quite flat, while N_3 displays a suppressed level at low pressure ratios. This suppression is the result of the rapid area convergence of the N_3 exit. N_4, on the other hand, displays high flow levels at low pressure ratios due to the divergence of the N_4 flow area near the exit.

10.3.2.2.3 <u>Installed Thrust Characteristics</u> _ A gross thrust coefficient is defined as:

$$C_{GMX} = \frac{F_g}{q_o S_w} \qquad (10-13)$$

and a ram drag coefficient is defined as

$$C_{D_{ram}} = \frac{D_{ram}}{q_o S_w} \qquad (10.14)$$

By using measured static and total pressures, total temperatures, and the calibrated C_v and C_{d_2} characteristics, C_{GMX} and $C_{D_{ram}}$ can be calculated for wind tunnel test results. Figures 10.7 and 10.8 present typical variations of these parameters with fan pressure ratio for inboard engine alone and for inboard + outboard engines.

It may be assumed that C_{GMX} is equal to C_μ for purposes of interpreting the results in Section 11.0.

10.3.3 <u>Isolated Nacelle Drag Estimates</u>

The nacelles in this type of installation cannot be tested "isolated" from the configuration, as they interface directly with the wing. Fairings of the nacelle could be used to provide quasi-isolated configurations, but such procedures might introduce ambiguities into the thrust-drag bookkeeping system that would be difficult to reconcile.

Methods of estimating isolated nacelle drag have been developed to a degree of refinement that estimated isolated drag characteristics of the nacelles were considered to be of satisfactory accuracy for this program.

10.3.3.1 <u>Nacelle External Drag, D_{ESF}</u> - The external drag of the nacelles was calculated using the relationship:

$$\frac{D_{ESF}}{q_o} = K \, C_f \, S_{wet}$$

where

  D = drag

  q_o = freestream dynamic pressure

  C_f = skin friction coefficient of a smooth flat plate with a turbulent boundary layer. C_f is a function of Mach and Reynolds number.

$\qquad$ K $\quad$ = form factor, based on Douglas empirical correlations with experimental data. These correlations are expressed in terms of equivalent body fineness ratio.

S_{wet} = wetted area of the exterior of the nacelle

Each of the nacelles has the same equivalent body fineness ratio, so the value of K = 1.246 was used for each nacelle. It should be noted that none of the nacelles was estimated to have any compressibility drag at the design point, and they were assumed to be free of flow separation.

The external nacelle drag accounted for the drag of that portion of the wing surface that would be hidden by the nacelles. The drag was estimated using turbulent skin friction relationships in a strip analysis that accounted for local variations in dynamic pressure and Mach number over that portion of the wing surface.

The base drag of the nozzle trailing edge (thickness = 0.0254 cm or 0.010 inch) was estimated, accounting for variations in local Mach number in the vicinity of the nozzle trailing edge, and included in the nacelle external drag.

10.3.3.2 Nacelle Internal Drag, Flow Through $(F_g - D_{ram})$ - The internal drag of the flow-through nacelles was estimated using relationships similar to those used externally, except that the form factor is unity and the variations of local internal Reynolds and Mach number and dynamic pressure are accounted for.

The mean static pressure at the nozzle exit for the installed flow-through nacelles was estimated based on the potential flowfield analysis (Reference 22) over a range of values of Mach number and lift coefficient. The nacelle internal Mach number distributions were then established as functions of free-stream conditions, Mach number, and lift coefficient over the ranges of the test. The sensitivity of internal drag to lift coefficient was found to be negligible.

10.4 Boundary Layer Transition Fixing

Early in the experimental program a decision was made to fix boundary layer transition near the leading edge of the wing to ensure consistency of the drag results with and without nacelles. Transition trips were applied on the wing at 7-1/2-percent chord for all configurations.

Using the Braslow transition charts (Reference 30), it was determined that a roughness height of 0.01143 cm (0.0045 inch) would trip the boundary layer without incurring excessive roughness drag. The transition trip took the form of a 0.318 cm (1/8 inch) wide band of finely graded glass beads (Ballatini), that were fixed to the wing by a colored laquer. Sublimation tests conducted at the beginning of the experimental program confirmed that this method of transition fixing did in fact cause transition from laminar to turbulent flow to occur at the trip.

Transition was also fixed externally near the leading edge of the nacelles by narrow bands of Ballatini beads; the bead size chosen being 0.0152 cm (0.0060 inch) for those components. Small discrete triangular pieces of 0.01 cm thick mylar tape were attached internally near the throat in lieu of glass beads to minimize the probability of ingesting beads into the simulators.

10.5 Flow Visualization Techniques

Several methods of flow visualization were evaluated during the experimental program, including sublimation, oil flow, and micro tufts.

10.5.1 Sublimation

The conventional procedure of spraying a solution of fluorene in a mixture of alcohol and acetone was used to confirm the effectiveness of the glass bead transition strips at typical test conditions.

10.5.2 Oil Flow Visualization - The model was equipped with pressure-fed oil reservoirs near the wing leading edges. The upper surfaces of these reservoirs consisted of sintered bronze material that was sufficiently porous to permit the slow "weeping" discharge of a mixture of low viscosity oil (Stoddard solvent) and fluorescent dye. Flash lamps, equipped with ultra violet filters designed to pass little visible light but considerable light in the wave lengths required to fluoresce the dyed oil, were located outside the transparent windows in the test section. Cameras synchronized with the flash lamps recorded the oil flow patterns. The primary advantage of this type of oil flow visualization technique is that many data points may be obtained during a single run. The Douglas Company has used this technique successfully on several occasions.

Technical problems were encountered with the oil flow procedures in this test and inadequate time was available to resolve the difficulties. The oil flow visualizations were relatively unsuccessful in this case.

10.5.3 Micro Tufts - Micro tufts have been extensively used by Douglas in other test programs where both force data and flow visualization experiments have been conducted simultaneously on a non-interfering basis. In another NASA-Douglas cooperative experimental program (Reference 31), nearly one thousand such tufts were installed on a high speed wind tunnel model in the NASA Ames 11-foot facility. Comparisons of the force data for configurations with tufts on and off indicated drag coefficient changes of less than 0.0002 for the worst case, and no change in many.

Micro tufts, consisting of 0.00178 cm (0.0007-inch) diameter monofilament nylon tufts, coated with fluorescent dye, were cemented to the model surfaces with duco cement. Lighting and photographic techniques similar to those used in the oil techniques were utilized to record the images. This technique was utilized only during the NASA conducted extension of the test following the joint Douglas-NASA portion of the program.

73
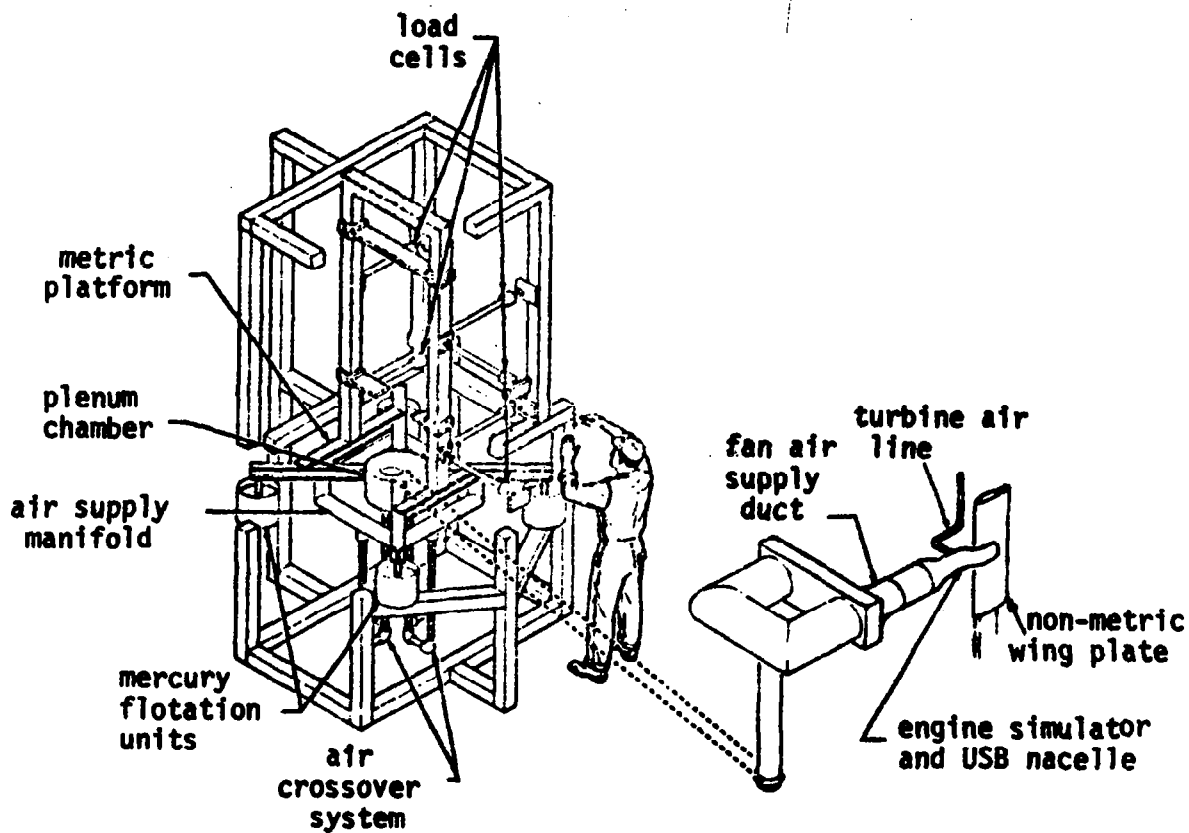
Figure 10.1. Powered Model Static Test Stand

engine simulator
and USB nacelle

load cells

metric plenum

non-metric
wing plate
(attached to
separate balance)

mercury
flotation
units

non-metric
air supply
manifold

pressurized
fan air
supply

fan air
crossover
system

turbine air line
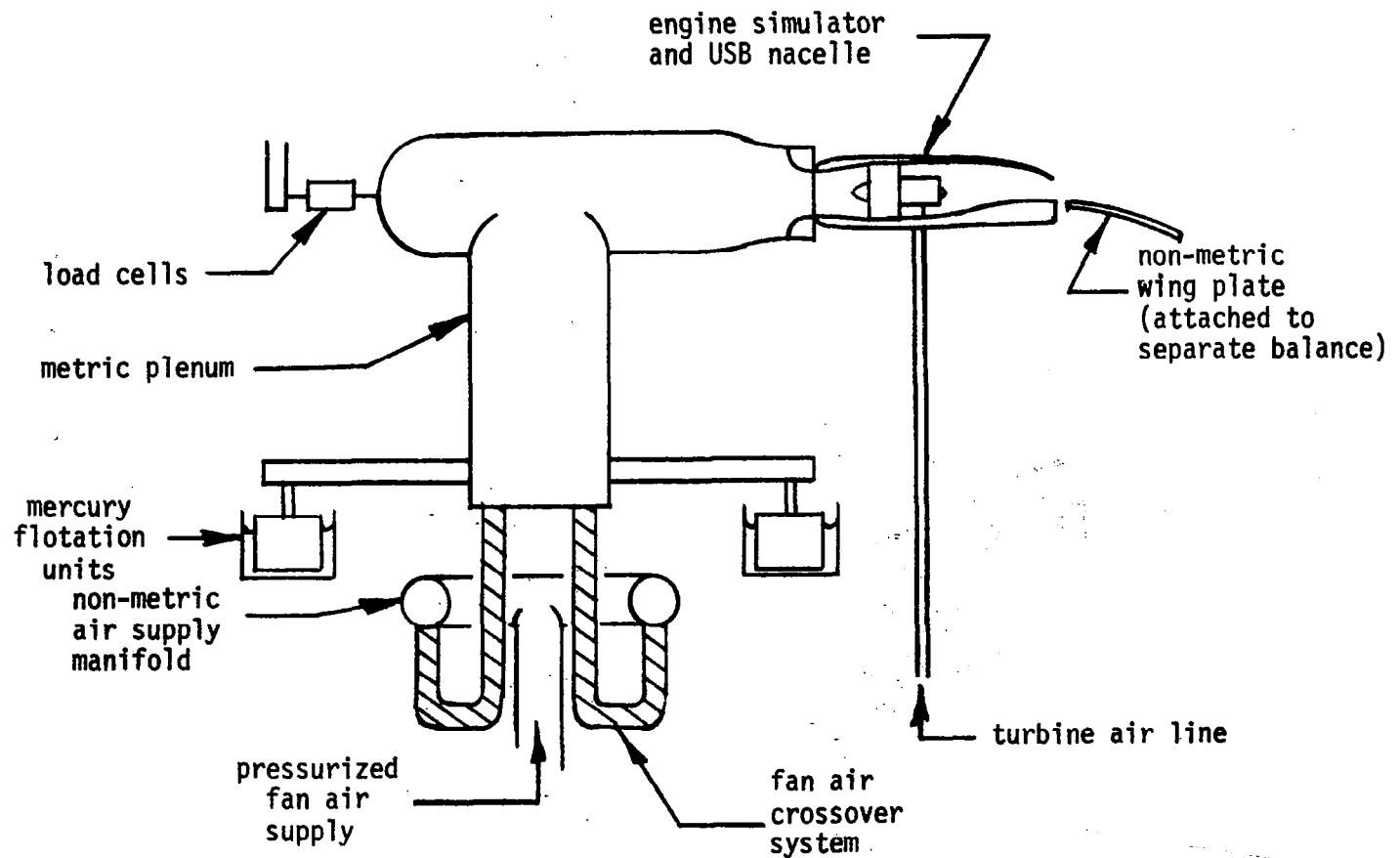
Figure 10.2.   Schematic of Powered Model Static Test Stand.
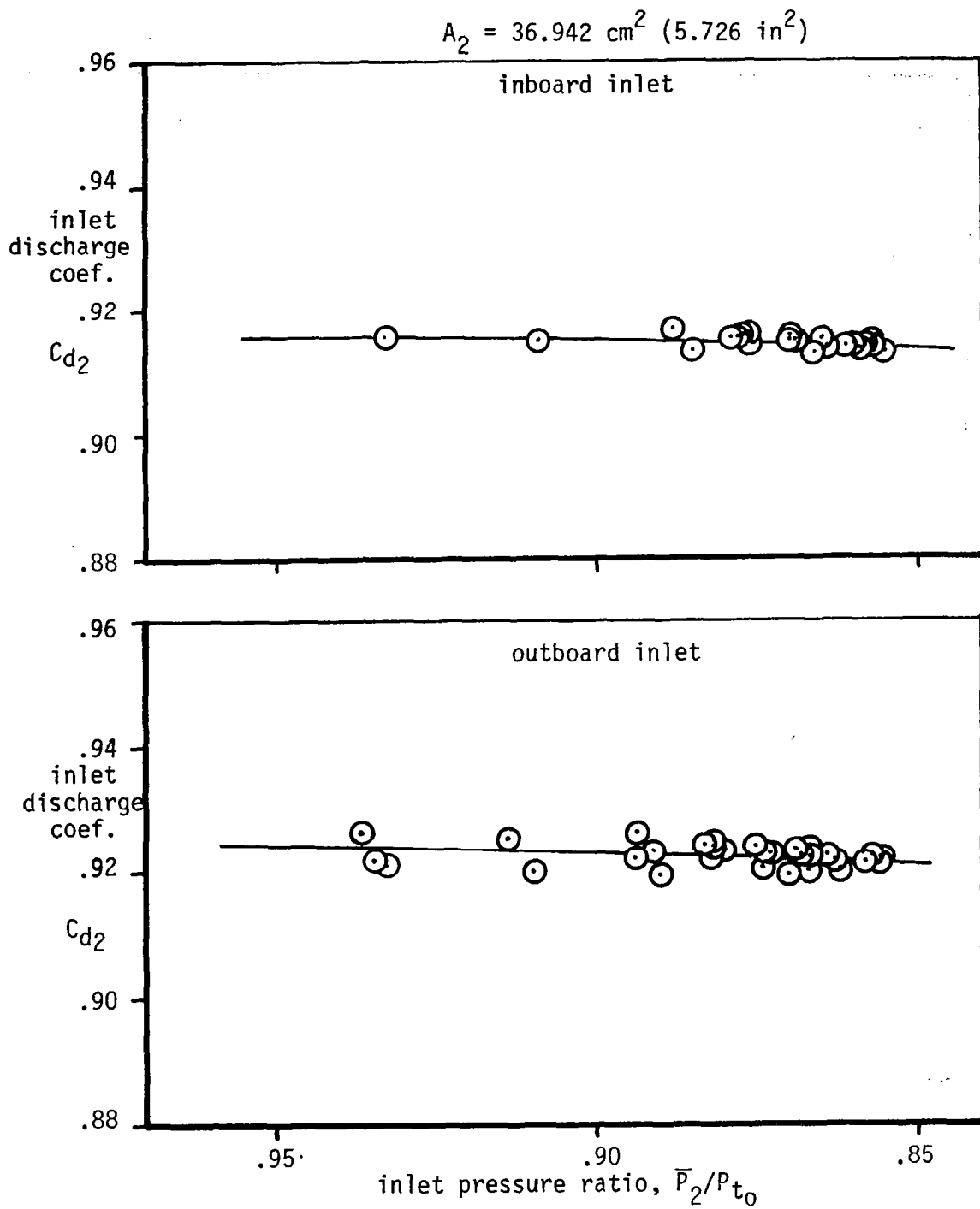
Figure 10.3. Static Calibration Results for Inlet Discharge Coefficient
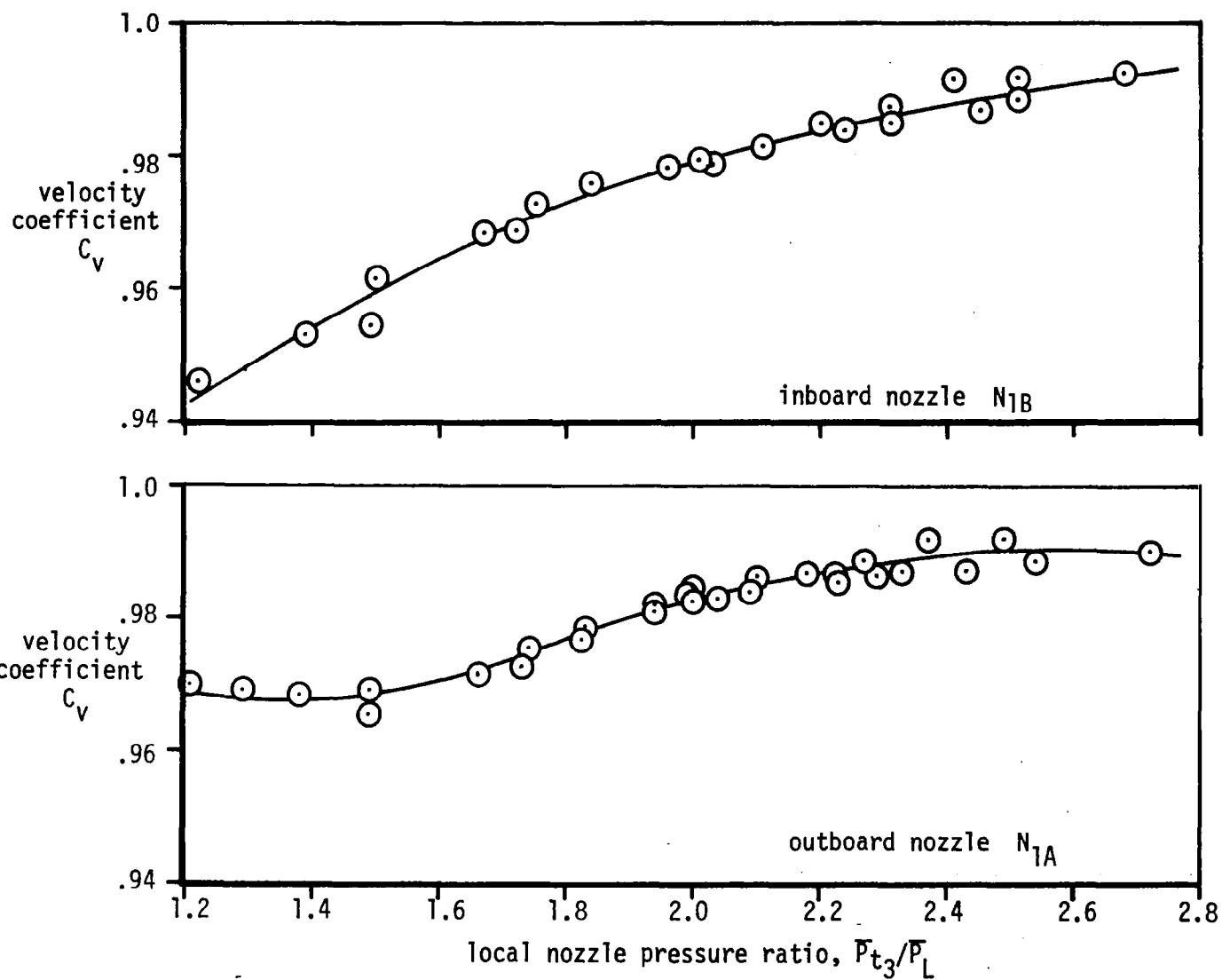
Figure 10.4. Static Calibration Results for Nozzle Velocity Coefficient
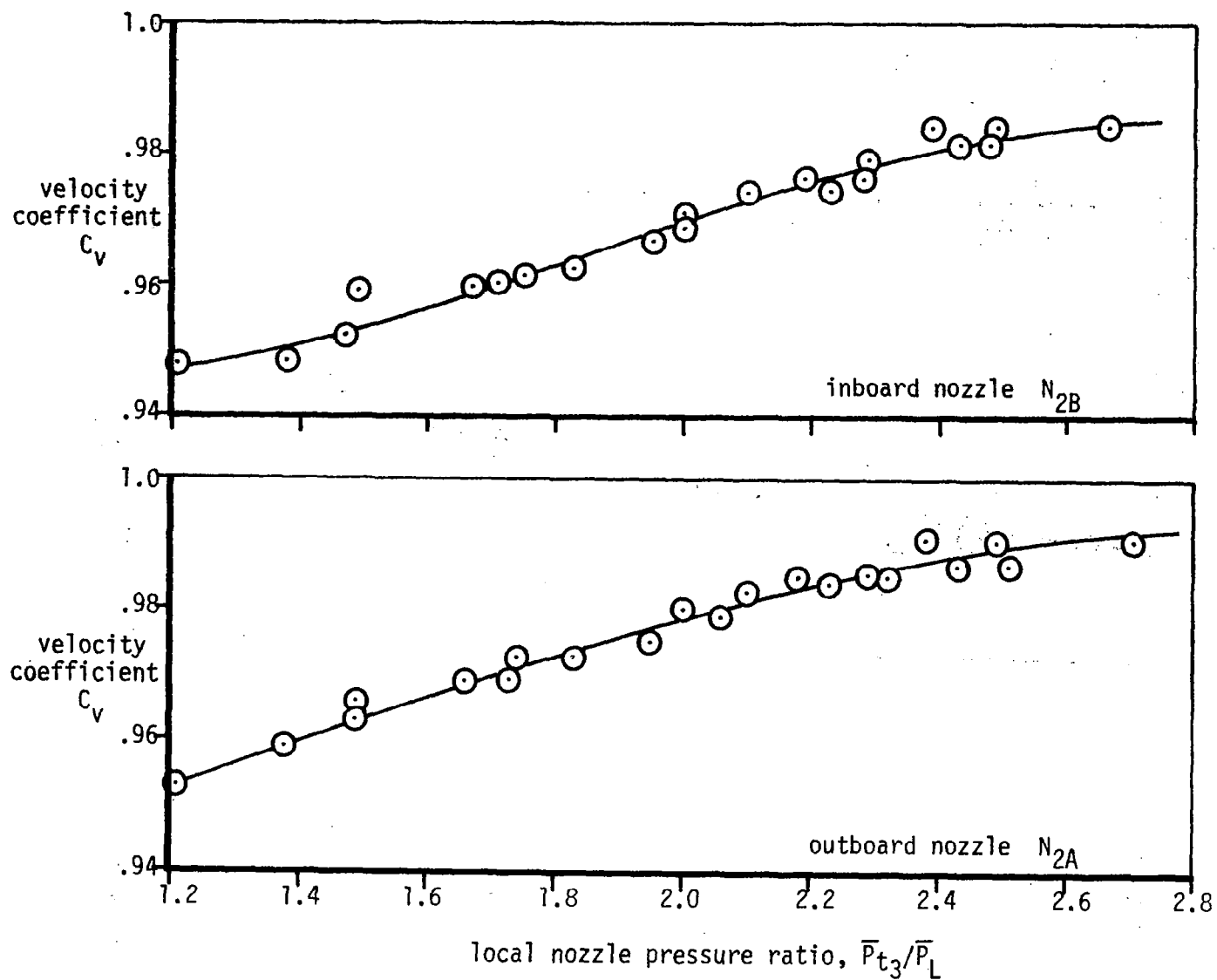
Figure 10.4. (Continued)
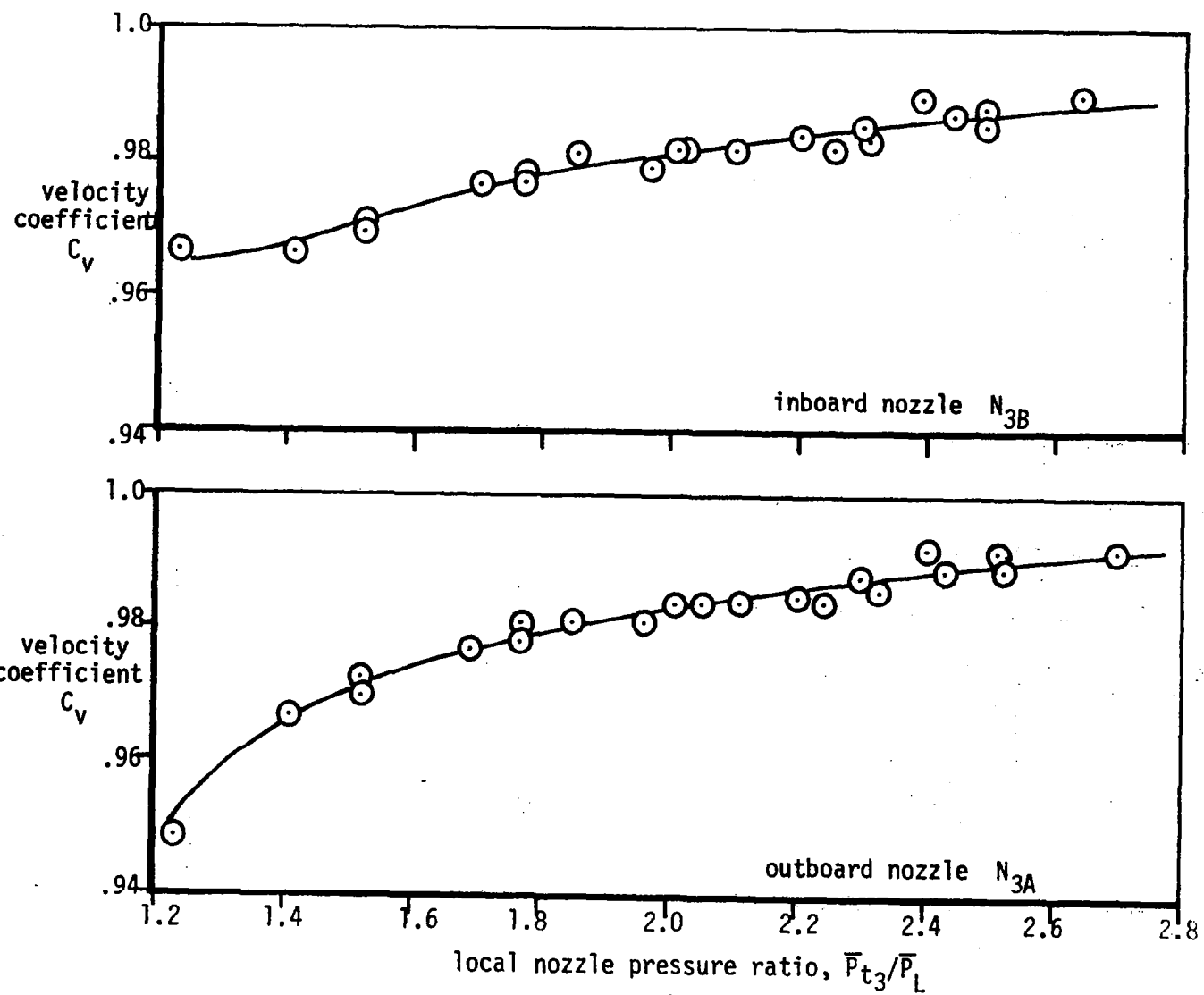
Figure 10.4. (Continued)
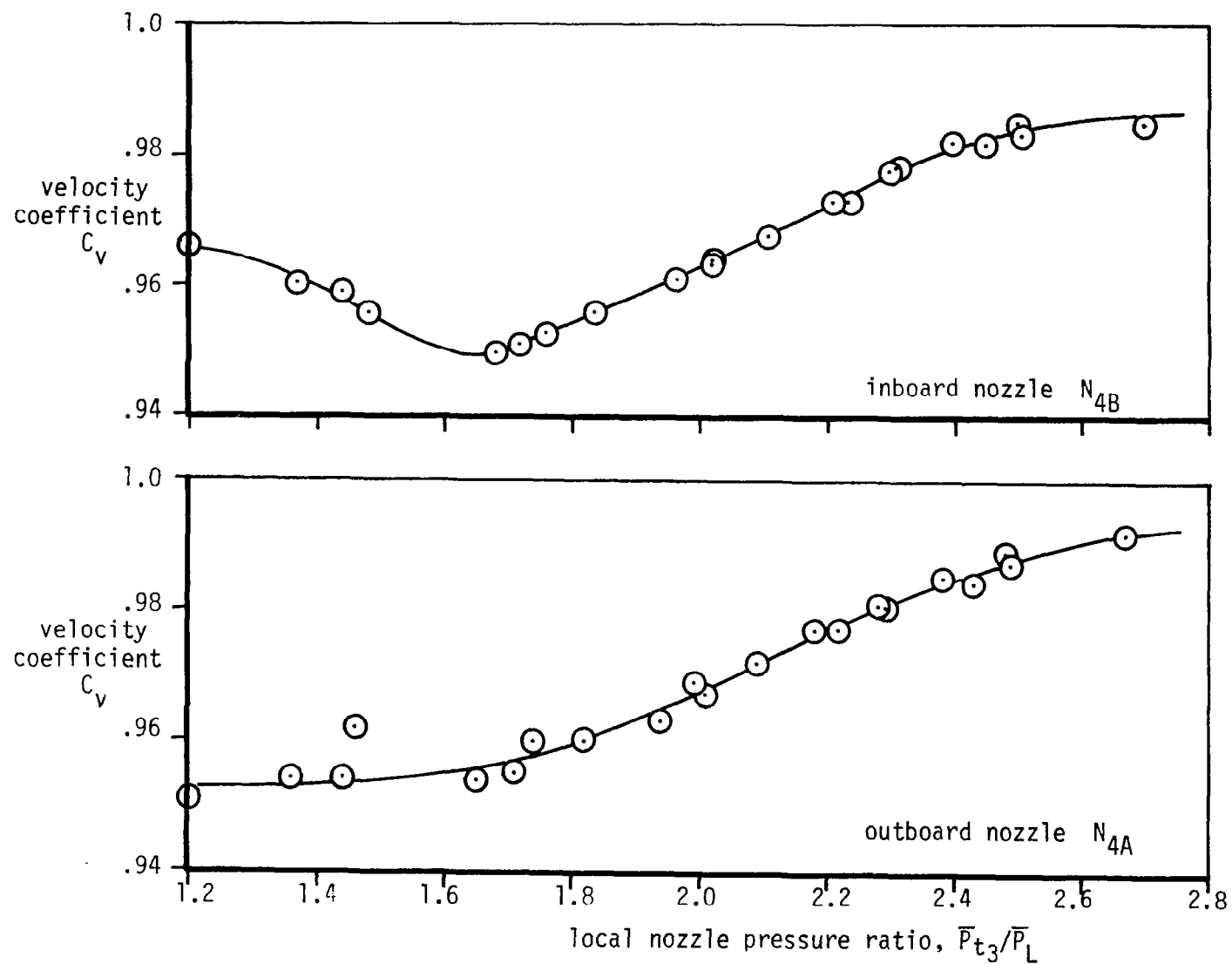
Figure 10.4 (Continued)
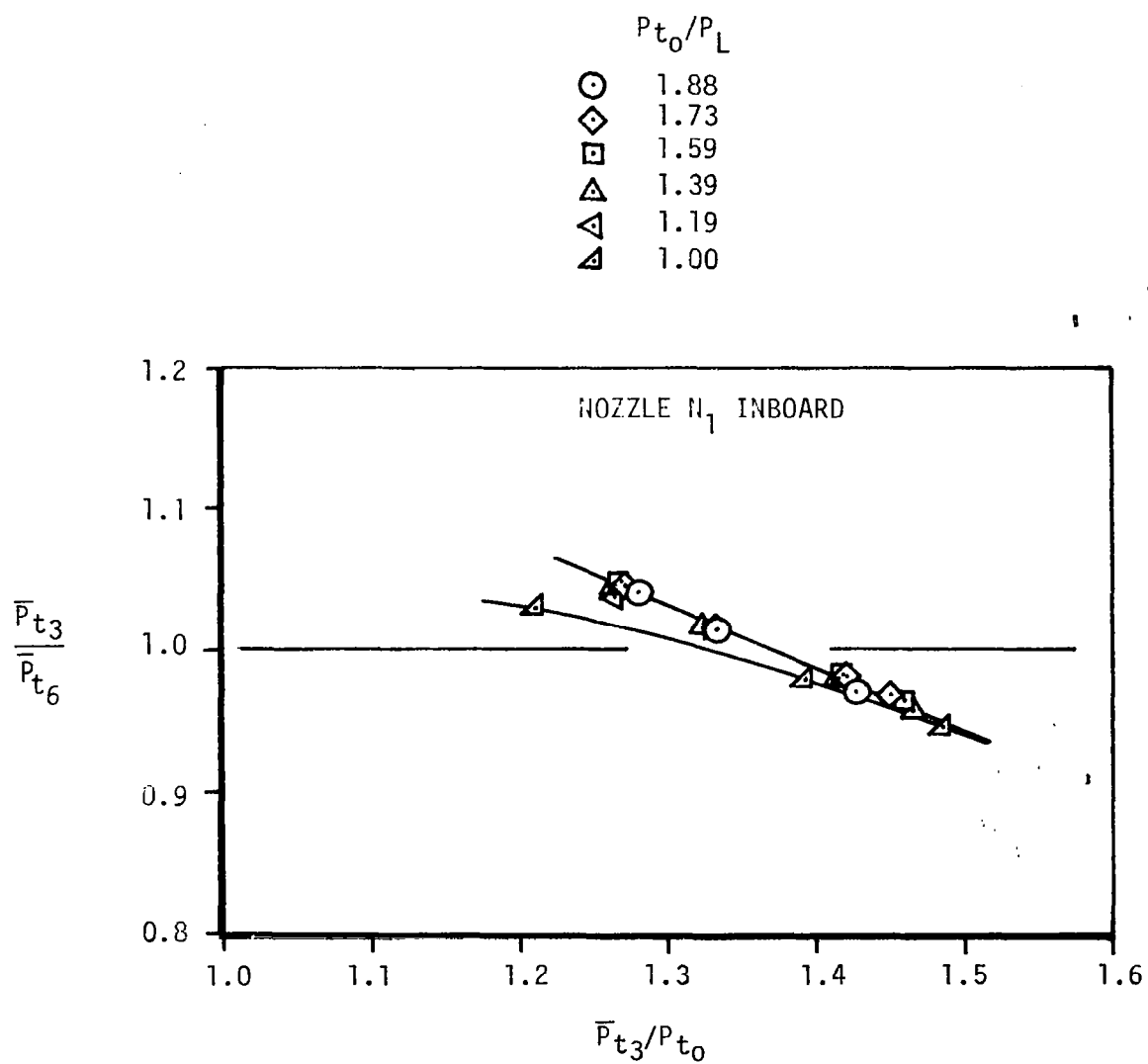
Figure 10.5. Variation of the Ratio of Fan and Turbine Discharage
Total Pressures with Fan Pressure Ratio.
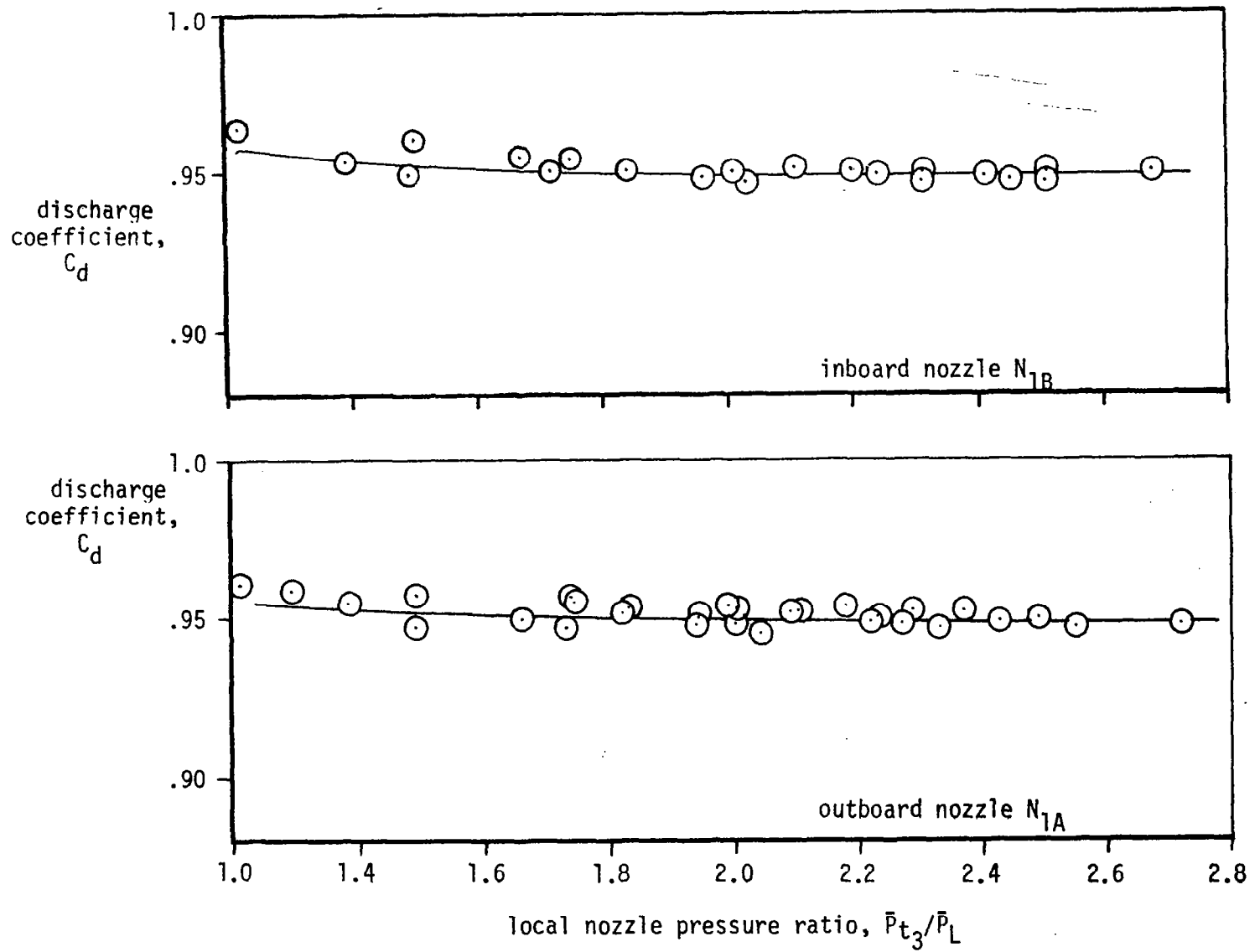
Figure 10.6. Static Calibration Results for Nozzle Discharge Coefficient

discharge
coefficient,
C_d

inboard nozzle N_{2B}

discharge
coefficient,
C_d

outboard nozzle N_{2A}

local nozzle pressure ratio, $\bar{P}_{t_3}/\bar{P}_L$
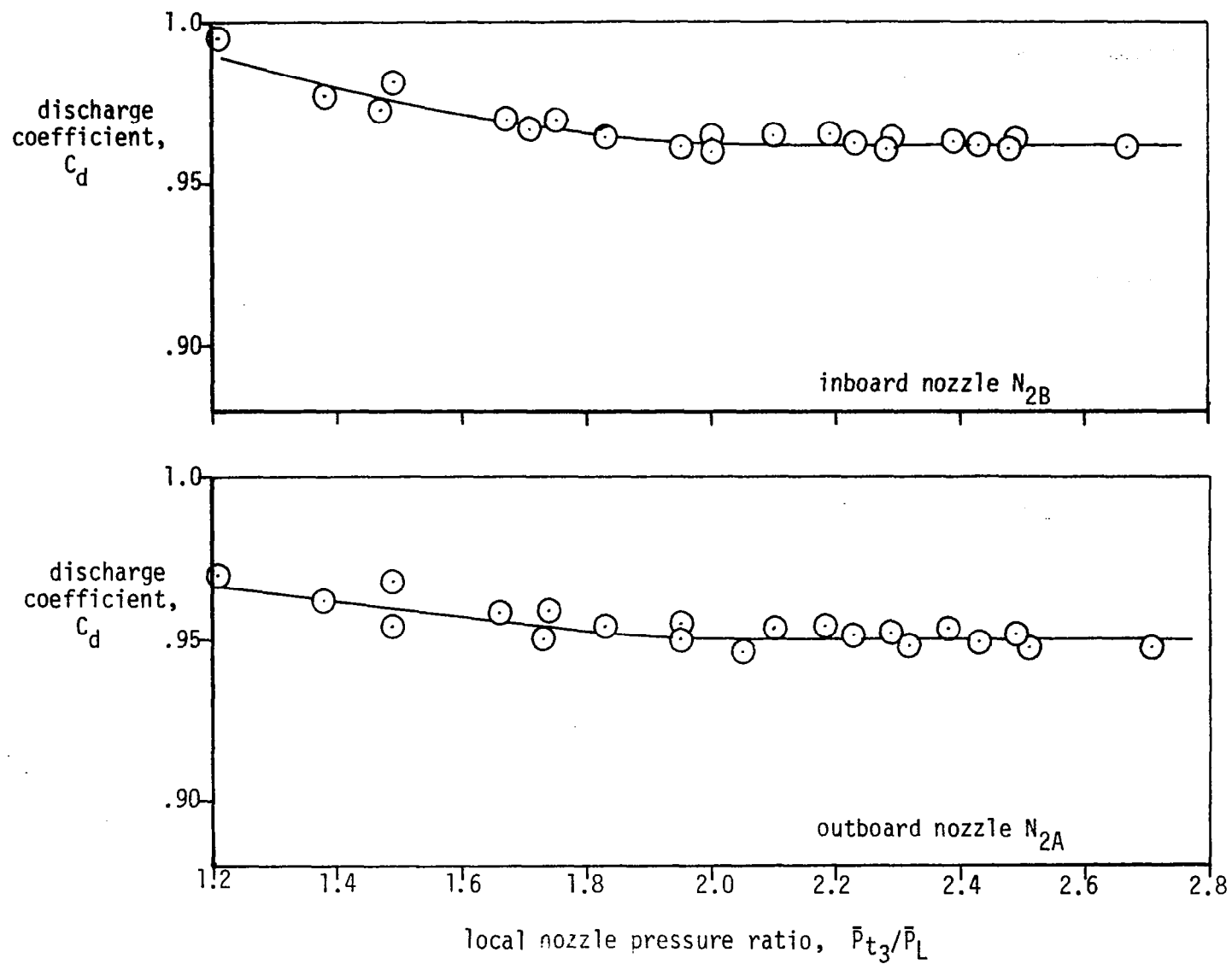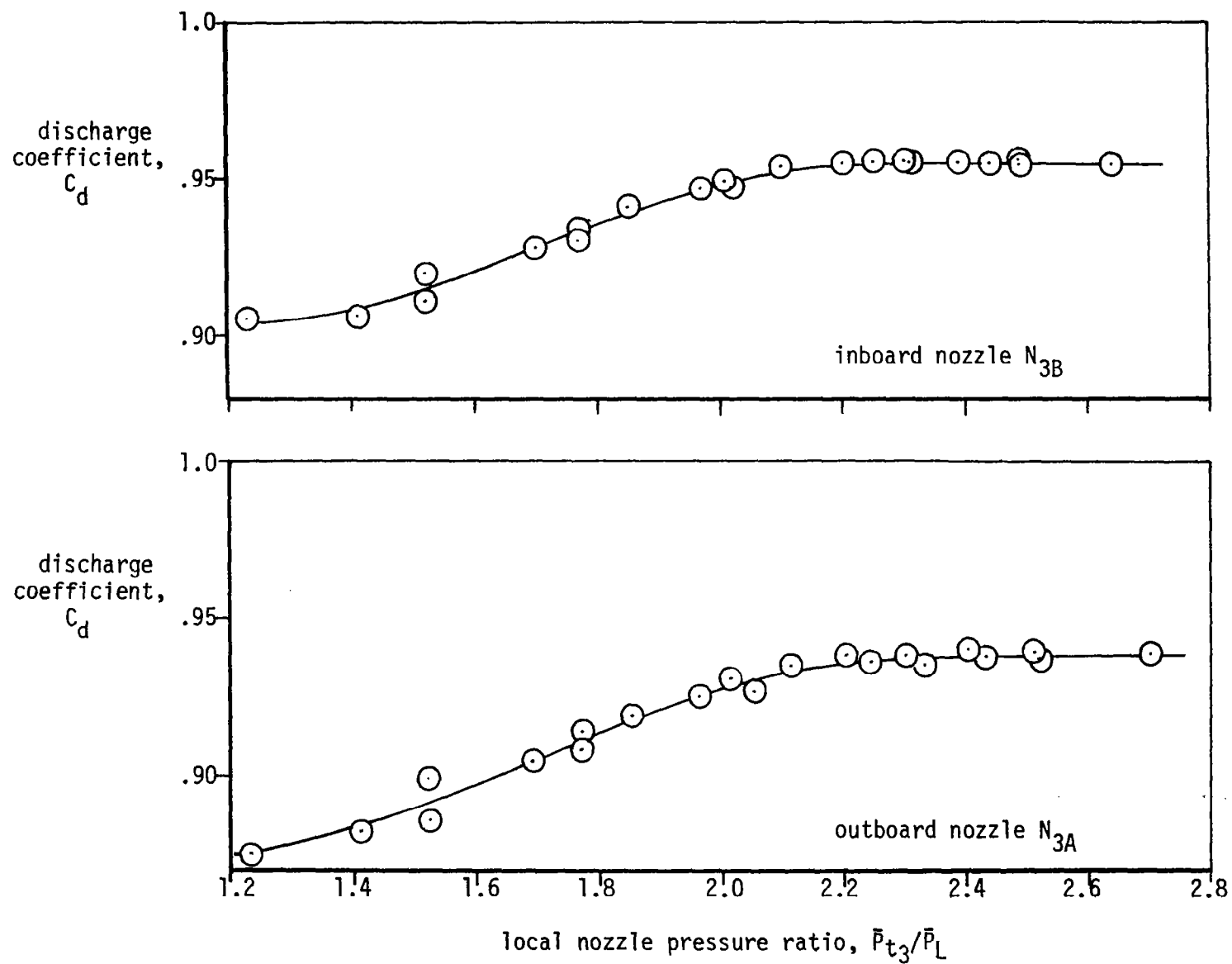
Figure 10.6 (Cont.)
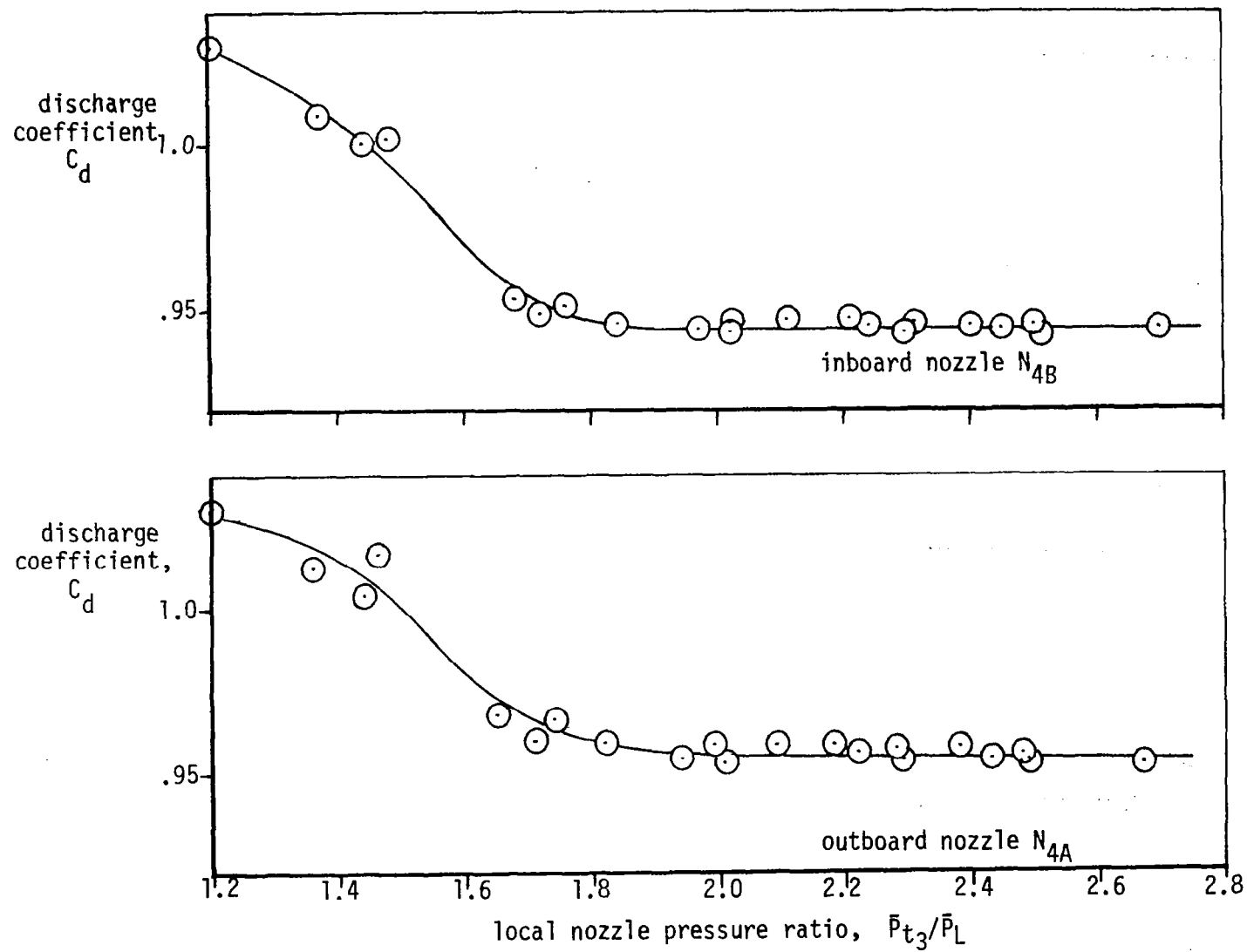
Figure 10.6. (Cont.)

Figure 10.6 (Cont.)
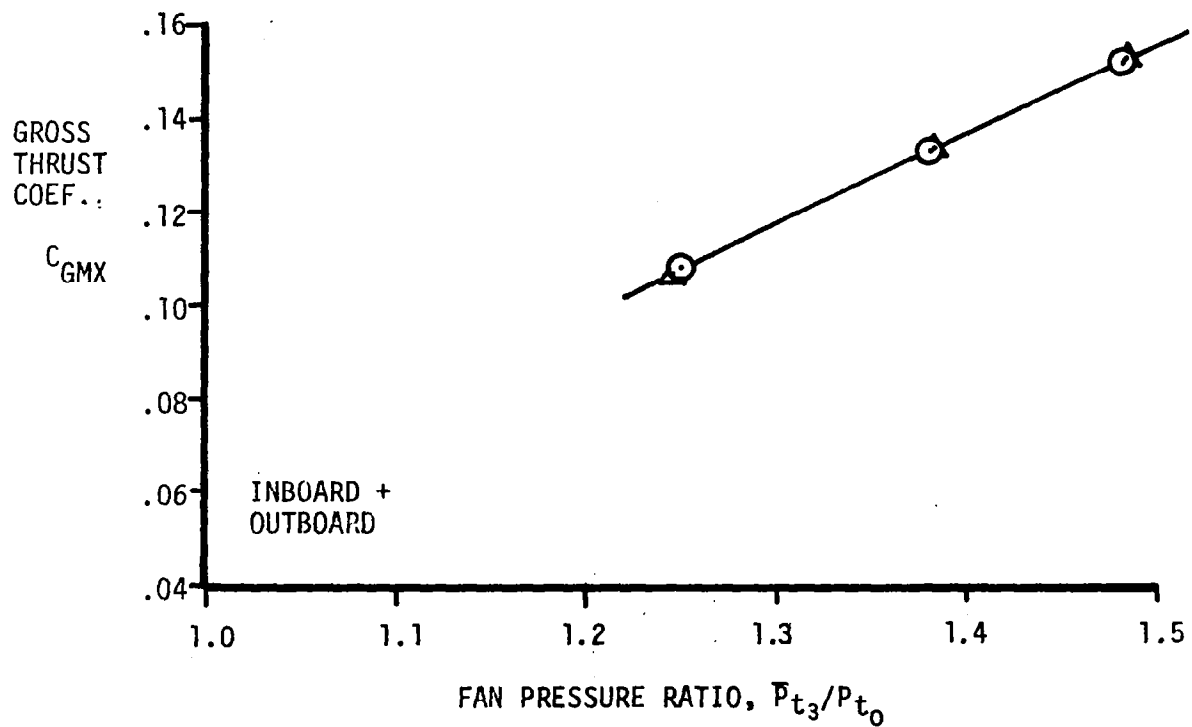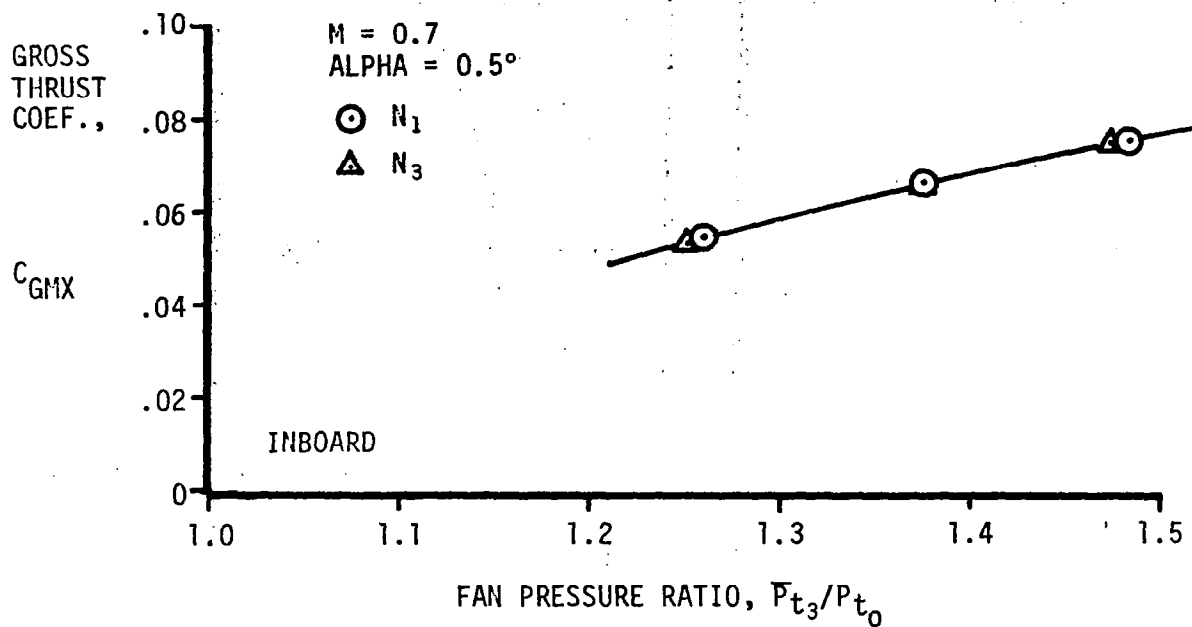
Figure 10.7. Typical Variation of Gross Thrust Coefficient with Fan Pressure Ratio
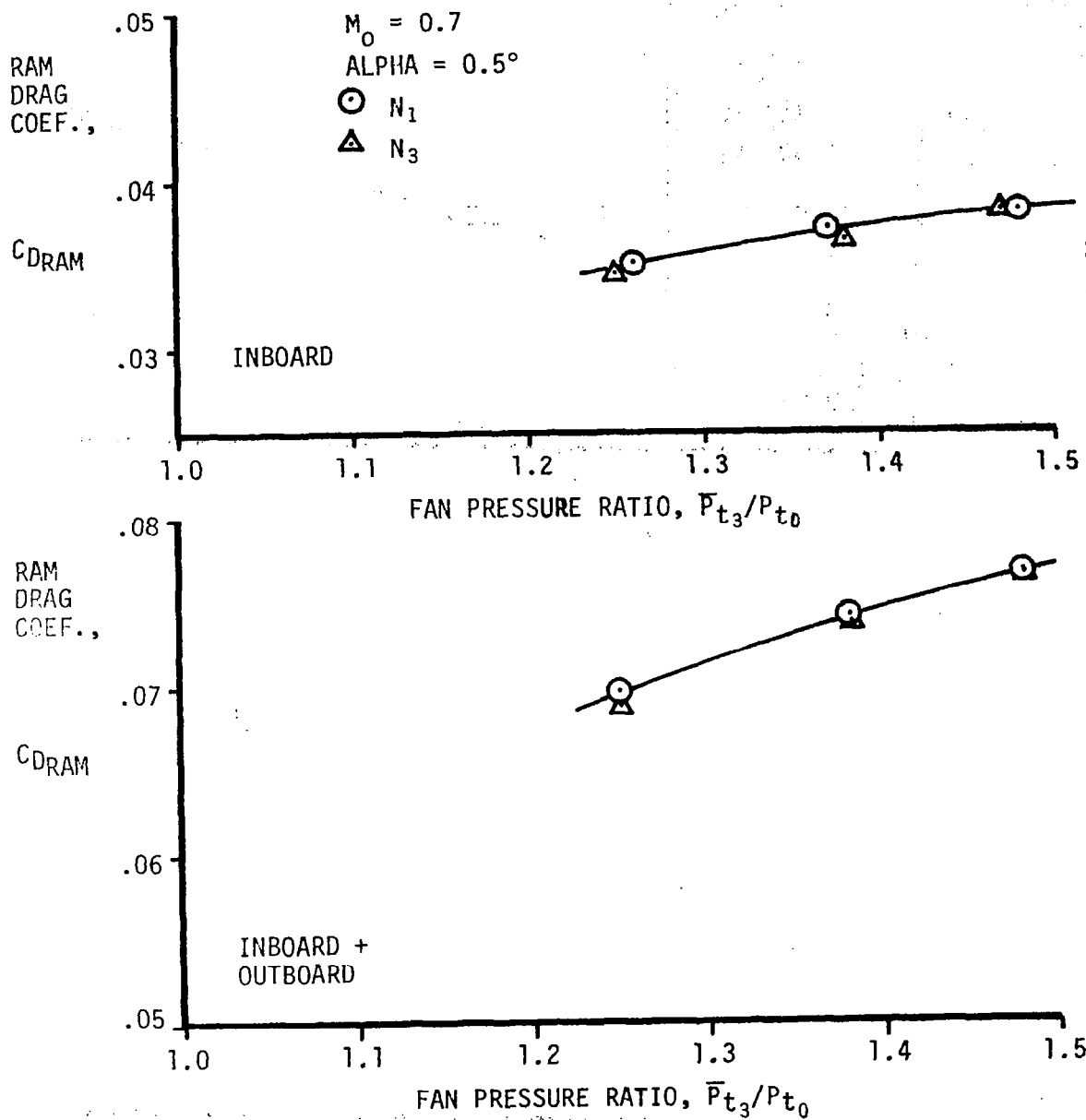
Figure 10.8. Typical Variation of Ram Drag Coefficient
with Fan Pressure Ratio

11.0 RESULTS AND DISCUSSION

11.1 Basic Wing-Body Configuration

11.1.1 Basic Wing-Body Characteristics and the Effects of Transition Fixing -
As previously discussed in Section 10.4, it was decided early in the program
to fix transition on the wing to give consistency in the data obtained from
the nacelles-on and nacelles-off configurations. Previous Douglas experience
in testing supercritical wings indicated that artificially fixing the tran-
sition point on the wing lower surface can critically affect the wing drag rise
characteristics. Therefore, some preliminary testing was conducted on the
wing-body alone to assess the effects of transition location on this model.
Figures 11.1 and 11.2 show the drag rise characteristics of the wing-body
with natural transition and with transition fixed at 7-1/2 percent chord on
the upper and lower surface. They show that fixing transition reduces the drag
rise Mach number* by about 0.01. Since the design conditions for this model
were set at M=0.70 based on the study results of Reference 3, this reduction
in drag rise Mach number should not affect the objectives of these tests.

Figures 11.3 and 11.4 show comparisons of pressure distribution measured with
transition fixed and free. These pressures were measured at 38-percent semi-
span, and show that transition fixing causes a loss of lift over the last
30-percent chord, especially on the lower surface of the wing. Previous
investigations of the aerodynamics of supercritical wings have attributed this
lift loss to a thickening of the boundary layer in the concavity on the lower
surface in the trailing edge region. Comparing these two figures shows that
this effect increases between M=0.7 and M=0.76. The lift and pitching moment
curves plotted in Figures 11.5 through 11.7 also show the effect of transition
on the aerodynamic characteristic of the wing-body, and that the effect
increased with Mach number. However, the linearity of the lift and pitching
moment curves, even at M=0.76, indicated that the characteristics of the wing-
body are well behaved over the C_L range of interest in this investigation.

Figure 11.8 through 11.17 show samples of the pressure distribution
measured across the wing. Again comparisons were made between transition
fixed data with natural transition. The M=0.7 data show clearly that at
this Mach number, the wing is operating conservatively, that is with only
small regions of supercritical flow and with very mild shock waves near the
leading edge of the wing, well ahead of the nacelle engine exhaust nozzle
location.

Integration of the transition fixed pressure data at M=0.7 and M=0.76 produce
the spanwise distribution of C_l shown in Figures 11.18 and 11.19.

A comment should be made about the section lift and spanload values at 13-
percent semispan throughout this report. The wing surface pressures at this
wing-fuselage juncture location were erratic thereby producing poor quality
section lift values. The values are included in the figures but they only
represent the order of magnitude of the true value.

_____

* Drag rise is defined as the Mach number at which the variation of drag with
  Mach number $(\partial C_D/\partial M)$ is 0.1.

It was concluded from the above results that, for the conditions of interest for this study, the remainder of the test could be conducted with transition fixed on the wing at 7-1/2-percent chord.

11.1.2 Comparison of Data with Theory - An objective of this program was to establish the validity of the existing analytical methods, by comparing these methods with test data. Several methods will be introduced as the results are discussed.

The DAC Neumann three-dimensional program (Reference 22) was the principle analytical tool used during this program. As previously described, this program uses a potential flow method in conjunction with Gothert compressibility corrections for Mach number effects. It is capable of calculating three-dimensional flowfields about lifting wing-body configurations. The wing and body were paneled using established techniques based on previous DAC experience. To allow for viscous effects, the displacement thickness of the boundary layer (δ^*) was calculated for several sections of the wing, using the two-dimensional boundary layer theory of Reference 24, and added to the basic wing ordinates. For these calculations it was assumed that transition occurred naturally; the boundary layer program indicating that transition occurred at eight-percent chord on the upper surface, and 44-percent chord on the lower surface. These "displaced" ordinates were used as input to the Neumann program.

The results of the Neumann program are compared to the transition free and fixed experimental lift curve data in Figure 11.20, at a Mach number of 0.7.

The discrepancies between the theory (which was for transition free conditions) and the data can be attributed to: a) inaccuracies of estimating the boundary layer effects on the wing, b) cross flow and wing carry over lift on the fuselage, and c) interference due to the wind tunnel such as solid body and wake blockage, bouyancy and lift interference effects.

The estimated incremental lift effect due to the walls for a 3.1-percent porosity is shown on Figure 11.20. These estimates were obtained using an unpublished DAC method (by M. L. Lopez) which calculates the tunnel boundary interference effects of an arbitrary wing in an open, closed or slotted wall wind tunnel of arbitrary geometry. The method has the capability of computing the aerodynamic characteristics of a clean wing in free air as well as in the wind tunnel. The approach used assumes the effect of the boundaries to be a small perturbation to the flow about the wing when in an infinite unbounded stream. A solution in terms of the induced velocity potential is obtained by considering the problem in the Trefftz-plane and replacing the tunnel boundary by a discrete source/vorticity distribution of singularities and the wing by a continuous distribution of vorticity corresponding to the trailing vortex strength of the wing. The final solution takes into account the total perturbation velocity, thus assuming that the spanwise loading is affected by the tunnel boundary, which in turn should lead to an improved estimation of induced drag corrections.

Comparisons of the wing surface pressure distribution between theory (transition free) and experiment (transition fixed) are shown in Figures 11.21 through 11.23. Generally, the comparisons are good except near the wing

trailing edge where viscous effects may not be correctly simulated.

Also shown in Figure 11.22, is a pressure distribution calculated by the DAC version of the Garabedian two-dimensional transonic theory (Reference 23). Viscous effects were accounted for by the addition of boundary layer displacement thickness as previously described. These data agree well with experiment although the transonic flow in the leading edge region is underpredicted. Again the discrepancy on the aft lower surface could be caused by inadequate simulation of the boundary layer in the trailing edge region.

The spanload distribution of Figure 11.24 shows a comparison between the Neumann program and the experimental data. There is very little difference between the transition free and fixed data except at the 13-percent semispan location. However, since the pressures were questionable at the 13-percent location these differences must be ignored. Accepting the values at the other spanwise locations, it is concluded that the fuselage and wing very close to the fuselage must be carrying more lift than predicted by the theory. The estimated increment in spanload using the method described previously due to the 3.1-percent porous wind tunnel walls was negligible indicating that the tunnel effects on spanload are small.

11.2 Nacelle Interference

11.2.1 Introduction to Nacelle Interference Drag Data - The various nacelle configurations previously described were tested on the wing-body and the results are presented in the following sections. The main emphasis of these results is consistent with the overall scope of the program, which was to assess the effects of installing overwing nacelles on a supercritical wing and assess the effects of a jet issuing from these nacelles. For the purposes of this technology study, the importance of the test program is to aid in an understanding of the aerodynamics, an assessment of existing methods and design techniques, and in the identification of areas that need further effort. It is in this light that the fuselage, wing, and nacelles were designed. For example, as described previously, operational aircraft requirements were compromised by eliminating the fuselage upsweep and designing the forebody and afterbody so as to be well away from drag divergence. One key point is that the nacelles were sized to be representative of a four-engine aircraft. The model, however, had the capability to test inboard engine alone or outboard engine alone. The interference drags obtained from these configurations are useful in understanding the aerodynamics of one nacelle type relative to the other even though the drag levels do not accurately represent a two-engine configuration because the nacelle size would represent an engine that would not satisfy the short field requirements.

11.2.2 Baseline Nacelle (N_1) - The baseline nacelle is basically a high speed design in that the exit aspect ratio is low and the boattail angles are moderate. The nacelle was not contoured to the local wing flowfield except for the inlet which was aligned with the local flow direction at the nominal design point. The spanwise locations were selected based on preliminary systems analyses. The vertical location was determined so that there were moderate curvatures in the internal duct forward of the nozzle and so that there were approximately equal external boattail angles on the nozzle upper surface and lower surface fairing.

90

11.2.2.1 Unpowered

Drag Characteristics - The drag coefficients for variations in location and number of nacelles are shown on Figure 11.25. The shape of the nacelle-on curves is generally the same as for the wing body except at the highest Mach numbers where the rate of drag increase with the nacelles-on is not as great as the wing body. These favorable drag effects often occur when nacelles are added to a wing in drag rise. The shift in level at the lower Mach numbers is due primarily to the skin friction and form drag on the nacelle and other wing-nacelle interferences.

The nacelle interference drag is defined by subtracting the estimated nacelle skin friction and form drag (internal and external) from the nacelle-on data and referencing the result to the wing-body results at the same C_L and M. These results are shown on Figure 11.26. In general, the interference drags are not excessive indicating that the installation of the nacelle does not produce significant shock waves, flow separations, or distortions in the spanloading.

There may be some adverse interference of the inboard nacelle with the fuselage since the interference drag for the outboard nacelle is not as high as for the inboard nacelle. The four engine interference drag is slightly more than the sum of the individual inboard and outboard interference drags. At M=0.70 the magnitude of this apparent drag penalty from interference between the nacelles is about 1.5-percent of wing-body drag with this value diminishing to about one-percent near M=0.76.

Pressure Distributions - The pressure distributions on the wing at 33-percent semispan (just outboard of the inboard nacelle N_{1B}) for all of the above configurations at M=0.70 are shown on Figure 11.27. The inboard nacelle alone increases the negative C_p near the leading edge only slightly and the four-engine configuration increases the negative C_p and strengthens the shock significantly, all of which is consistent with the drag data. The outboard nacelle alone increases the C_p about as much as the four-engine configuration. However, the shock strength is weaker since the pressure level at the base of the shock pressure rise is more negative. Just outboard of the outboard nacelle N_{1A} the effects on the wing pressures due to installing the nacelle are very similar to those just outboard of N_{1B}. Even though the region inboard of N_{1A} didn't significantly affect the drag, the pressures do indicate a potential problem area for an outboard nacelle installation.

There is a significant forward movement of the wing shock near the drag divergence Mach number of the wing as shown in Figure 11.28. These data indicate the effects on the wing flow due to the interference effects of the nacelle body without any jet present and will be referred to again during the discussion on jet effects.

Analytic Comparisons of Pressure Distributions - The Douglas Neumann program (Reference 22) was used to calculate the pressure distributions on the configuration. These results were compared with the test data. The wing and nacelle were both paneled using established techniques. Forty chordwise elements and nine airfoil defining sections were used on the wing. Elements were concentrated in regions of high curvatures. With the nacelles installed,

91

,pproximately 1000 elements were used. The wing surface used with the program was defined by adding a boundary layer displacement thickness for natural transition to the physical wing surface. The boundary layer was neglected on the other surfaces.

The entering and exiting streamtubes to and from the nacelle were modelled, or mathematically described in the Neumann program, as solid bodies. The solid bodies were defined by tracing streamlines in the nacelle-off flowfield forward from the nacelle highlight and aft from the nozzle exit. The surfaces defined by these streamlines were then input into the program as solid surfaces. Another approach that could have been used was to panel both the inside and the outside nacelle surface and impose the Kutta condition at the nacelle trailing edge to fix the proper mass flow ratio. The entering flow to the nacelle and the flow exiting from the nozzle would both be properly represented in the basic solution. Both approaches were tried and the results were found to be sufficiently similar. The solid body approach was selected because it had the advantage of being able to approximate the effects of power or fan pressure ratios (FPR) higher than 1.0 since the Neumann program does not currently have the capability of computing flows with energy addition. The effect of power was represented by modifying the flow-through jet surface using the method of characteristics as will be discussed later under the discussion of power effects.

A description of the Neumann paneling used for the four-engine configuration is shown on Figure 11.29.

The results obtained from the Neumann program are compared to the test data for the inboard engine only on Figures 11.30 through 11.32. The agreement for the inboard engine alone configuration is generally good with the exception of the wing trailing edge. These discrepancies can be caused by viscosity effects which were only approximated in the Neumann program. The predicted pressures on the nacelle boattail upper surface are low because of the nacelle boundary layer and the approximation made in modeling the exiting streamtube from the nacelle.

The four-engine results are shown on Figures 11.33 through 11.36. The local Mach number in the region between the nacelles becomes quite high and the Neumann program does not adequately represent the flow in this region. Except for that, the results are good subject to the comments given above on the inboard engine only configuration.

Lift and Pitching Moment - The inboard engine only or outboard engine only configuration have very little effect on $C_{L_{\alpha=0}}$ or C_{L_α} as indicated by the data shown on Figure 11.37. The nacelles do have an effect on the pitching moments moving the aerodynamic center (a.c.) forward and increasing the negative pitching moment at zero lift (C_{M_0}).

The four-engine configuration lift, shown on Figure 11.38, does increase due to the nacelle installation but the C_{L_α} remains constant. The increased lift for the four-engine configuration is consistent with the nacelle-nacelle interference effects observed for the interference drag and wing surface pressure distributions. The aerodynamic center is moved further forward and C_{M_0}

92

is decreased further over those of the outboard or inboard engine alone configuration as illustrated by the pitching moments also shown on Figure 11.38.

Analytic Comparisons of Lift Curve - The Neumann program using the configuration modeling previously described was used to predict the configuration lift characteristics. These results are shown on Figure 11.39 along with the test data. Some discrepancies are observed. The angle of attack for a given C_L is in error by .2 to .25 degrees, the increments in lift due to adding the nacelles increases experimentally and decreases analytically and the wing body C_{L_α} is slightly underpredicted. (The C_{L_α} for the nacelle-on case is accurately predicted.) The reasons for these discrepancies are associated with viscosity, the location of transition used in the Neumann calculation, with the methods used to represent the nacelle entering and exiting streamtubes, or with the wind tunnel wall effects. Further analysis is required to identify the important factors contributing to the small discrepancies.

Spanwise Lift Distribution - The nacelles affect the spanwise lift only slightly as indicated on Figure 11.40. This result, together with the negligible effects on overall lift discussed before, indicates that the lift carried by that part of the span occupied by the nacelle is very little different than the lift carried by the basic wing alone. The spanwise lift results also verify the fact that the change of induced drag is not significantly affected by the installation of the nacelles.

Analytic Comparison of Spanload - The predicted spanload distributions for all three flow-through configurations are compared to the data on Figures 11.41 through 11.43. Generally the agreement is good, especially in the immediate vicinity of the nacelles. Discrepancies are probably associated with the lack of modeling viscous effects, fuselage lift effects, or with interference caused by the tunnel walls. The poor quality of the data at 13-percent semispan has been mentioned previously in Section 11.1.1.

11.2.2.2 Powered

Drag Characteristics - The drag characteristics for the nacelles at the design power setting are nearly the same as the flow-through case shown before. The powered results are shown in Figure 11.44. To obtain the interference drag, the engine thrust and external skin friction and form drag are removed from the powered balance data (see Section 10). The difference between this value and the wing-body drag is the nacelle interference drag, which is then divided by the wing-body drag to form a percentage. The interference drags are still low and the favorable effects occur in the higher Mach numbers because of the absence of strong shock waves and flow separations. Interference drags at several power settings are shown for the inboard engine alone and the four-engine configuration on Figures 11.45 and 11.46. The results shown on these figures still contain the jet scrubbing drag. The scrubbing drag was calculated from flat plate skin friction coefficients and the jet Reynolds number and dynamic pressure. The width of the scrubbed area was assumed equal to the nozzle width at the wing-nozzle exit intersection. If the calculated scrubbing drag is removed from these data it is concluded that the effects of power at FPR = 1.26 and 1.38 are slightly favorable. For example, the following results are obtained at M=0.70 for the four-engine configuration:

Condition	%$\Delta C_{D_{NAC}}$ UNCORRECTED	%$\Delta C_{D_{SCRUBBING}}$	%ΔC_D CORRECTED
Flow Through	3.0	-0-	3.0
FPR = 1.26	1.6	1.4	0.2
= 1.38	2.4	1.8	0.6
= 1.48	7.6	2.5	5.1

Pressure Data - The pressure distributions on the wing at several power settings for $\alpha=0.5$ are shown on Figures 11.47 and 11.48. The effects of the jet are minimal although applying power increases the peak C_p slightly on the upper surface near the leading edge of the wing.

A suppression of the wing pressure is observed near the nozzle exit which does not change much with variations in power. Similar effects are observed for the four-engine case shown on Figure 11.49.

The pressure distributions on the wing upper surface at the centerline of the jet show the typical cyclic pressure distribution common to under-expanded sonic nozzles. These pressure distributions are shown on Figures 11.50 and 11.51. The pressure ratios relative to the local static pressure at the nozzle exit were 1.97, 2.15, and 2.29 at FPR's of 1.25, 1.37, and 1.48. Referring back to the wing pressure distributions, evidence of the cyclic pattern does not seem to appear on the wing supporting the conclusion that the effects of the jet on the wing flowfield are minimal.

A similar presentation of data on the wing and in the jet near the drag rise Mach number (M=0.76) are shown on Figures 11.52 through 11.55. The largest effect on the wing flow is the significant forward movement of the wing shock due to the installation of the unpowered flow-through nacelles. Effects of the jet on the wing can be observed at this Mach number. These effects are a small additional forward movement of a wing shock of constant pressure rise (strength) and a reacceleration of the wing flow near x/c = 50 percent which increases with power setting. The forward movement of the shock wave is caused by the added blockage of the jet plume aft of the shock. The reacceleration region is produced by the jet expansion immediately downstream of the nozzle exit. The minimum pressure in the jet is at the same streamwise location (x/c = 50%, Figure 11.55) as the wing reacceleration region. This indicates that near the wing drag rise Mach number, the jet does interact with the wing flowfield and methods of treating the jet expansion (C-D nozzle and C-E panel) should be more effective at these conditions.

Analytic Comparison of Pressure Distributons with Powered Data - The effects of the jet pressure ratio were estimated using the Neumann program by modifying the geometry used for the previous flow-through nacelle case.

The pressure distribution along the top of the flow-through nacelle jet boundary obtained from the wing-body-nacelle Neumann solution was used with the Method of Characteristics (MOC) solution, to find the jet shape at a FPR = 1.4. The static pressure distribution from the Neumann solution was assumed to be the pressure that existed on the FPR = 1.4 jet outer surface. The 2-D option of the MOC solution was used and a uniform M=1.001 flow was assumed at the nozzle exit. The MOC program was used to solve for the

94

supersonic flowfield downstream in the region bounded by the nozzle exit, the wing upper surface and the free jet boundary. The jet free boundary was determined to be at the point where the predetermined static pressure was reached in the MOC solution.

The difference in the jet boundary between FPR = 1.4 and flow through conditions formed the basis for the definition of the FPR = 1.4 boundary in the 3-D Neumann. The 2-D difference between the jet boundaries was translated into a 3-D correction which was applied to the flow through jet boundary already used. The assumption was made that the ratio of the jet areas for the 2-D jet was equivalent to an axisymmetric area ratio.

The jet cross-sectional shape was assumed constant aft of the wing trailing edge and the lower surface was assumed to lie along a trajectory defined from a solution which solves for the shape of a partial span thin jet sheet issuing from the wing trailing edge (the EVD solution of Reference 15). The center-line of the jet in the plan view was unchanged from the flow-through definition.

The resultant jet shape input into the 3-D Neumann solution is shown in Figure 11.56. This work was done for the outboard engine only configuration but this configuration was not run during the test program. So the predicted increments on the wing are compared to the experimental results of an inboard engine only. The analytical and experimental results are shown on Figures 11.57 and 11.58. The increments are small but quite well predicted by the method.

Effect of C_L on Interference Drag - Decreasing the configuration C_L increases the interference drag as shown on Figures 11.59 and 11.60. The effect of changes in the direction of the jet vector on lift and drag are not significant. For the four-engine configuration, assuming that the jet turning angle relative to the chord line of the wing remains unchanged, the ΔC_L due to jet reaction is .002 for a total ΔC_L of 0.1. Also the changes in C_D caused by the jet turning losses remain essentially unchanged.

For reference, the drag curves corrected only for thrust are shown on Figures 11.61 and 11.62. The nacelle skin friction and form drag have not been removed from this data.

Lift and Pitching Moment - The C_{L_α} is not affected significantly by the effects of the jet at the design power setting (FPR = 1.37, C_μ = .13) but there is an increase in configuration C_L as indicated on Figure 11.63. The incremental C_L at a given angle of attack is produced by the reaction and circulation effects produced by the jet at the trailing edge of the wing. By comparing the ΔC_L results from the EVD program run at several turning angles to the test data, the effective turning angle of the jet for the four-engine configuration at a FPR = 1.37 and C_μ = .13 was determined to be 10.4 degrees relative to the chord line of the wing. The 10.4 degrees is 1.6 degrees less than the slope of the upper surface of the wing which was 12 degrees.

The predicted C_{L_α} using the EVD solution and a 10.4 degrees jet turning angle agreed favorably with the test data as shown on Figure 11.63.

95

The pitching moments also shown on Figure 11.63 establish that the a.c. moves progressively forward as more nacelles are added and that the a.c. shift is similar to those for the flow through nacelle. There is a much larger incremental decrease in the C_{M_0} for the addition of the powered nacelles than for the flow-through nacelles, as would be expected from theory. Theoretically, for a simple jet flap, the center of pressure of the circulation lift moves aft with increasing power and the vertical component of the jet reaction acts at the wing trailing edge.

Results of lift and pitching moment as a function of power setting for the inboard engine only and the four-engine configurations are shown on Figures 11.64 and 11.65. Small increases in C_{L_α} can be identified for the highest power setting.

The pitching moments indicate constant a.c. and decreasing values of C_{M_0} as the power is increased.

Spanwise Lift Distribution - The unloading of the wing outside of the jet region caused by the jet effect is illustrated by the spanwise lift distributions shown on Figures 11.66 through 11.68. The wing is unloaded in a uniform manner across the outboard part of the span. There are not any large increases in the lift near the nacelle.

The spanwise lift distributions for several power settings are shown on Figure 11.68. The increments are small and do not vary consistently with power across the span. However, it can be concluded that the highest power setting does unload the wing outside the jet the most as would be expected.

11.2.2.3 Trailing Edge Flap Deflection - The relatively high upper surface trailing edge slopes utilized on modern wings utilizing supercritical airfoil technology tend to produce relatively high exhaust plume deflections for USB configurations during cruise flight. The deflected plume produces distortion in the span load distribution with associated penalties in induced drag.

Theoretical predictions of the induced drag penalties associated with the baseline configuration described in Section 8 were made using the EVD method (Reference 15), as functions of thrust and mean jet plume deflection.

In order to verify this methodology, and investigate the effects of varying the jet deflection on induced drag, 20-percent chord trimmer flaps were incorporated in the model aft of the nacelles.

The drag, lift, and pitching moments due to trailing edge flap deflections are shown in Figures 11.69 through 11.71. The drag due to a trailing edge up (-3°) or trailing edge down (+3°) deflection always has a detrimetnal effect. The increment in drag from the undeflected case is 2-1/2 percent of the wing body drag at -3 degrees and 8 percent for +3 degrees as indicated in Figure 11.69.

The drag polar for the three trailing edge flap settings is shown on Figure 11.70. The value of the induced drag efficiency factor "e" (which is equivalent to the slope of the $C_L{}^2$ vs. C_D curve and is used for example in the parameter $C_L{}^2/\pi\!R\,e$) is the same for the $\delta = 0$ and $\delta = 3°$ cases; the drag

difference between these two geometries being independent of C_L. The "e" for the $\delta = -3°$ case is slightly higher up to a C_L between 0.4 and 0.45 after which the "e" decreases significantly. At the C_L's below 0.45 the flap-up deflection has a favorable effect on the variation of C_D with C_L.

The estimated lift and drag increments using the EVD program and an effective turning angle of 10.4 degrees determined previously are compared to the test data in Figure 11.72. The shaded area represents the interference drag decrease applied to the test data corresponding to a calculated thrust loss of normal shock waves that occur in the jet flow as the flaps are deflected. The strength of the normal shock was determined from the pressure distributions measured on the wing upper surface scrubbed by the jet flow. The thrust increment was calculated from the product of jet mass flow and incremental jet velocity based on the normal shock total pressure loss and ambient static pressure. It was assumed that the strength of the shock was constant throughout the jet. After removing the shock losses, benefits similar to those predicted by the EVD theory are achieved. But to obtain these performance levels the normal shocks that existed in the model need to be eliminated. A means of eliminating these shocks is available by the combined use of the Neumann and MOC programs to smooth and properly shape the wing.

The other losses between the shock adjusted level of the data and the EVD solution can be identified as being on the wing lower surface, where pressure measurements were not obtained, or in the region created by the discontinuity of the wing trailing edge when the flap was deflected.

The differences in loading due to flap deflection occurs primarily outboard of the outboard nacelle and not between the nacelles as shown on Figure 11.73. The increments of spanwise lift are accurately predicted by the EVD program but the levels are somewhat overpredicted by the method. The agreement in level of the EVD method is about the same as for the Neumann shown earlier.

11.2.2.4 Effect of Alternate Spacing - To evaluate the sensitivity of the spacing of the nacelles on the high speed drag interference, an alternate four-engine configuration was tested which had the nacelles closer together. This was accomplished by moving the inboard nacelle outboard five percent of the semispan. This should increase the nacelle to nacelle interference but should decrease any nacelle-fuselage interference.

The test data indicates that the drag results are not very sensitive to the spanwise spacing. This conclusion is based on the negligible increase in drag at the design Mach number of 0.70 due to decreasing the spanwise spacing as shown on Figure 11.74. Near the drag divergence Mach number of the wing (M=0.76) there is an increase in the drag of about two percent.

Only small changes in the velocity occur on the wing between the nacelle as shown on Figure 11.75.

11.2.3 High Boattail Angle Nacelle (N_3) - The design of the N_3 nozzle, supplied by NASA and representing a QCSEE nozzle configuration, incorporates very high internal and external boattail angles on the upper surface of the nozzle. This design is intended to produce adequate spreading and thinning

of the exhaust plume in the high lift configurations to achieve satisfactory flap effectiveness (i.e., flow turning capability) without external flow deflectors.

The sidewall extensions are canted inward to prevent excessive plume spreading in the cruise configuration. One or both of the sidewalls would be hinged to simultaneously provide the desired nozzle area for low speed operations and remove the restraints to lateral spreading of the exhaust plume.

The high boattail angles required on this type of nozzle increase the severity of the nacelle integration problem, and are likely to produce higher levels of nacelle interference drag.

11.2.3.1 Unpowered

Engine Interference Drags - Without power the interference drag for N_3 is much larger than for the N_1 nacelle. The drag differences for the flow-through inboard engine only configuration is shown on Figure 11.76.

Two contributors to the high drag of this configuration are: 1) low pressures and flow separations over the nozzle afterbody and 2) a strengthening of the wing shock caused by adverse nacelle-wing interference.

The high boattail angle causes a large disturbance to the wing flowfield increasing the wing upper surface velocities and, therefore, the magnitude of the shock losses. This is illustrated by the wing pressure distributions shown on Figures 11.77 and 11.78. At M=0.76, the wing shock is significantly stronger contributing to the increased drag at the higher speeds.

Recently new data has been released (Reference 32) which supports the interpretation that the boattail is separated. The data from Reference 32 indicates that boattail angles as low as 18 degrees can produce flow separation on nozzles of this type.

11.2.3.2 Powered

Interference Drags - The effects of power do not change the basic conclusions discussed above. The drags and pressure distributions are shown in Figures 11.79 through 11.81.

Effects of Jet Pressure Ratio - The effects of various pressure ratios on the interference drag is shown on Figure 11.82. Initial applications of power decrease the interference drag increment. This decreased interference drag is possibly caused by an aspiration of the boattail flow by the jet flow which reduces the afterbody separation. The aspiration could occur because of viscous mixing of the jet flow and the external flow. Further increases in the FPR then either increases the jet pluming which in turn increases the afterbody separation, or increases the drag caused by negative pressures on the afterbody resulting from the jet aspiration. Underexpansion shock losses within the jet and scrubbing drag also contribute to the drag increase. At M=0.70 and a FPR OF 1.48, the scrubbing drag penalty is estimated to be 1.4 percent of wing-body drag (1/2% of C_μ).

The jet does strengthen the wing shock system as illustrated by the wing pressure distributions on Figure 11.83. Once power has been applied, further increases in the FPR have a negligible effect on the wing flow as shown on Figure 11.84.

A series of pressure distributions on the wing in the jet flow are shown on Figures 11.85 and 11.86. The increasing cyclic pressure pattern is typical of an underexpanded nozzle and there is an orderly progression in the magnitude of the pressure peaks of the cycles from the flow-through level to the highest FPR.

Jet Suppression - The external flow over the high boattail angle does suppress the jet (and probably causes it to spread although this could not be confirmed). The evidence of this suppression is illustrated by the more positive initial pressure distributions on the upper wing surface in the jet stream which is illustrated in Figures 11.87 and 11.88.

Four-Engine Interference Drags - Analysis of the four-engine data indicates that the interference drags are still much higher than N_1 as shown on Figure 11.89. The interference drags at M=0.70 are roughly five-percent of the wing-body drag higher than twice the inboard engine only configuration, indicating the magnitude of the drag increment caused by the superposition of the flowfields for each nacelle. The five-percent penalty is partly due to significant increases in the wing velocities and stronger shocks on the wing as indicated on Figures 11.90 through 11.92, and partly due to drag increments caused by span load distortions.

Contrary to the results observed for the inboard engine only configuration, the effect of increasing FPR on the four-engine configuration is to continually increase the interference drag as shown on Figure 11.93. At M=0.70, 1.3 percent of the drag increment between FPR = 1.25 and 1.48 can be attributed to the scrubbing drag. (The four-engine flow-through case was not tested.)

Effect of C_L on Interference Drags - Increasing the configuration lift coefficient had a negligible effect on the drags of the inboard engine only configuration. Hence, the interference drag is primarily due to effects other than those associated with the circulation lift. Slight increases in the drags were observed for the four-engine configuration above the design Mach number. The results are indicated on Figures 11.94 and 11.95.

Lift and Pitching Moment - The lift and pitching moment characteristics of the inboard engine only and the four-engine configuration are shown on Figure 11.96. There is a larger increment in lift for the four-engine configuration than would be estimated by doubling the inboard engine only configuration lift increment. Also the ΔC_L for N_3 is slightly greater than N_1 indicating slightly more spreading or turning of the jet or more nacelle-nacelle interference. There is a negligible effect of the jet on C_{L_α} as evidence by the slope of the lift curve being essentially unchanged from the slope of the wing-body configuration.

The slope of the pitching moment curves reveal an expected forward movement

of the aerodynamic center, the location moving progressively forward as more nacelles are added. The pitching moments for N_1 and N_3 are almost the same.

The variation of C_L and C_M with power for the four-engine N_3 are shown on Figure 11.97. Small changes in C_{L_α} due to power can be observed at the highest power setting.

Span Lift - The spanwise lift for the four-engine configuration is shown on Figure 11.98. The wing is unloaded due to the reaction and circulation effects of the jet. The resulting section lifts are little different than for N_1.

11.2.4 Streamline Contoured Nacelle (N_2) - The installation of nacelles on the wing will cause a disruption of the flow about the wing. This disruption can cause premature drag rise by strengthening the shock on the wing, can cause separations by increasing adverse pressure gradients or can cause increases in induced drag by unfavorable effects on the span load. In an effort to eliminate any of these adverse effects, a contoured nacelle (N_2) was designed which conformed as closely as possible to the flowfield about the wing-body configuration. The design of the nacelles is described in Section 8.0.

11.2.4.1 Unpowered

Interference Drag - The interference drag for N_2 is slightly less than for N_1 at M=0.70 as shown on Figure 11.99. N_2 did not have a large favorable effect since there was little adverse effect due to the installation of N_1. That is, N_1 did not cause large adverse effects on the wing pressure distribution or span loading and did not have any significant separations for a streamline contoured nacelle to eliminate. N_2 did do what it was designed to do in that it did bring the wing upper surface pressures closer to the wing alone values, as shown in Figure 11.100. However, neither pressure distribution has a strong shock or indicates separation so the drags are not affected by either nacelle. The drag for N_2 was not increased even though there was a significant influence on spanwise lift due to the installation of N_2. Large losses in lift occurred in the region of the nacelle forcing the wing to carry more lift as illustrated in Figure 11.101. Since the nacelle upper surface was contoured to the wing flowfield, this lift loss must be produced by the distortions to the local streamlines resulting from the compromises required in the lower surface fairing.

The lift loss is also illustrated by the lift curve shown on Figure 11.102. The configuration angle of attack had to increase by 0.5 degree to maintain a constant lift.

Also shown on Figure 11.102 are the pitching moments indicating that, as was the case with N_1 and N_3, the aerodynamic center has moved forward.

At the higher Mach numbers, the N_2 nacelle had a larger interference drag than N_1. There were at least two causes for this, both associated with the wing shock. One was that at a given angle of attack the wing shock occurred at a higher local supersonic Mach number, as shown on Figure 11.103, thereby

100

incurring greater losses. The nacelle contouring did move the shock back to the wing alone location. However, it must be mentioned that the contouring was done at $M_0=0.70$ and some shortcomings in the method will occur at the higher Mach number of 0.76.

Another reason for the higher drag was that there was also a lift loss associated with the nacelle installation. This causes the wing to operate at a higher angle of attack which tends to strengthen the magnitude of the wing shock losses. The wing pressure distribution at one degree angle of attack shown on Figure 11.103 represents about the same C_L as the 0.50 angle of attack N_1 case.

Separations or shocks on the lower surface fairing did not contribute to the drag at either Mach number because of the absence of high velocity regions or adverse gradients as illustrated on Figure 11.104.

Comparisons of Predicted Lift and Pressure Distribution with Data - An approximate Neumann predicted pressure distribution at 38-percent semispan compared well to data as shown in Figure 11.105. The analytical results were available for an outboard N_{2A} configuration, but, there was only an opportunity to test the inboard N_{2B} configuration during the wind tunnel program. So an approximate analytical result was obtained for the inboard location by correcting inboard N_{1B} results for the difference between N_2 and N_1 at the outboard location. The procedure is illustrated on the figure.

The loss in lift due to the installation of the nacelle was predicted fairly well as shown on Figure 11.106, despite the fact that this is not a one to one comparison because of the reasons discussed above. The slope of the curve (C_{L_α}) is predicted accurately.

11.2.4.2 Powered

The effectiveness of the streamline contouring of the upper portions of the N_2 nacelle produces local static pressures in the vicinity of the nozzle that closely match those of the basic wing body at the design point as shown on Figure 11.107. The degree of exhaust plume expansion required is then greater than for the N_1 nacelles (as illustrated by the higher velocities in the jet shown on Figure 11.108) which suppress the local velocities at 35-percent chord.

As described in Section 8.2.2, C-D nozzles were originally planned for the N_2 nacelles to deliver the exhaust plume expanded to the local static pressure near the exit. Practical considerations related to internal ducting led to a separate evaluation of the C-D nozzles in N_4. This choice was substantially influenced by the desire to minimize the development risks related to internal ducting design of the model.

The unfavorable drag increment between N_2 and N_1 is greater than the flow-through increment when the configurations are compared at an $M>0.67$ as shown on Figures 11.109 and 11.110. The unfavorable effect due to power for N_2 at the higher Mach numbers does not appear to be caused by additional adverse effects on the wing flow, as seen by comparing Figure 11.111 with Figure 11.103, but from shock losses within the jet flow (thrust losses) as

illustrated by the significantly increased peak local Mach number within the jet indicated on Figure 11.112. This increase results from the large difference in local velocities at the nozzle exit location (35-percent chord) between the N_1 and N_2 installations, which is evident on Figure 11.111. With the N_1 installation the wing shock is upstream of the nozzle exit, while with N_2 it is downstream and close to the clean wing position. These differences were also noted with the flow-through nacelles (Figure 11.103).

The effects of pressure ratio on the wing pressures are shown on Figure 11.113 and the pressure on the wing surface in the jet are shown on Figures 11.114 and 11.115 for a Mach number of 0.76. The wing shock is moved forward and it interacts with the plume effects of the jet. These plume effects are illustrated by the reacceleration in the wing pressure distribution occurring between 45 and 55-percent chord at the higher FPR's.

This reacceleration corresponds with the region of maximum velocity in the jet, which should correspond to the maximum jet cross sectional area, near 50-percent chord shown on Figures 11.114 and 11.115.

Effect of C_L on Interference Drag - Increasing the C_L seems to have a favorable effect on the interference drag at M=0.70 as illustrated on Figure 11.116. At Mach numbers on either side of 0.70, there seems to be no definite trend.

Lift and Pitching Moment - As previously discussed, there is a loss in lift when the flow-through nacelles are installed. The application of power restores some of this lift, as shown on Figure 11.117, but never returns it to the N_{1B} configuration level. Also very little increase in lift is experienced beyond the level for a FPR=1.25. The constant C_{L_α} with or without power indicates negligible effect of power.

The pitching moments, also shown on Figure 11.117, become more negative as power is increased. The aerodynamic center remains unchanged and at the same level as the N_{1B} configuration.

Spanwise Lift Distribution - The effect of applying power to the spanwise lift distribution is shown on Figure 11.118. The distribution of lift outside of the jet for the powered case is more uniform and closer to the wing-body lift distribution than for the unpowered case.

11.2.5 Methods of Reducing the Effects of the Jet Plume (N_4 and CE Panel) -

Disturbances to the wing upper surface flowfield can cause significant drag penalties. The introduction of the jet present with a USB configuration can unfavorably interact with the wing flow causing significant interference penalties. These penalties can result from a separation of the flow on the wing due to the jet normal shocks, normal shock losses in the jet itself or jet plume-wing shock interactions. These effects can be minimized by expanding the jet flow to the local conditions of the wing flow using a C-D nozzle. Use of the C-D nozzle will eliminate the normal shocks in the jet and pluming of the jet. Another technique is to contour the wing upper surface scrubbed by the jet to cancel the cyclic pattern of the jet.

C-D Nozzle (N_4) - The interference drags of the N_{4B} configuration are compared to the N_{1B} configuration on Figure 11.119. At a Mach number of 0.70 the drag penalties are the same for either configuration. Above M=0.70, the drag for the N_{4B} configuration is slightly better.

There is a smaller effect on the interference drag due to power for N_{4B} than for N_{1B} as indicated by comparing Figure 11.120 with Figure 11.45. All of the variation between FPR 1.20 and 1.46 for N_{4B} can be attributed to the scrubbing drag. This reduced variation with power indicates that there is an increasing advantage available for using the C-D nozzle at the higher FPR's.

The influence of the C-D nozzle on the wing upper surface flow is not greatly affected by the jet until Mach numbers near 0.76 are reached. Figures 11.121 and 11.122 indicate the differences that the two nozzle types produce on the wing. At M=0.76 the effects of the jet are reduced using N_{4B}. The wing shock and wing pressure distribution are nearer to the wing alone pressures. Also the reacceleration region at 50-percent x/c is eliminated using the C-D nozzle.

Since the nozzle was designed for a FPR of 1.54, the nozzle was not properly expanded at a FPR of 1.37 as indicated by the presence of the cyclic pressure distribution on the wing scrubbed by the jet shown on Figures 11.123 and 11.124. The nozzle is overexpanded at these conditions, causing the static pressure at the exit to be less than the local pressure. The adjustment to the local pressure is made through a compression shock which shows up on the wing surface as an initial compression for N_{4B} as opposed to the initial expansion of N_{1B}. Increasing the FPR to near the design value does practically eliminate the cyclic pattern of the jet as shown on Figure 11.125.

Controlled Expansion (CE) Panel - The data shown on Figure 11.126 illustrates that the interference drag for N_{1B} with the CE panel is higher than for N_{1B} without the CE panel. Observations of the pressure distributions on the wing upper surface in the jet flow indicated that the design surface pressure distribution was not achieved and that there were strong normal shocks within the jet flow. These strong shocks will decrease the gross thrust produced by the simulator and this thrust loss will manifest itself as an increase in the interference drag.

Several reasons can be suggested for the lack of agreement between the expected and actual pressure distributions. Some of these are: 1) Since there wasn't an opportunity to test the CE panel in conjunction with sideplates, the jet was free to expand laterally into the wing flowfield. The theoretical analysis assumed that the jet was constrained from expanding laterally. 2) The design depended on knowing the static pressure distribution on the free boundary of the jet. Since these pressures were obtained using the Neumann program in the absence of the nacelle, small but significant errors could have occurred. 3) In addition, the 3-D "D-shaped" jet was approximated with a 2-D MOC solution.

Because the design has higher surface curvatures than the baseline, higher velocities and stronger shocks can occur if the design conditions are not met, i.e., if the supersonic expansions and compressions don't occur at the right

place on these higher curvatures, then amplifications instead of suppressions of the cyclic pattern will occur.

11.2.6 Summary of Interference Drags

Inboard Engine - The interference drag results are compared for all four nacelles on Figure 11.127. At the design point of M=0.70 the N_{1B}, N_{2B}, and N_{4B} nacelle configurations yield the same interference drag. N_{3B} is the exception and its high drag can be attributed primarily to nacelle boattail low pressures and flow separation.

At the higher Mach numbers, the N_3 configuration produces significant increases in the strength of the wing shock, further increasing the interference drag over the level present for the boattail seperation. The N_{2B} configuration interference drag increases primarily because of normal shock losses in the jet aft of the nozzle resulting from expansion into a lower local pressure field.

Four-Engine Configuration - The interference drag results for the four-engine configurations are shown on Figure 11.128. The N_3 configuration drags are high for the same reasons stated above. There is a small advantage in increasing the spacing of the N_1 configuration, reducing a small nacelle-nacelle interference penalty.

11.3 Installation Effects on Internal Engine Characteristics

To optimize the engine cycle for the mission, the engine manufacturer must know the exhaust nozzle airflow characteristics. These exhaust nozzle characteristics can be altered by the presence of external flow if the nozzle is unchoked. At nozzle pressure ratios higher than the choking limit, external flow disturbances can no longer influence the operating characteristics of the engine exhaust system.

The installation effect on the choking limit for the four engine N_1 configuration is shown on Figure 11.129. These results were obtained using the experimental local to freestream static pressure ratio (P_L/P_0) and an assumed nozzle choking pressure ratio of 1.9. The data on the figure indicates that the nozzle chokes at lower FPR when installed on the wing. The installation increment on FPR at the design point Mach number of 0.70 is about 0.17 for either the inboard or outboard nacelle location.

104
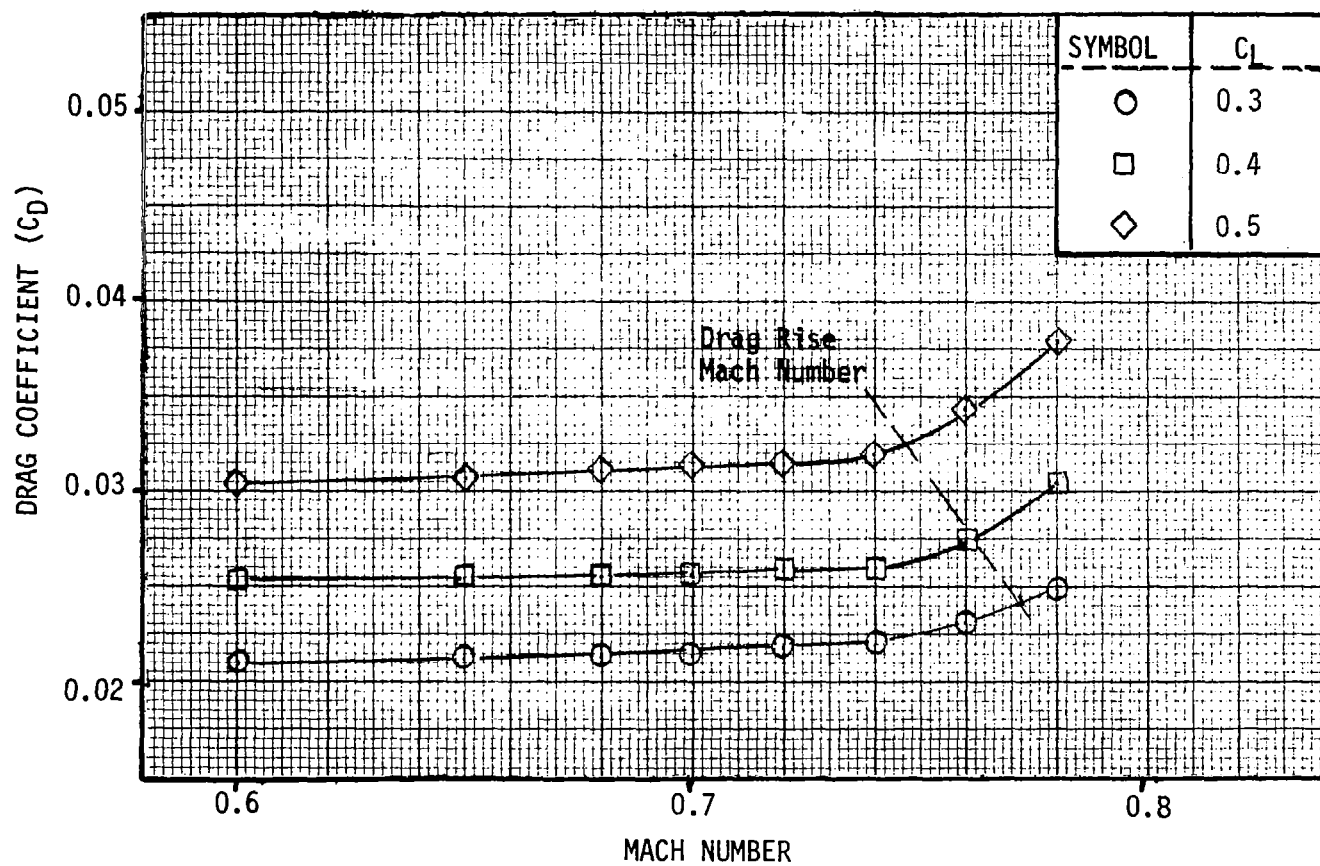
Figure 11.1. Wing-Body Drag-Natural Transition
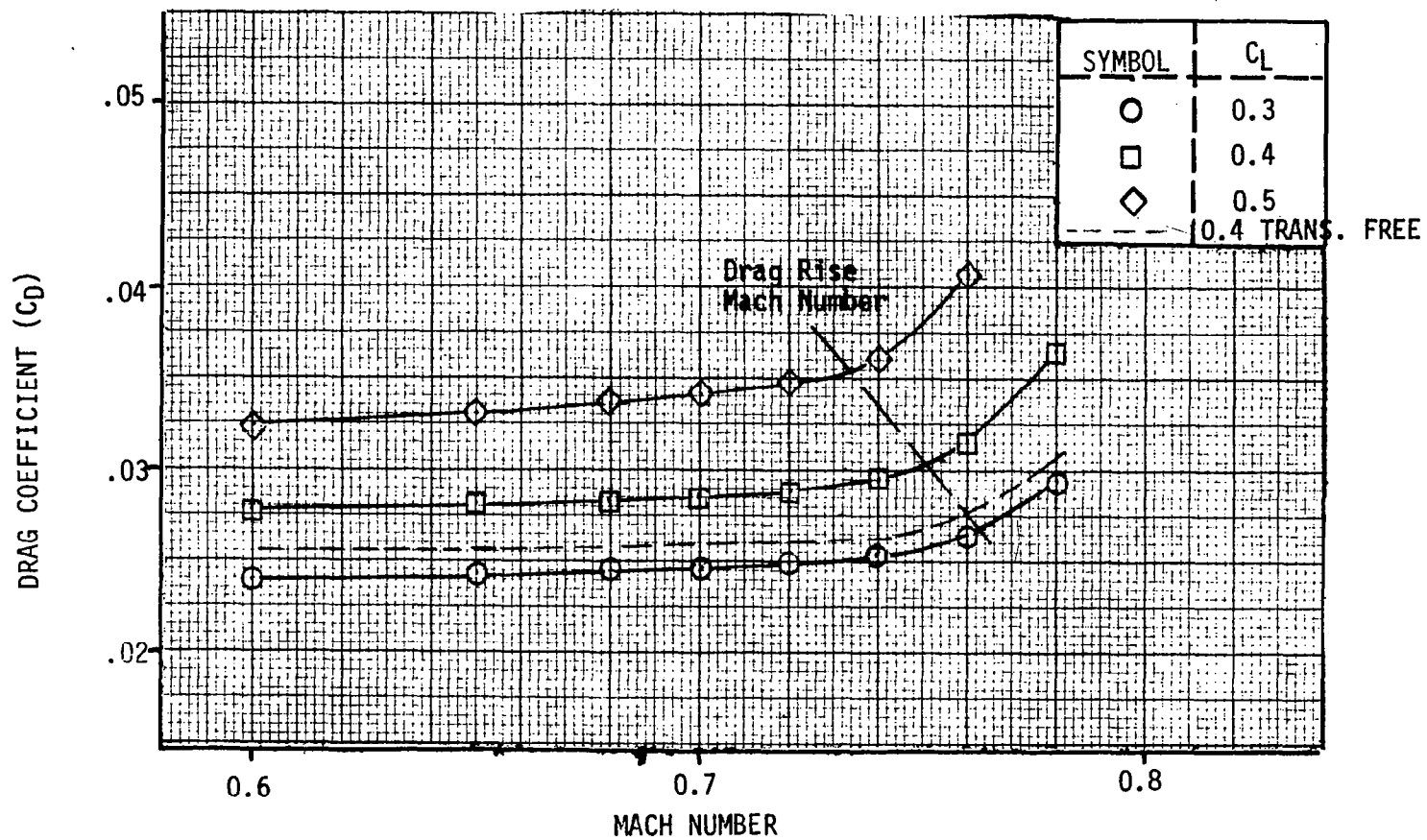
Figure 11.2. Wing-Body Drag - Transition Fixed

Figure 11.3. Wing-Body Pressure Distribution at M = 0.70 and η = .38

ALPHA = 0.5°

38 PERCENT SEMI-SPAN
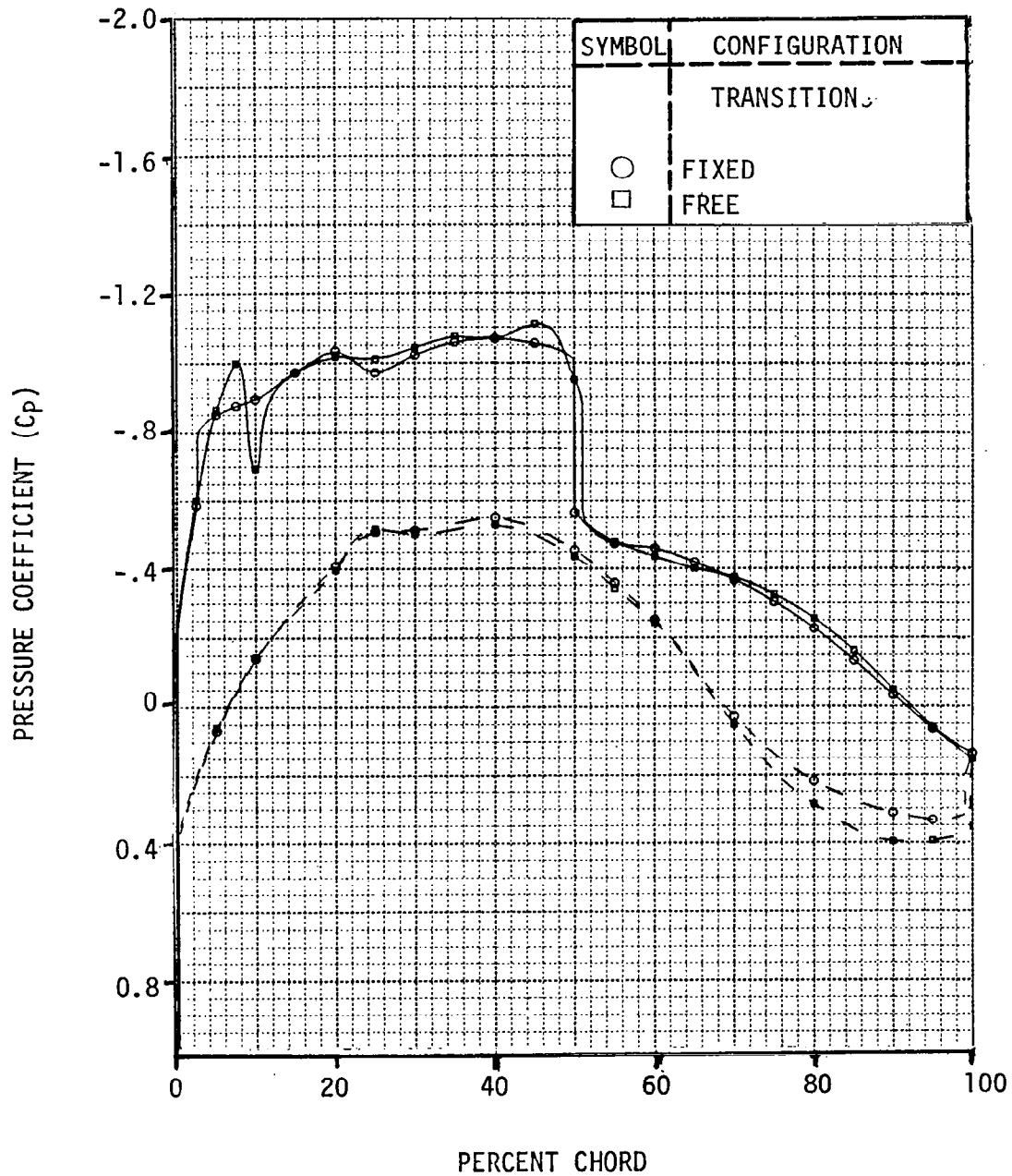
MACH NUMBER = 0.76

Figure 11.4. Wing Body Pressure Distribution at M = 0.76 and η = .38.
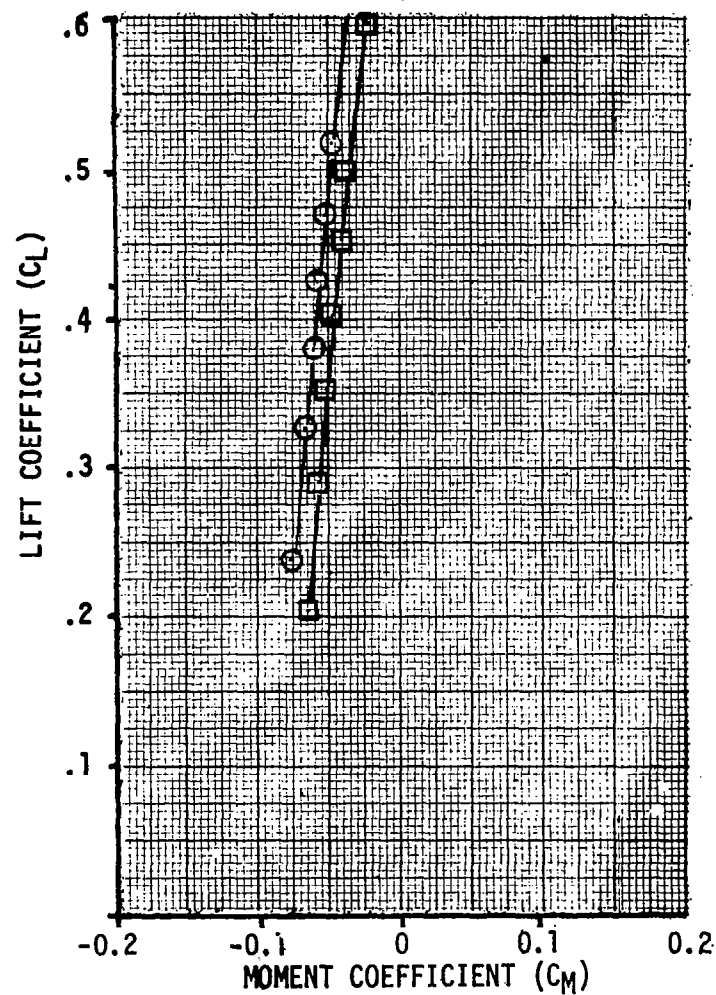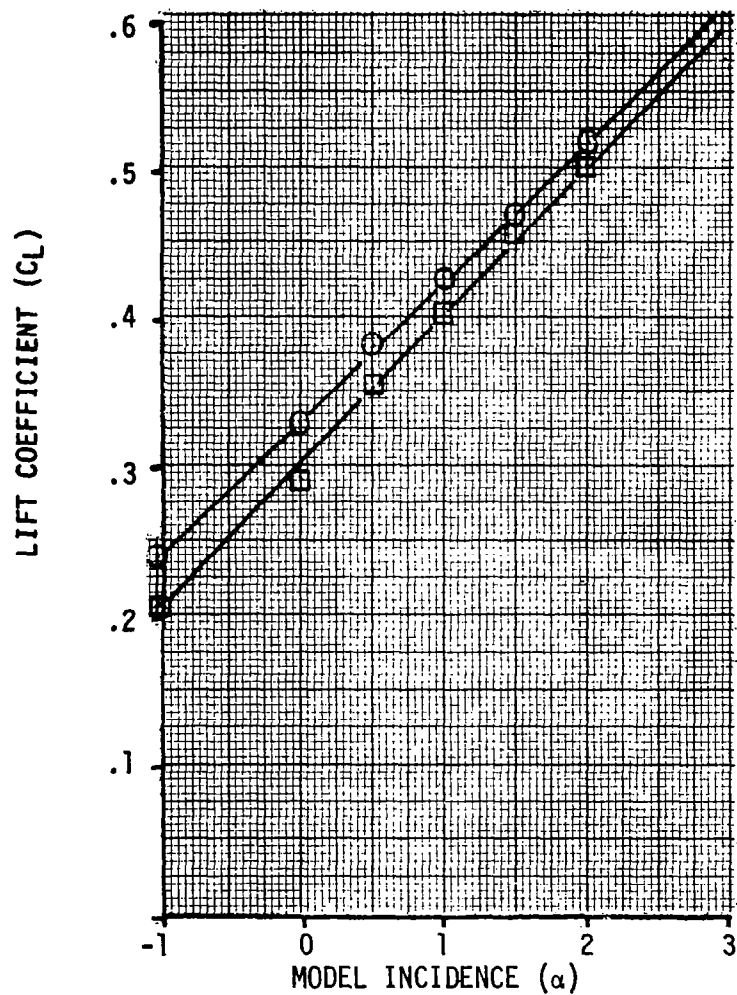
Figure 11.5. Wing-Body Lift and Pitching Moment at M = 0.6.
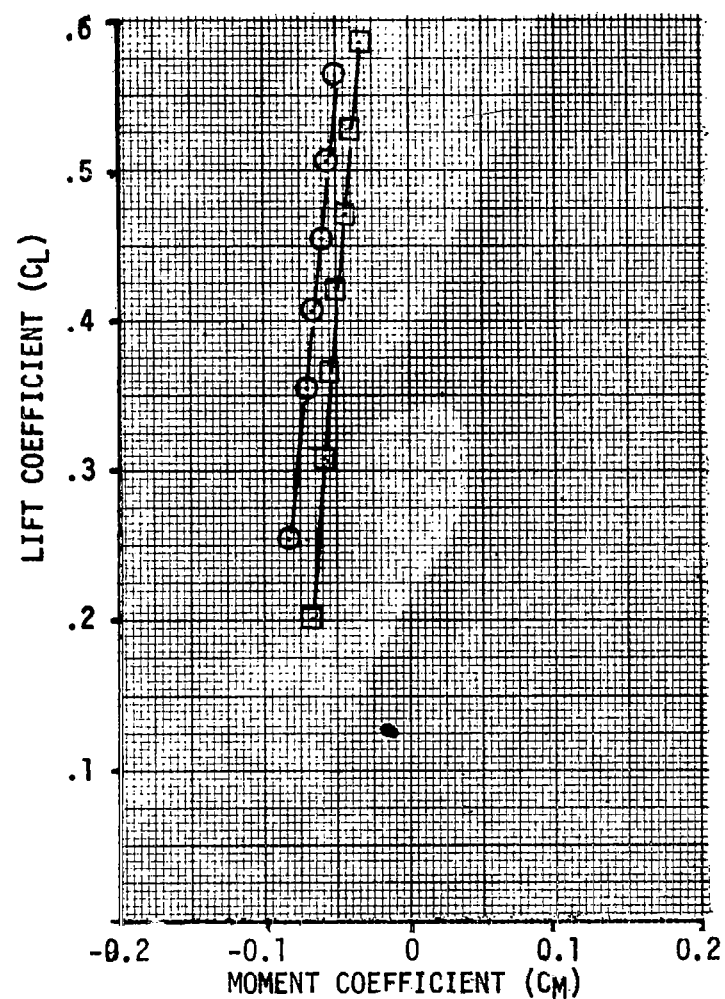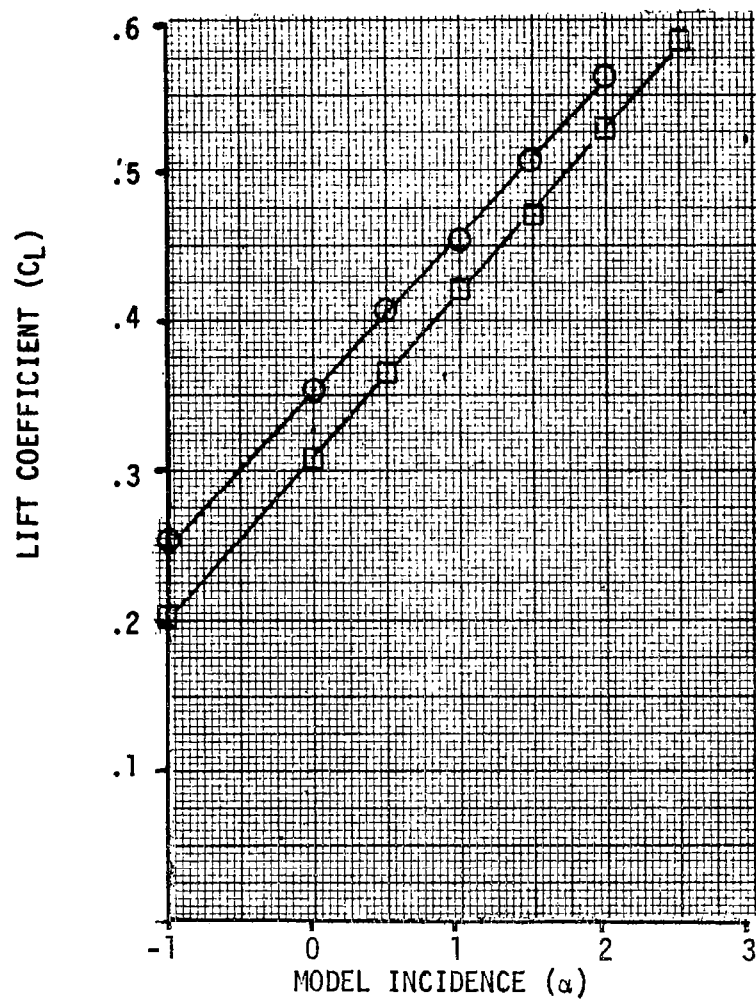
Figure 11.6. Wing-Body Lift and Pitching Moment at M = 0.70.
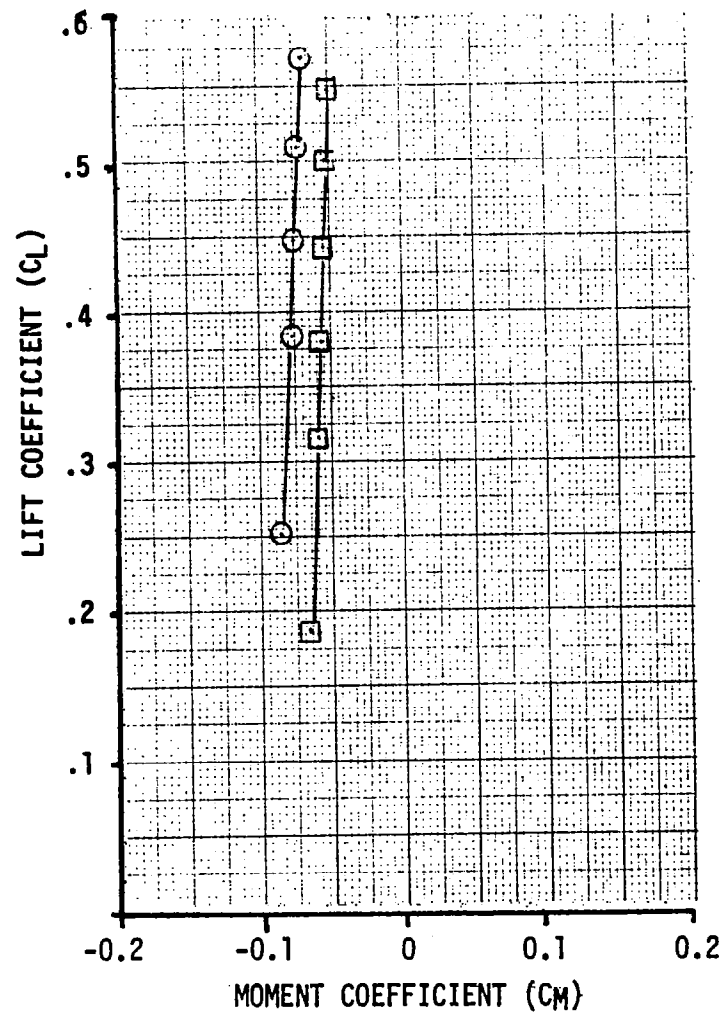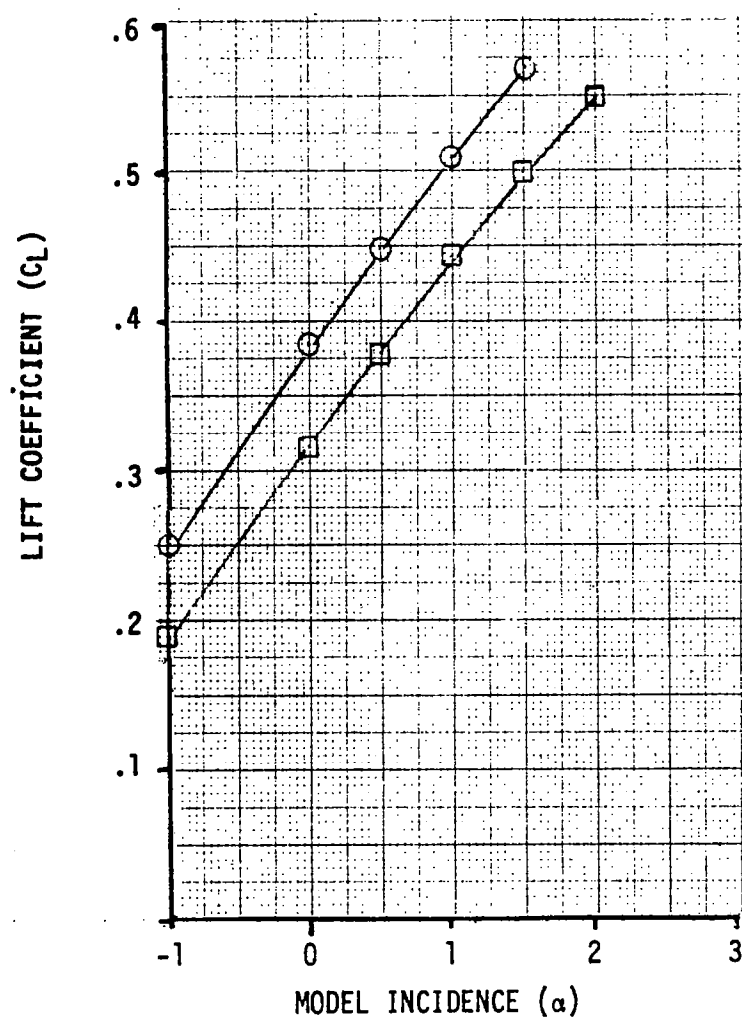
Figure 11.7. Wing-Body Lift and Pitching Moment at M = 0.76.

ALPHA = 0.5°

13 PERCENT SEMI-SPAN
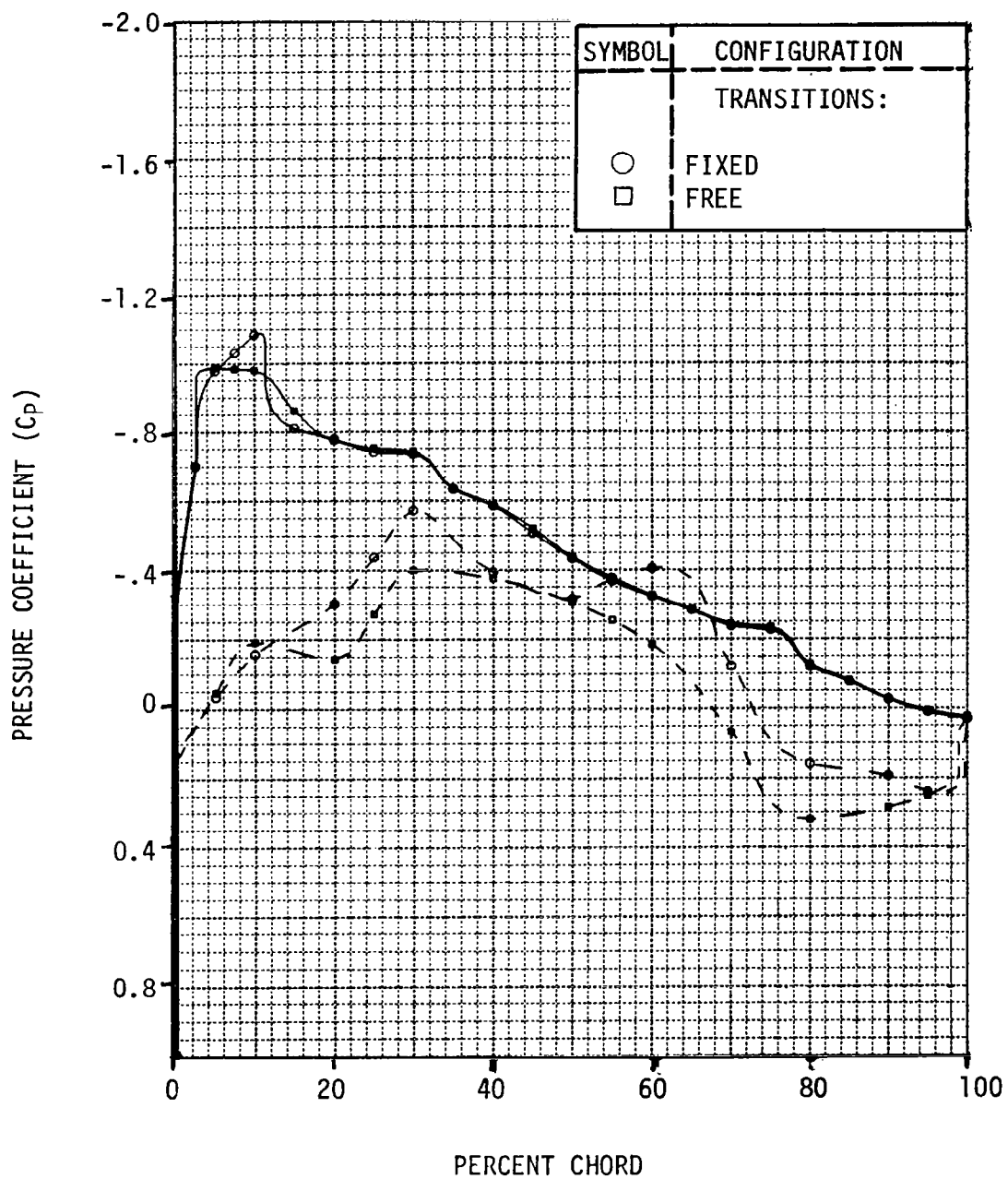
MACH NUMBER = 0.70

Figure 11.8. Wing-Body Pressure Distribution at M = 0.70 and η = .13.

ALPHA = 0.5°

33 PERCENT SEMI-SPAN

MACH NUMBER = 0.70

SYMBOL	CONFIGURATION
	TRANSITION:
○	FIXED
□	FREE
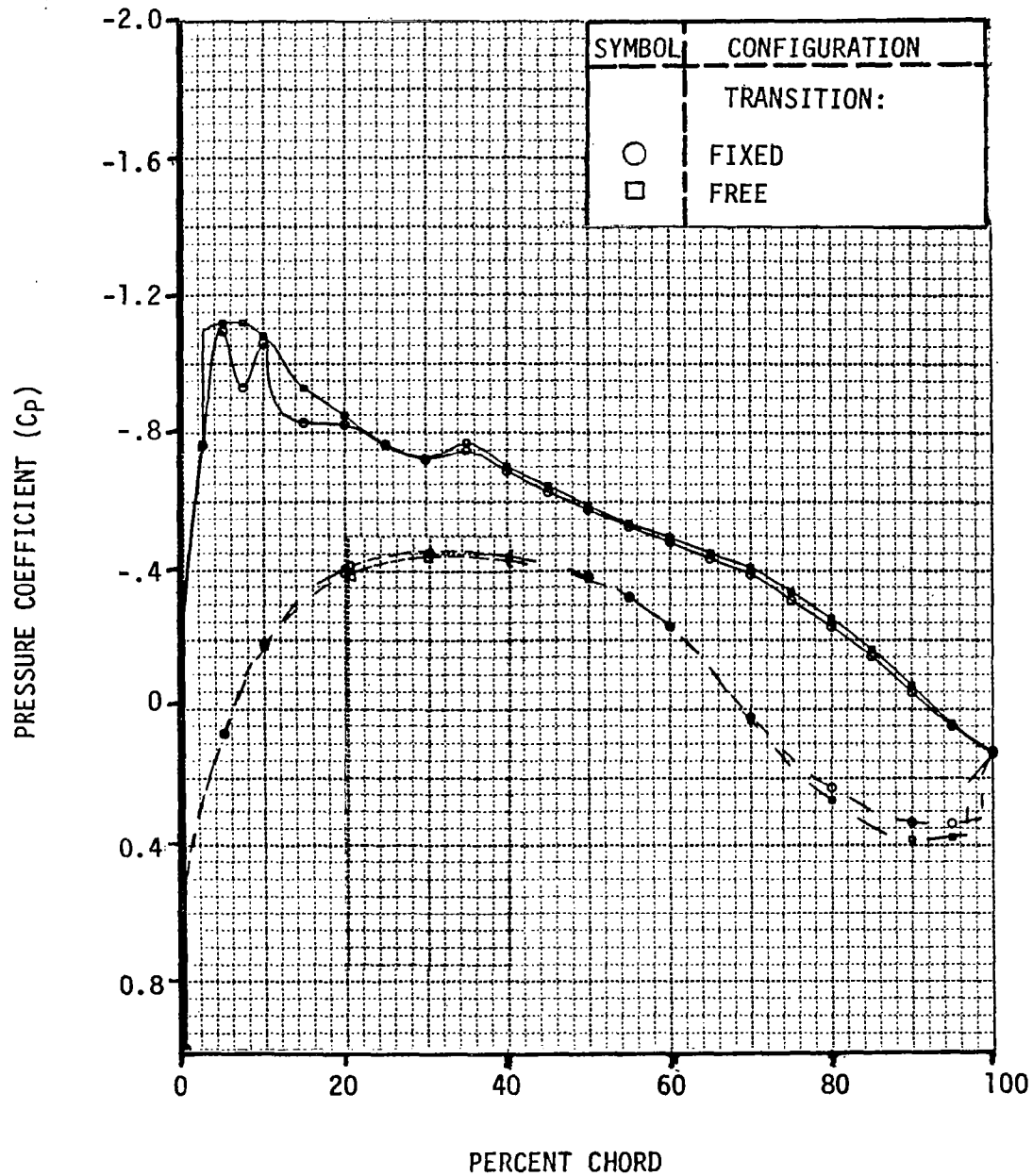
Figure 11.9. Wing-Body Pressure Distribution at M = 0.70 and η = .33.

ALPHA = 0.5°

58 PERCENT SEMI-SPAN
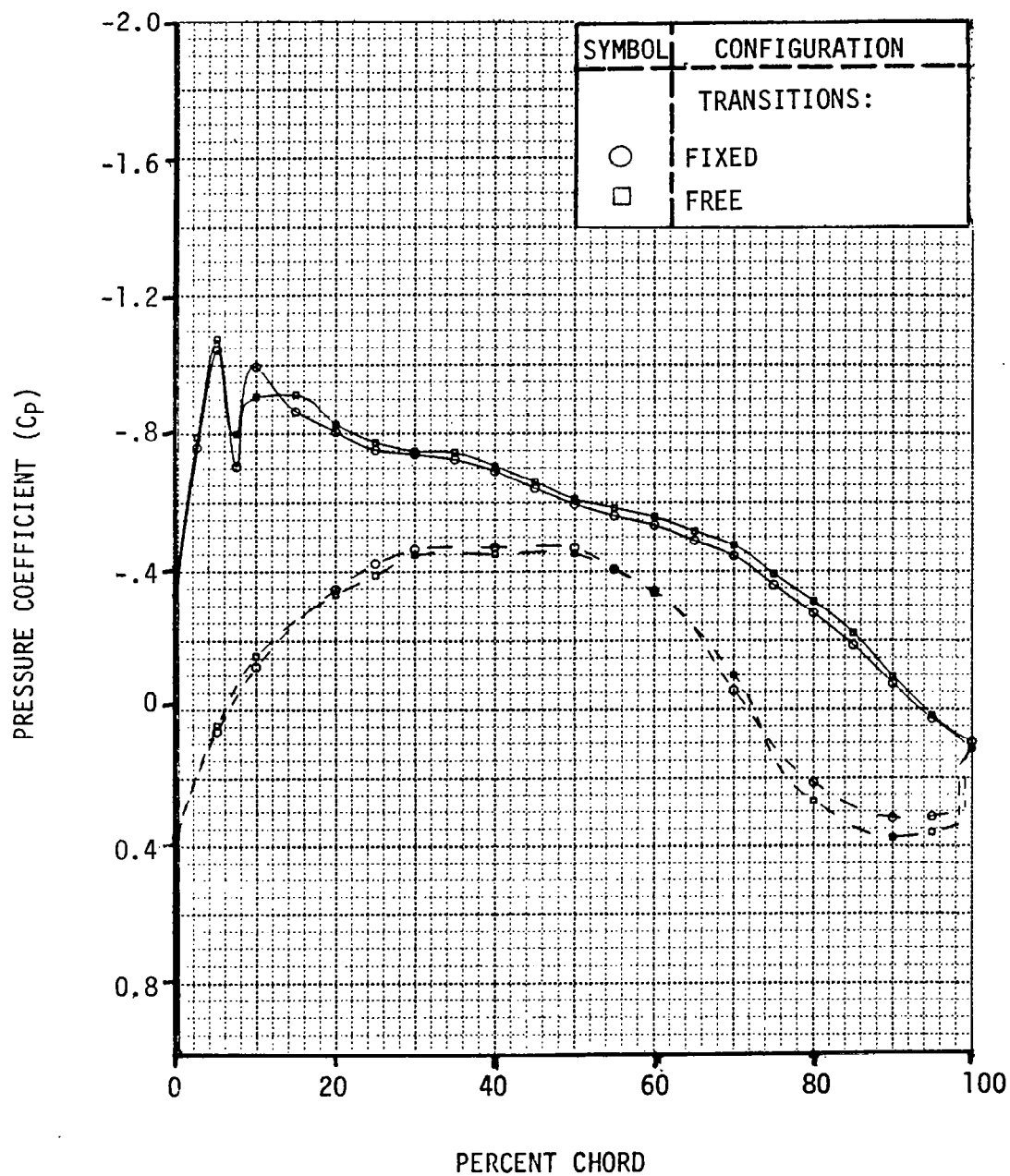
MACH NUMBER = 0.70

Figure 11.10. Wing-Body Pressure Distribution at M = 0.70 and η = .58.

ALPHA = 0.5°

70 PERCENT SEMI-SPAN
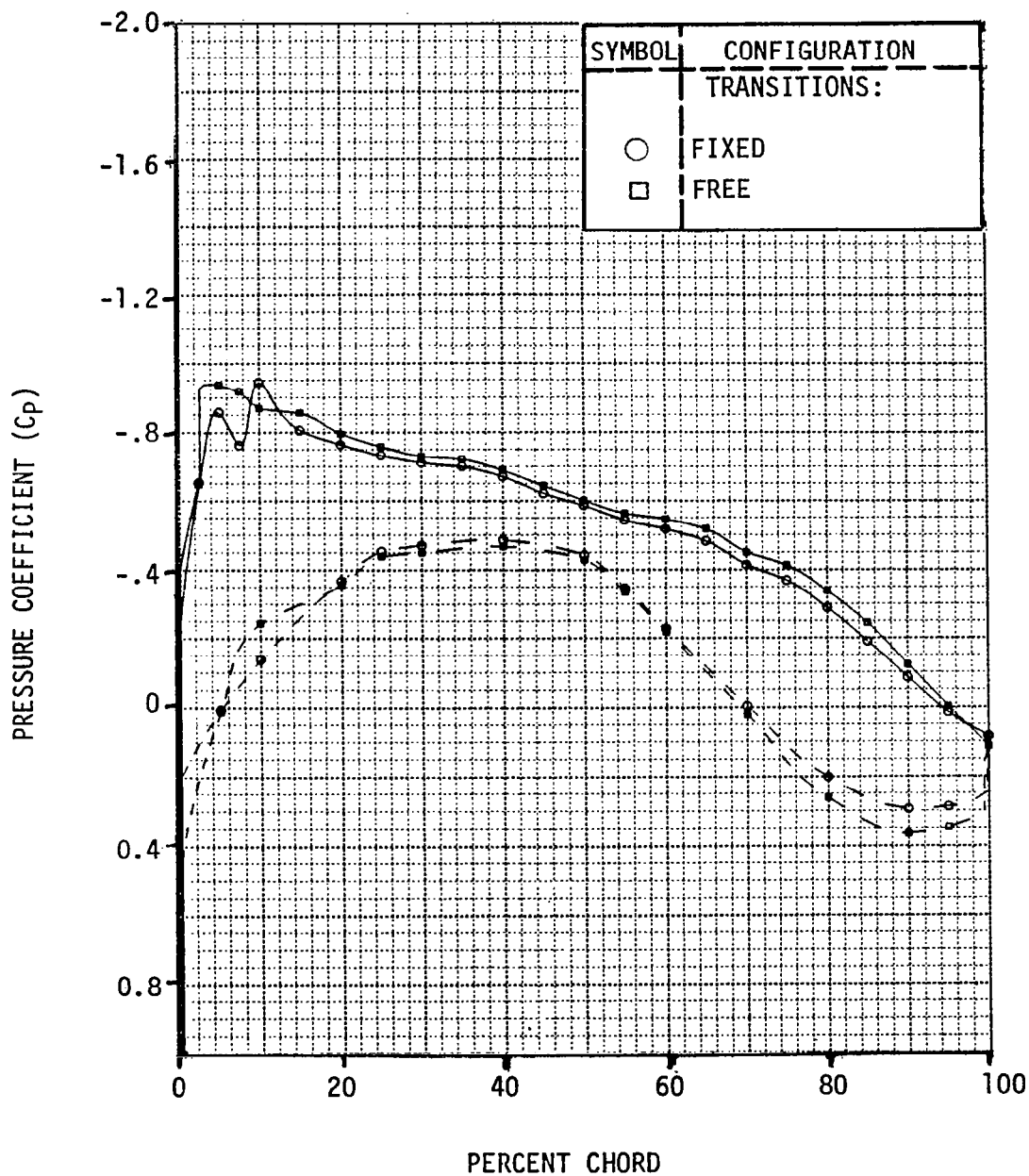
MACH NUMBER = 0.70

Figure 11.11. Wing-Body Pressure Distribution at M = 0.70 and η = .70

ALPHA = 0.5°

90 PERCENT SEMI-SPAN
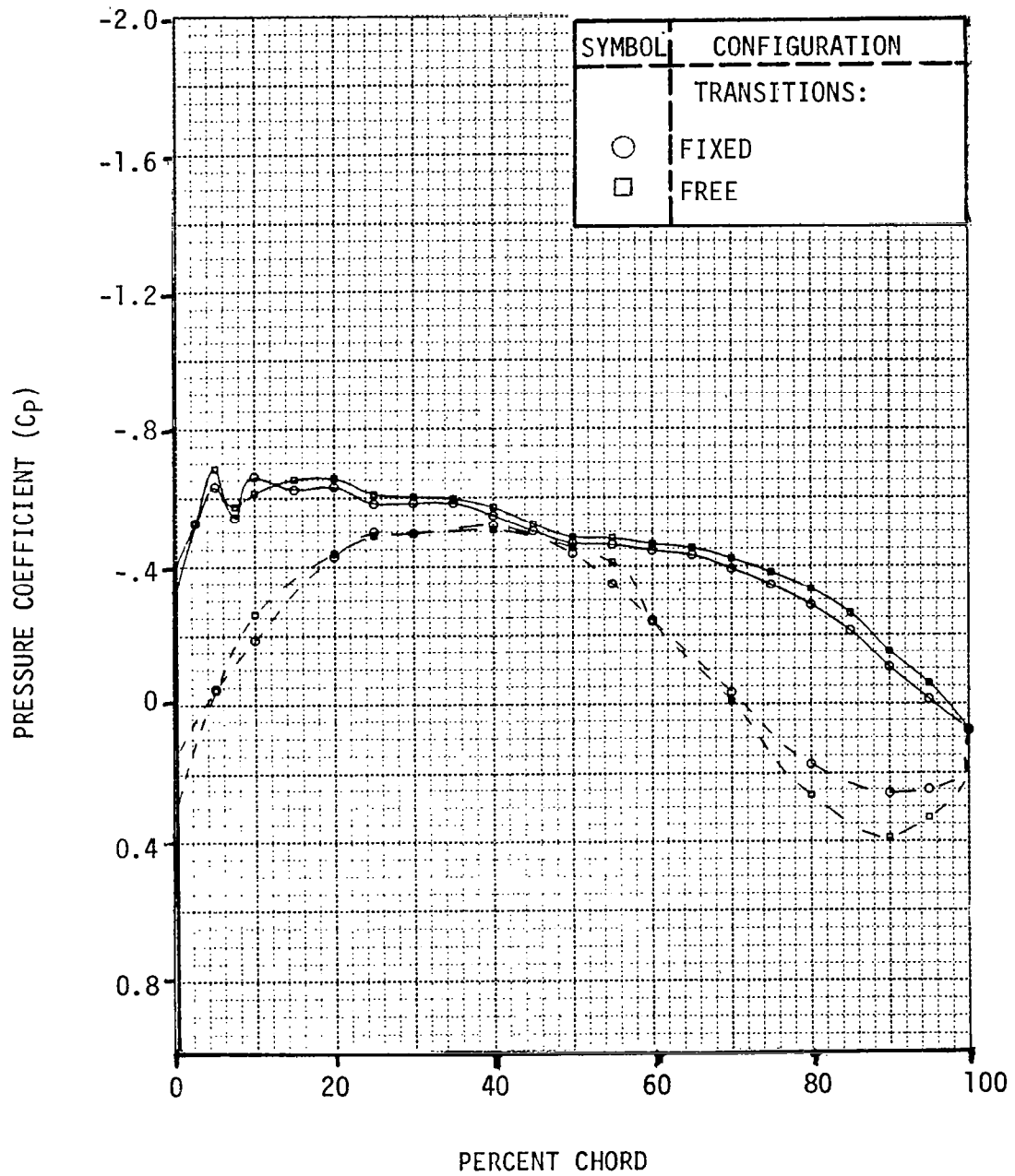
MACH NUMBER = 0.70

Figure 11.12. Wing-Body Pressure Distribution at M = 0.70 and η = .90.

ALPHA = 0.5°

13 PERCENT SEMI-SPAN
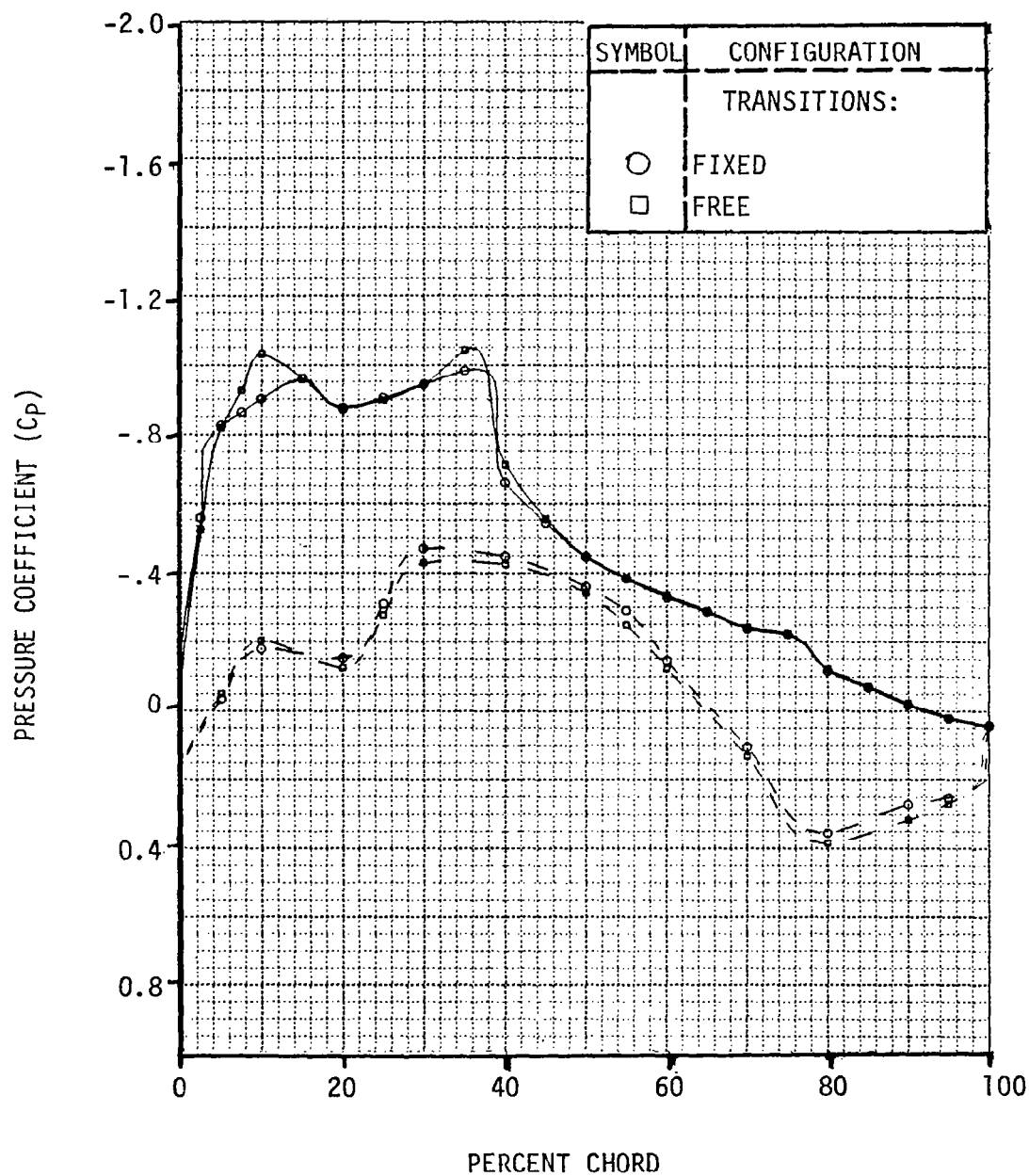
MACH NUMBER = 0.76

Figure 11.13. Wing-Body Pressure Distribution at M = 0.76 and η = .13.

117

ALPHA = 0.5°

33 PERCENT SEMI-SPAN
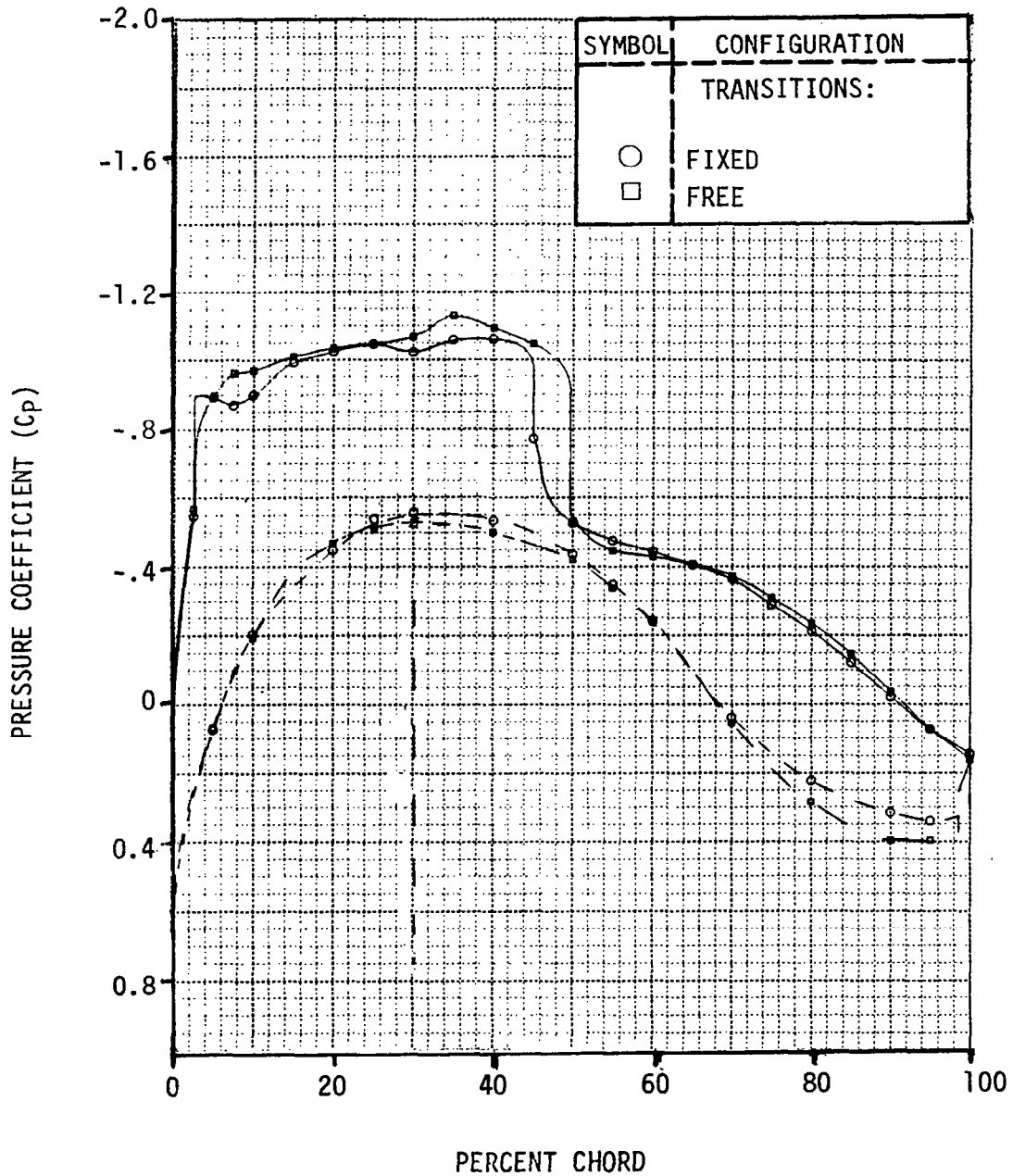
MACH NUMBER = 0.76

Figure 11.14.   Wing-Body Pressure Distribution at M = 0.76 and η = .33.

ALPHA = 0.5°

58 PERCENT SEMI-SPAN
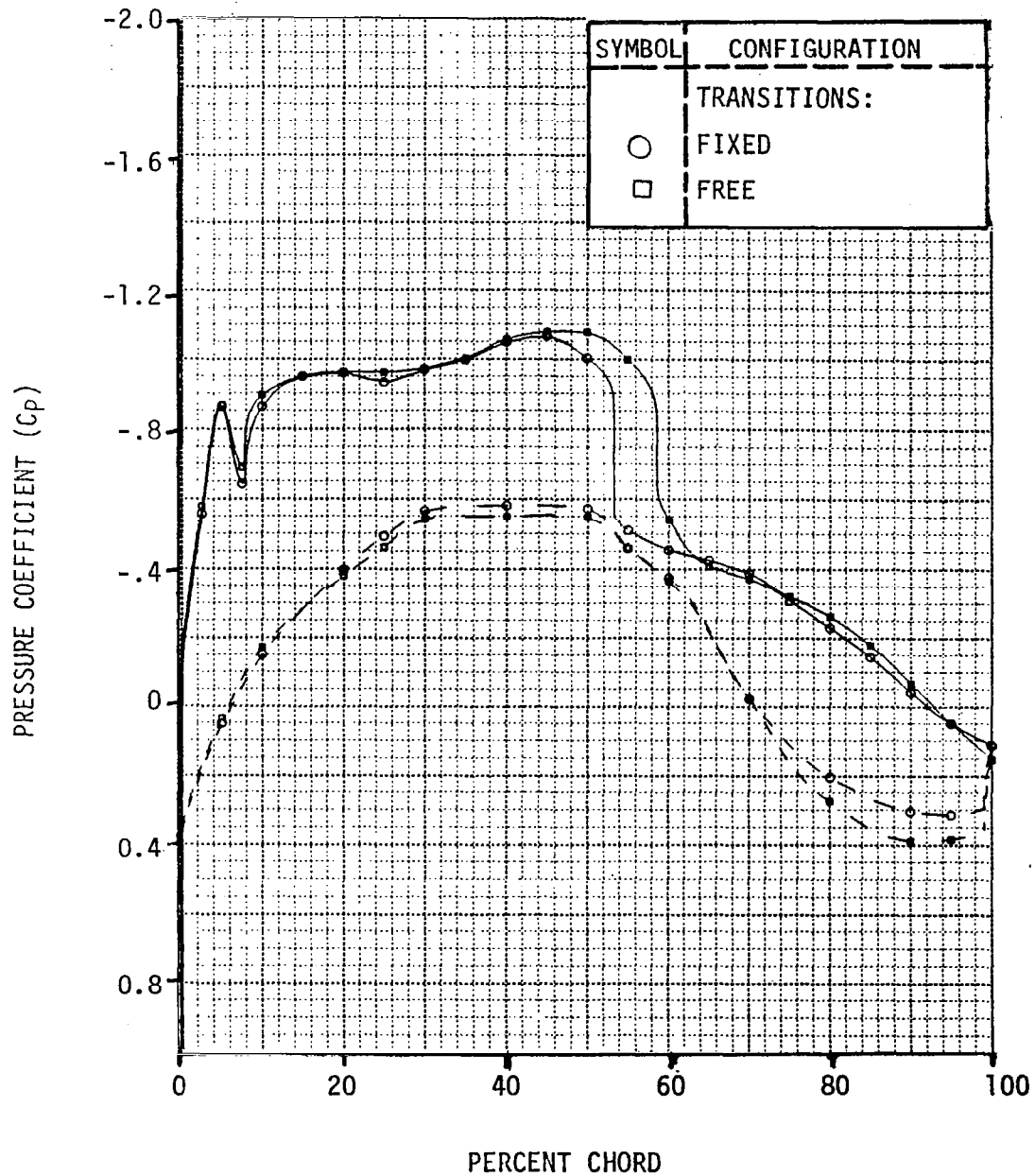
MACH NUMBER = 0.76

Figure 11.15. Wing-Body Pressure Distribution at M = 0.76 and η = .58.

ALPHA = 0.5°

70 PERCENT SEMI-SPAN
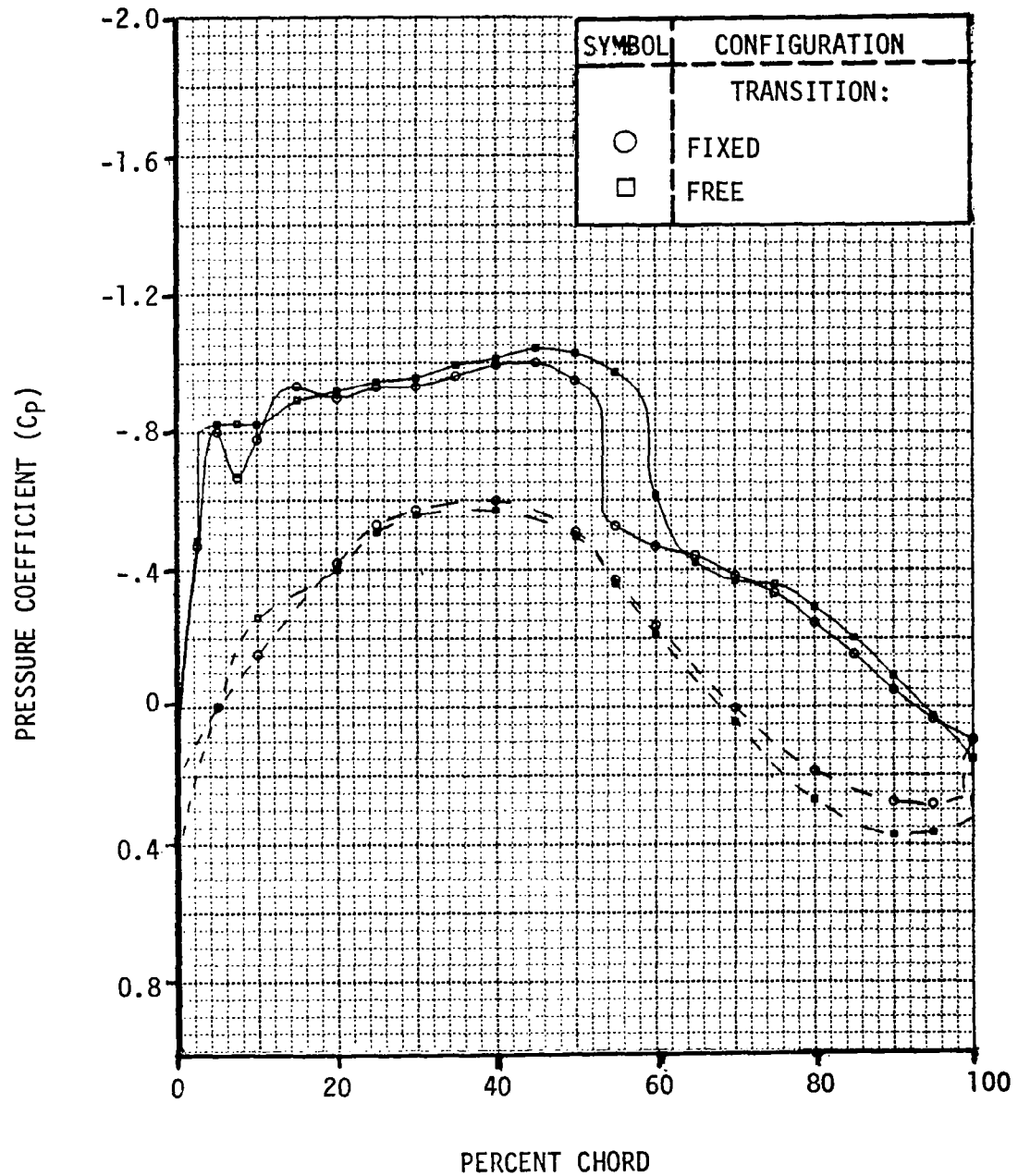
MACH NUMBER = 0.76

Figure 11.16. Wing-Body Pressure Distribution at M = 0.76 and η = .70.

ALPHA = 0.5°

90 PERCENT SEMI-SPAN
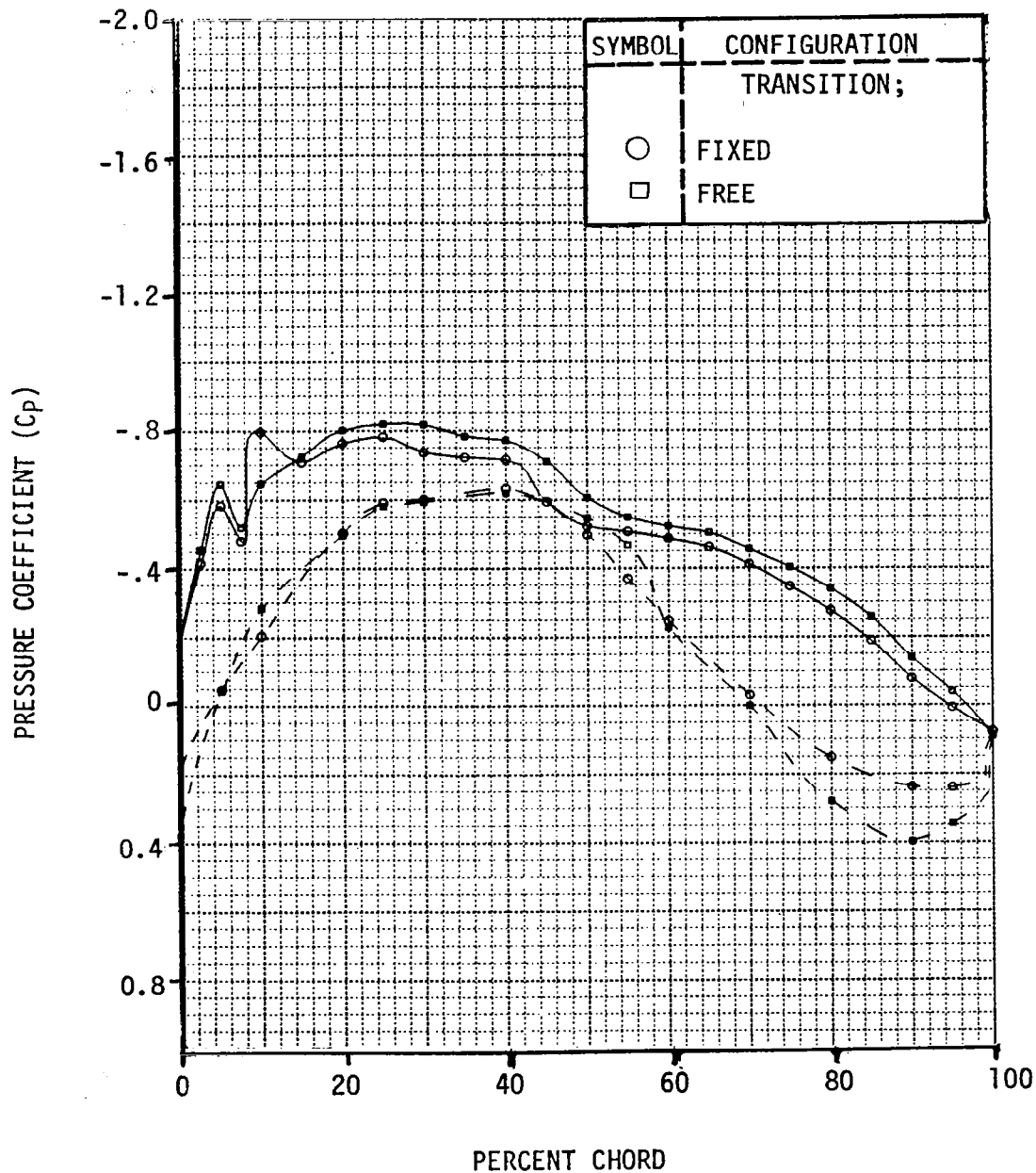
MACH NUMBER = 0.76

Figure 11.17. Wing-Body Pressure Distribution at M = 0.76 and η = .90.
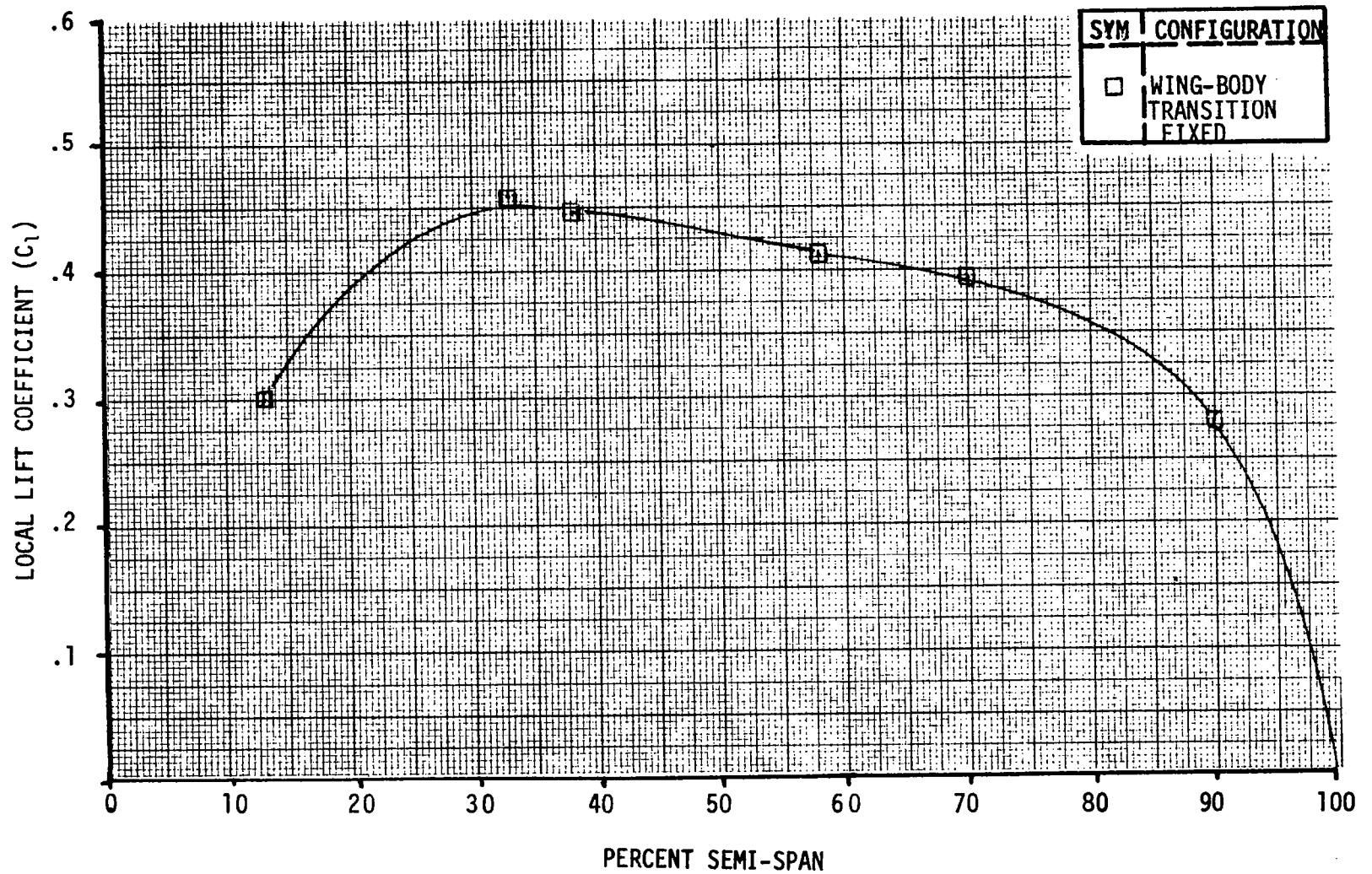
Figure 11.18. Spanwise Lift Distribution for Wing-Body at M = 0.70.
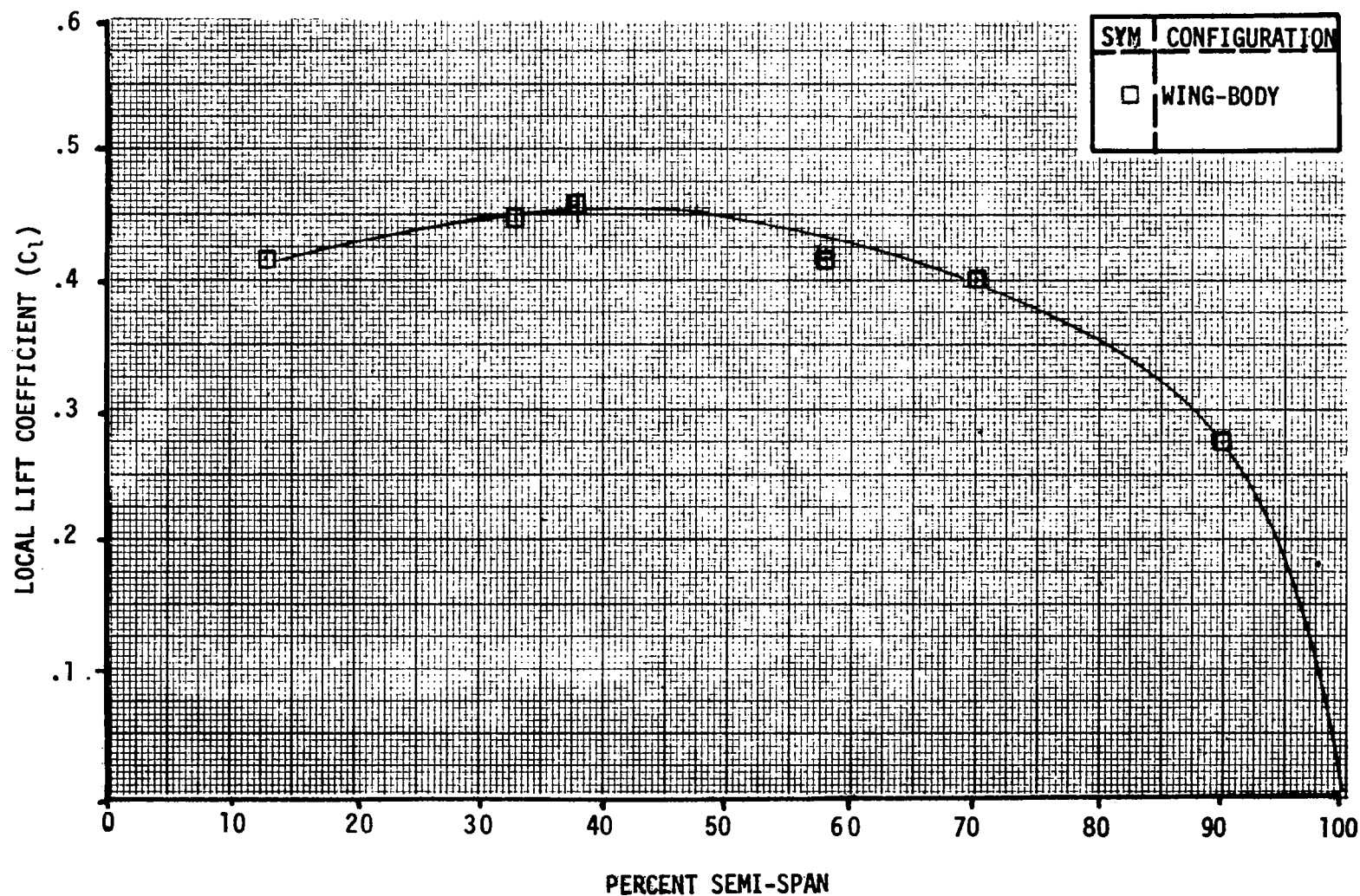
Figure 11.19.   Spanwise Lift Distribution for Wing-Body at M = 0.76.
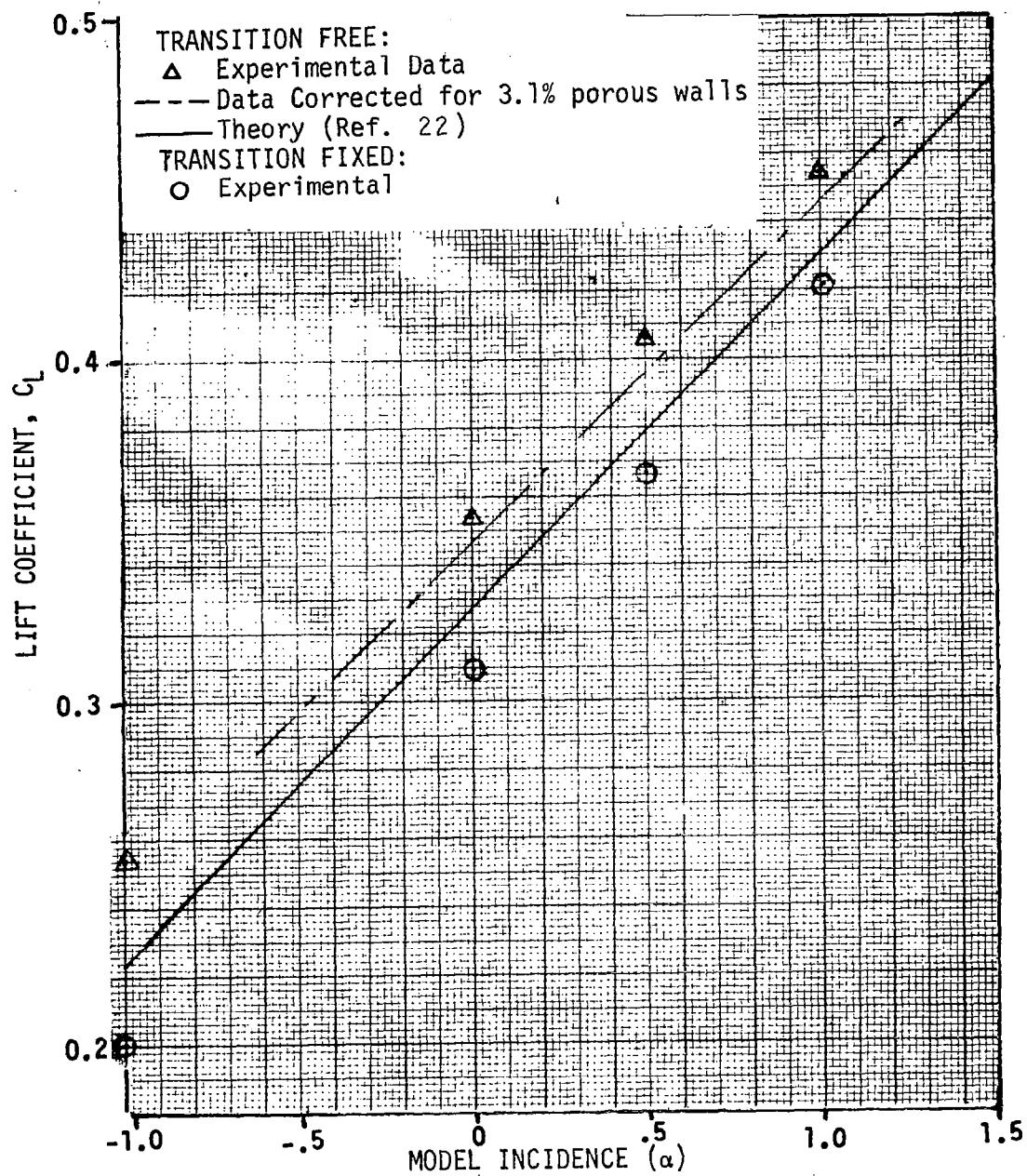
Figure 11.20. Comparison of Estimated Lift Curve with
Experiment for the Wing-Body at M = 0.7.
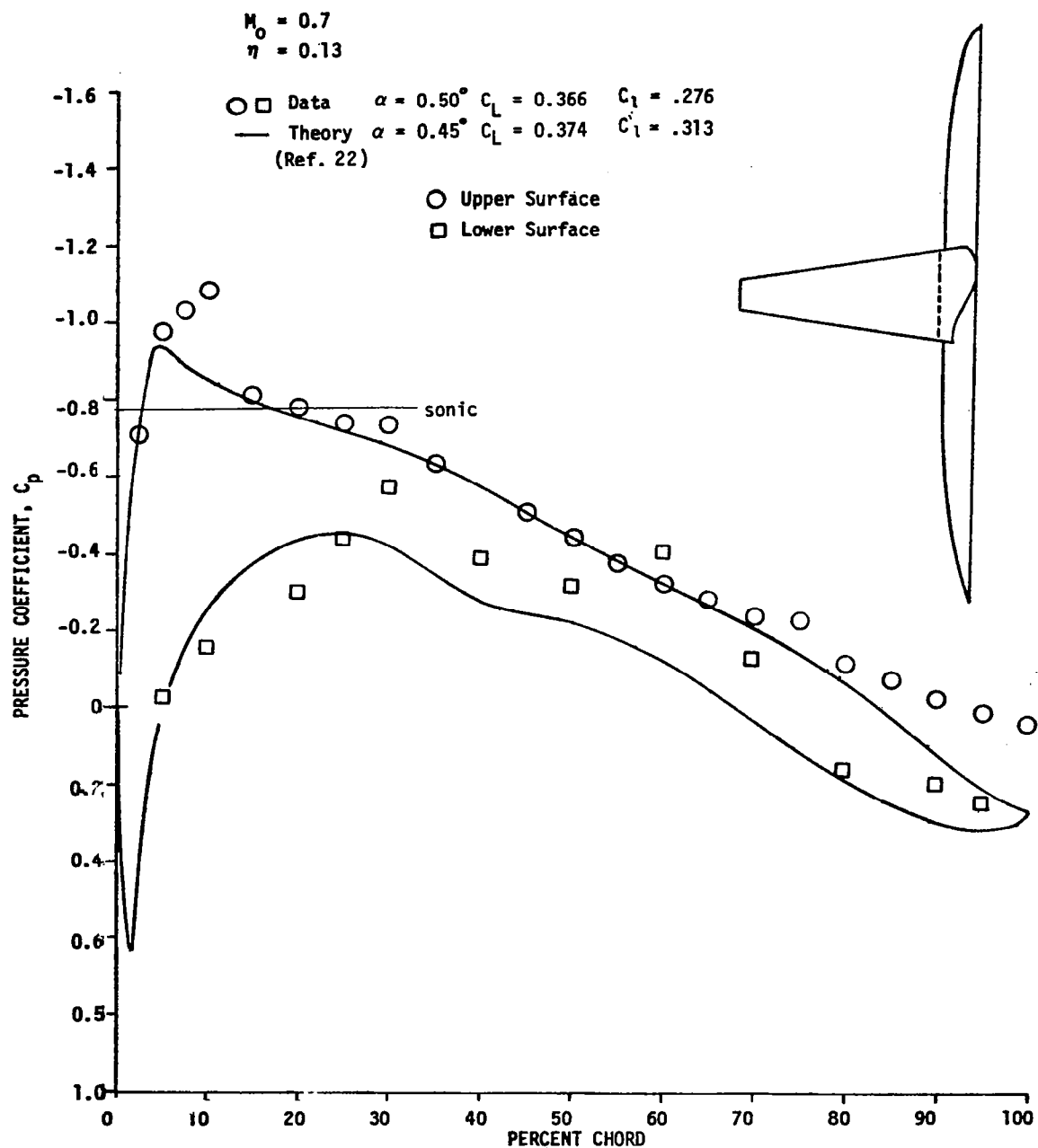
Figure 11.21. Theory-Data Comparison for Wing-Body at 13% Semispan
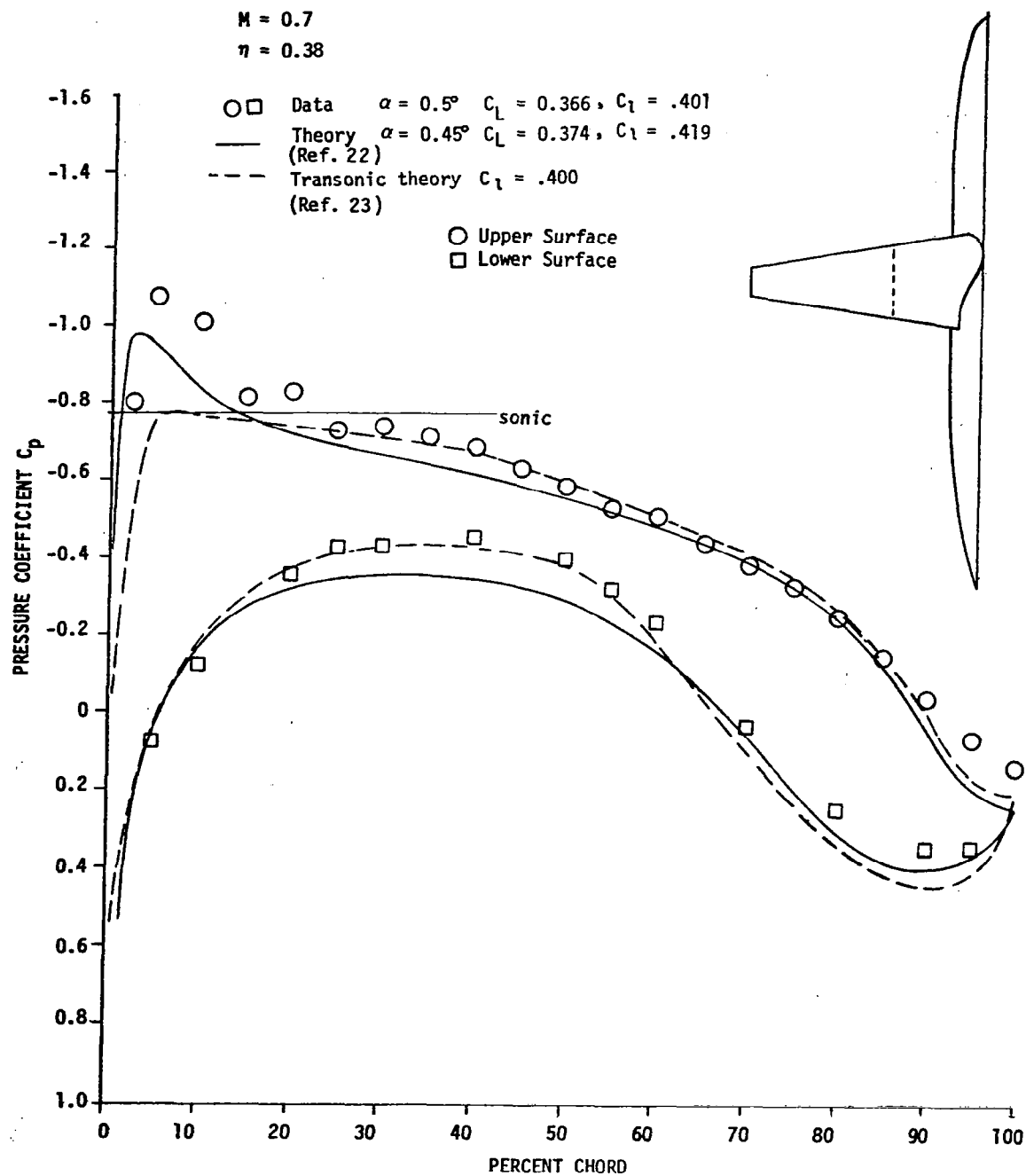
Figure 11.22. Theory-Data Comparison for Wing-Body at 38% Semispan

126

$M_0 = 0.7$
$\eta = 0.58$

OD Data	$\alpha = 0.5°$	$C_L = 0.366$	$C_l = .373$
— Theory	$\alpha = 0.45°$	$C_L = 0.374$	$C_l = .415$
(Ref. 22)			

O Upper Surface
□ Lower Surface

sonic

PRESSURE COEFFICIENT C_p

PERCENT CHORD
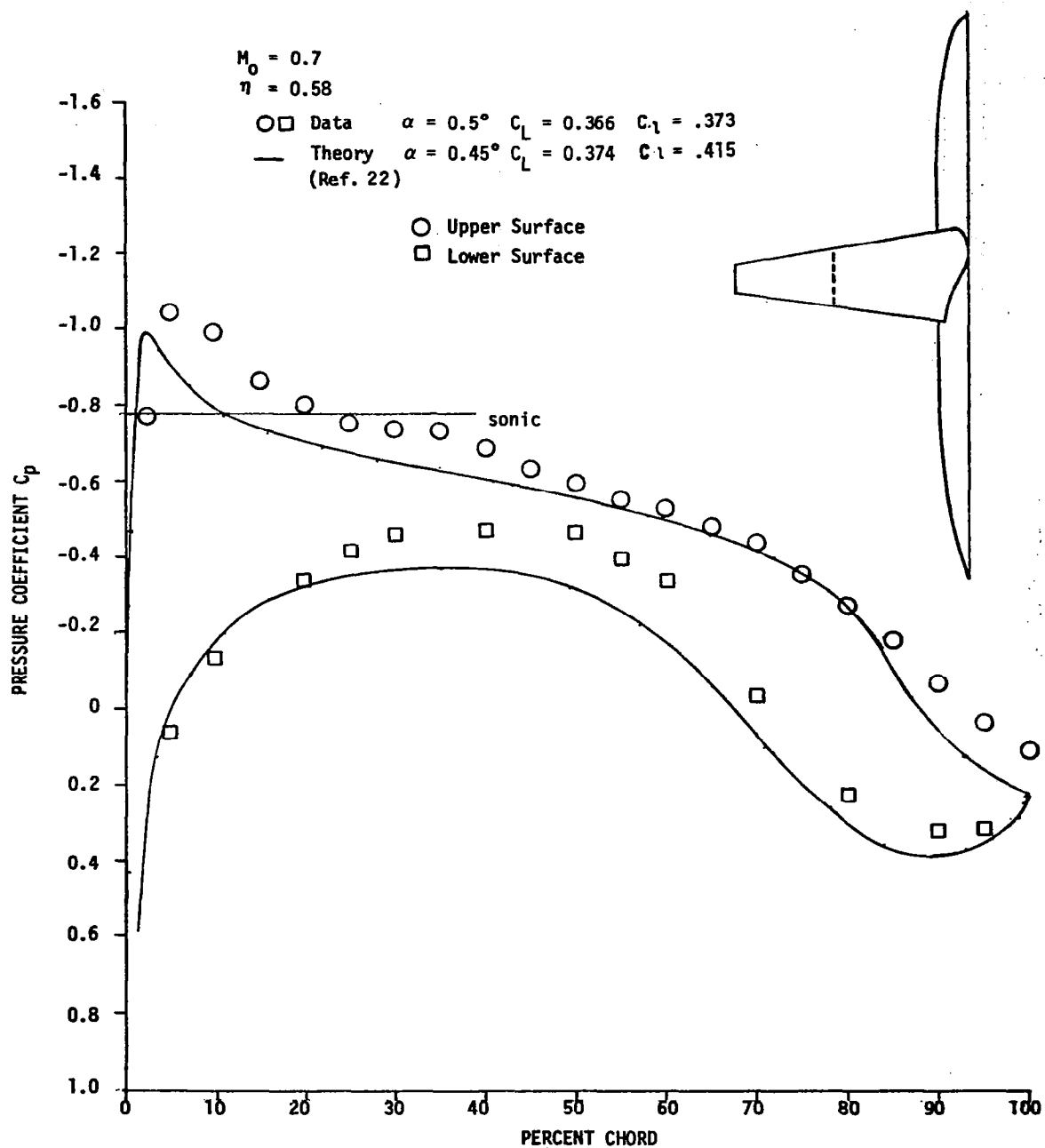
Figure 11.23.   Theory-Data Wing Pressure Comparison for Wing-Body at 58% Semispan
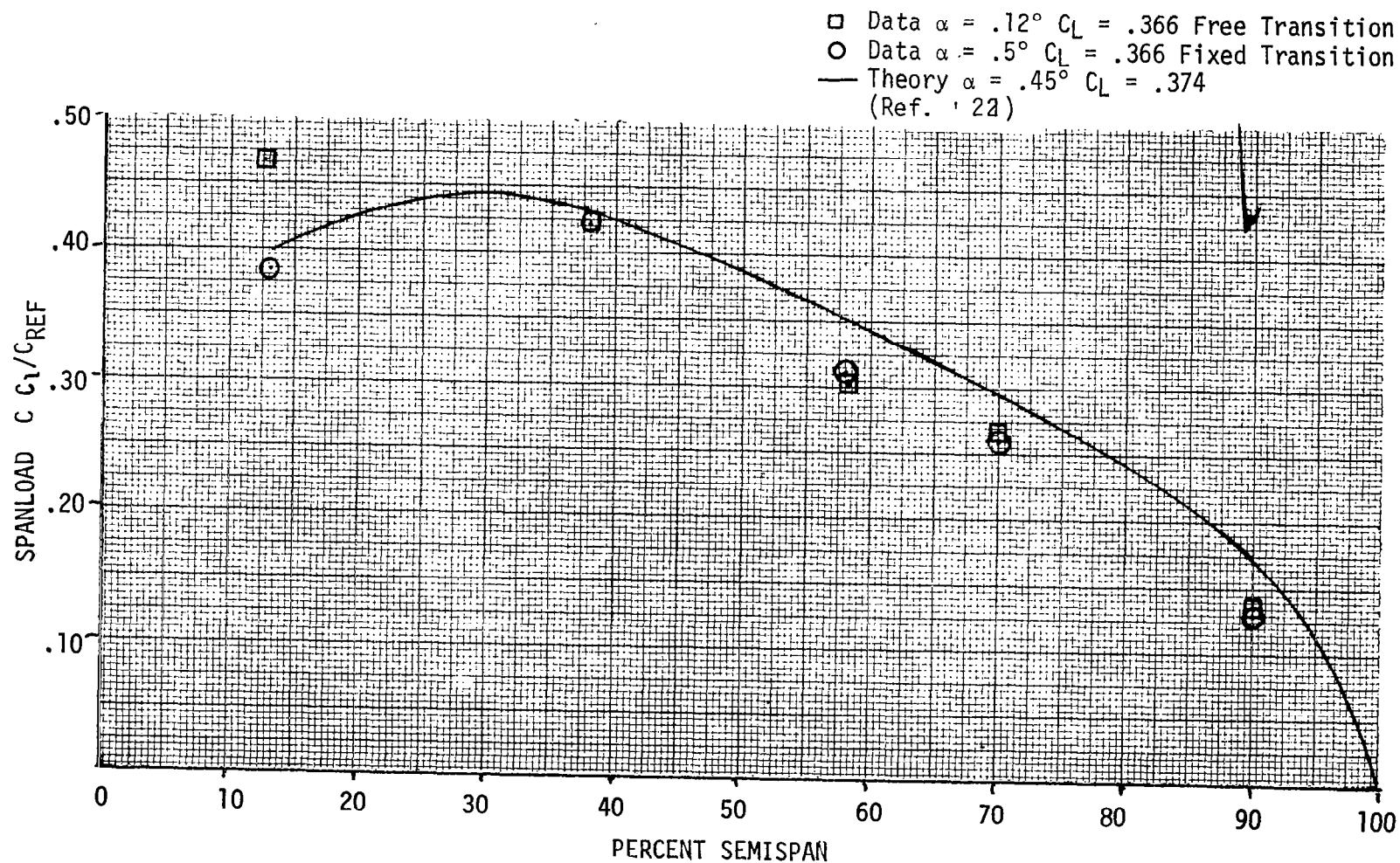
Figure 11.24. Comparison of Theoretical Spanload with Test Data for Wing-Body at M = 0.7.
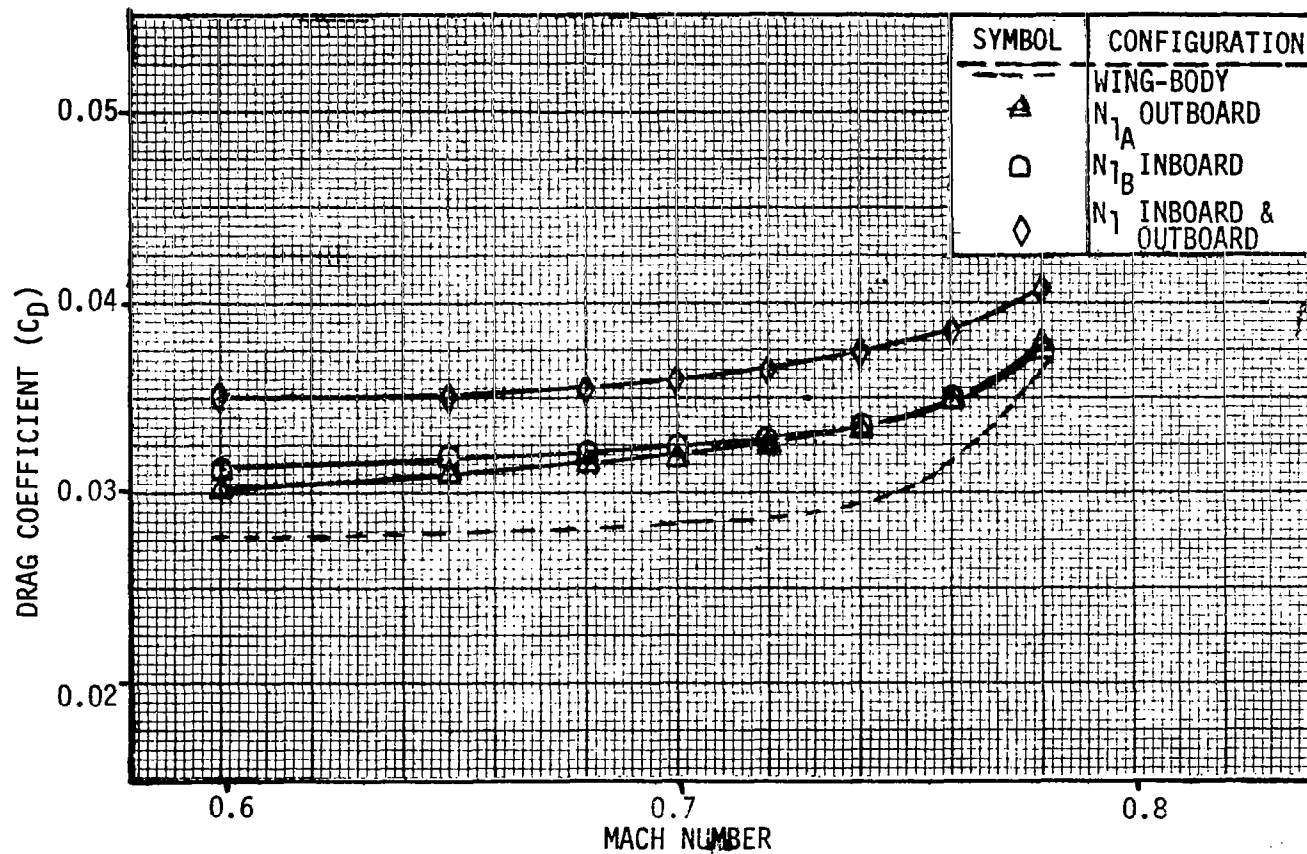
Figure 11.25. Wing-Body and Nacelle Drag, Baseline Flow Through Nacelles, $C_L = 0.4$
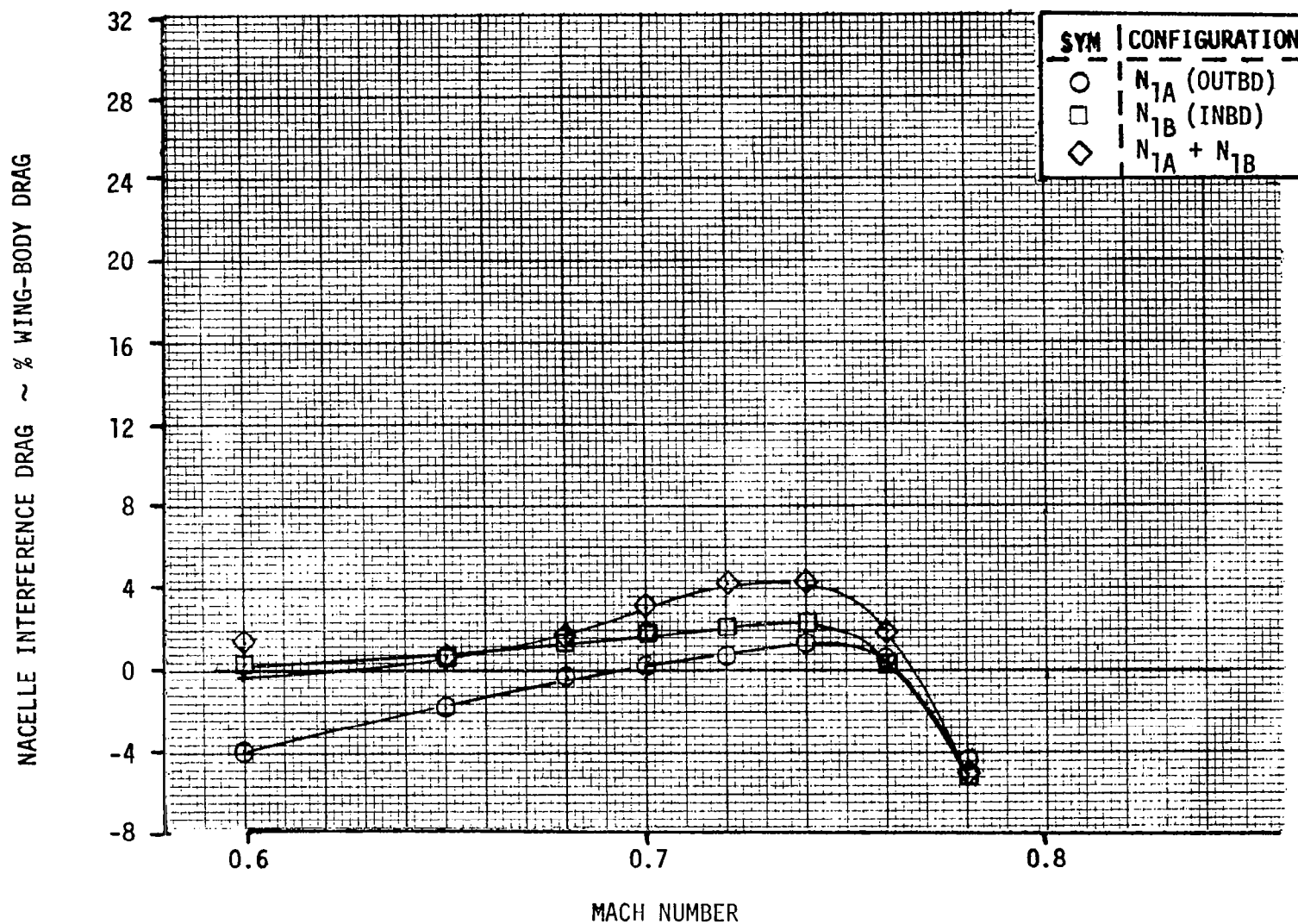
Figure 11.26.   Variation of Nacelle Interference Drag for N_1 Flow Through Nacelles.

ALPHA = 0.5°

33 PERCENT SEMI-SPAN

MACH NUMBER = 0.7

FLOW-THROUGH

SYMBOL	CONFIGURATION
◯	WING BODY
◻	N_{1B} (INBD)
△	N_{1A} (OUTBD)
✕	$N_{1A} + N_{1B}$
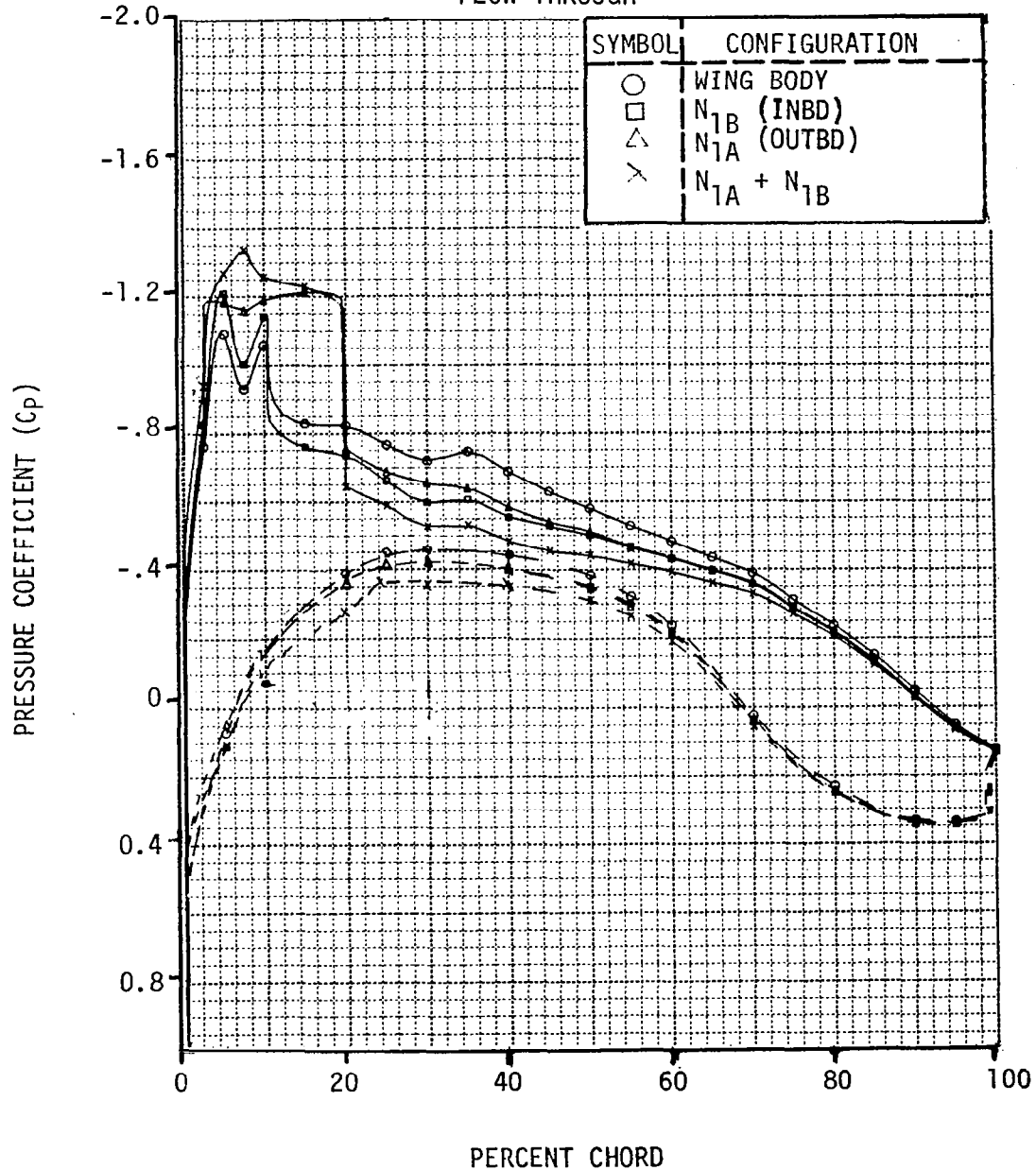
Figure 11.27. Wing Surface Pressure Distributions for Several N_1 Configurations at Flow-Through Conditions, 33% Semispan and M = 0.70.

131

ALPHA = 0.5°

33 PERCENT SEMI-SPAN

MACH NUMBER = 0.76

FLOW-THROUGH

SYMBOL	CONFIGURATION
○	WING BODY
□	N_{1A} (INBD)
△	N_{1B} (OUTBD)
✕	$N_{1A} + N_{1B}$

PRESSURE COEFFICIENT (C_P)

PERCENT CHORD
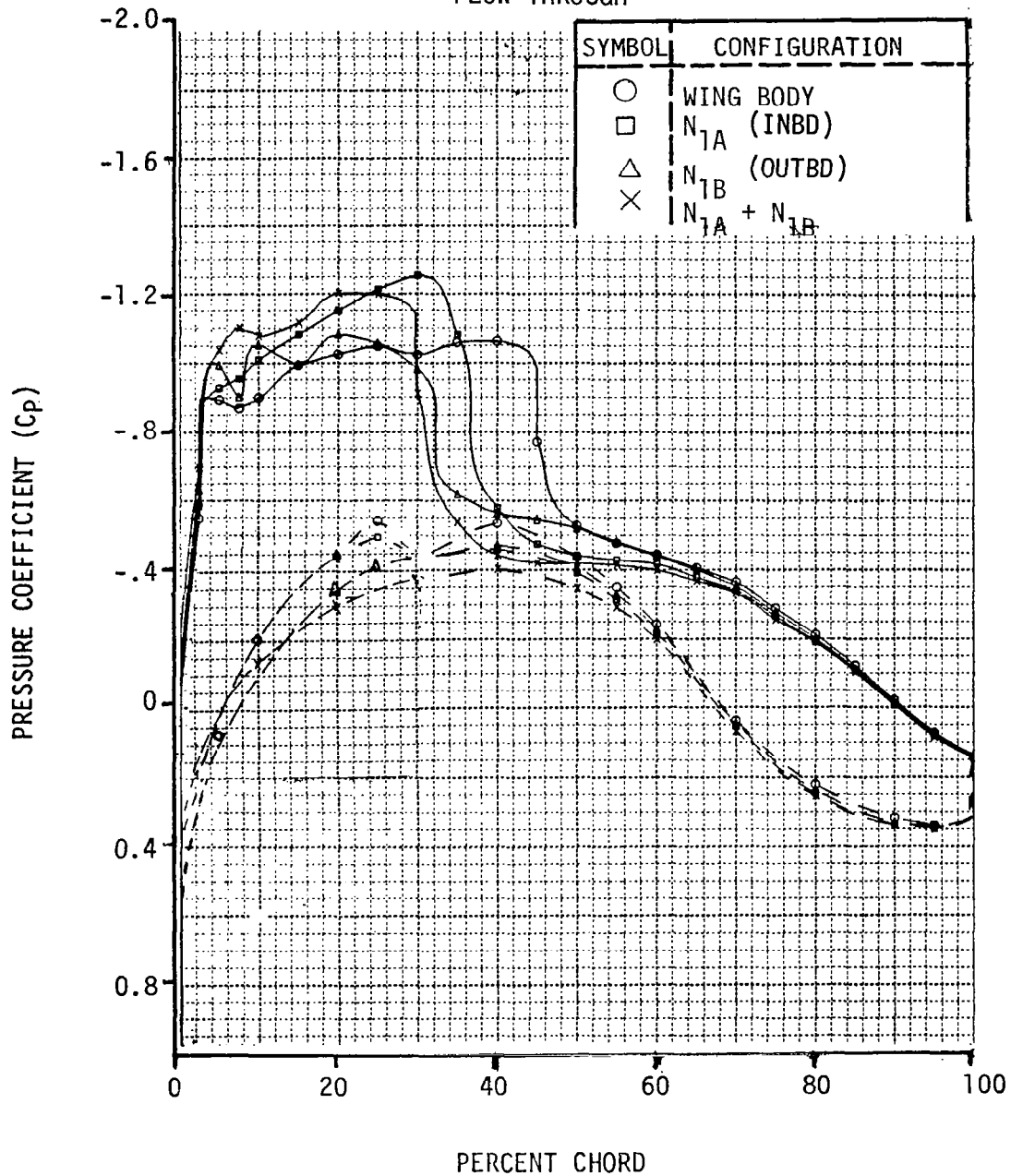
Figure 11.28. Wing Surface Pressure Distribution for Several N_1 Configurations at Flow-Through Conditions, 33% Semispan and M = 0.76.
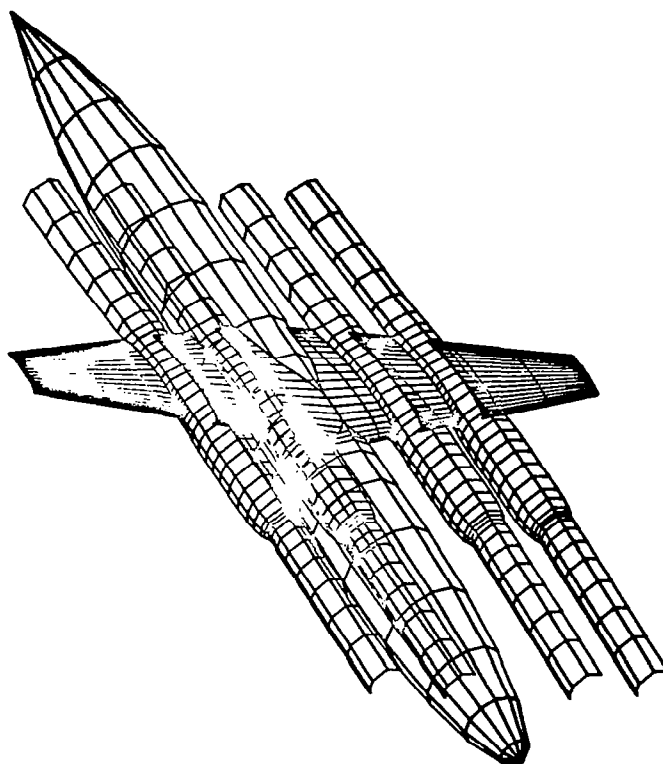
Figure 11.29. Machine Drawn Sketch of Neumann Wing-Body-Nacelle Paneling.
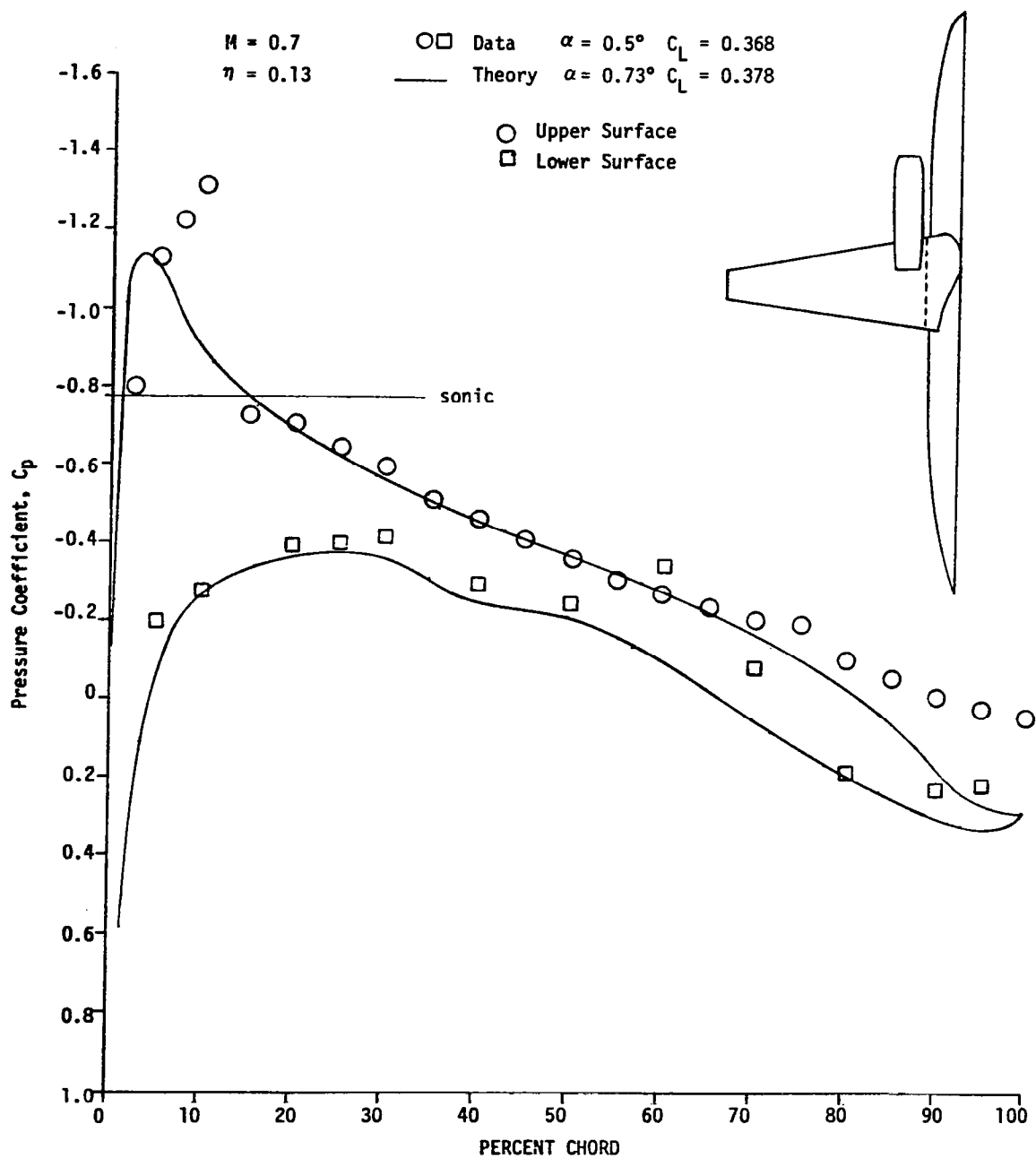
Figure 11.30. Theory-Data Comparison for 2 Inboard Engines N_{1B} at 13% Semispan

134
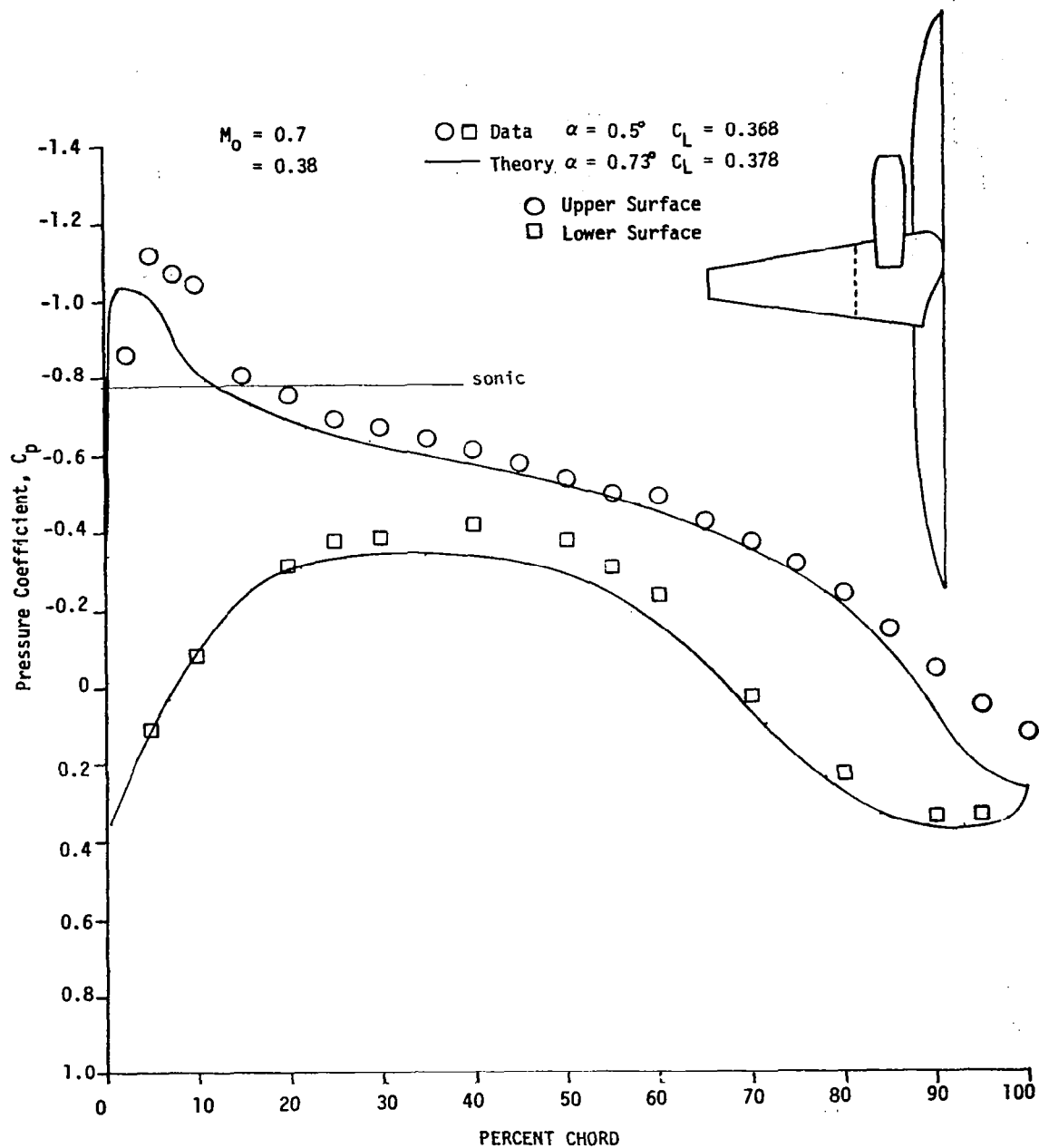
Figure 11.31. Theory-Data Comparison for 2 Inboard Engines N_{1B} at 38% Semispan
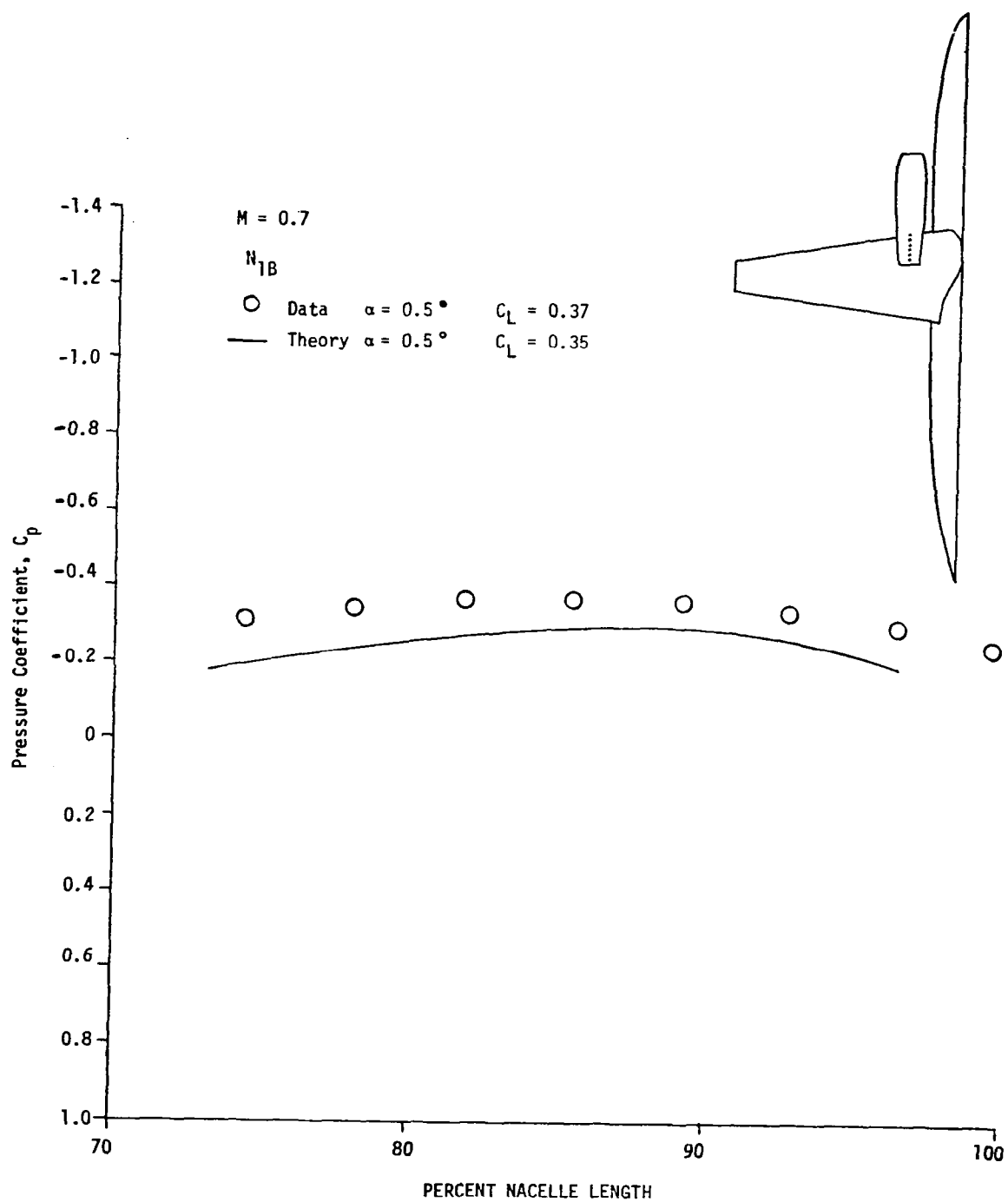
Figure 11.32. Comparison Between Theory and Data for External Nozzle Pressures on N_{1B}
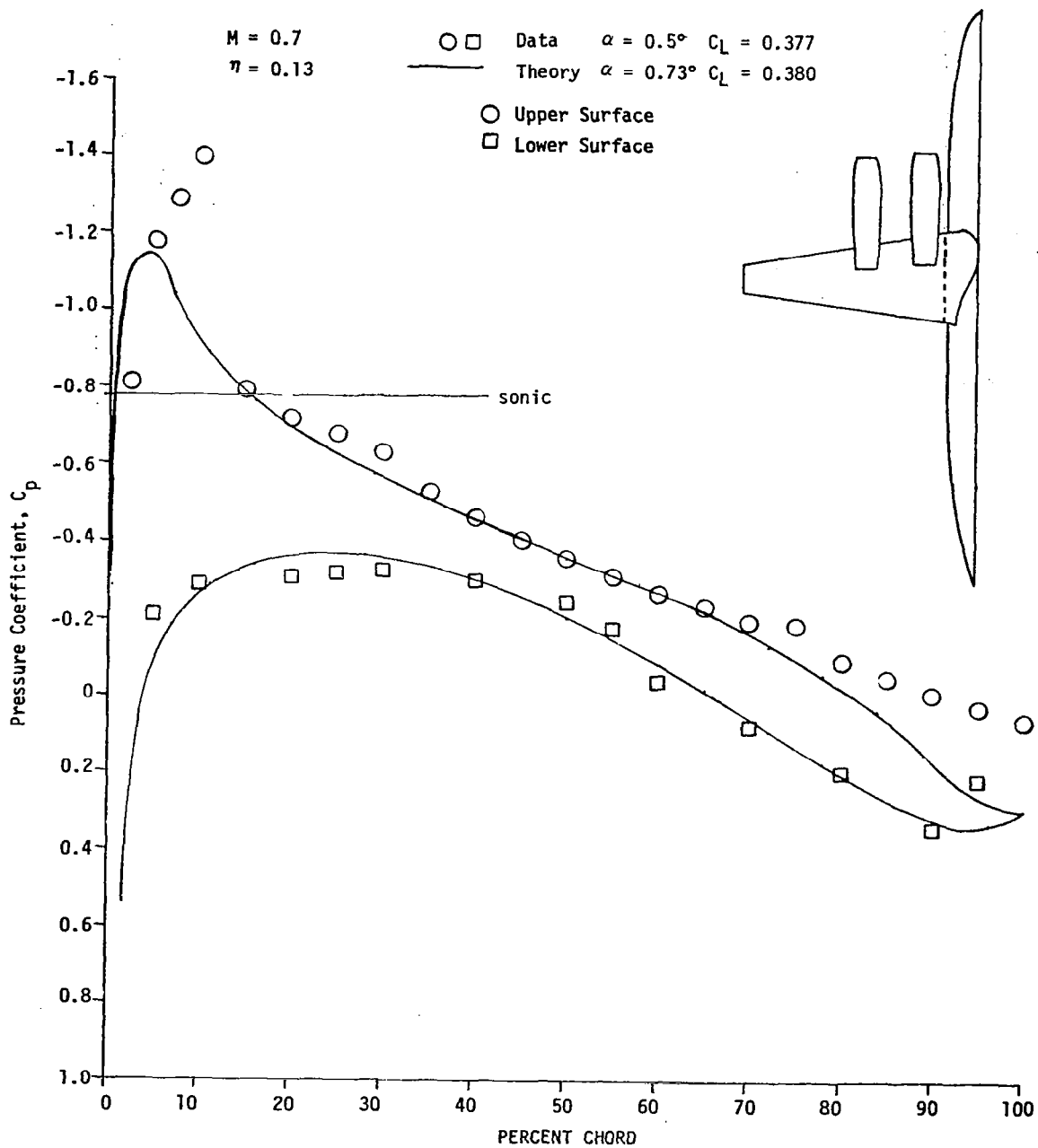
Figure 11.33. Theory-Data Comparison for 4 Engine N_{1A} + N_{1B} at 13% Semispan
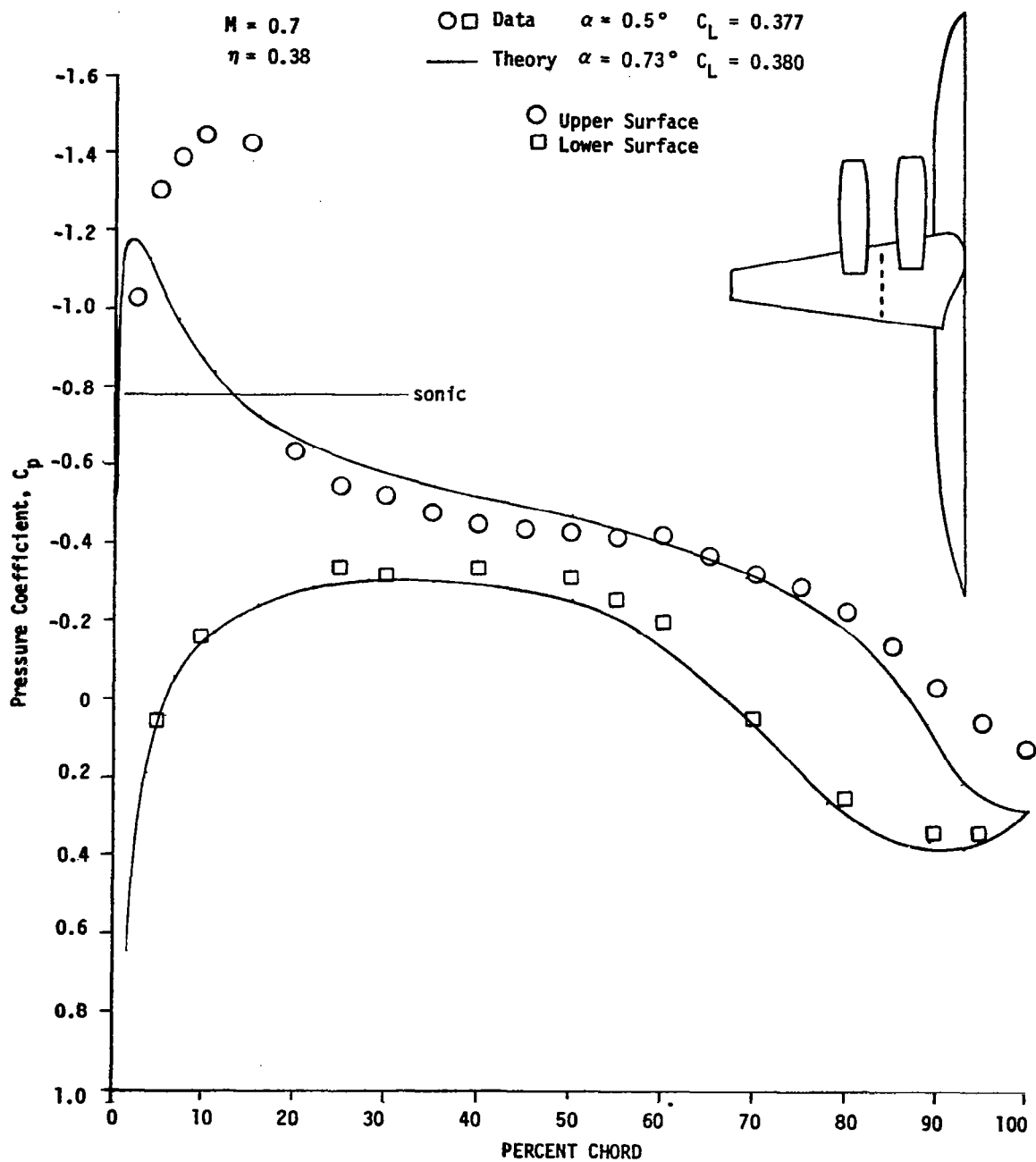
Figure 11.34. Theory-Data Comparison for 4 Engine N_{1A} + N_{1B} at 38% Semispan

M = 0.7   ⊙□ Data $\alpha = 0.5°$ $C_L = 0.377$
$\eta = 0.58$ —— Theory $\alpha = 0.73°$ $C_L = 0.380$
   ⊙ Upper Surface
   □ Lower Surface

sonic

Pressure Coefficient, C_p

PERCENT CHORD
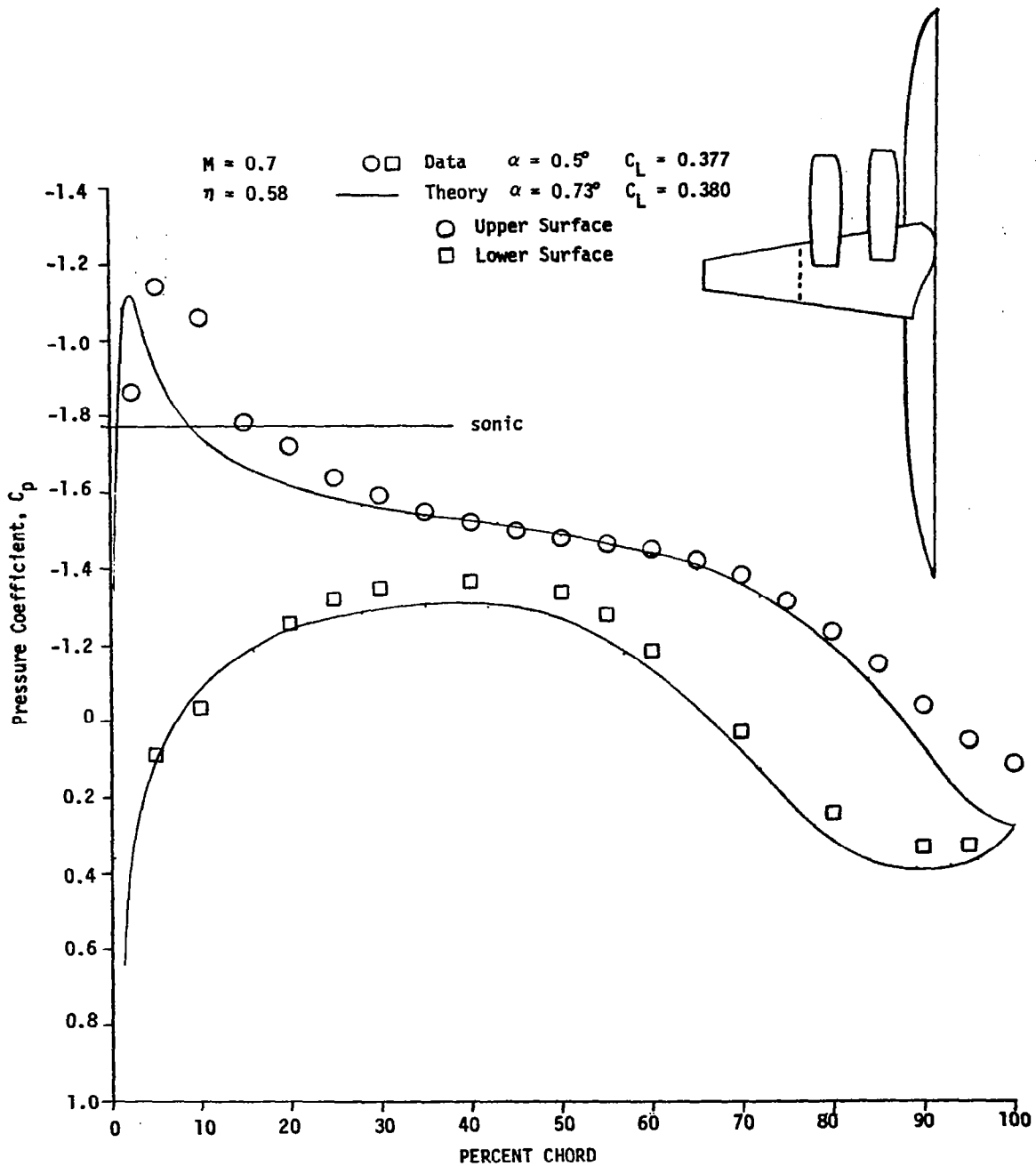
Figure 11.35. Theory-Data Comparison for 4 Engine $N_{1A} + N_{1B}$ at 58% Semispan
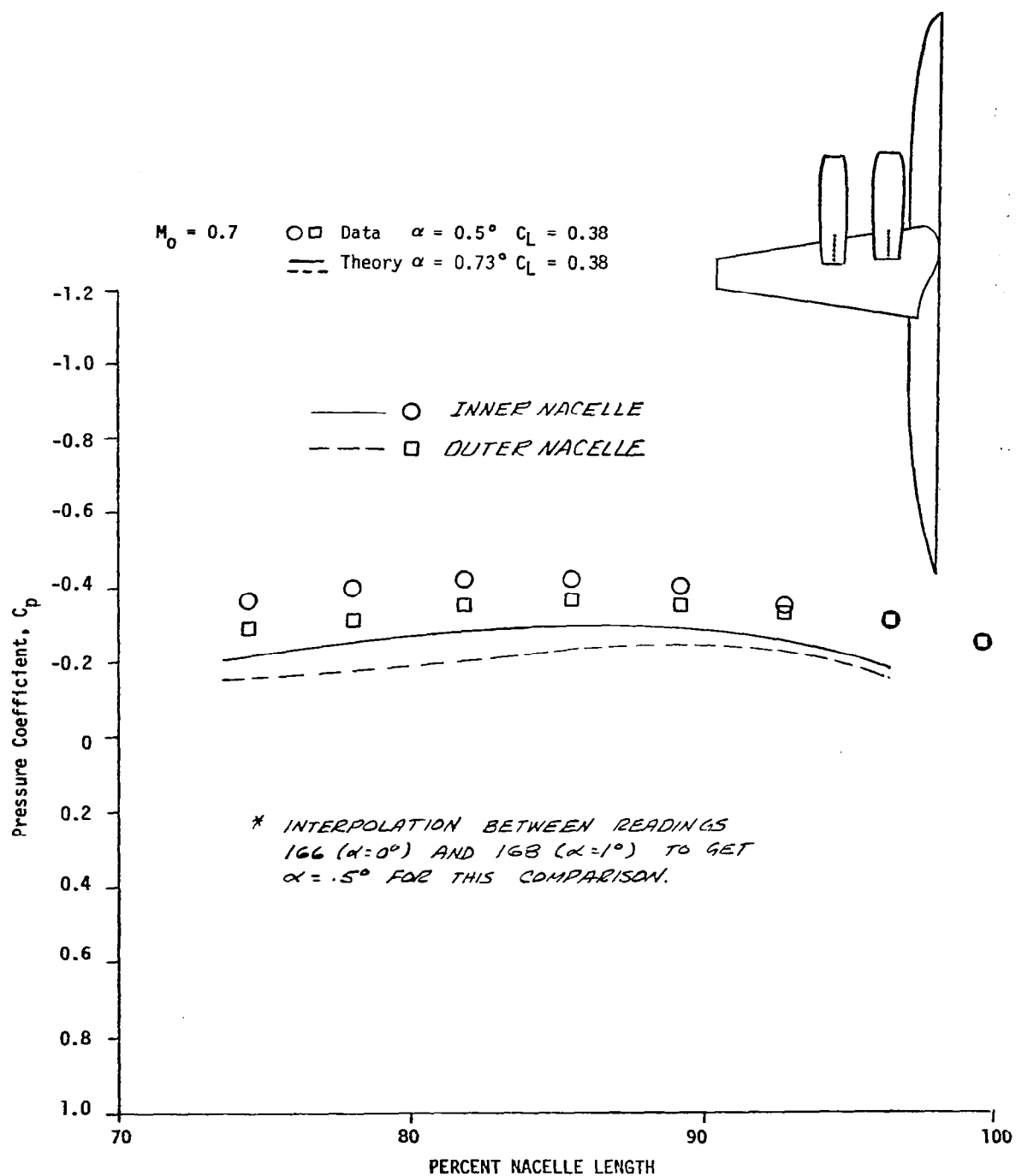
Figure 11.36. Comparison Between Theory and Data for External Nozzle Pressures on $N_{1A} + N_{1B}$

Figure 11.37. Lift and Pitching Moment for Flow Through N_{1A} or N_{1B} at M = 0.7

SYMBOL	CONFIGURATION
▢	WING BODY
– – –	N_{1A} or N_{1B}
◇	N_{1A} + N_{1B} FLOW THRU

MACH NUMBER = 0.7
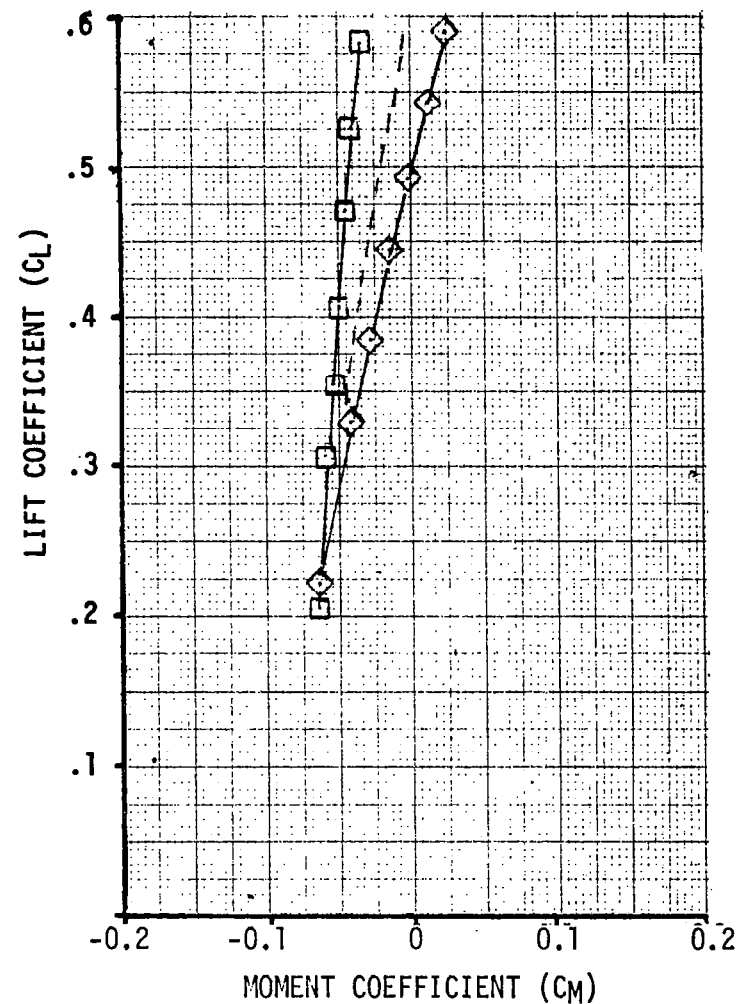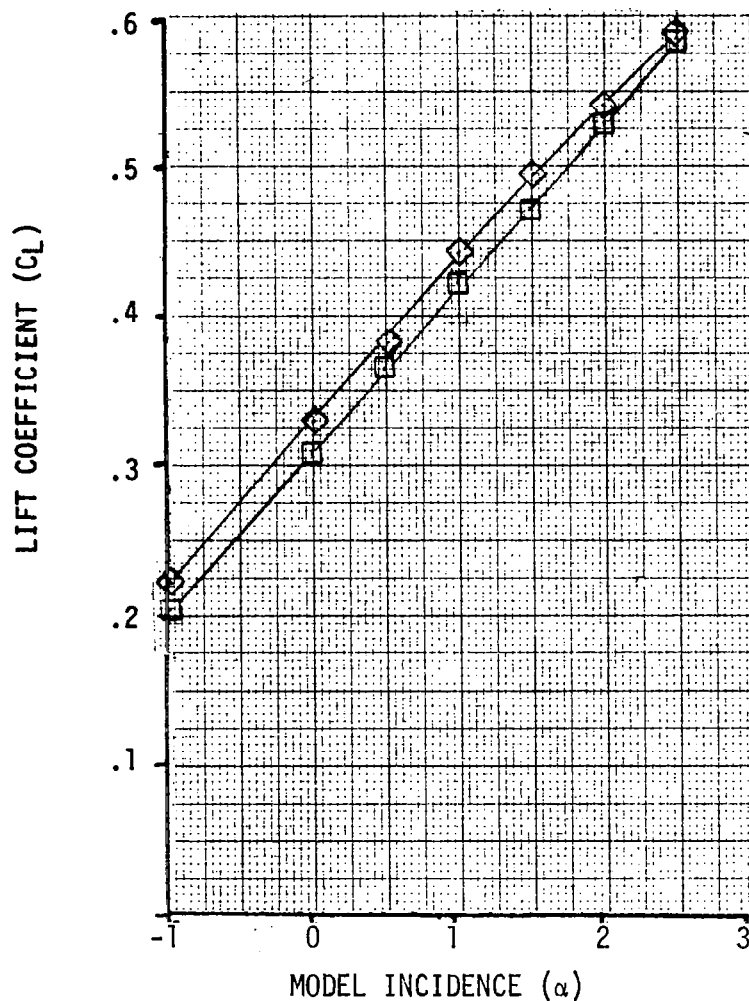
Figure 11.38. Lift and Pitching Moment for Flow Through N_{1A} + 1_{1B} at M = 0.70
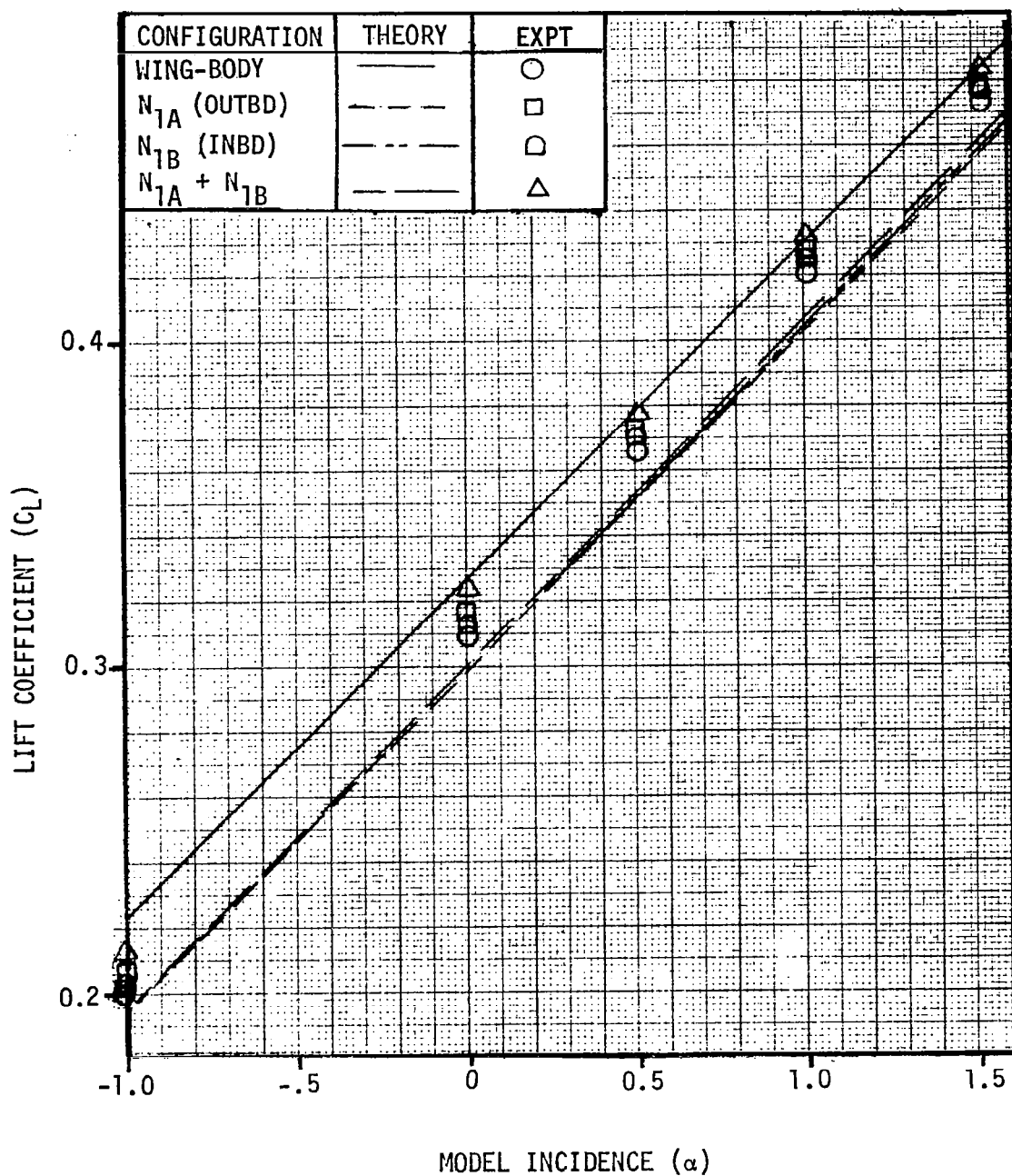
Figure 11.39. Comparison of Theoretical and Experimental Lift Curves at M = 0.70.

MACH NUMBER = 0.70   CONFIGURATION C_L = 0.40

144
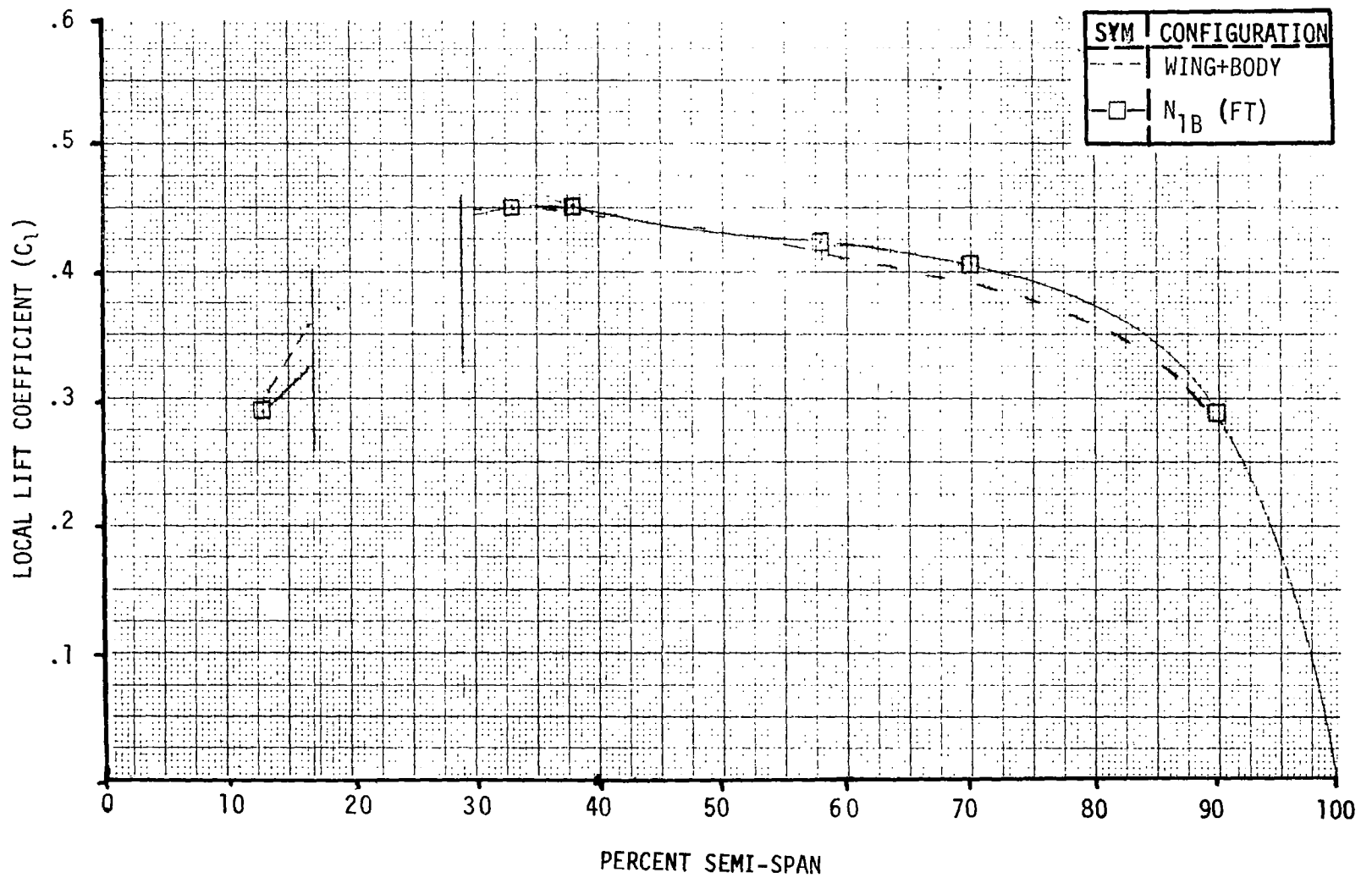
Figure 11.40. Spanwise Lift Distribution for "Flow-Through" N_{1B} at M = 0.70.
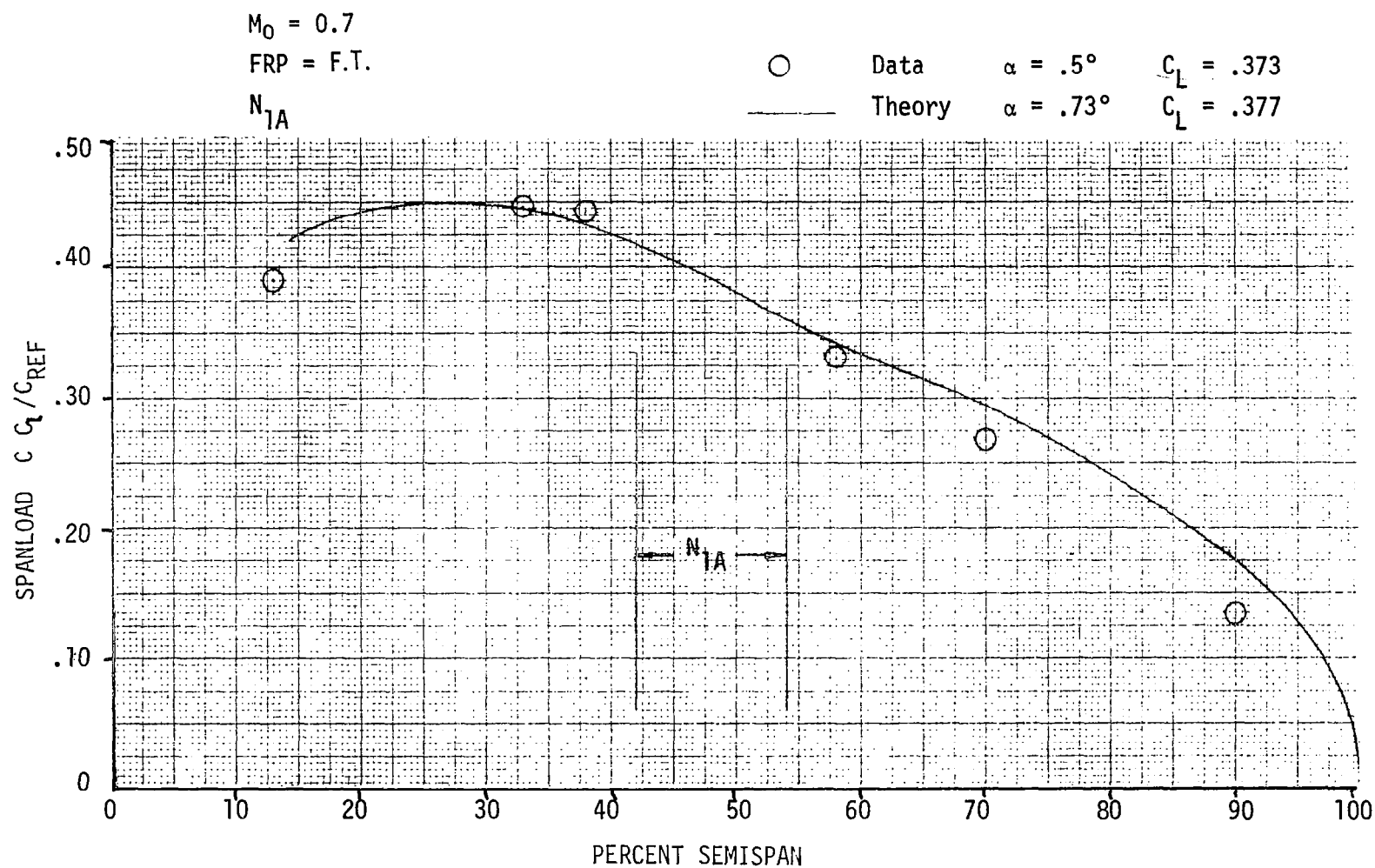
Figure 11.41. Comparison of Theoretical Spanload with Test Data for Two Outboard Engines N_{1A}.
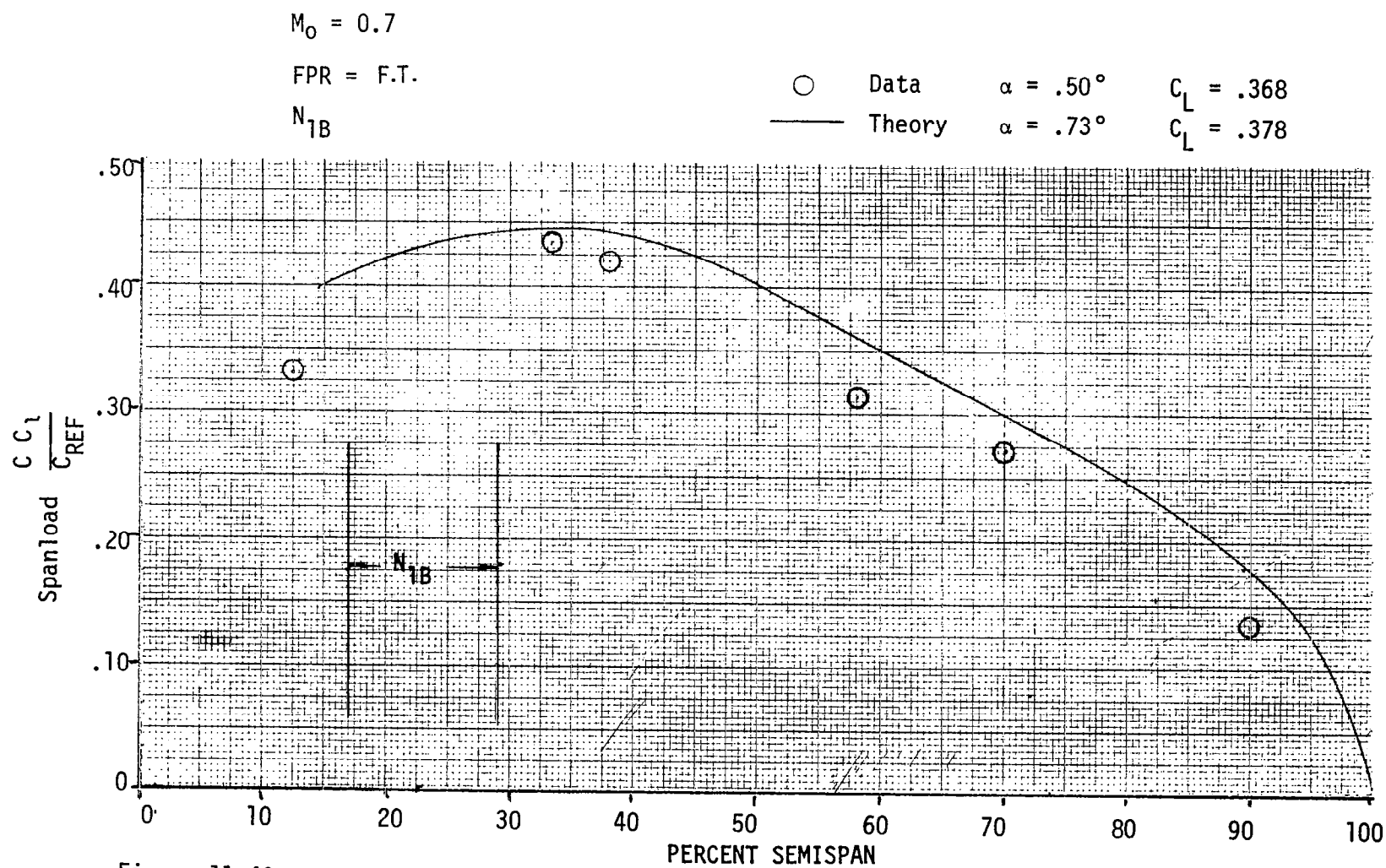
Figure 11.42. Comparison of Theoretical Spanload with Test Data for Two Inboard Engines N_{1B}.

$M_O = 0.7$

$FPR = F.T.$

$N_{1A} + N_{1B}$

○ Data $\alpha = .50°$ $C_L = .377$

—— Theory $\alpha = .73°$ $C_L = .380$

Spanload $\dfrac{c\,c_l}{\bar{c}_{REF}}$

PERCENT SEMISPAN
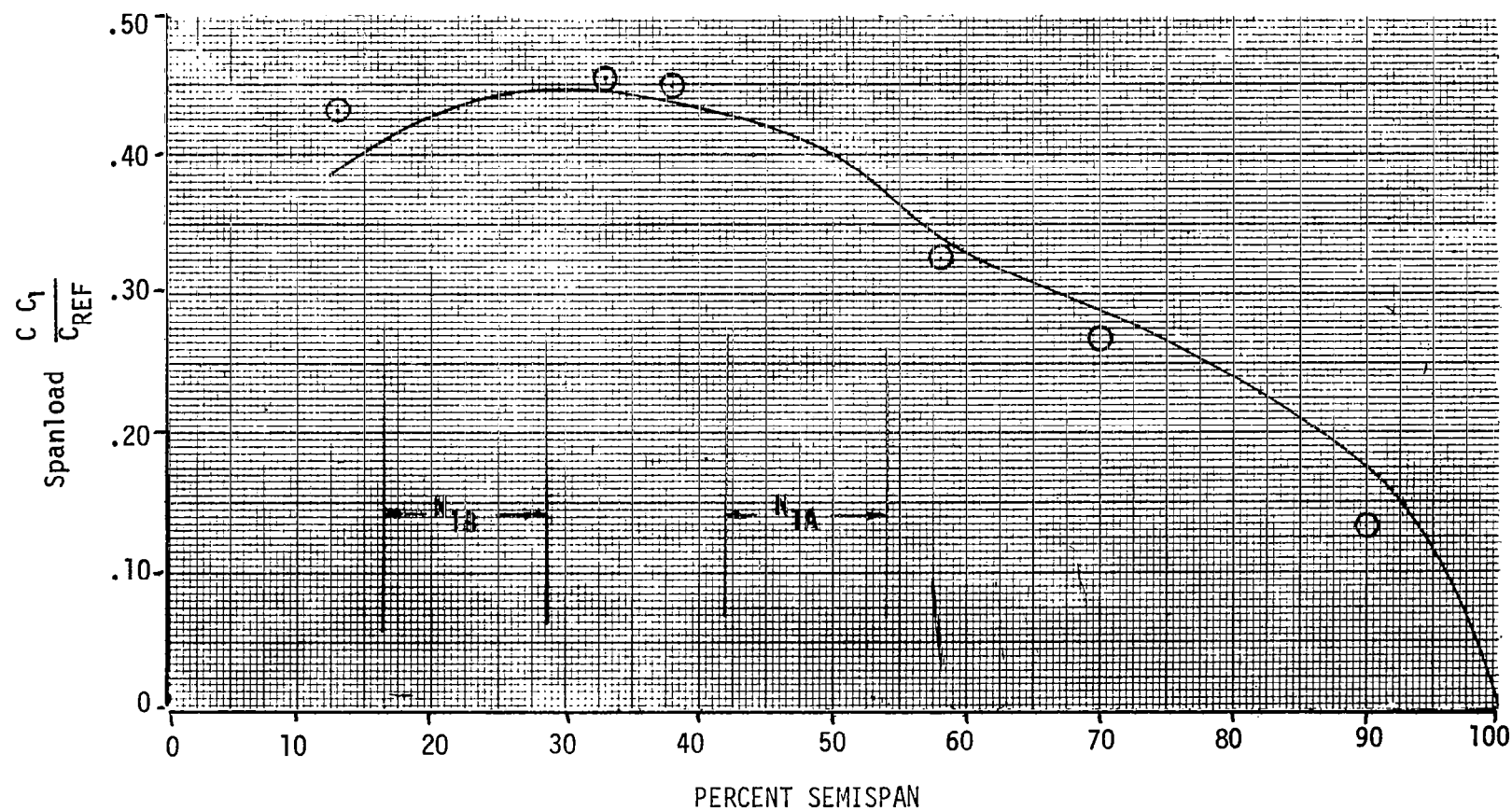
Figure 11.43.   Comparison of Theoretical Spanload with Test Data for $N_{1A} + N_{1B}$.

CONFIGURATION C_L = 0.4   FAN PRESSURE RATIO = 1.37

SYM	CONFIGURATION
□	N_{1B}
○	$N_{1A} + N_{1B}$

NACELLE INTERFERENCE DRAG ~ % WING-BODY DRAG
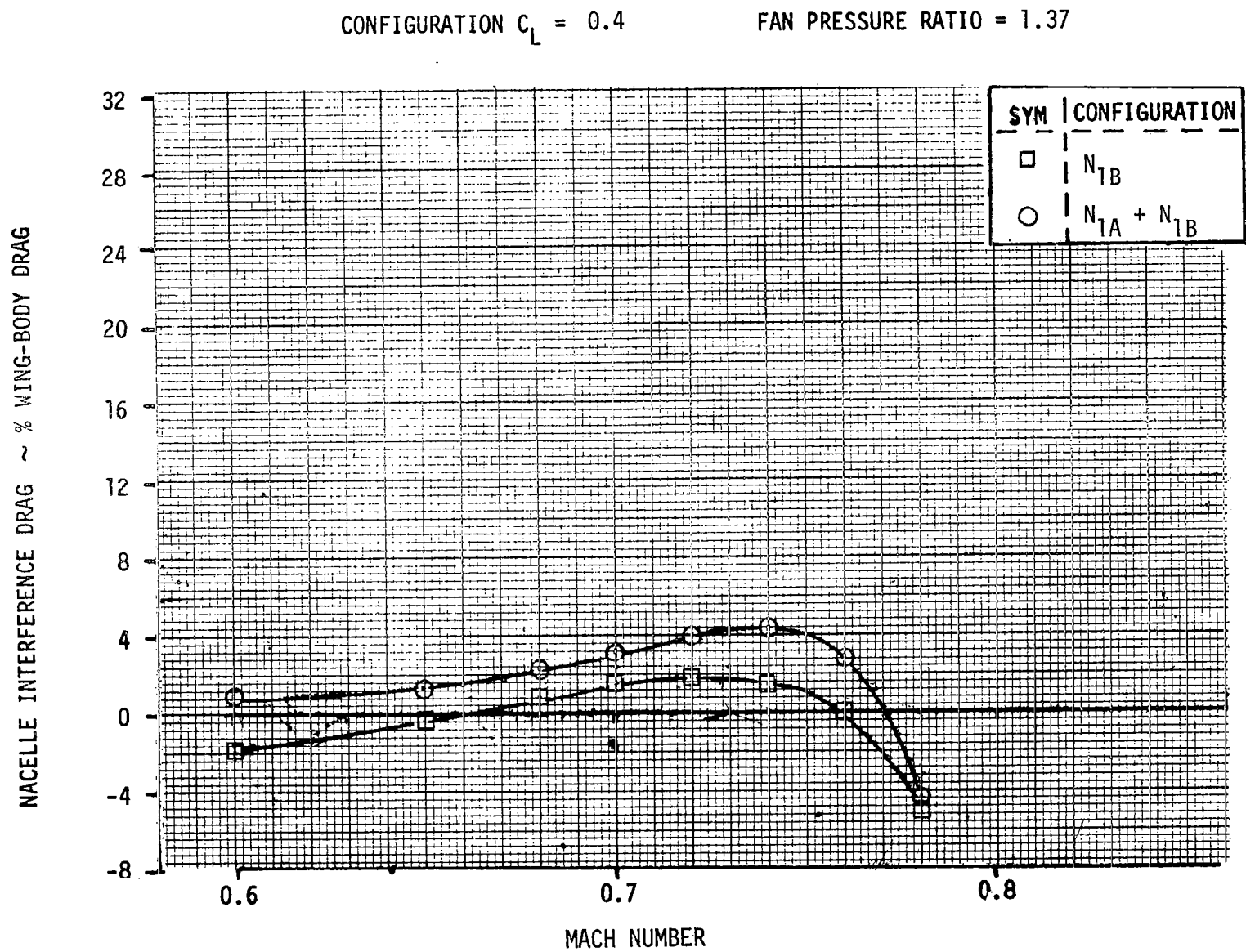
MACH NUMBER

Figure 11.44.   Variation of Nacelle Interference Drag with Mach Number for N_1 Twin Engine and Four-Engine Configurations.
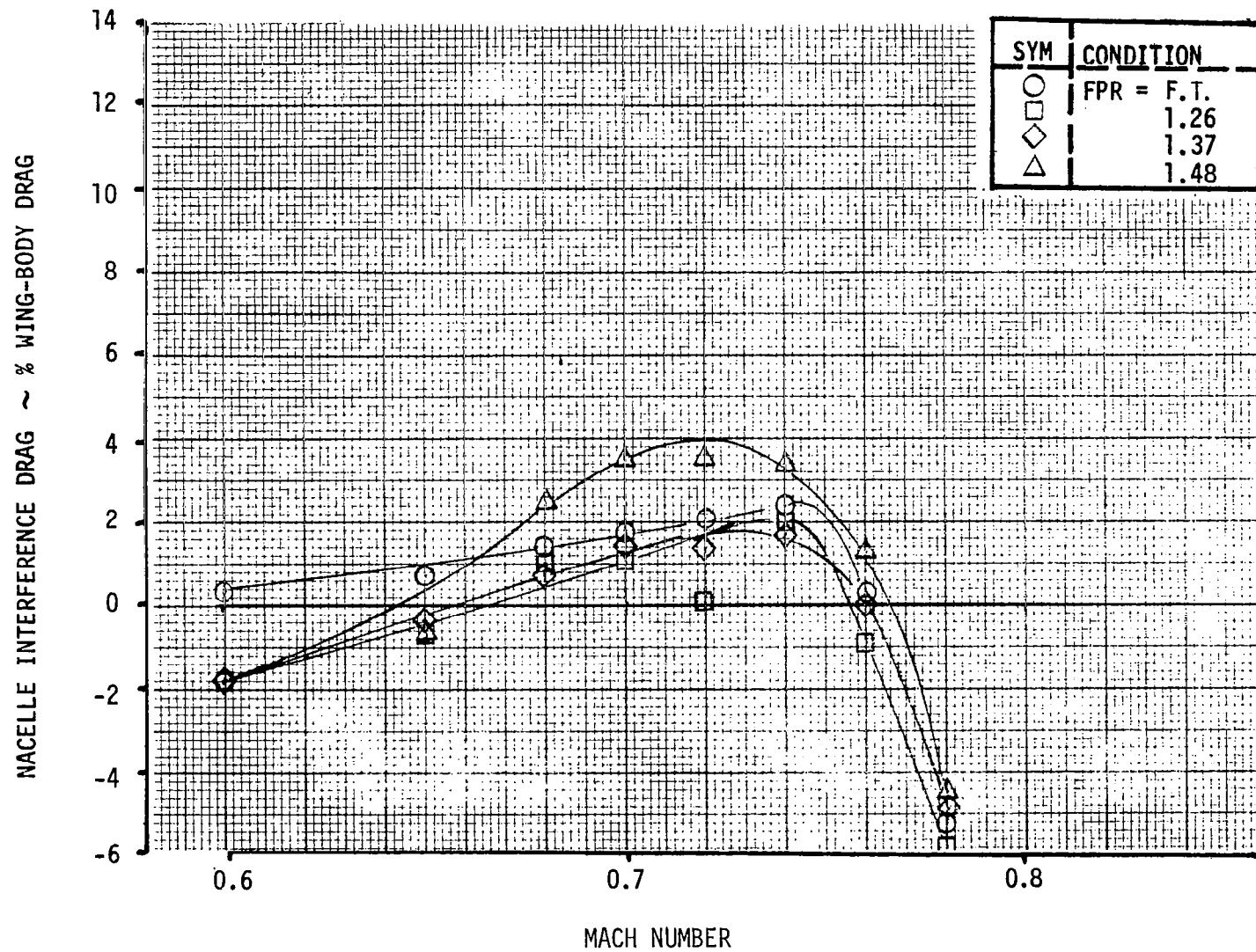
Figure 11.45. Variation of N_{1B} Nacelle Interference Drag with Fan Pressure Ratio.

CONFIGURATION $C_L = 0.4$ $N_{1A} + N_{1B}$ POWERED

SYM	CONDITION
X	FPR = F.T.
O	1.25
□	1.38
◇	1.46

NACELLE INTERFERENCE DRAG ~ % WING-BODY DRAG
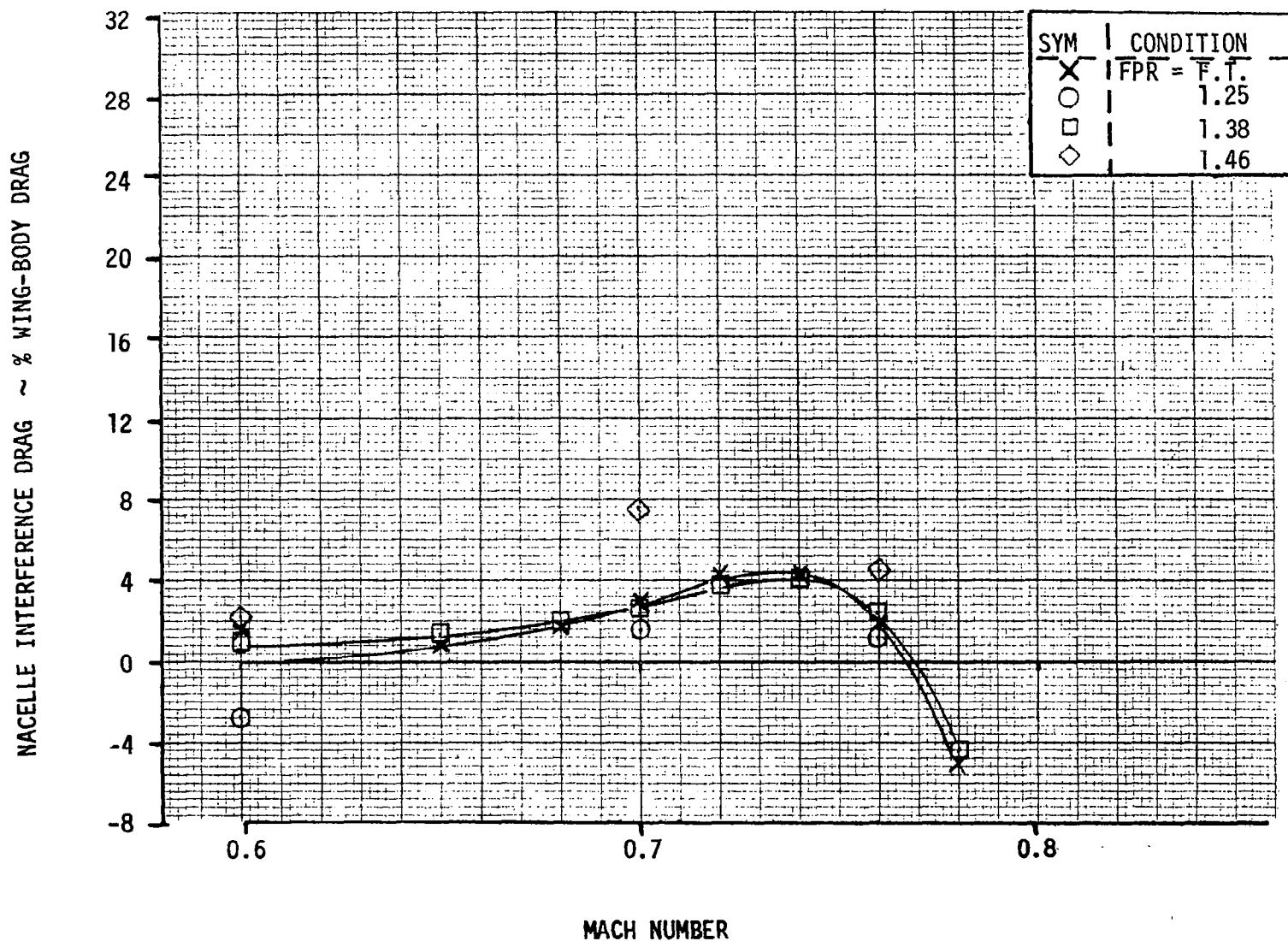
MACH NUMBER

Figure 11.46.   Variation of four engine N_1 Nacelle Interference Drag with Fan Pressure Ratio.

ALPHA = 0.5°

33 PERCENT SEMI-SPAN

MACH NUMBER = 0.7

PERCENT CHORD
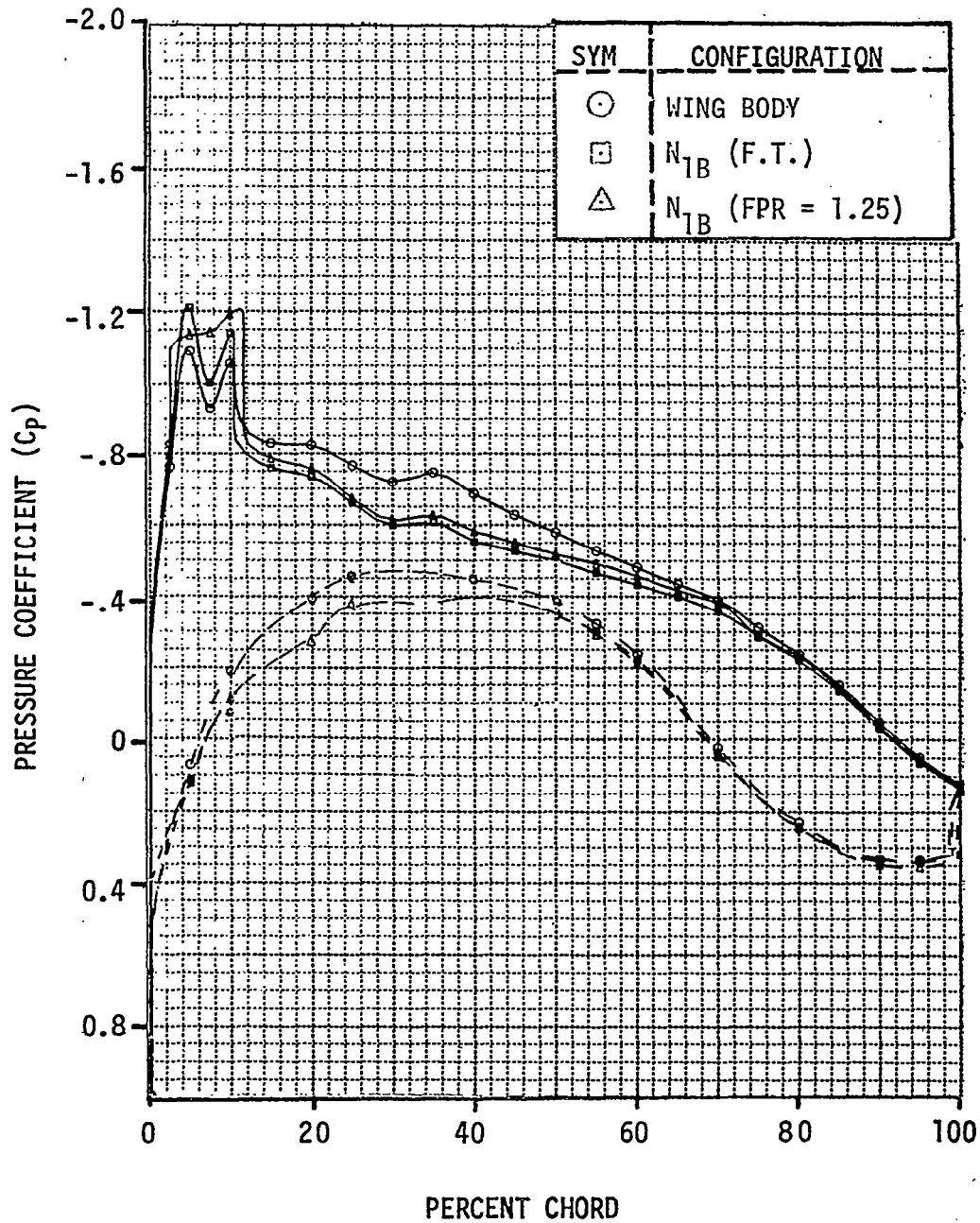
Figure 11.47.   Effect of Fan Pressure Ratio on the Wing Surface Pressures
at 33% Semi-Span for N_{1B} at FPR FT and 1.25 at M = 0.70.

ALPHA = 0.5°

33 PERCENT SEMI-SPAN

MACH NUMBER = 0.7

SYM	CONFIGURATION
⊙	WING + BODY
▢	N_{1B} (FPR = 1.37)
△	N_{1B} (FPR = 1.48)

PRESSURE COEFFICIENT (C_P)

PERCENT CHORD
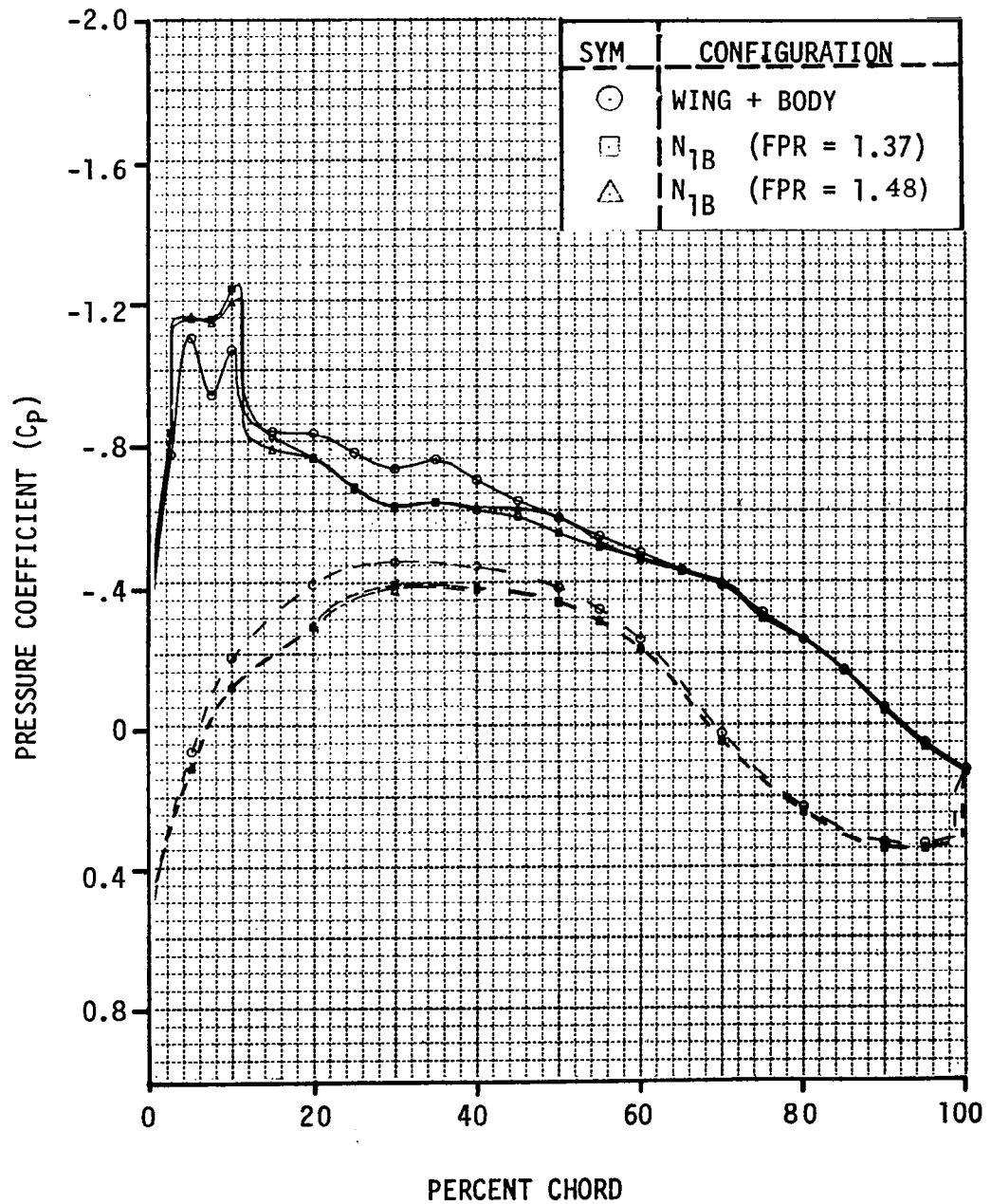
Figure 11.48. Effect of Fan Pressure Ratio on the Wing Surface Pressures at 33% Semispan for N_{1B} at FPR = 1.37 and 1.48 at M = 0.70.

ALPHA = 0.5°

33 PERCENT SEMI-SPAN

MACH NUMBER = 0.7

PERCENT CHORD
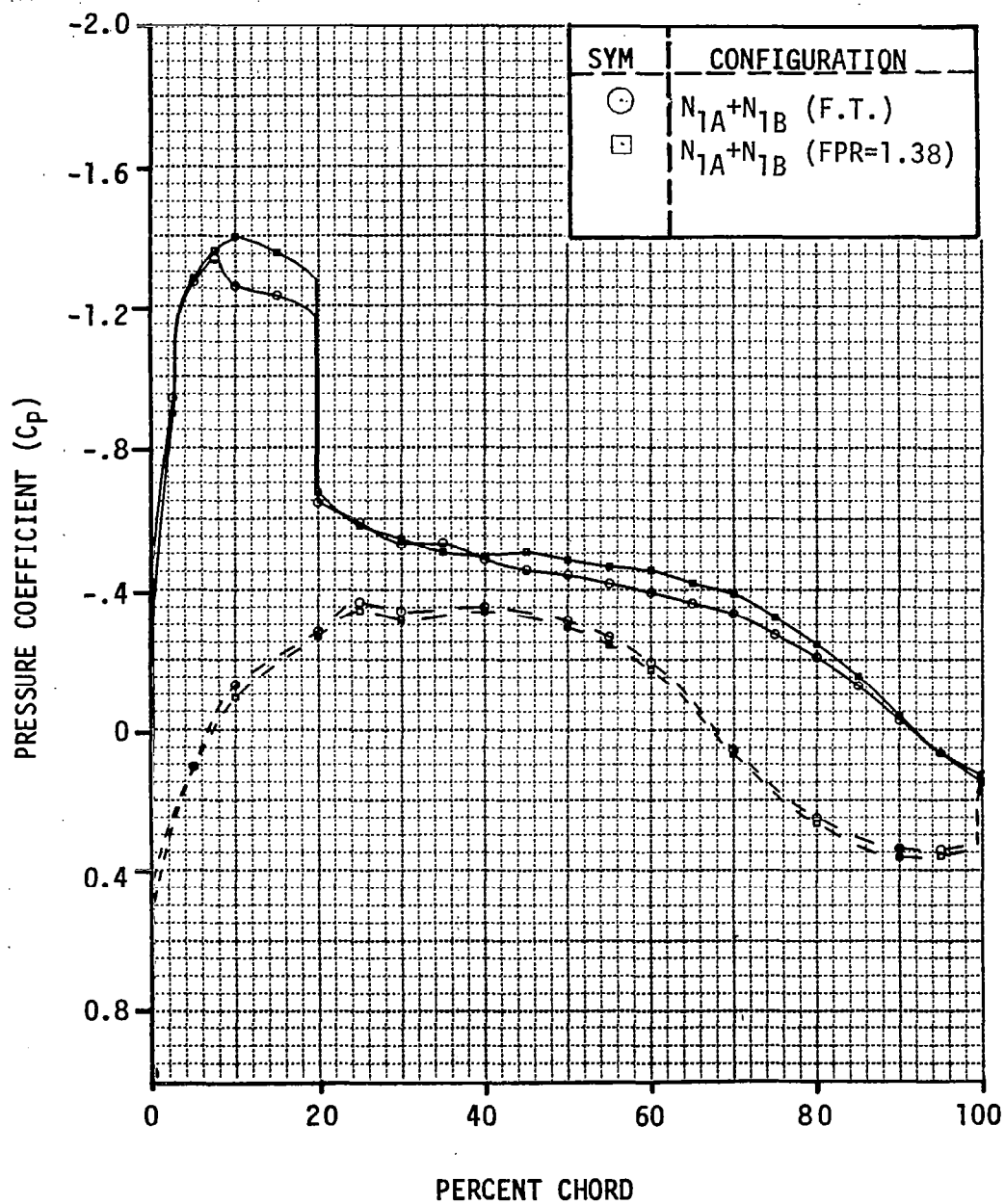
Figure 11.49. Effect of Fan Pressure Ratio on the Wing Surface Pressures at 33% Semispan for N_{1A} + N_{1B} at FPR of F.T. and 1.38 at M = 0.70.

ALPHA - 0.5°

23 PERCENT SEMI-SPAN
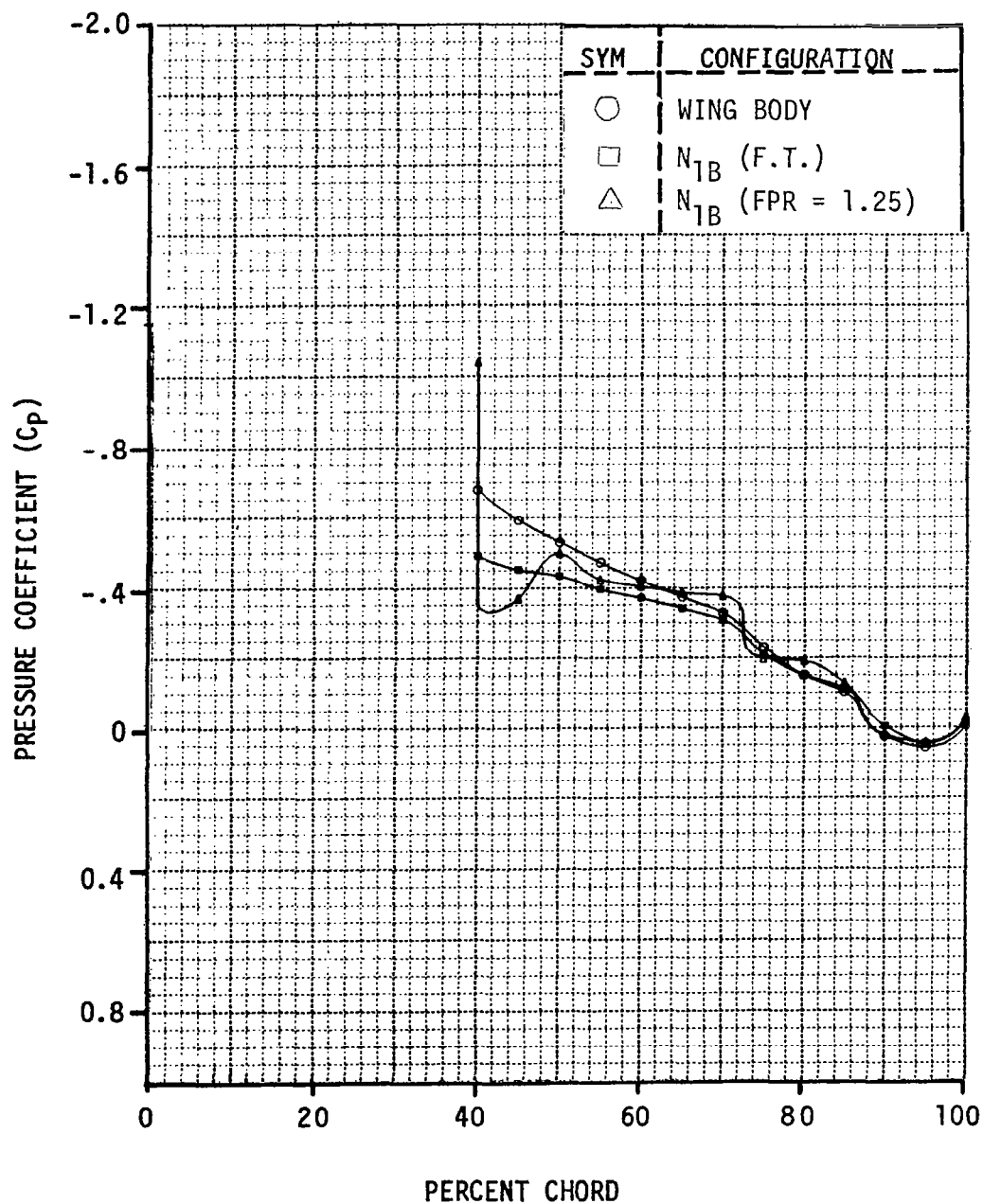
MACH NUMBER = 0.7

Figure 11.50.   Wing Surface Pressure in the Jet for the Wing-Body
and N_{1B} at FPR = F.T. and 1.25 at M = 0.70.

ALPHA = 0.5°

23 PERCENT SEMI-SPAN
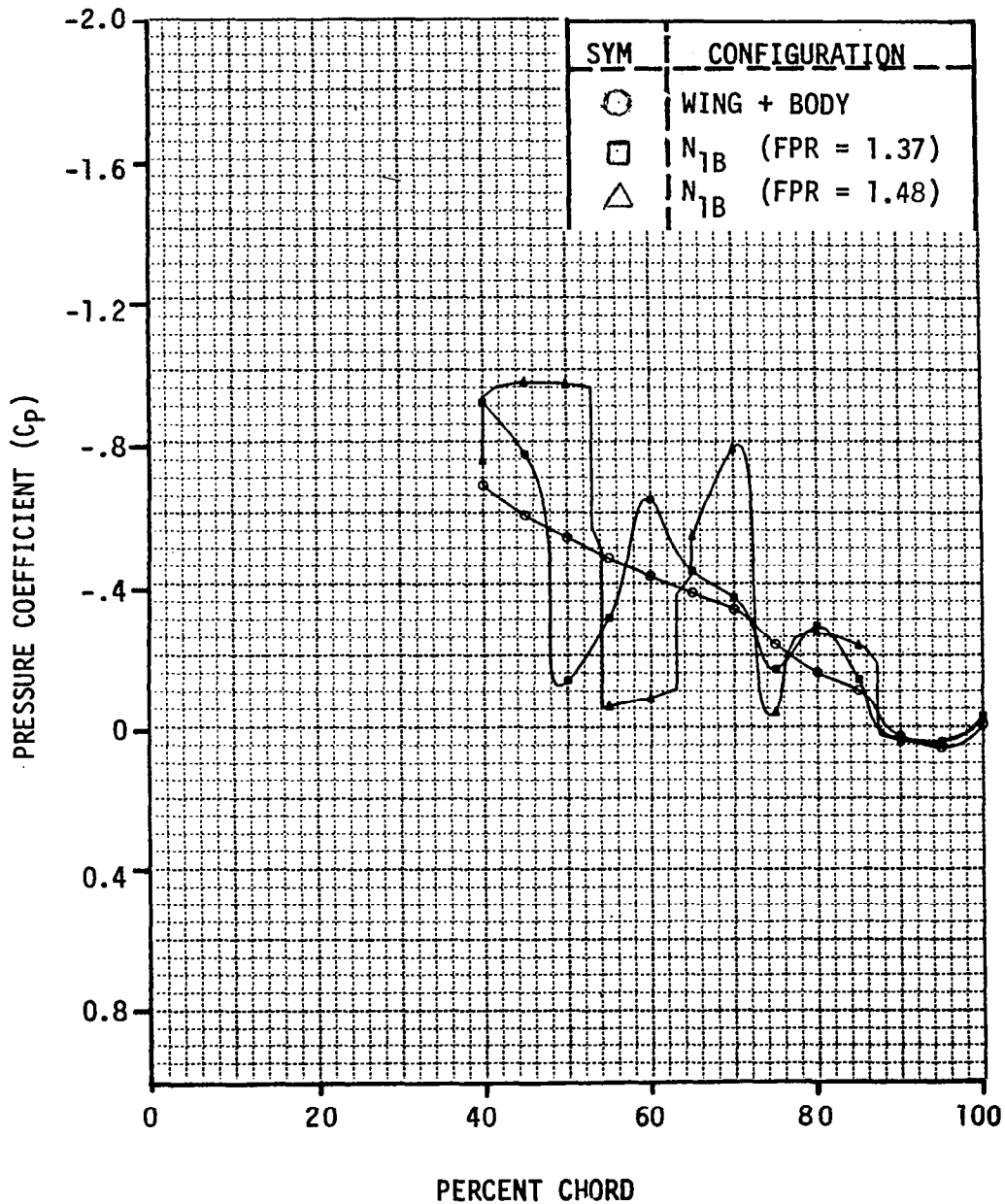
MACH NUMBER = 0.7

Figure 11.51.   Wing Surface Pressures in the Jet for the Wing-Body and N_{1B} at FPR = 1.37 and 1.48 and M = 0.70

ALPHA = 0.5°

33 PERCENT SEMI-SPAN
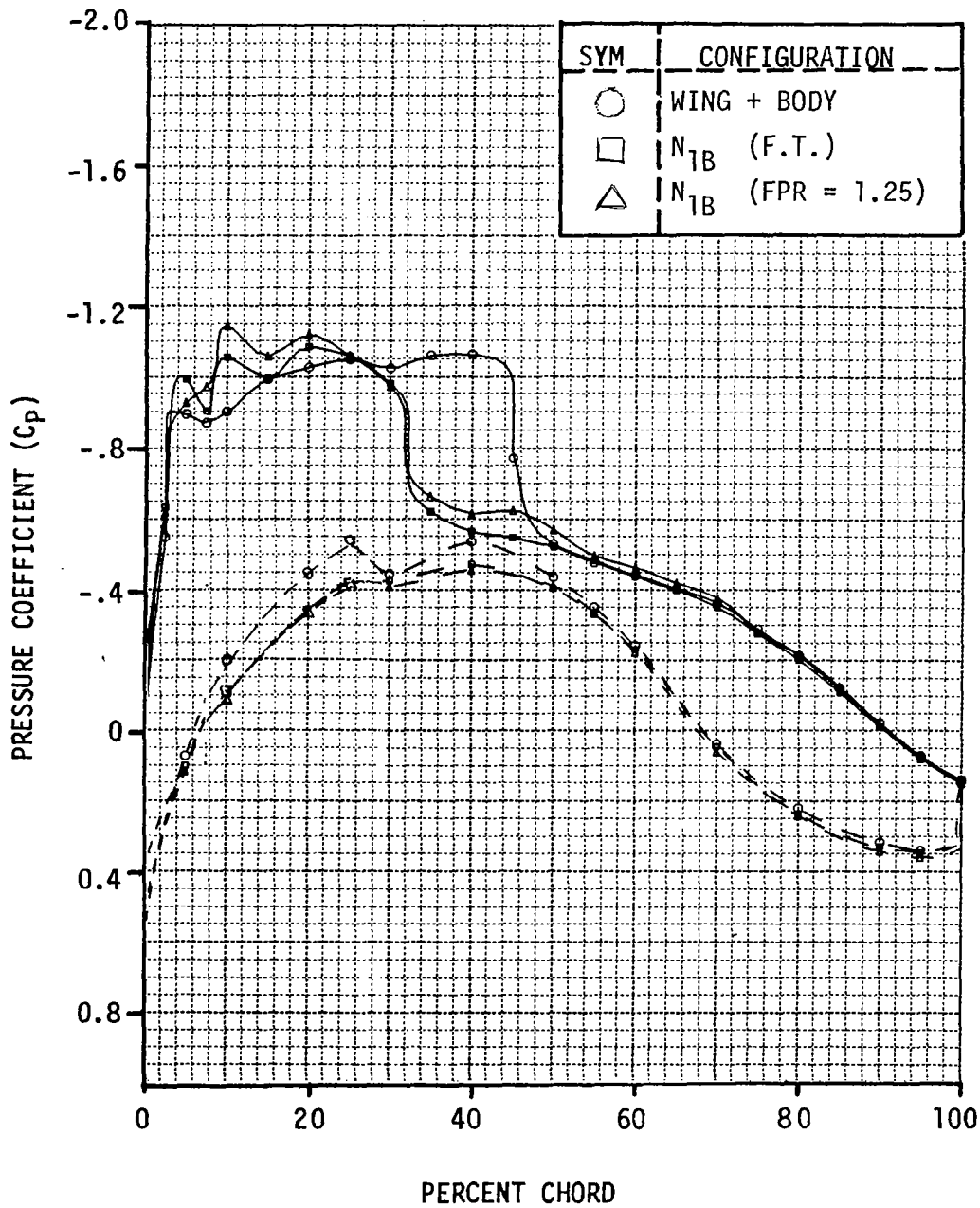
MACH NUMBER = 0.76

Figure 11.52. Effect of Fan Pressure Ratio on the Wing Surface Pressures at 33% Semispan for N_{1B} at FPR = F.T. and 1.25 and M = 0.76

ALPHA = 0.5°

33 PERCENT SEMI-SPAN
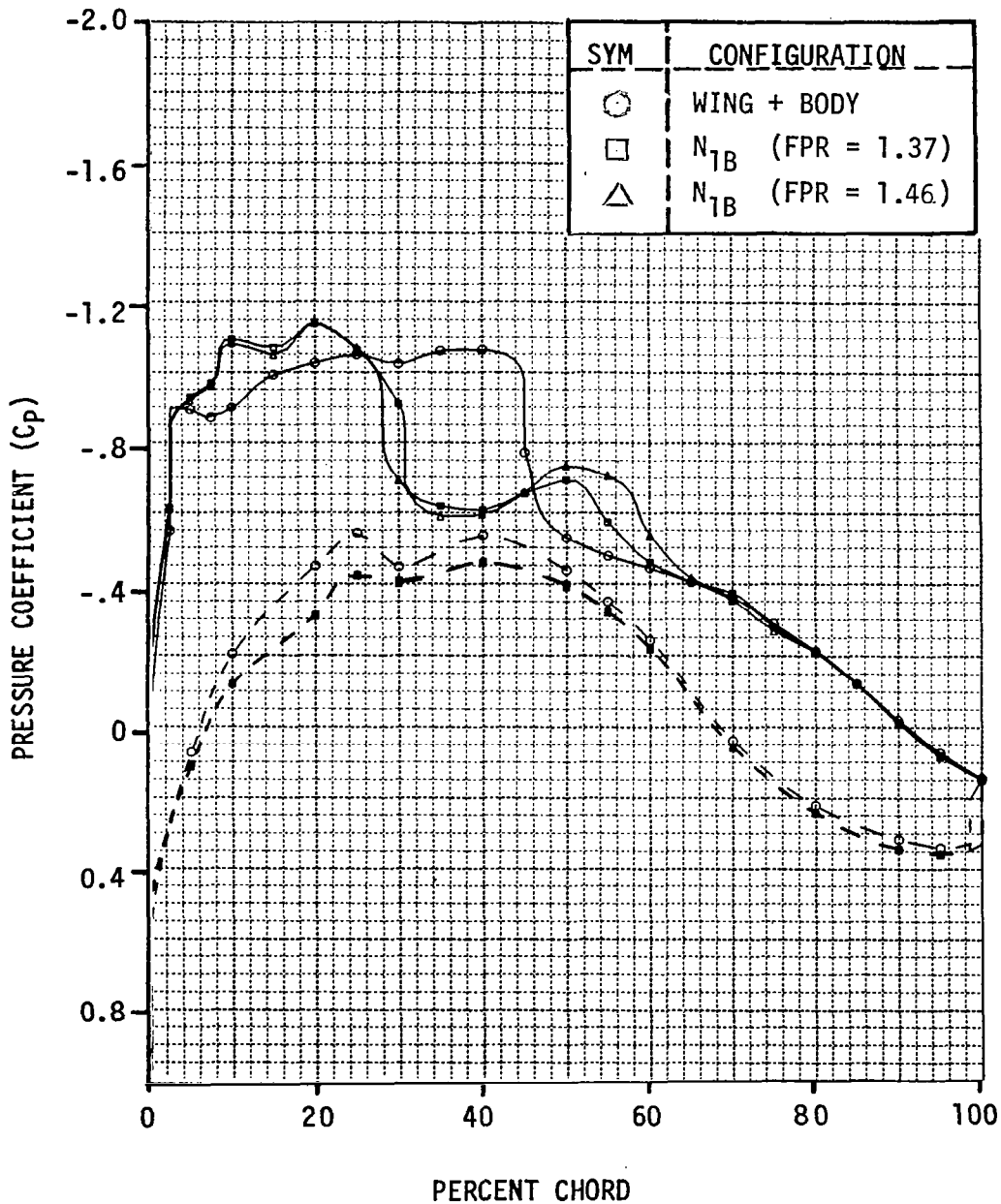
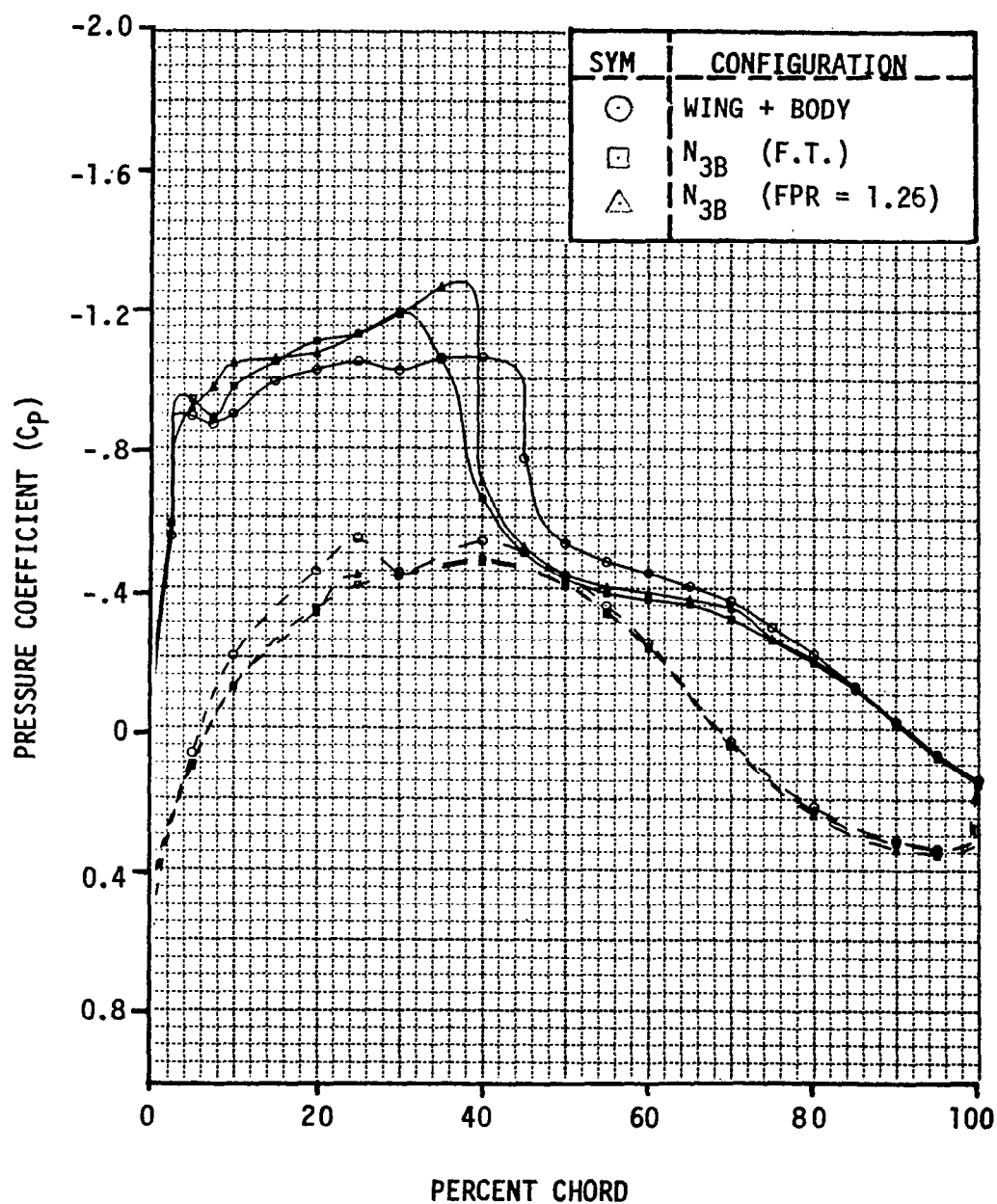MACH NUMBER = 0.76

Figure 11.53. Effect of Fan Pressure Ratio on the Wing Surface Pressures at 33% Semispan for N_{1B} at FPR = 1.37 and 1.46 and M = 0.76

ALPHA = 0.5°

23 PERCENT SEMI-SPAN

MACH NUMBER = 0.76

SYM	CONFIGURATION
⊙	WING + BODY
▢	N_{1B} (F.T.)
△	N_{1B} (FPR = 1.25)
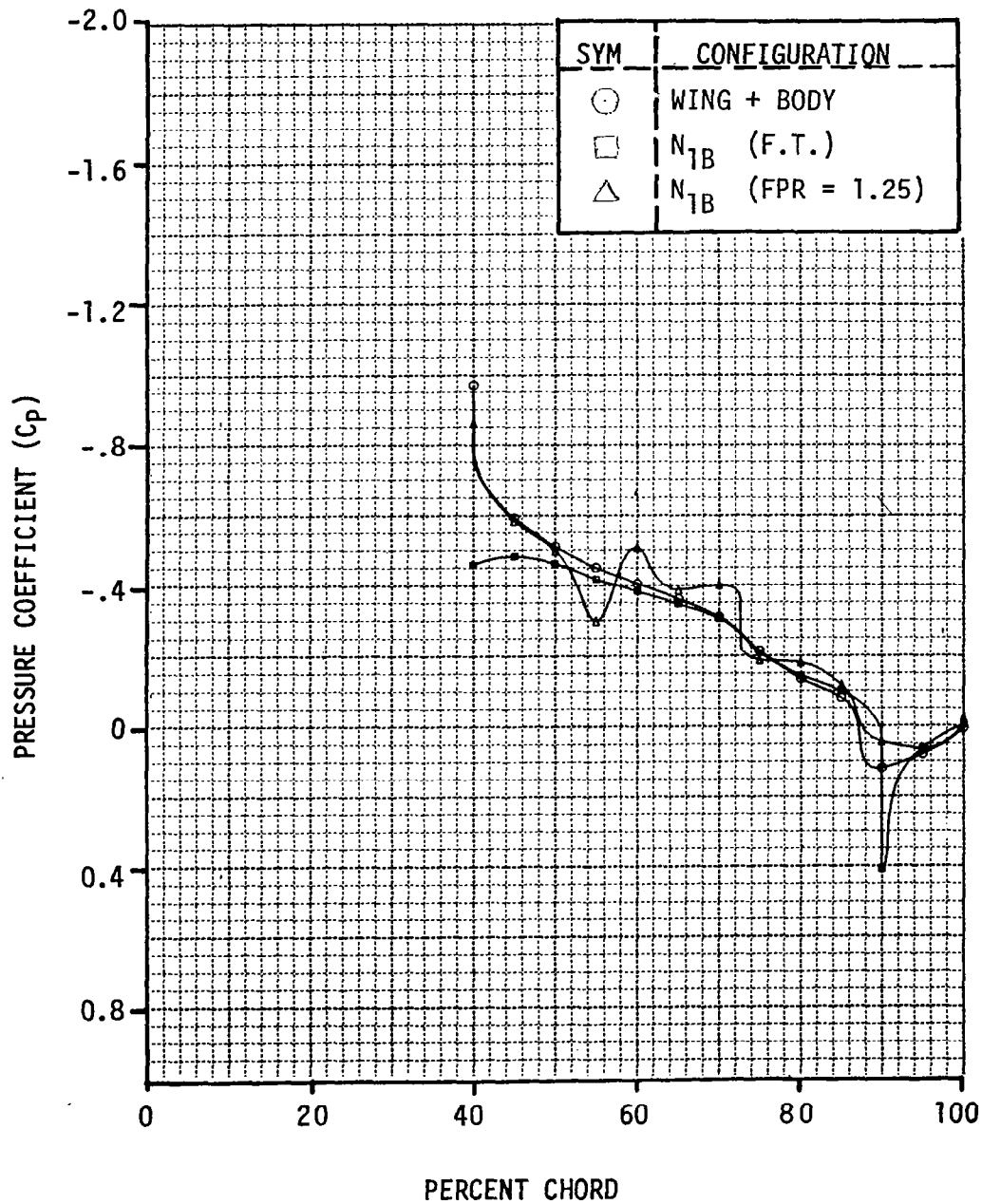
Figure 11.54.   Wing Surface Pressures in the Jet for the Wing-Body and N_{1B} at FPR of F.T. and 1.25 and M = 0.76

158

ALPHA = 0.5°

23 PERCENT SEMI-SPAN

MACH NUMBER = 0.76

SYM	CONFIGURATION
⊙	WING + BODY
⊡	N_{1B} (FPR = 1.37)
△	N_{1B} (FPR = 1.46)

PRESSURE COEFFICIENT (C_P)

PERCENT CHORD
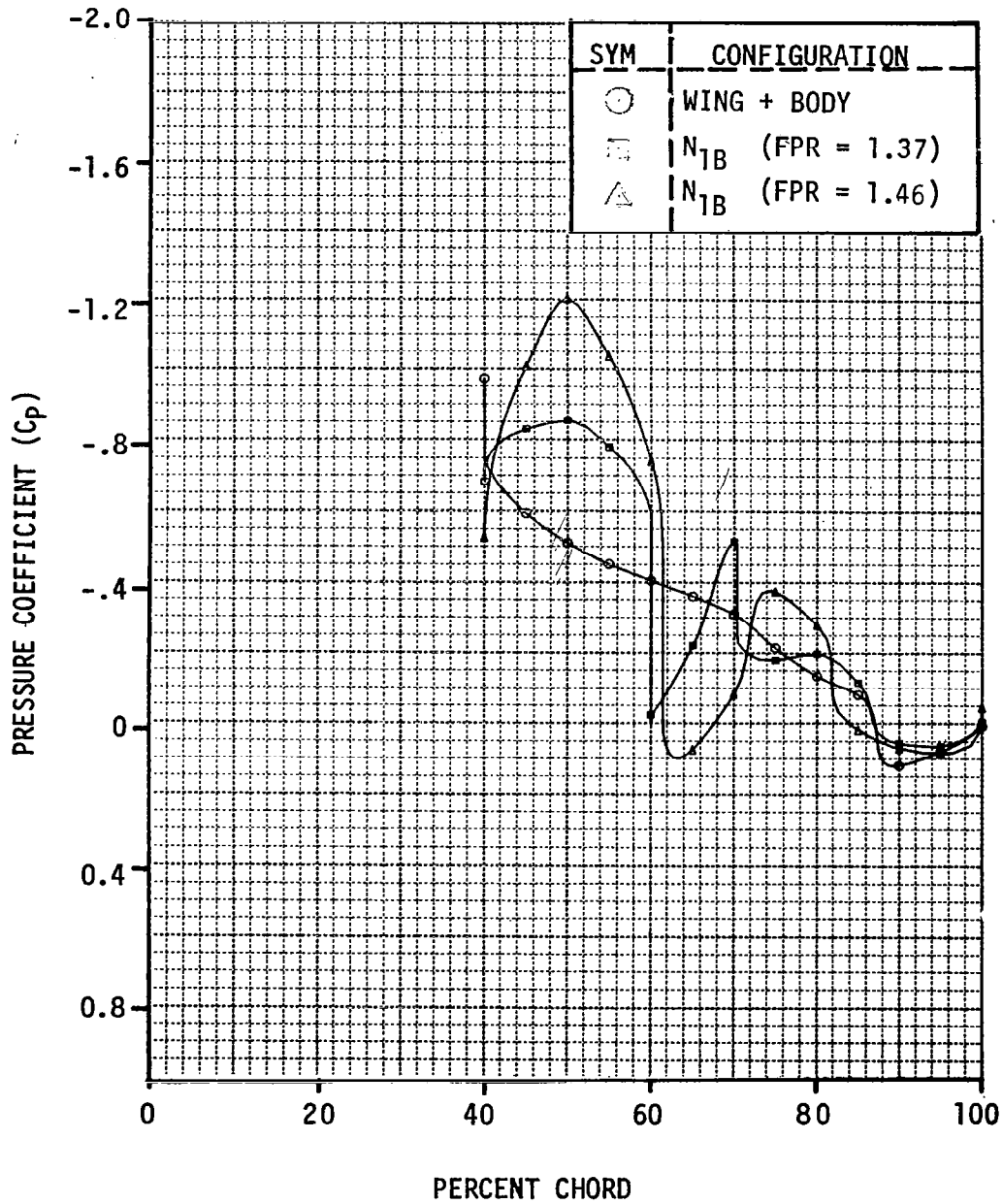
Figure 11.55. Wing Surface Pressures in the Jet for the Wing-Body and N_{1B} at FPR of 1.38 and 1.46 and M = 0.76
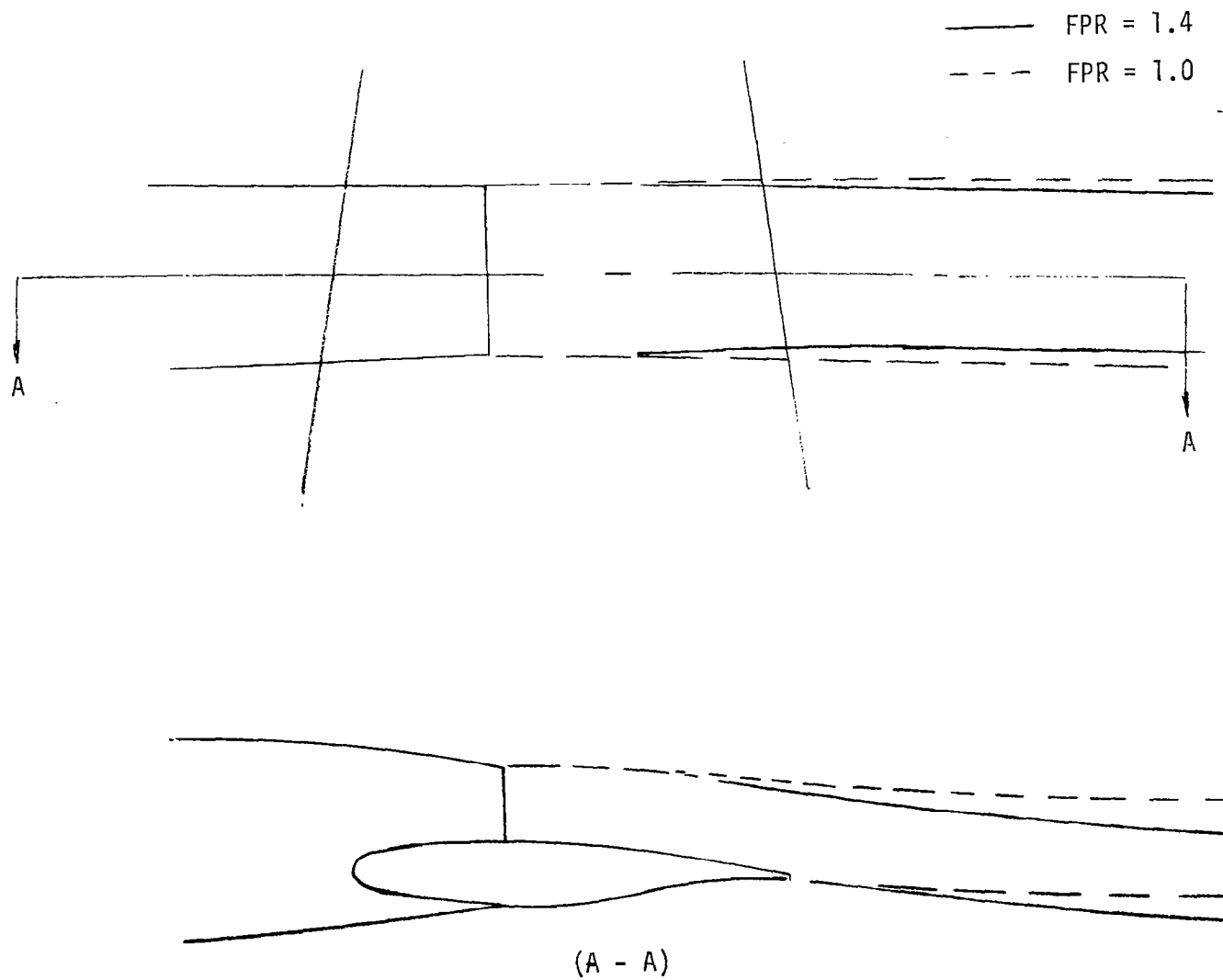
Figure 11.56. Jet Shapes Used in the Neumann Solution to Predict the Effects of Power.
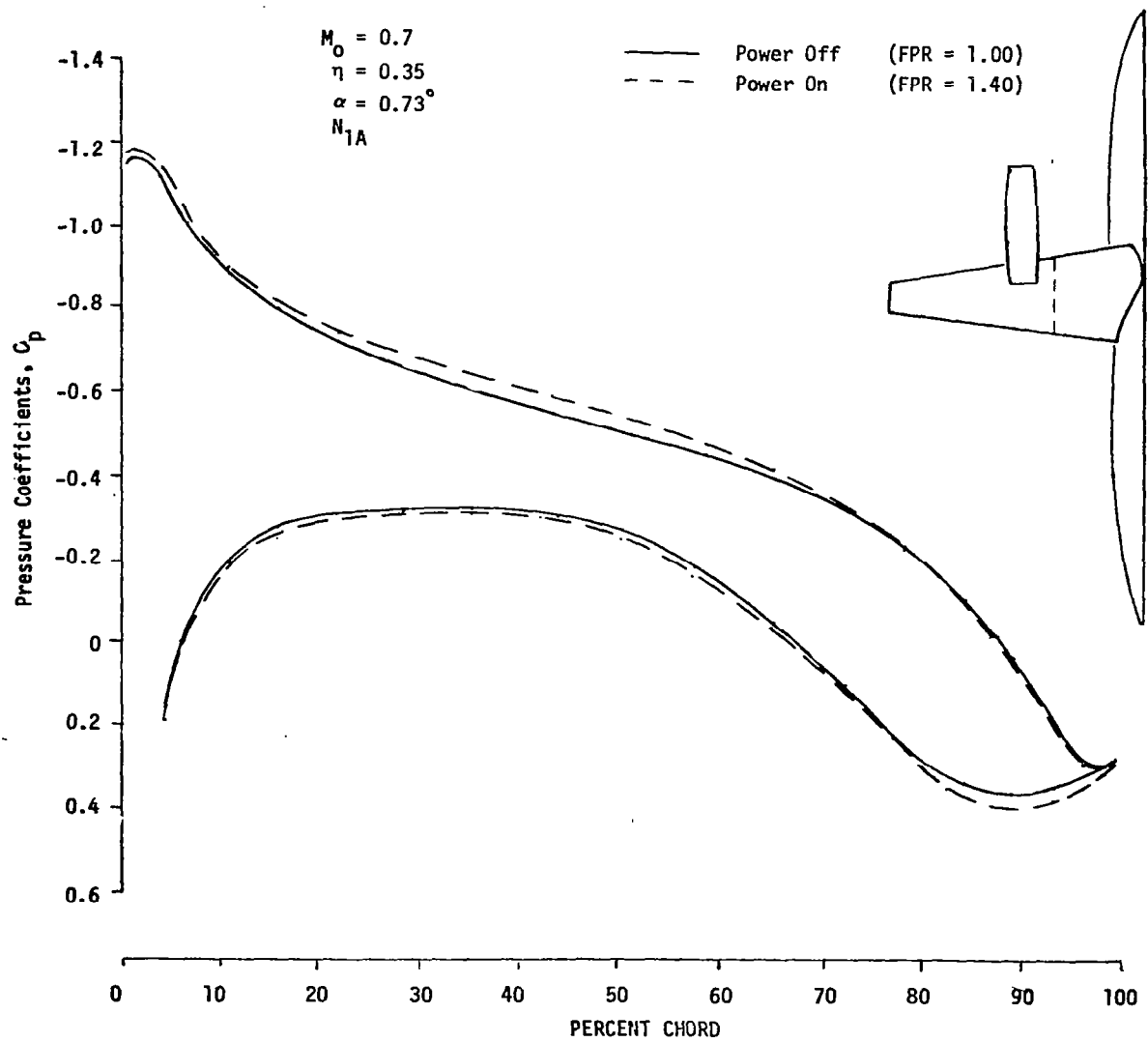
Figure 11.57. Theoretically Predicted Increment in Wing Surface Pressures Due to Power
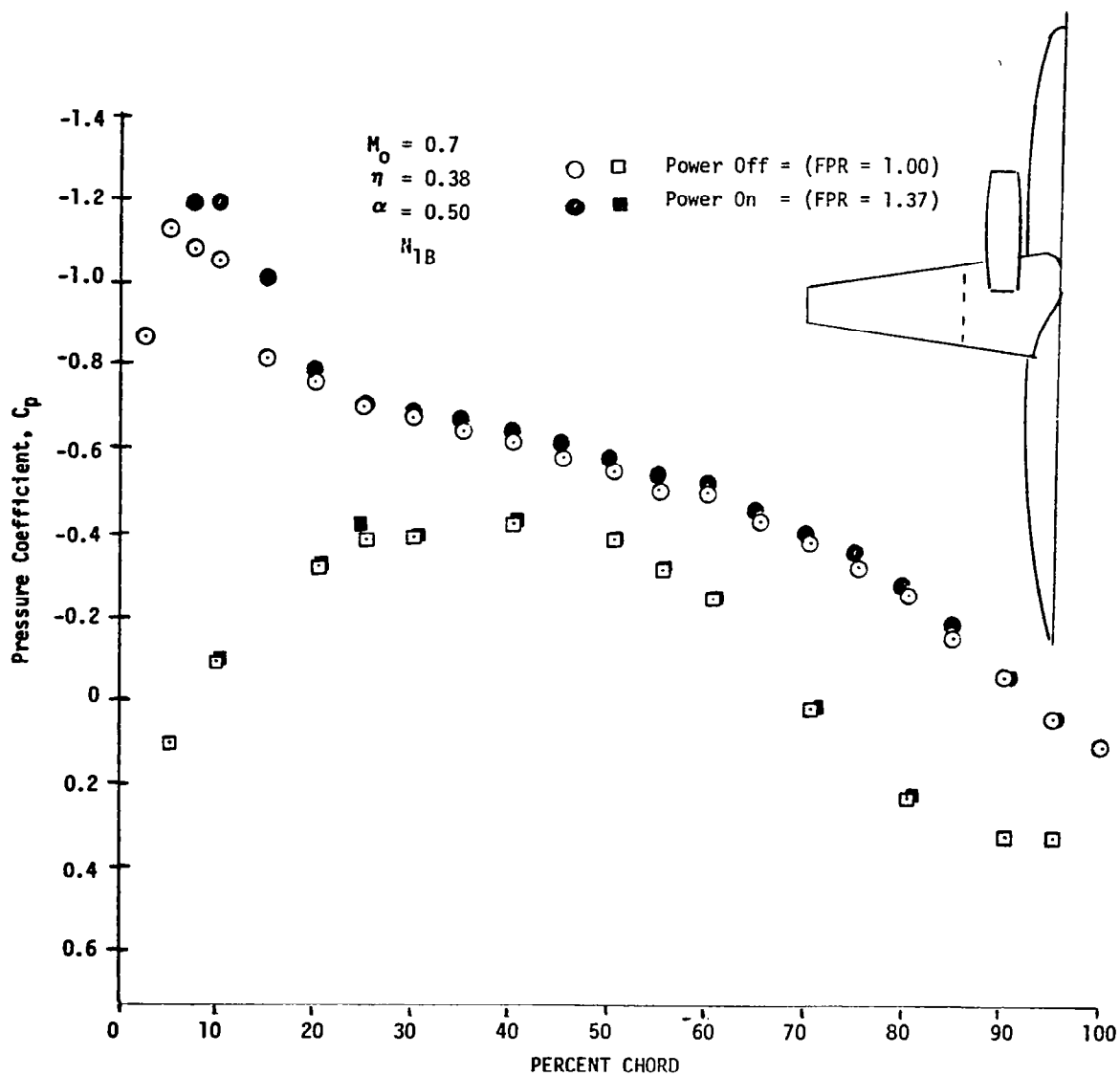
Figure 11.58. Effect of Power on Wing Pressure Distribution for N_{1B}

NACELLE INTERFERENCE DRAG ~ % WING-BODY DRAG

MACH NUMBER
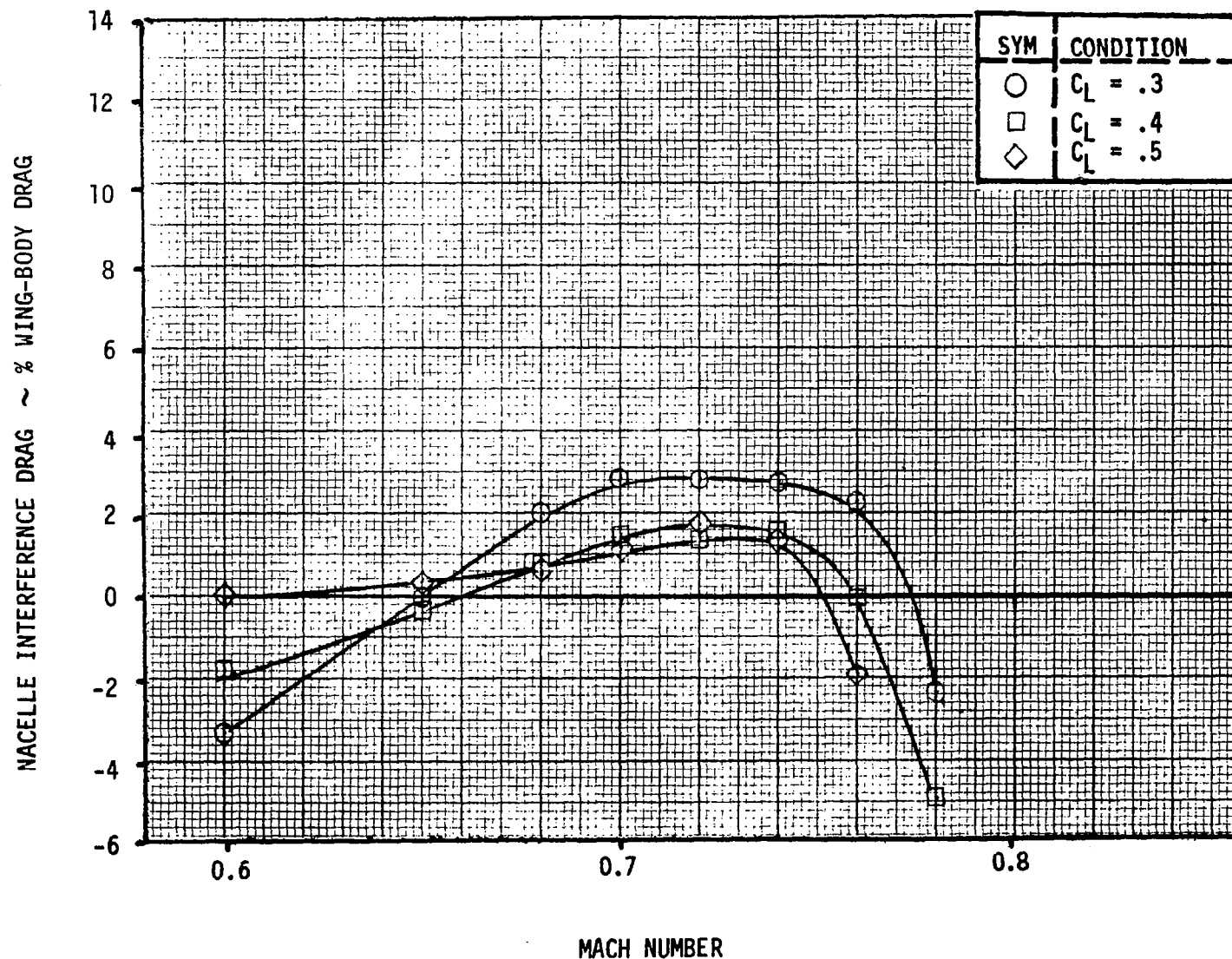
Figure 11.59. Variation of N$_{1B}$ Nacelle Interference Drag with C$_L$.

$N_{1A} + N_{1B}$

FAN PRESSURE RATIO = 1.37

SYM	CONDITION
○	$C_L = .3$
□	$C_L = .4$
◇	$C_L = .5$

NACELLE INTERFERENCE DRAG ~ % WING-BODY DRAG

MACH NUMBER
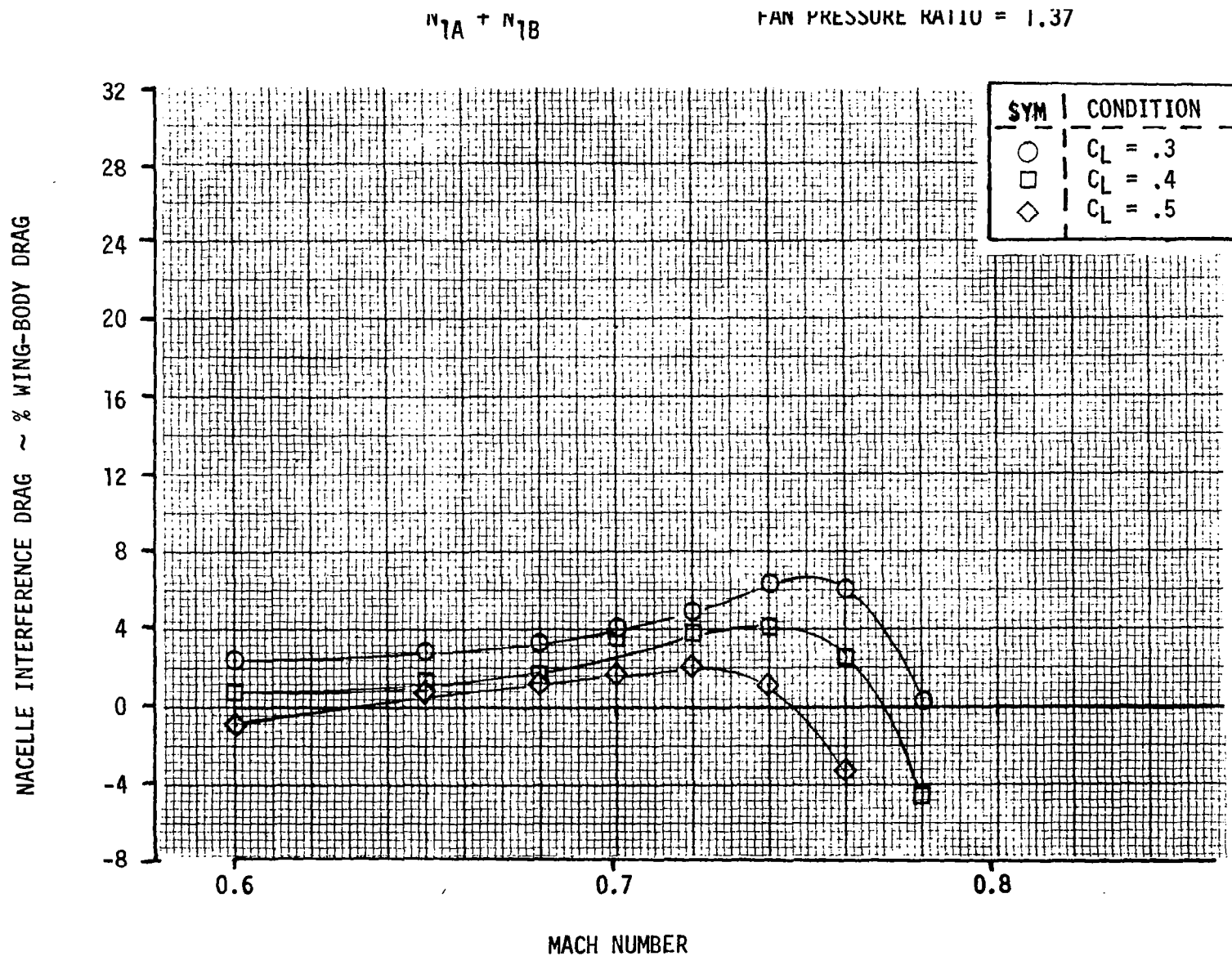
Figure 11.60. Variation of Four Engine $N_{1A} + N_{1B}$ Interference Drag with C_L.
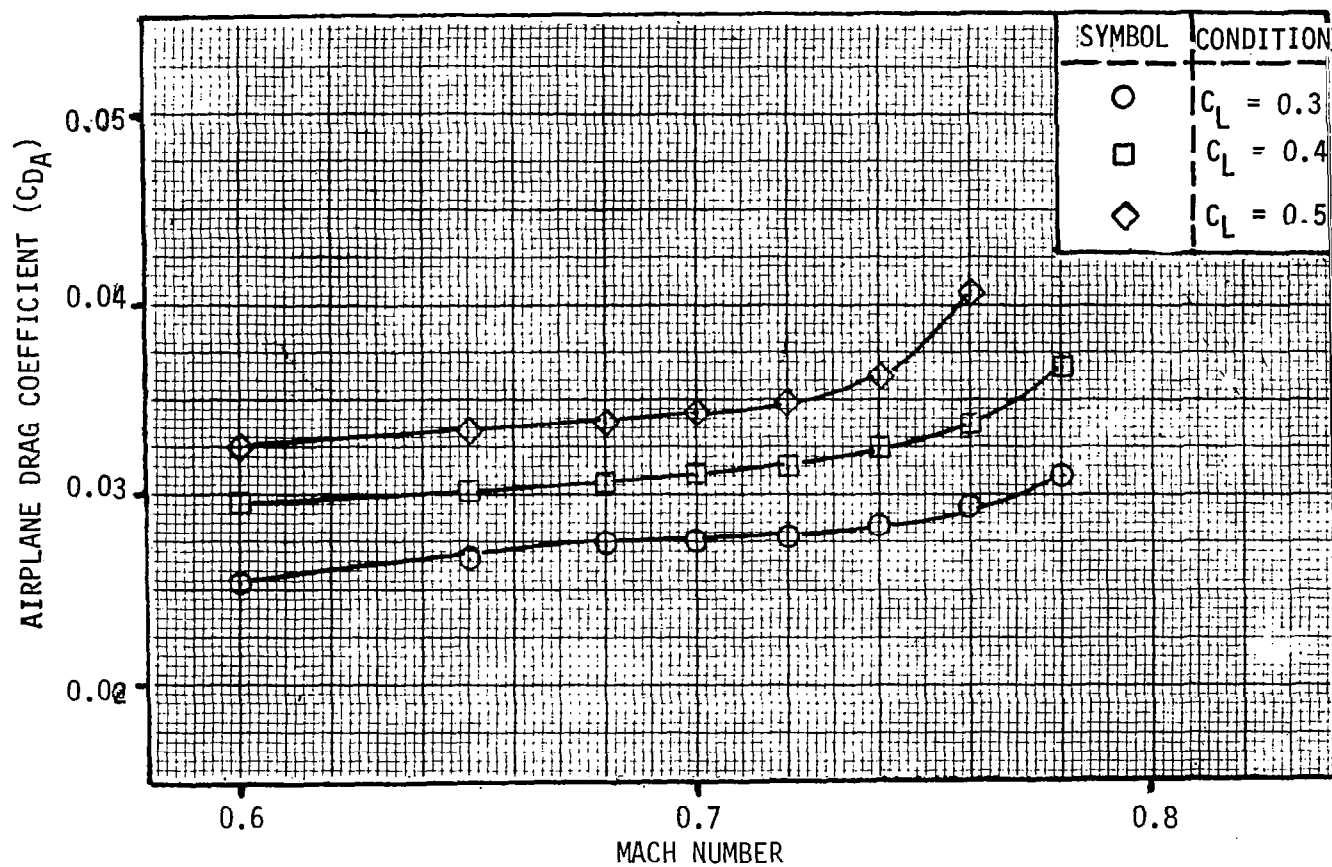
Figure 11.61. Wing-Body and Nacelle Drag, N_{1B} Inboard Nacelle, Powered (FPR = 1.37).
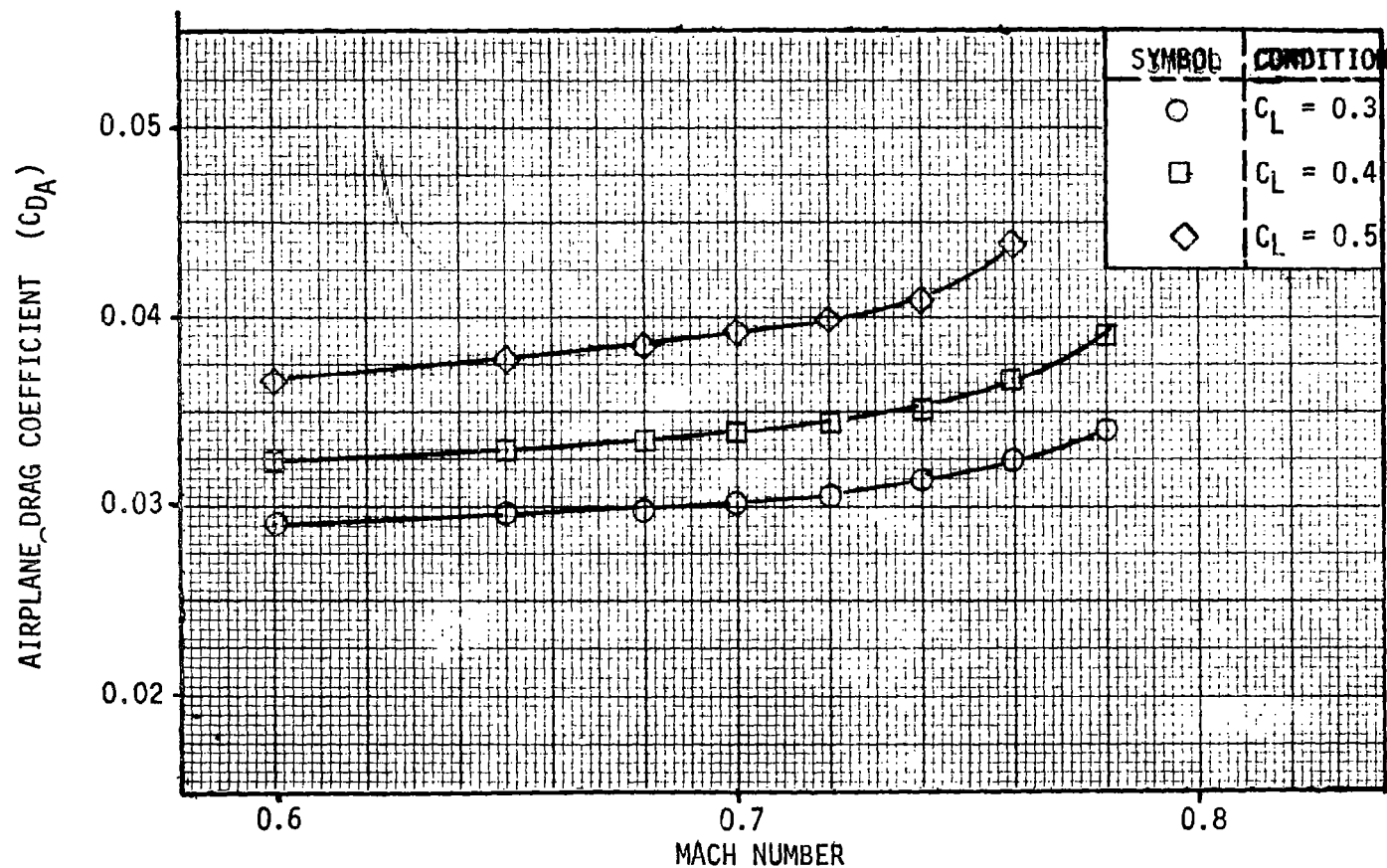
Figure 11.62. Wing-Body and Nacelle Drag, Four Engine N_1 Nacelle, Powered (FPR = 1.37).
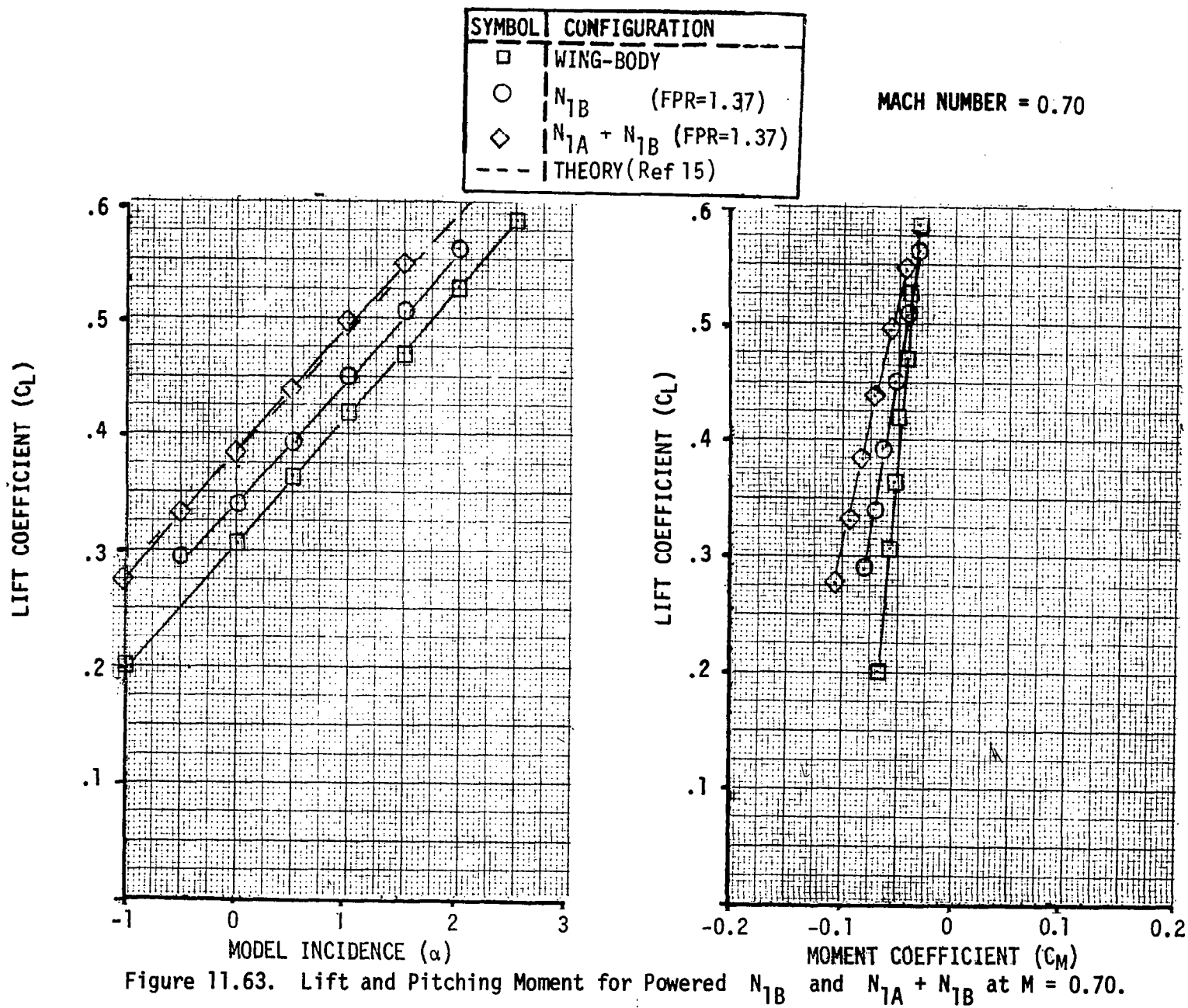
Figure 11.63. Lift and Pitching Moment for Powered N_{1B} and $N_{1A} + N_{1B}$ at M = 0.70.
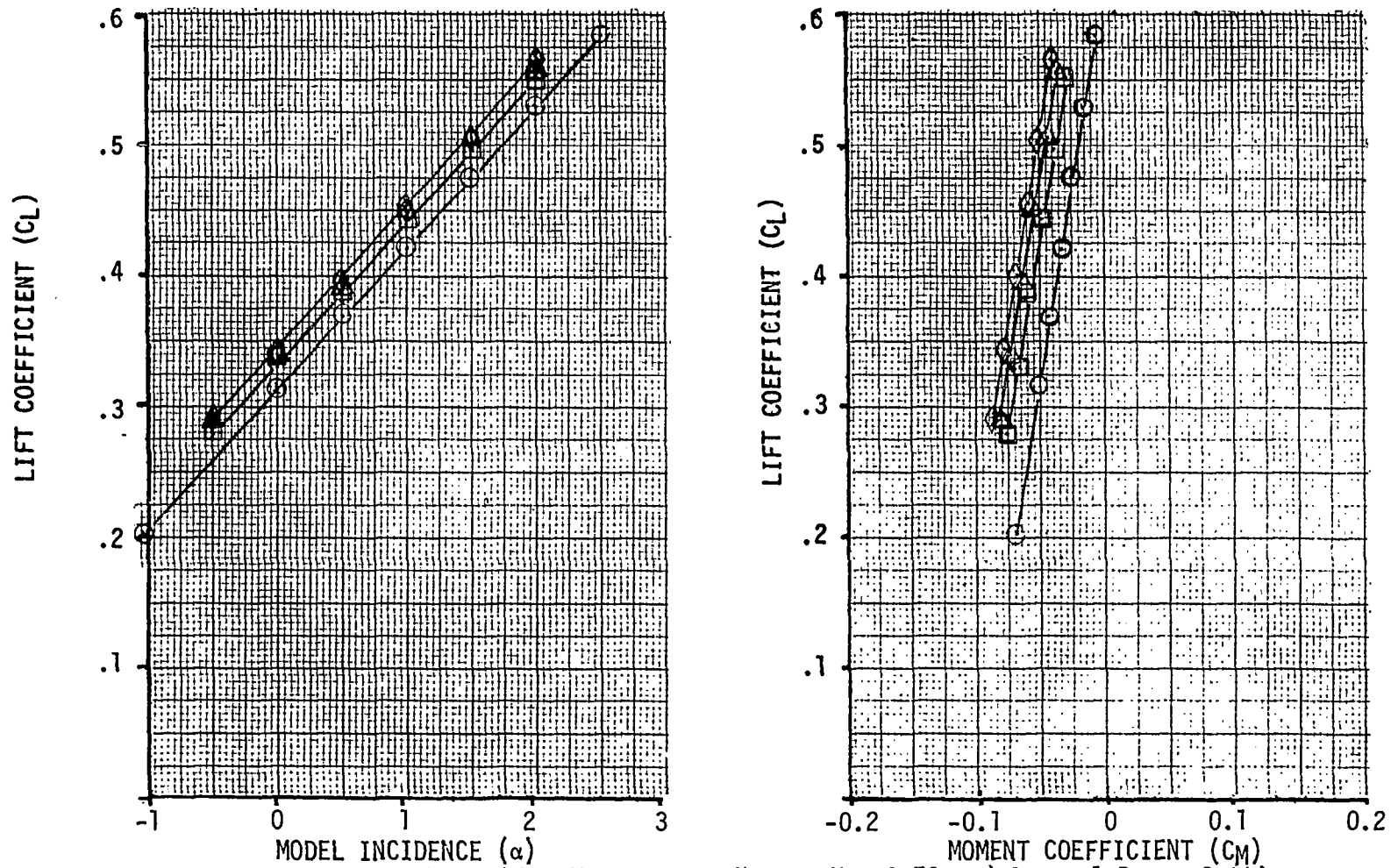
Figure 11.64.   Lift and Pitching Moment for N_{1B} at M = 0.70 and Several Power Settings.
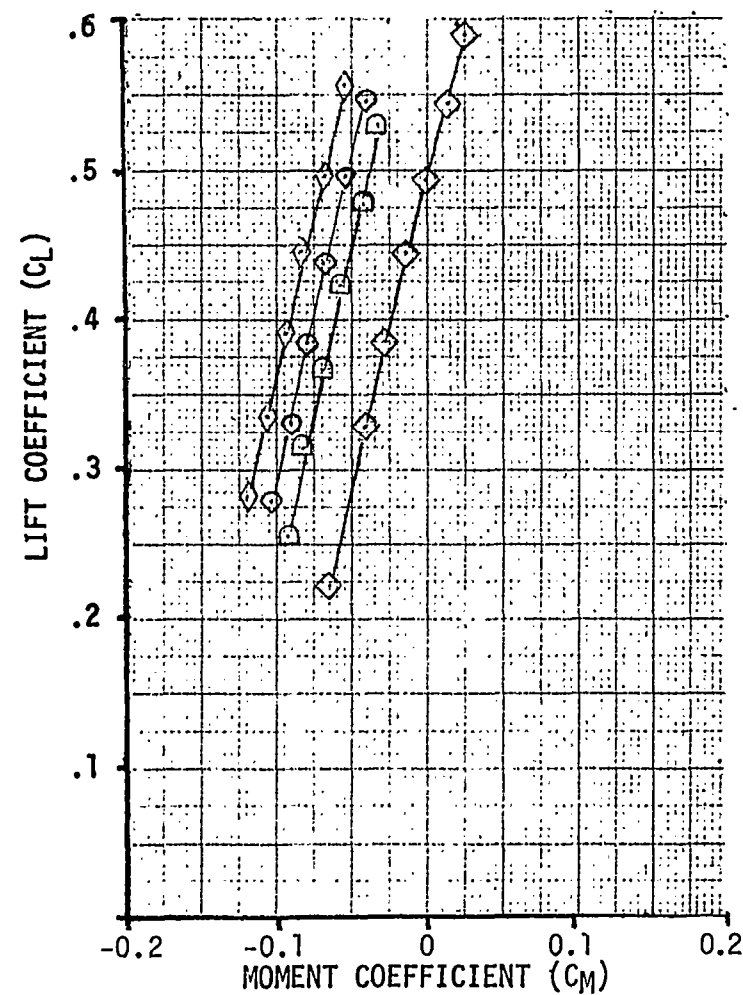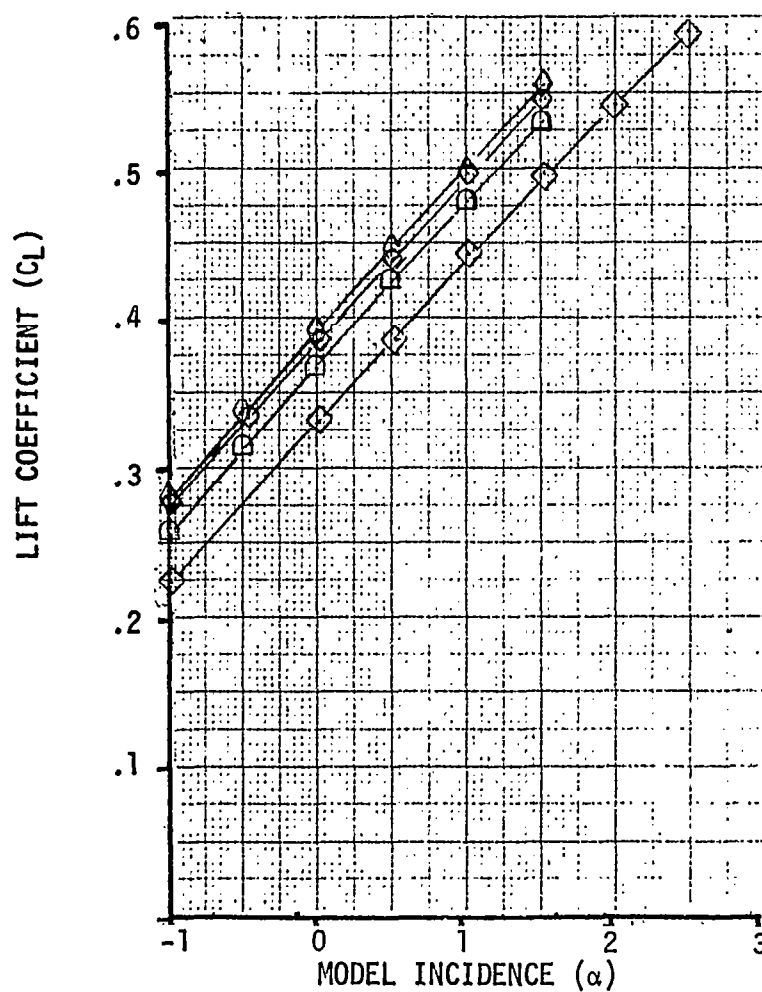
Figure 11.65. Lift and Pitching Moment for $N_{1A} + N_{1B}$ at M = 0.70 and Several Power Settings.
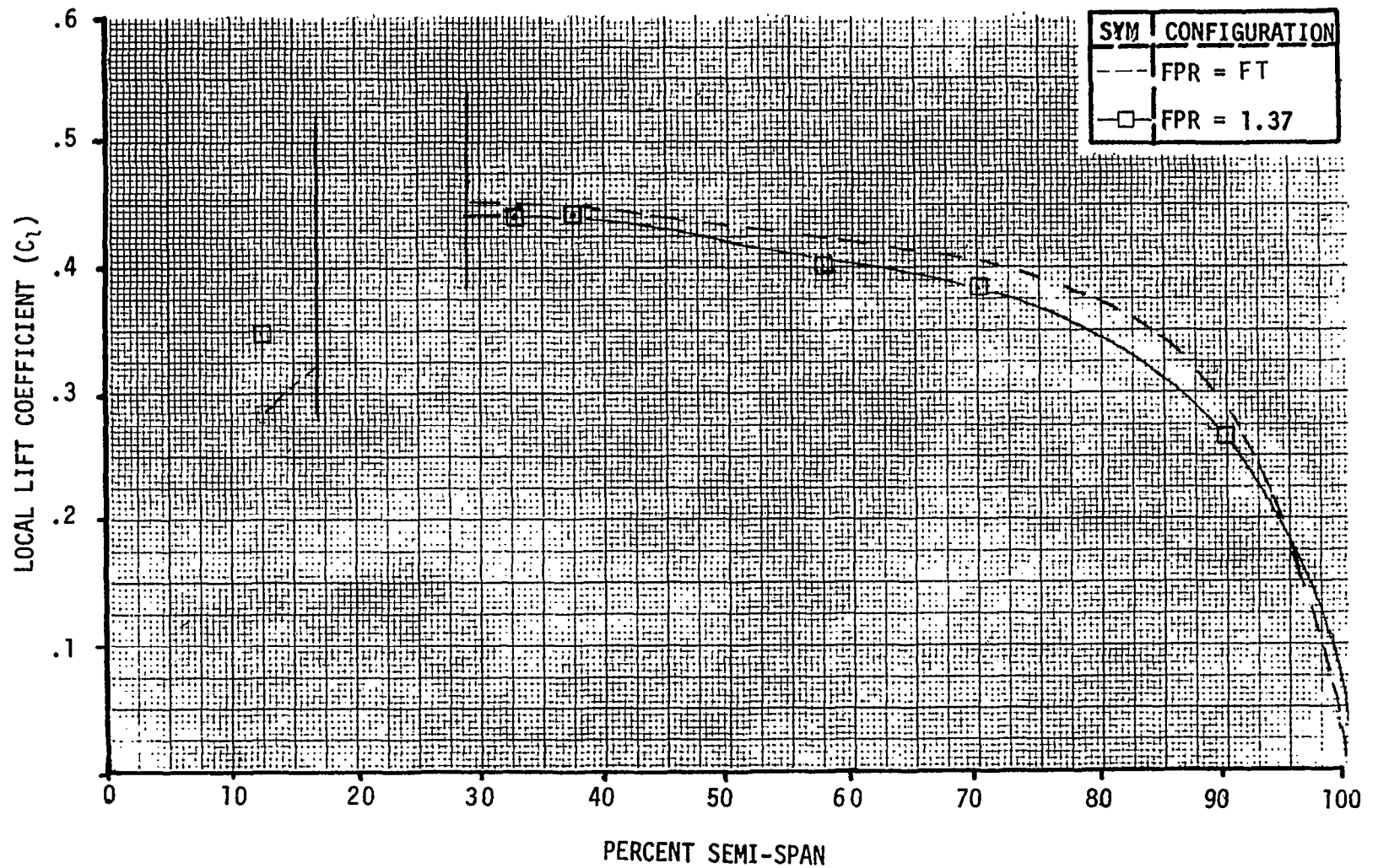
Figure 11.66.   Effect of FPR on Spanwise Lift Distribution for N_{1R} at M = 0.70.

FPR = 1.37   MACH NUMBER = 0.70   CONFIGURATION C_L = 0.40
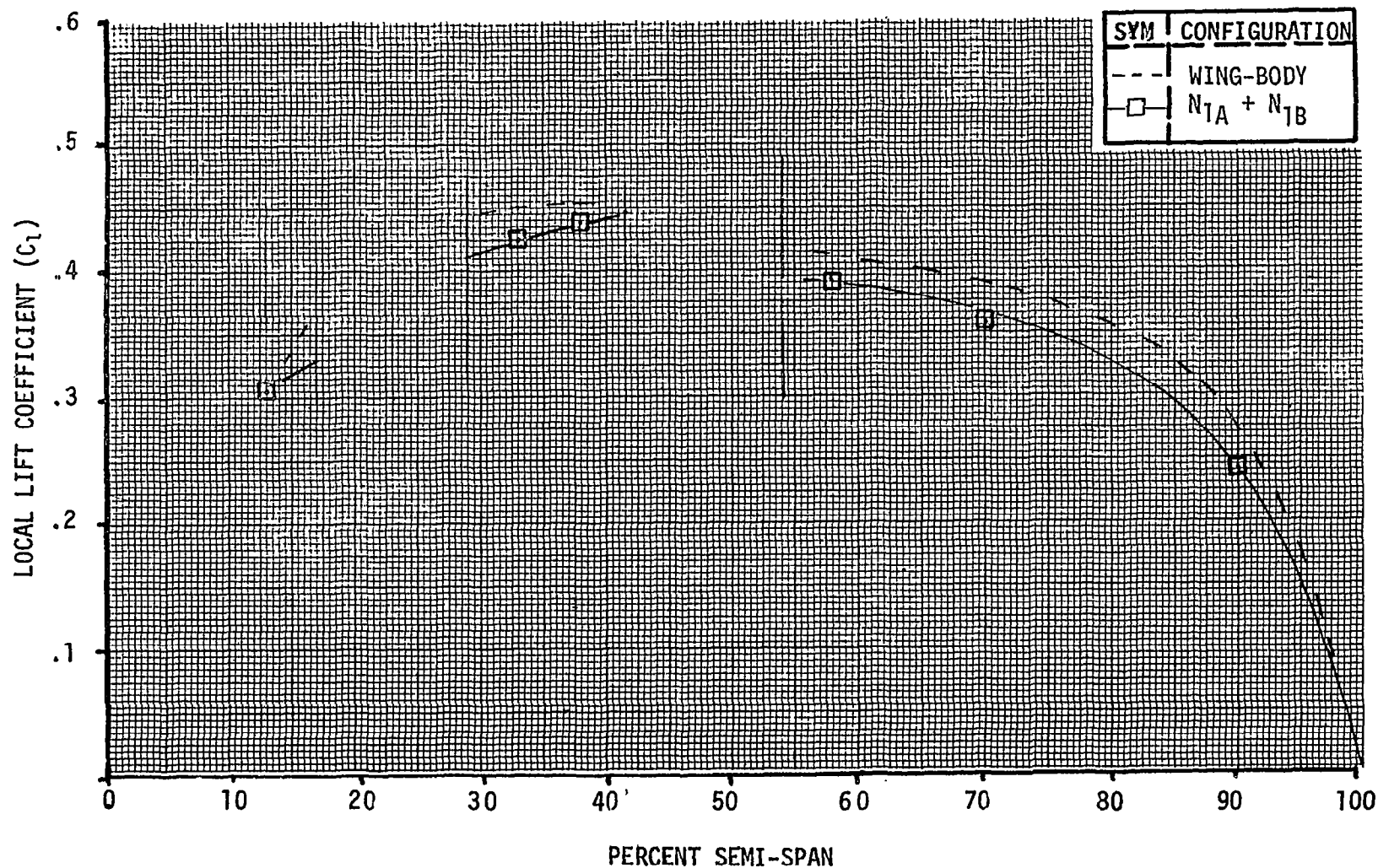
Figure 11.67.   Spanwise Lift Distribution for Four Engine N_{1A} + N_{1B} at M = 0.70.
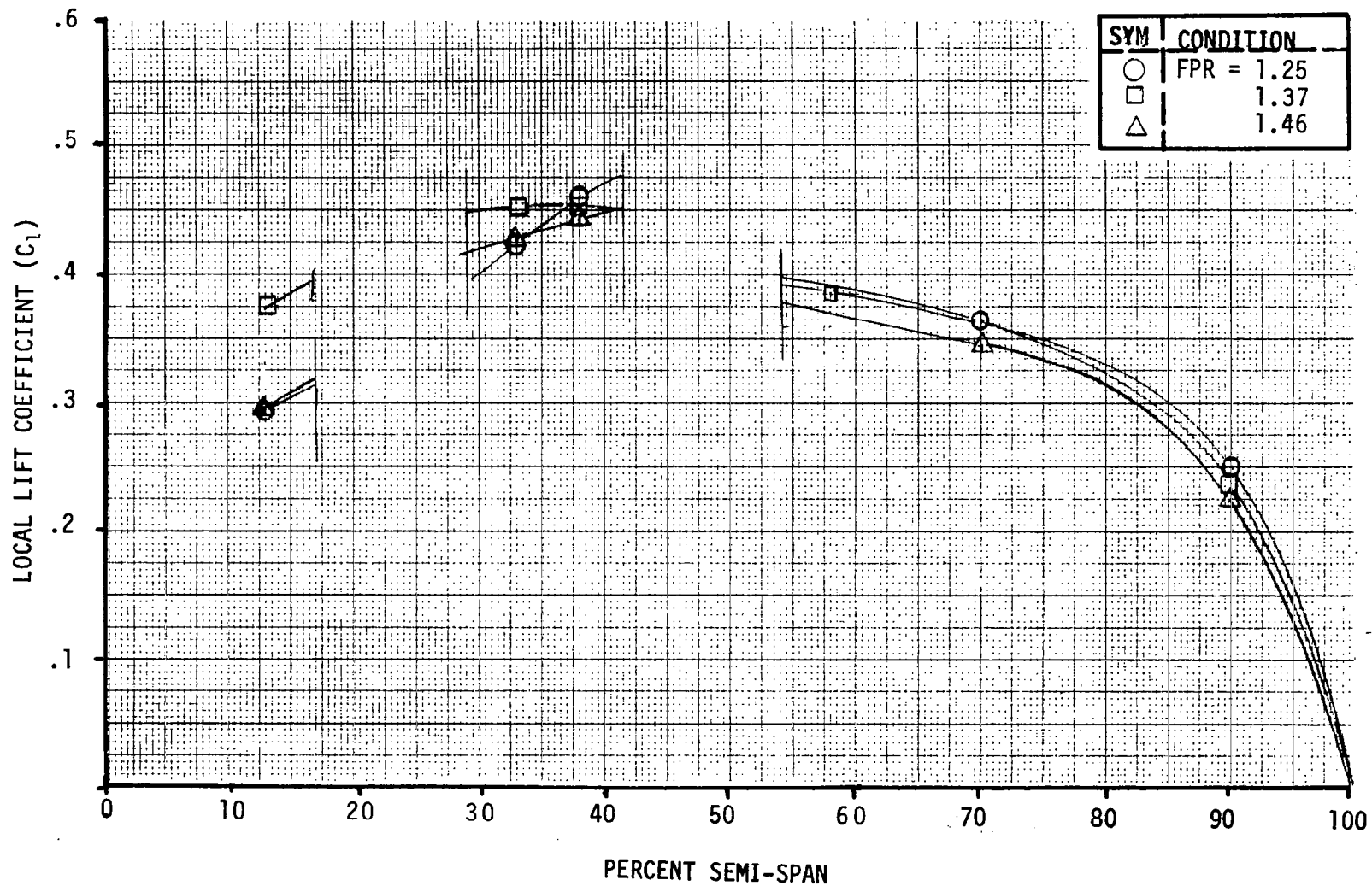
Figure 11.68.   Effect of FPR on the Spanwise Lift Distribution for Four Engine N_{1A} + N_{1B}.

CONFIGURATION C_L = 0.40   FAN PRESSURE RATIO = 1.37
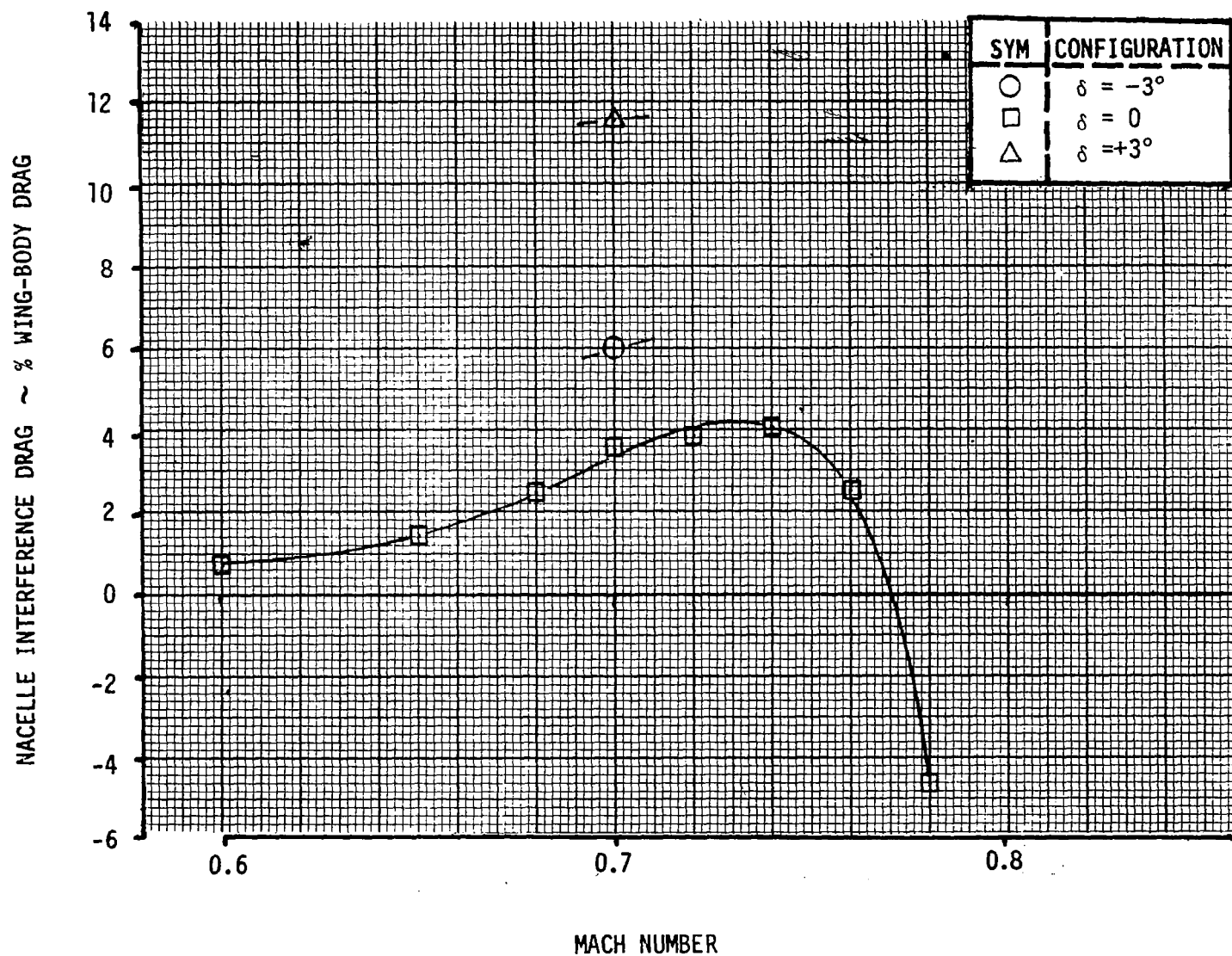
Figure 11.69. Effect of Trimmer Flap Setting for Four-Engine N_1 at FPR = 1.37.

M = 0.7
FPR = 1.37

▢   δ = -3° (T.E. UP)
△   δ = 0°
◇   δ = +3° (T.E. DOWN)
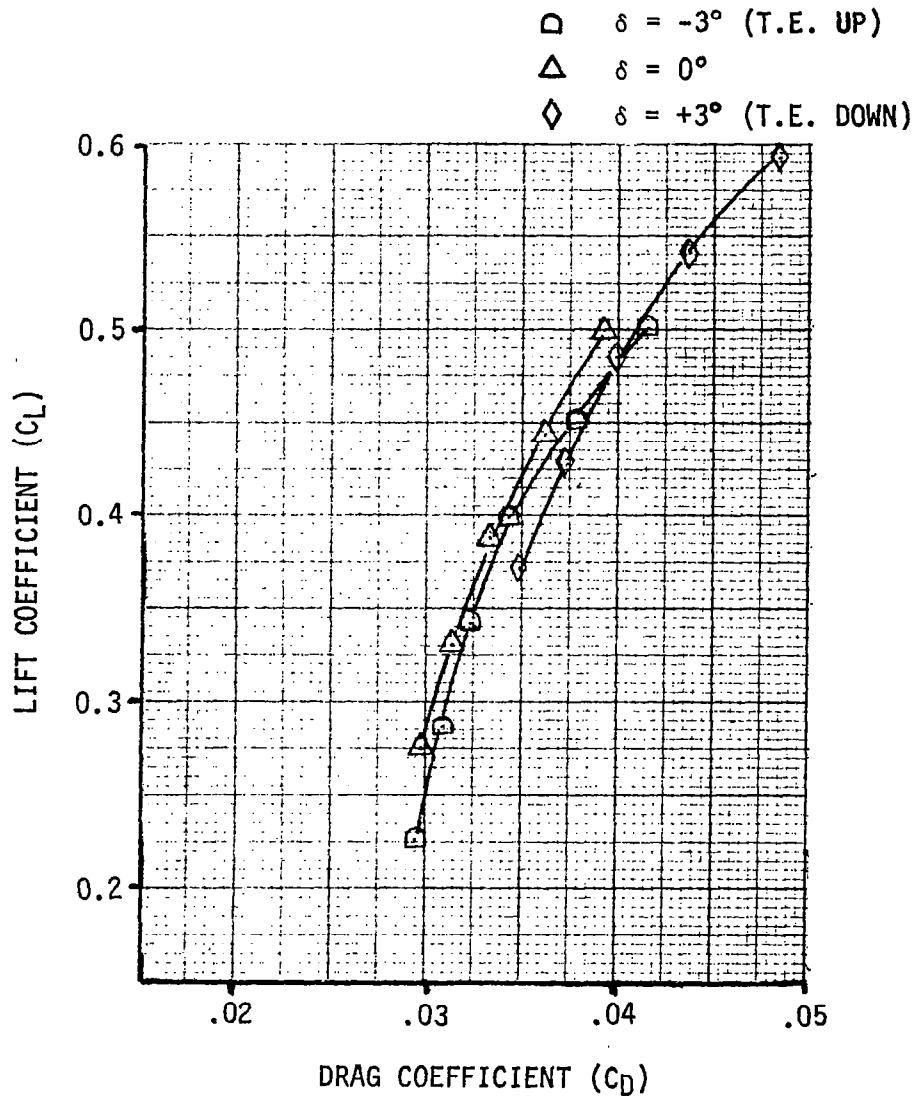
Figure 11.70.   Effect of Trimmer Flap on Airplane Drag for
                Four Engine N_{1A} + N_{1B} Nacelle Configuration.

SYMBOL	CONFIGURATION
◻	$\delta = -3°$
△	$\delta = 0$
◇	$\delta = +3°$

MACH NUMBER = 0.7

FPR = 1.37
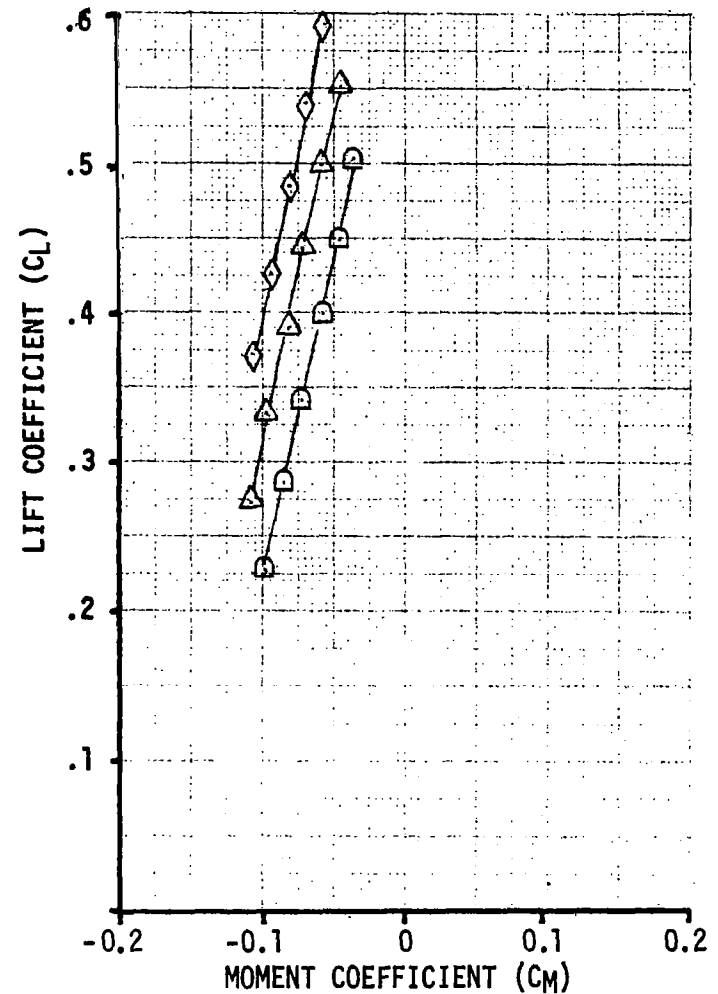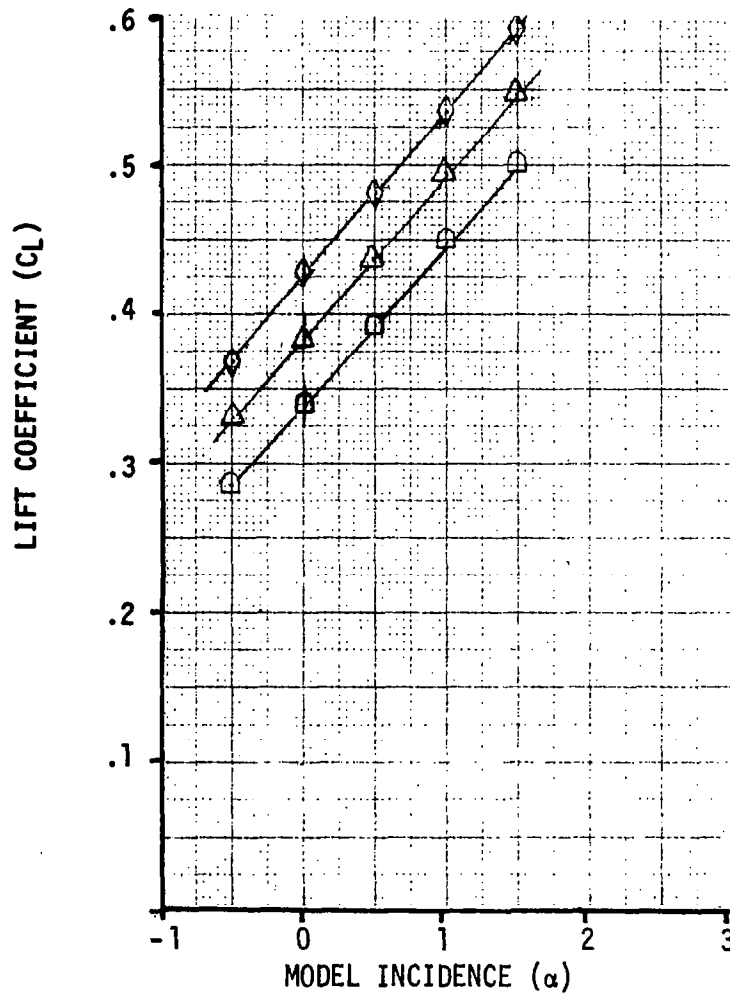
Figure 11.71. Lift and Pitching Moment for Various Trimmer Flap Settings.
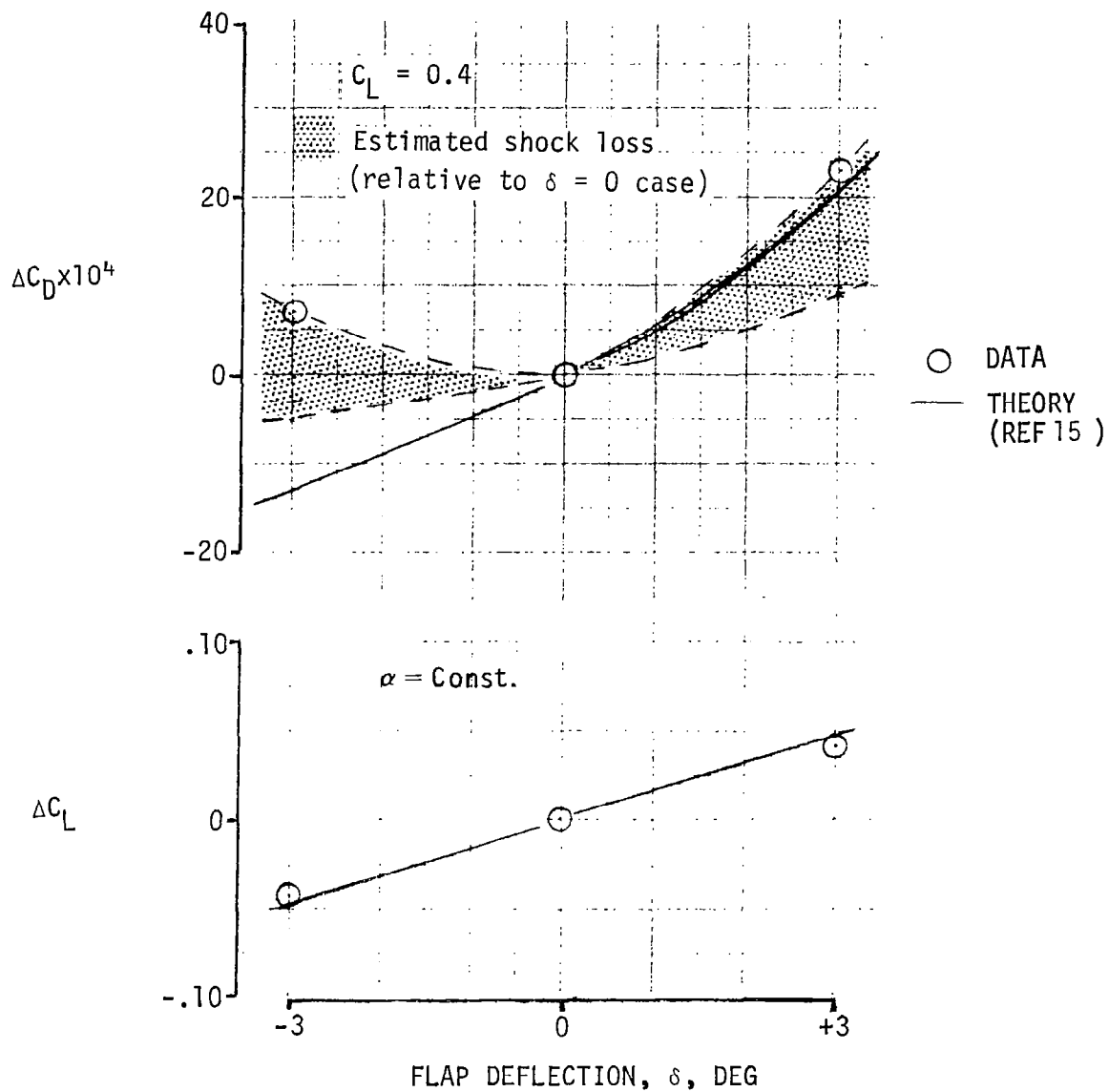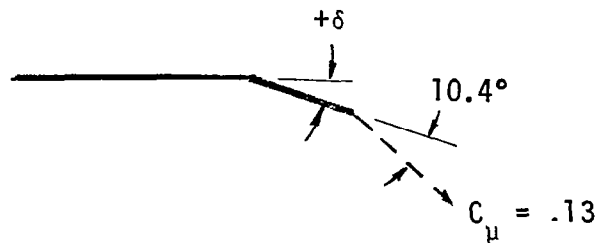
Figure 11.72. Comparison of Theory (EVD) and Data for Various Flap Deflections.

176
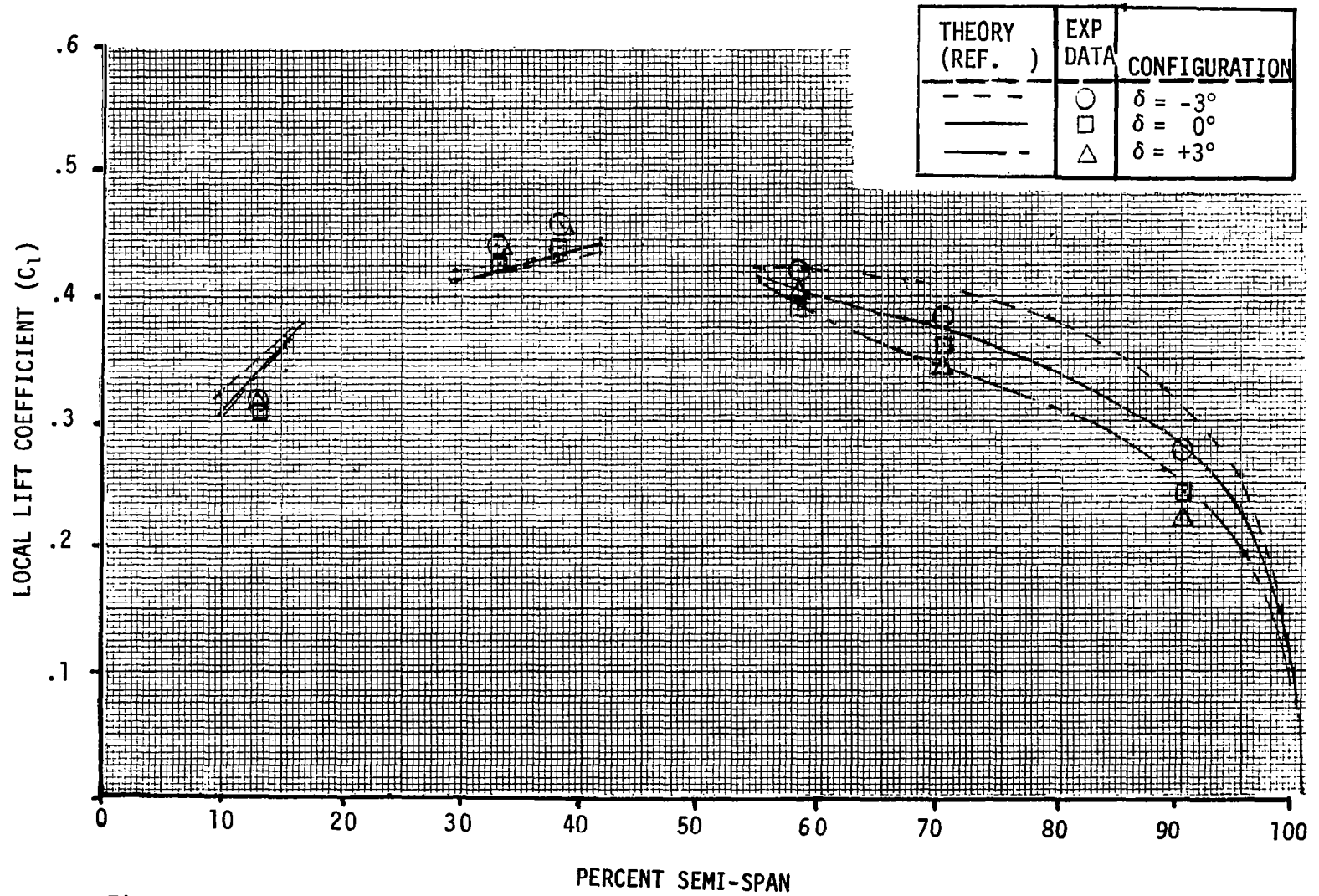
Figure 11.73. Effect of Trimmer Flap Deflection on Spanwise Lift for Four-Engine $N_{1A} + N_{1B}$.

CONFIGURATION C_L = 0.4   FAN PRESSURE RATIO = 1.37
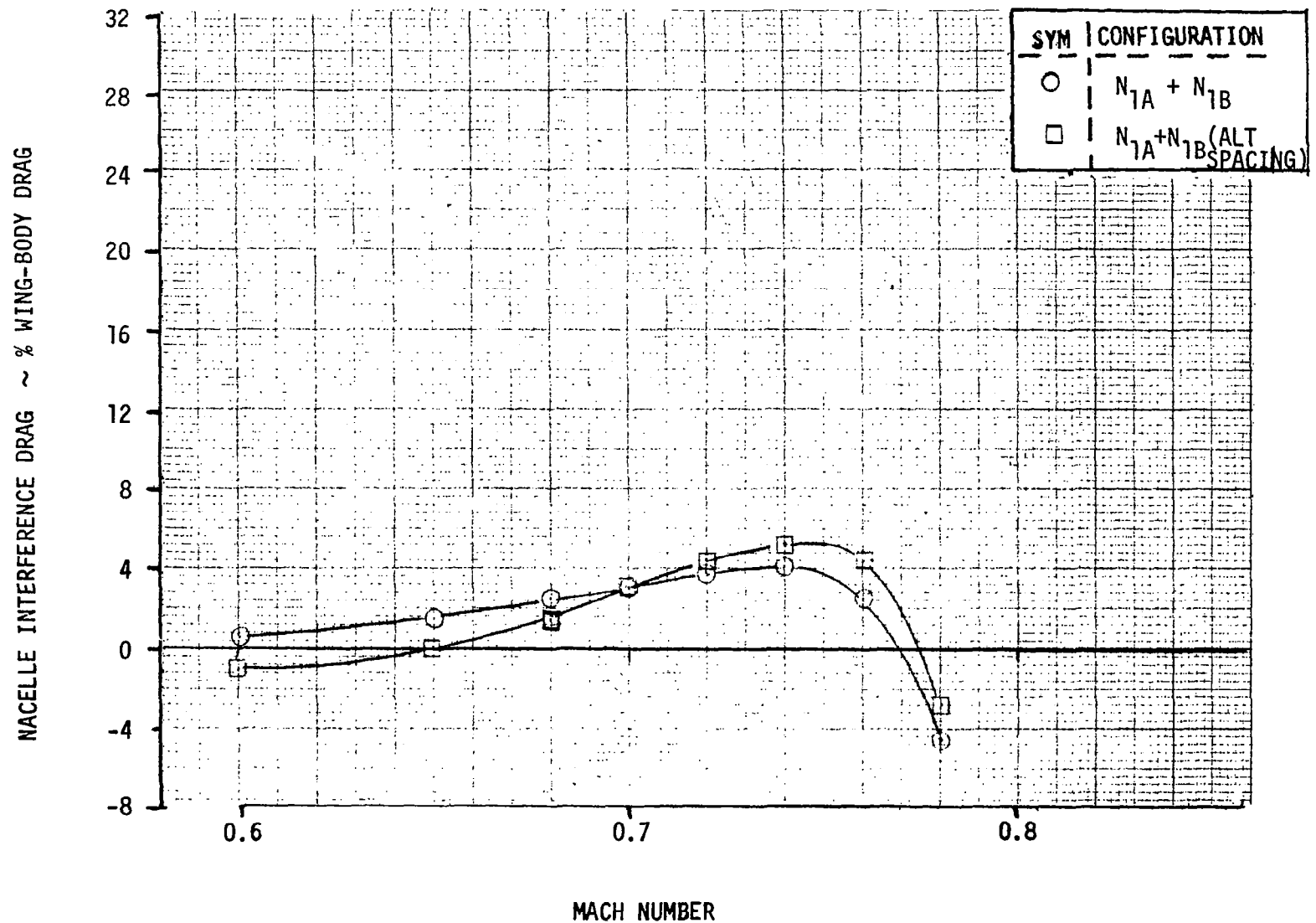
Figure 11.74.   Effect of Alternate Nacelle Spacing on Interference Drag
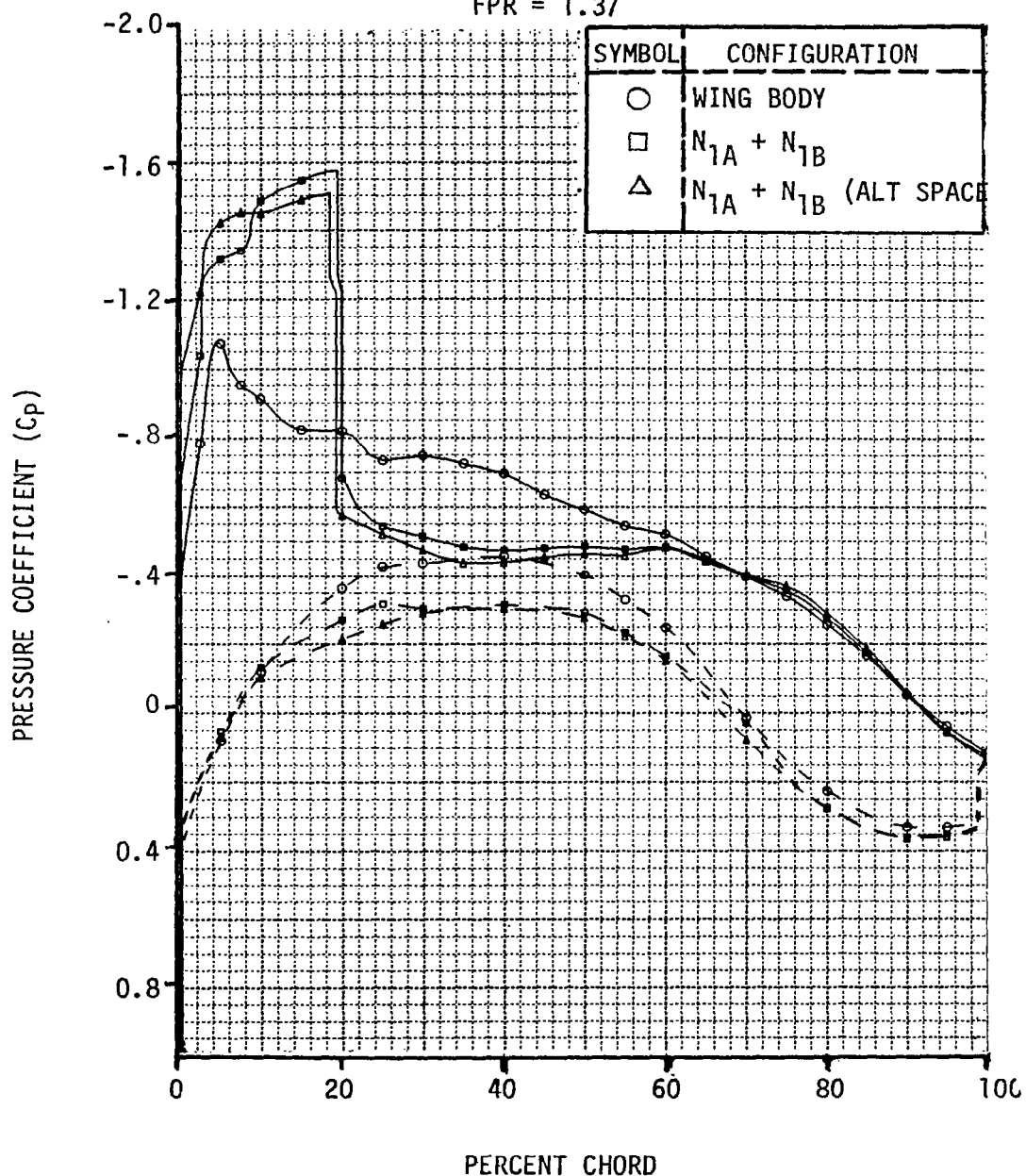
Figure 11.75. Influence of Alternate Nacelle Spanwise Spacing on Wing Surface Pressures at 38% Semispan.

179
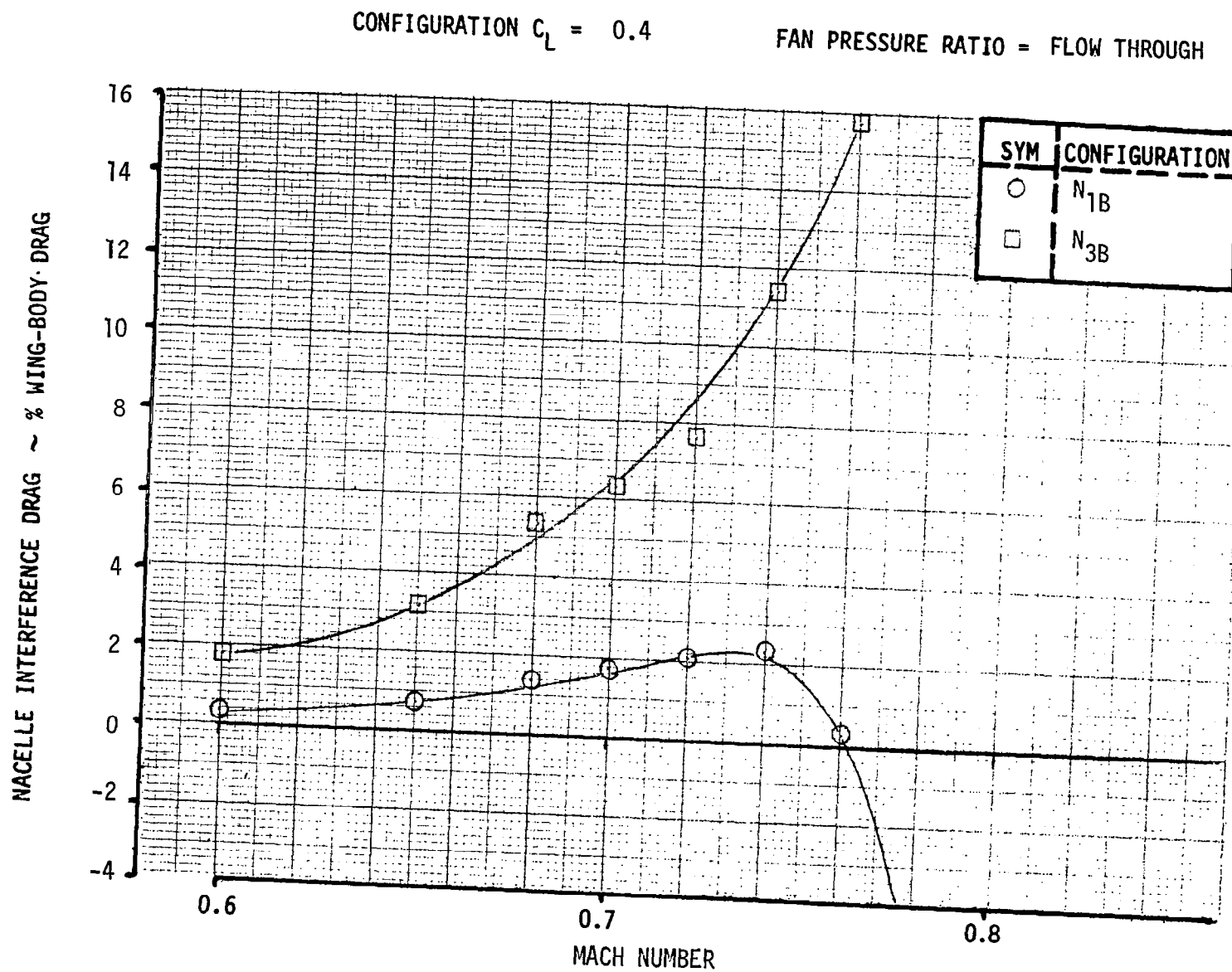
Figure 11.76.   Comparison of Flow Through Nacelle Interference Drag - N_{1B} vs N_{3B}.

ALPHA = 0.5°

33 PERCENT SEMI-SPAN
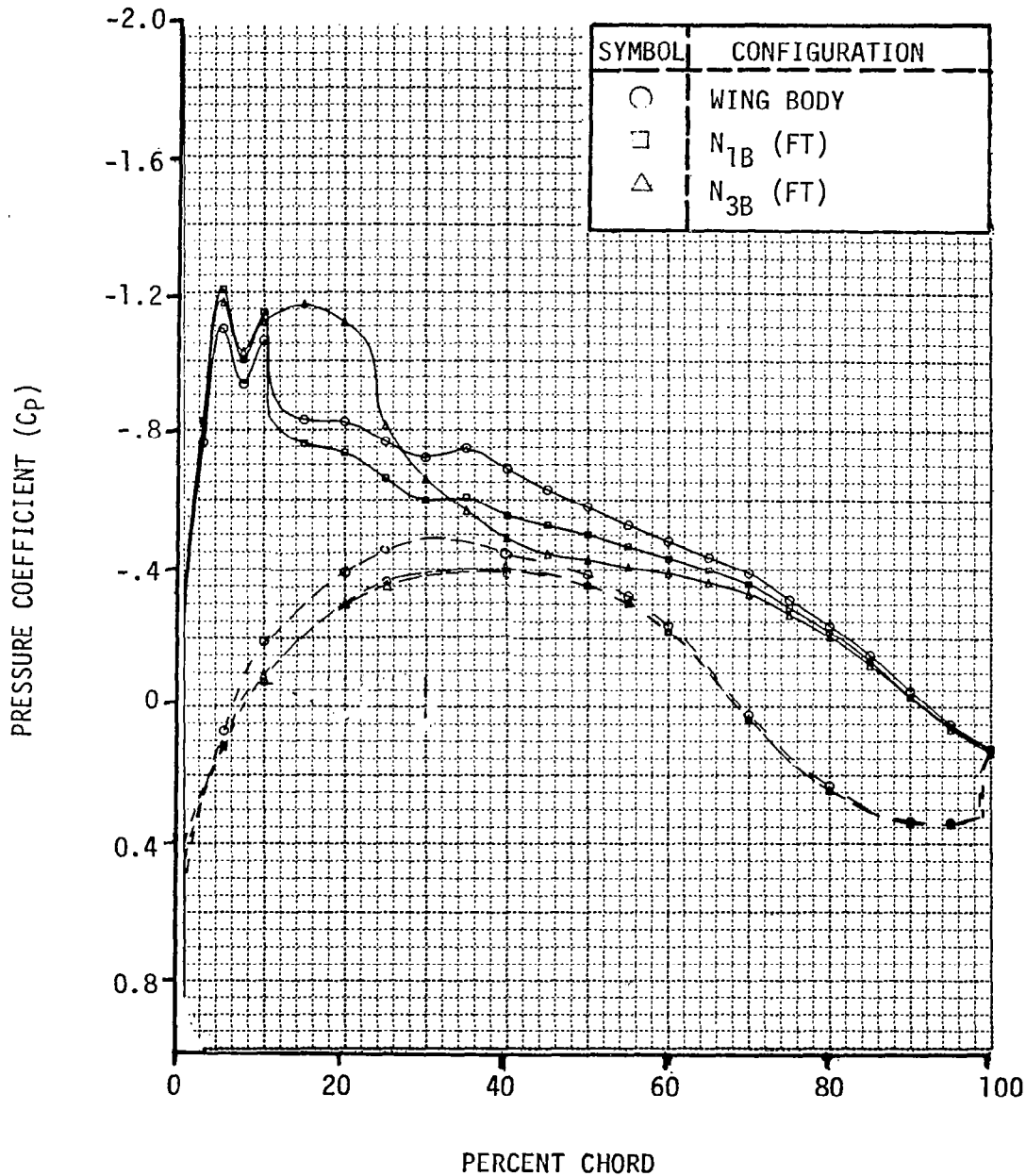
MACH NUMBER = 0.70

Figure 11.77. Wing Surface Pressure Distribution for Wing-Body,
N_{1B} and N_{3B} at M = 0.70 and Flow Through Conditions.
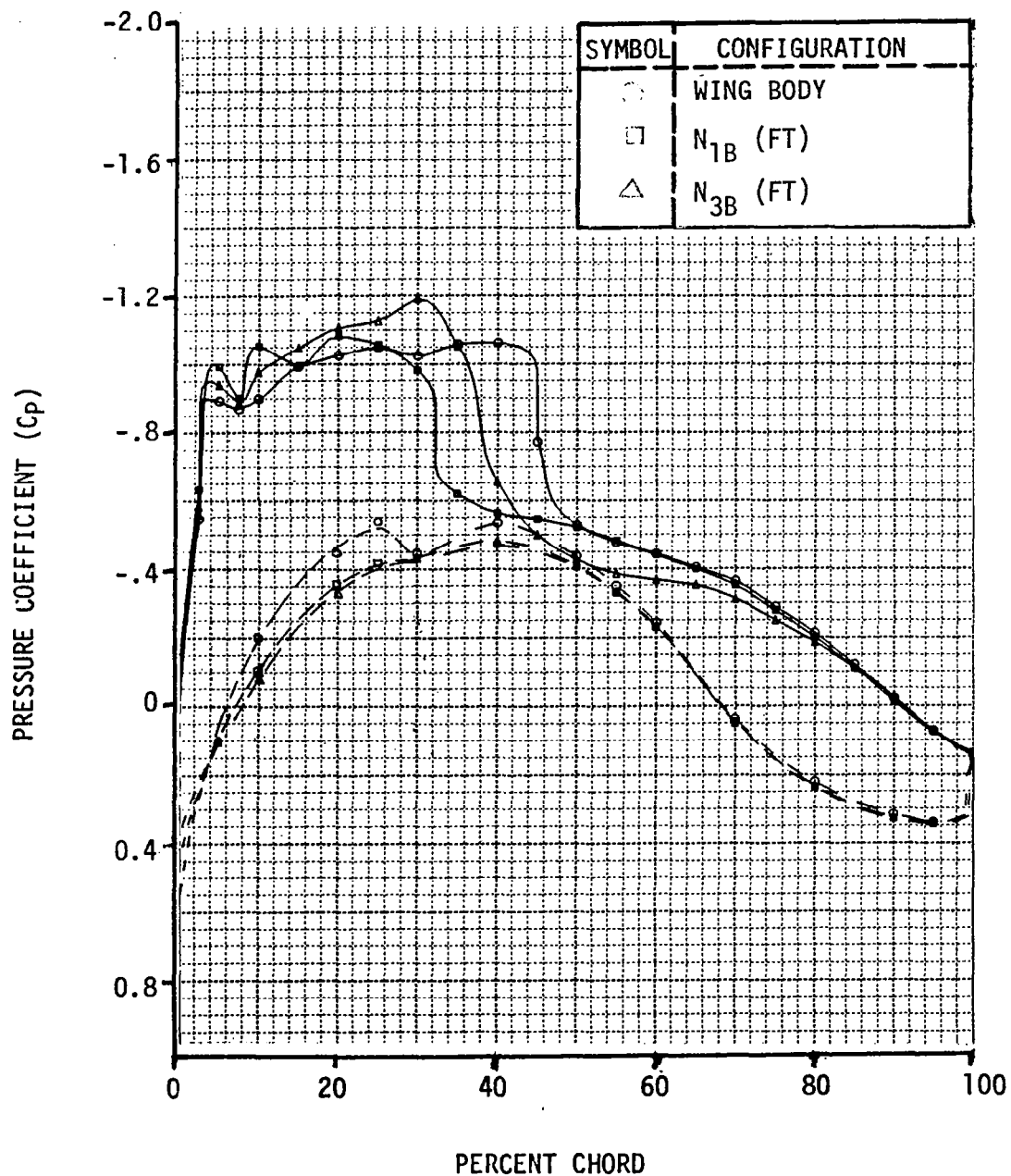
Figure 11.78. Wing Surface Pressure Distribution for Wing-Body, N_{1B} and N_{3B} at M = 0.76 and Flow Through Conditions.

CONFIGURATION C_L = 0.4   FAN PRESSURE RATIO = 1.37
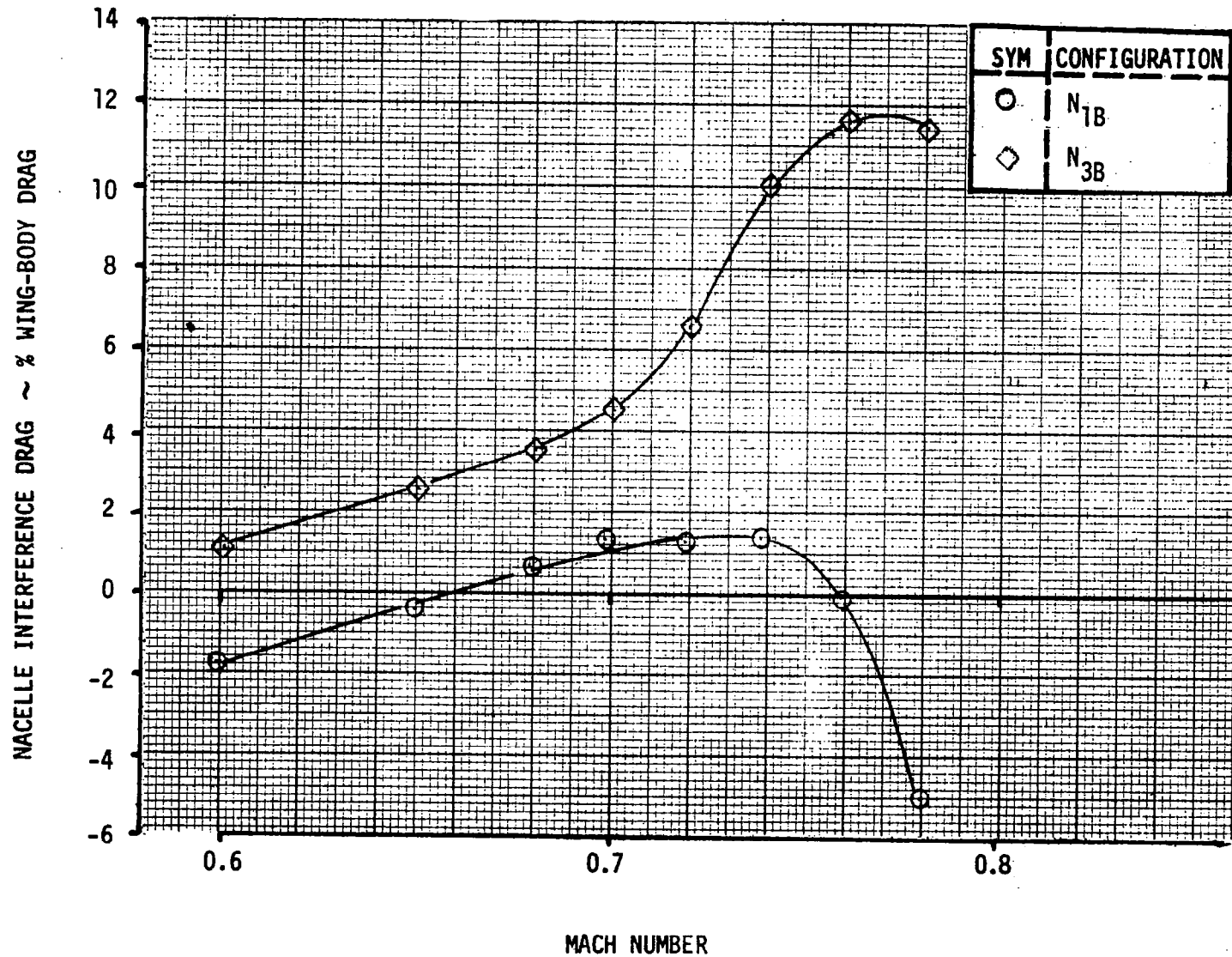
Figure 11.79.   Comparison of Powered Nacelle Interference Drag - N_{1B} vs N_{3B}.

ALPHA = 0.5°

33 PERCENT SEMI-SPAN
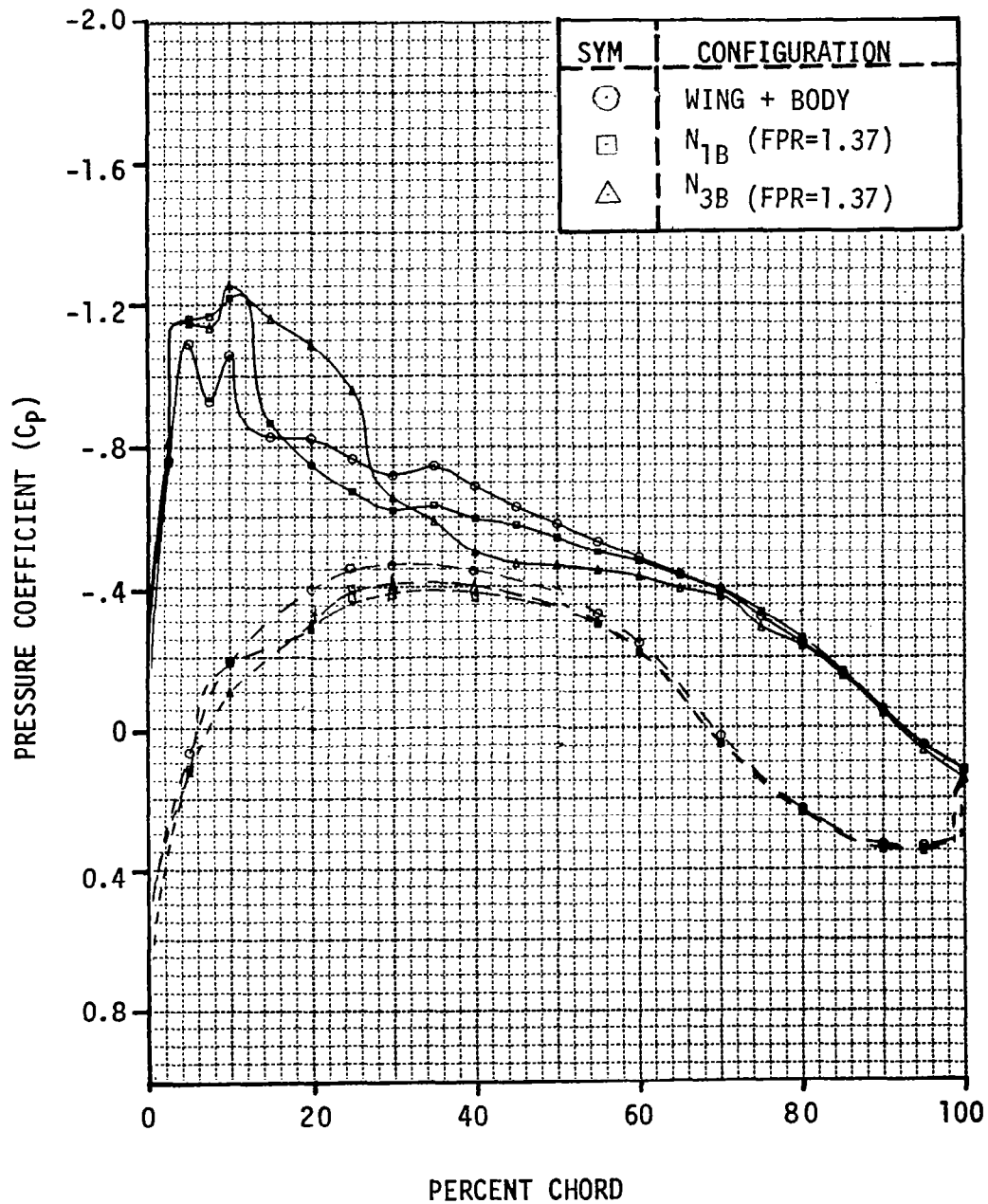
MACH NUMBER = 0.7

Figure 11.80. Wing Surface Pressure Distributions for the Wing-Body, N_{1B} and N_{3B} at 33% Semispan and M = 0.7
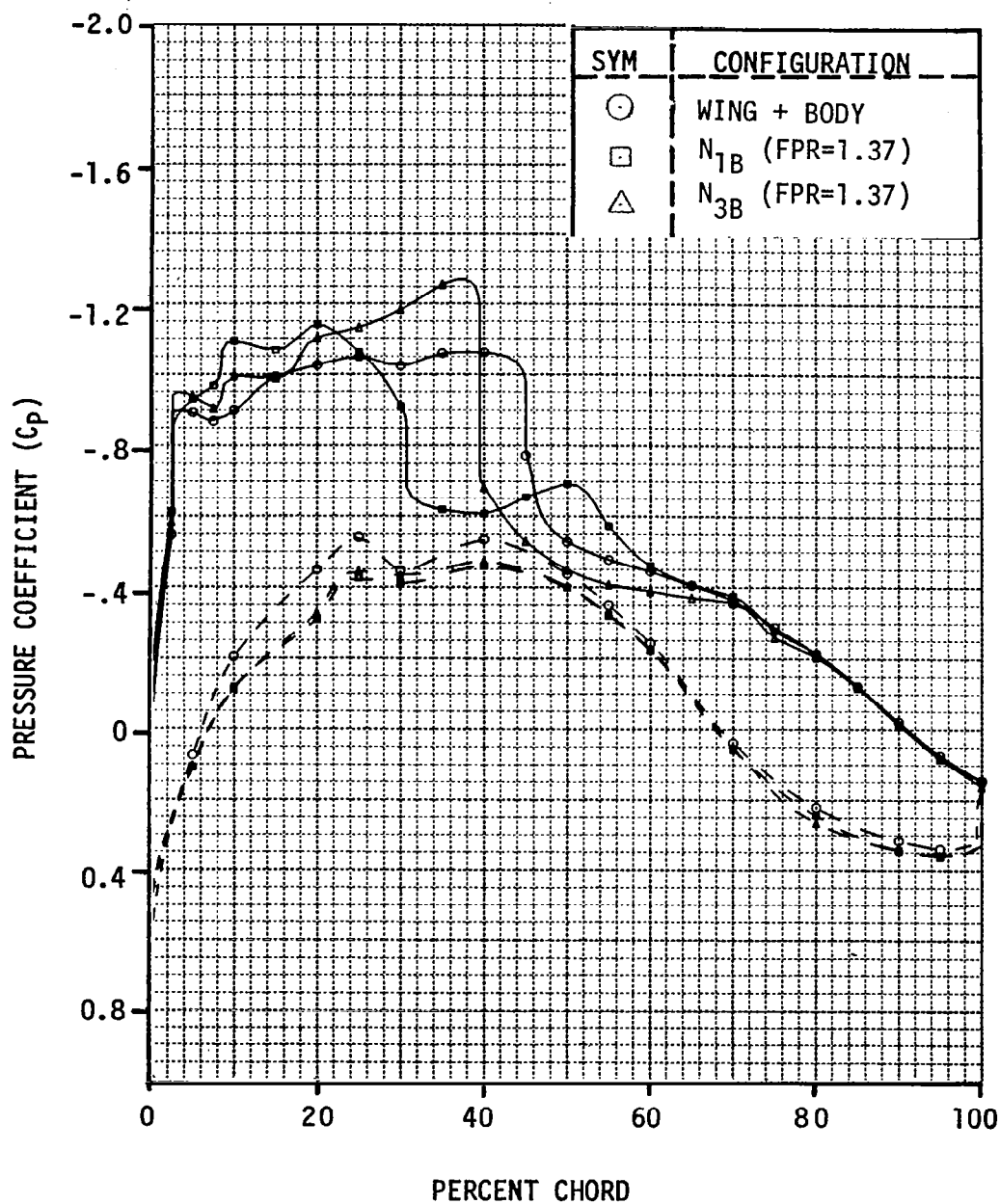
Figure 11.81. Wing Surface Pressure Distributions for the Wing-Body, N_{1B} and N_{3B} at 33% Semispan and M = 0.76

CONFIGURATION C_L = 0.40 $\quad\quad$ N_{3B}

SYM	CONDITION
○	FPR = FT
□	1.25
◇	1.37
△	1.48

NACELLE INTERFERENCE DRAG ~ % WING-BODY DRAG
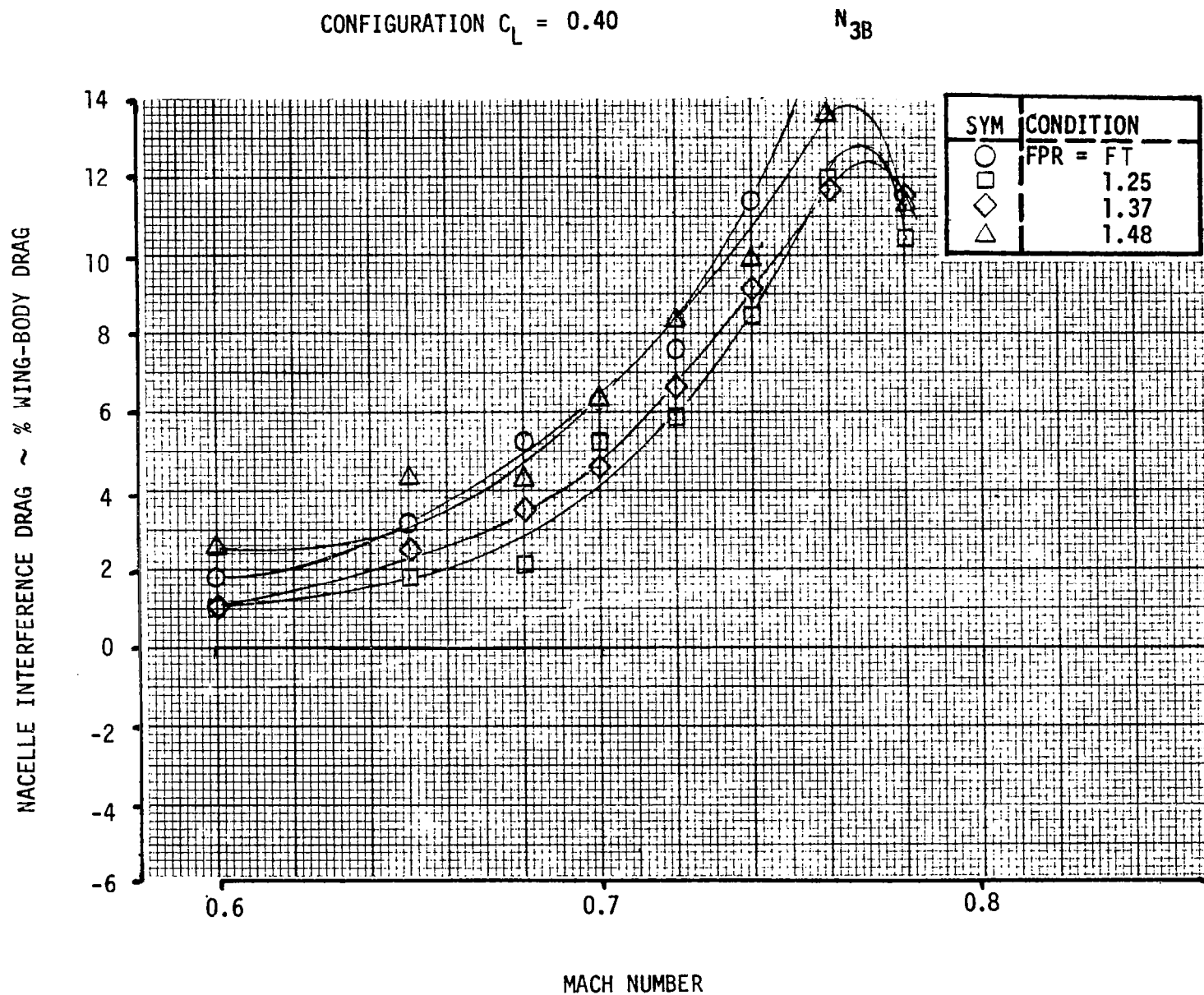
MACH NUMBER

Figure 11.82. Variation of N_{3B} Nacelle Interference Drag with FPR.

ALPHA = 0.5°

33 PERCENT SEMI-SPAN

MACH NUMBER = 0.76

Figure 11.83. Effect of Fan Pressure Ratio on the Wing Surface Pressures at 33% Semispan for N_{3B} at FPR = F.T. and 1.25 and M = 0.76

187

ALPHA = 0.5°

33 PERCENT SEMI-SPAN
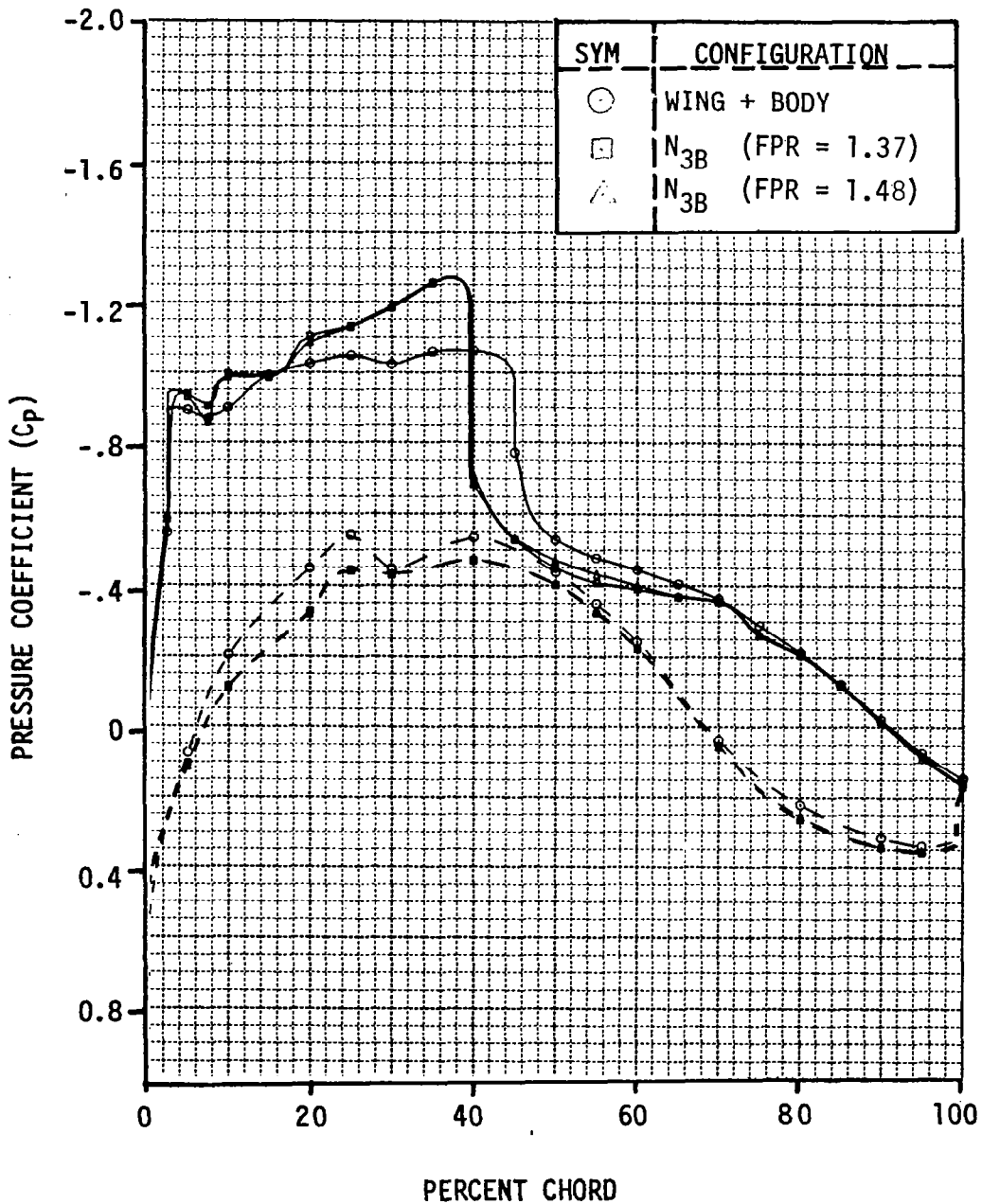
MACH NUMBER = 0.76

Figure 11.84. Effect of Fan Pressure Ratio on the Wing Surface Pressures at 33% Semispan for N_{3B} at FPR = 1.35 and 1.48 at M = 0.76

ALPHA = 0.5°

23 PERCENT SEMI-SPAN

MACH NUMBER = 0.76

SYM	CONFIGURATION
⊙	WING + BODY
▣	N_{3B} (F.T.)
△	N_{3B} (FPR = 1.25)

PRESSURE COEFFICIENT (c_P)

PERCENT CHORD
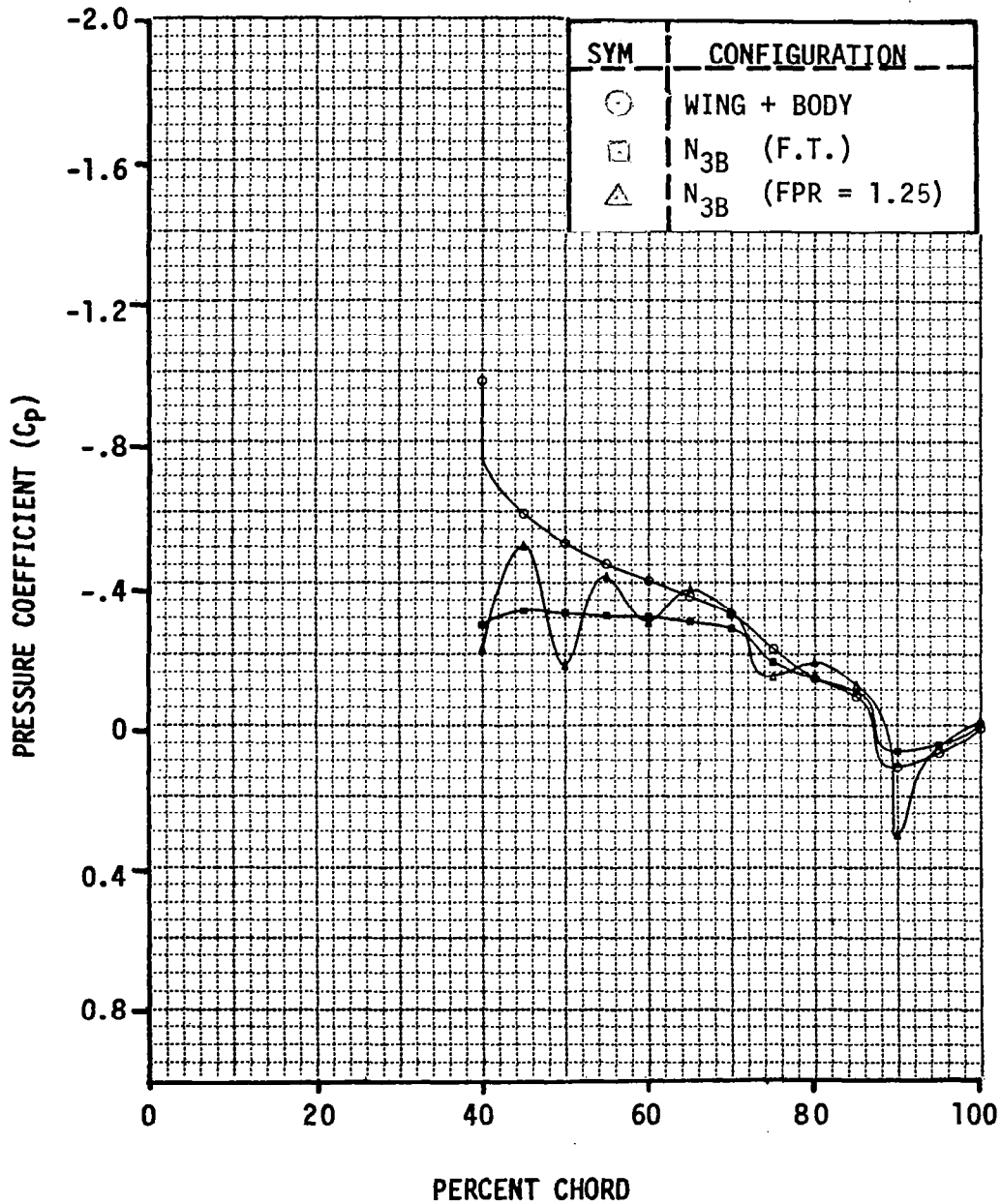
Figure 11.85. Wing Surface Pressures in the Jet for the Wing-Body and N_{3B} at FPR = F.T. and 1.25 and M = 0.76

ALPHA = 0.5°

23 PERCENT SEMI-SPAN

MACH NUMBER = 0.76

SYM	CONFIGURATION
⊙	WING + BODY
⊡	N_{3B} (FPR = 1.37)
△	N_{3B} (FPR = 1.48)

PERCENT CHORD
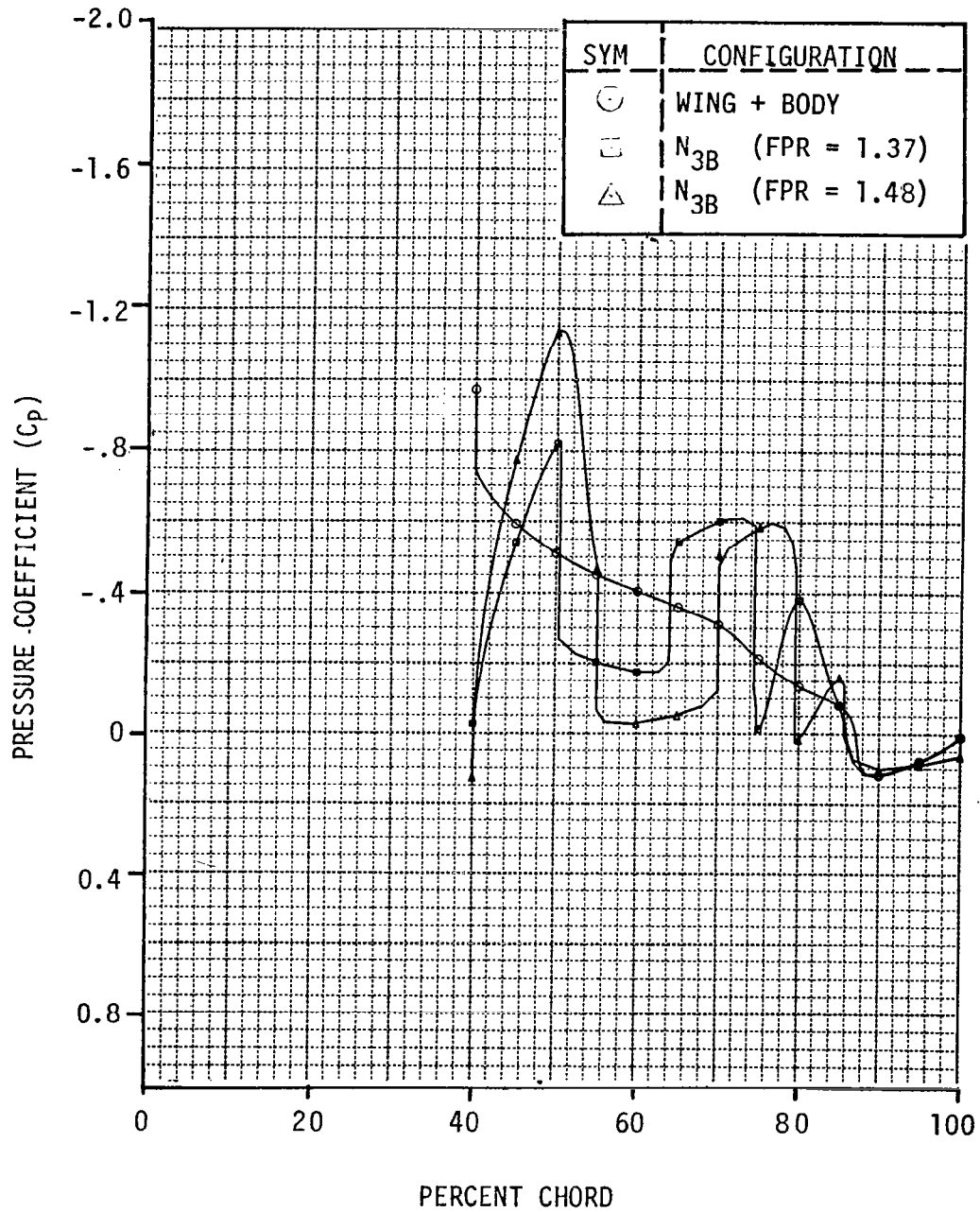
Figure 11.86. Wing Surface Pressures in the Jet for the Wing-Body and N_{3B} at FPR = 1.35 and 1.48 and M = 0.76

ALPHA = 0.5°

23 PERCENT SEMI-SPAN
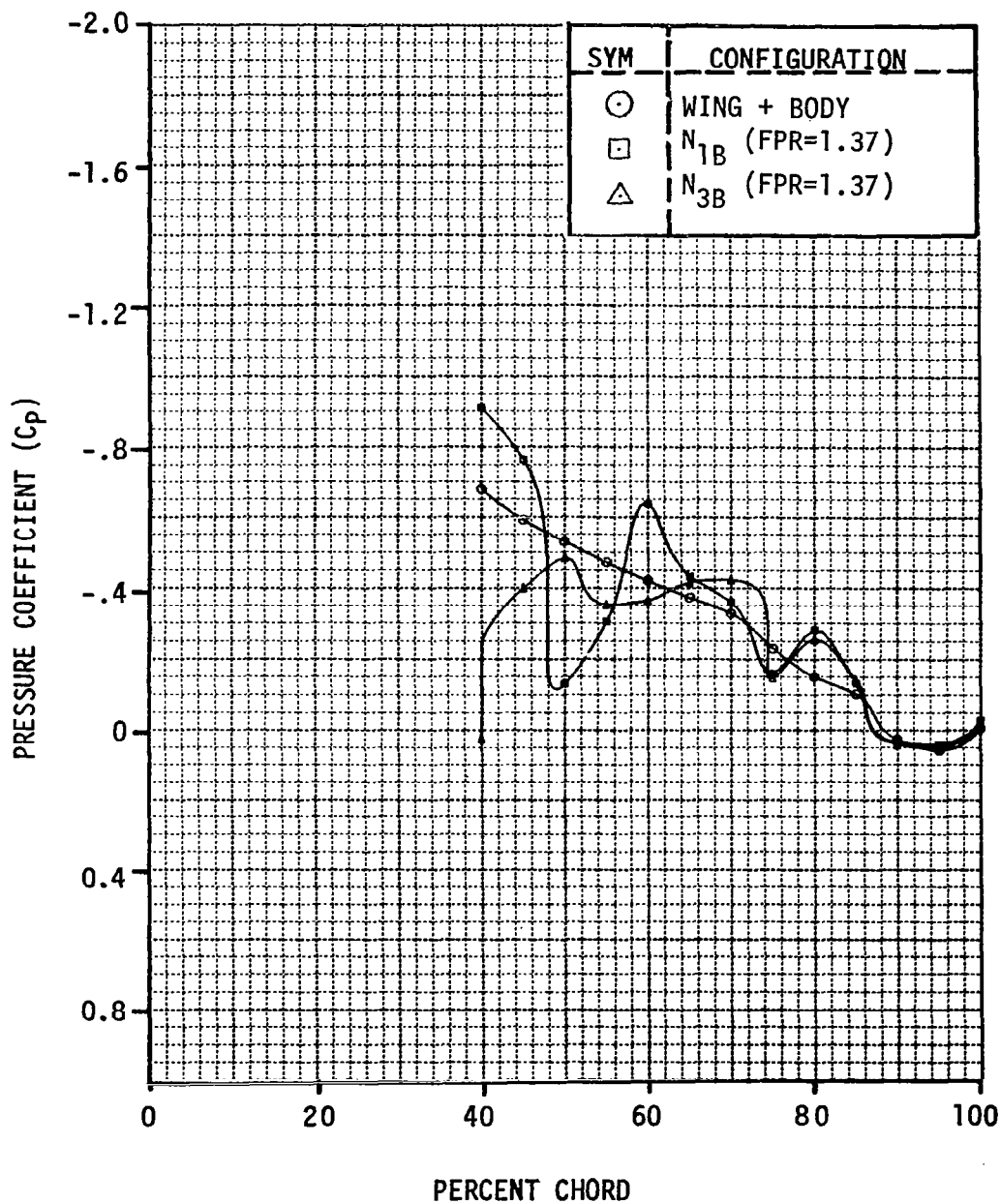
MACH NUMBER = 0.7

Figure 11.87. Wing Surface Pressures in the Jet for the Wing-Body, N_{1B} and N_{3B} at 23% Semispan and M = 0.7

ALPHA = 0.5°

23 PERCENT SEMI-SPAN

MACH NUMBER = 0.76

SYM	CONFIGURATION
⊙	WING + BODY
▢	N_{1B} (FPR=1.37)
△	N_{3B} (FPR=1.37)
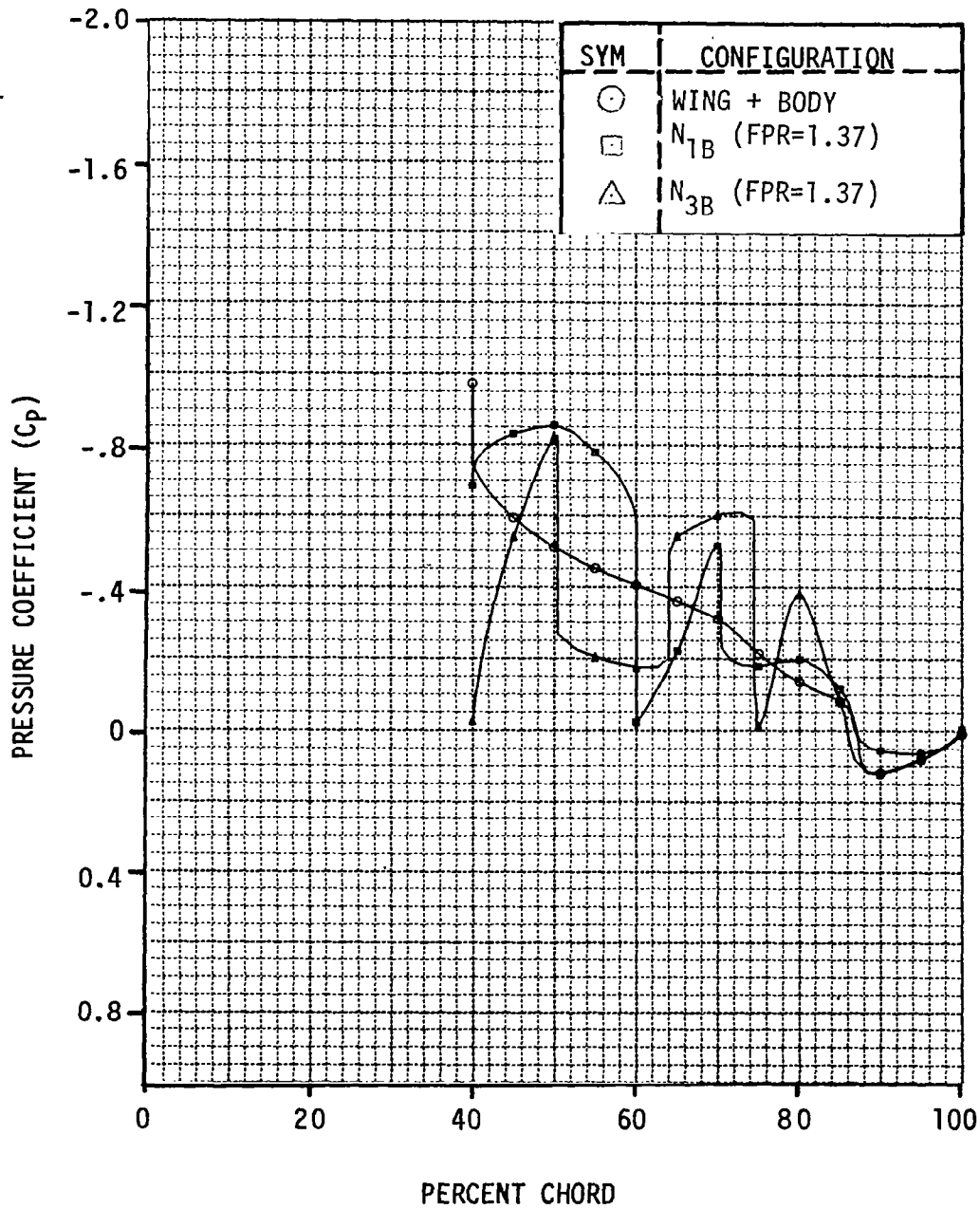
Figure 11.88. Wing Surface Pressures in the Jet for the Wing-Body, N_{1B} and N_{3B} at 23% Semispan and M = 0.76
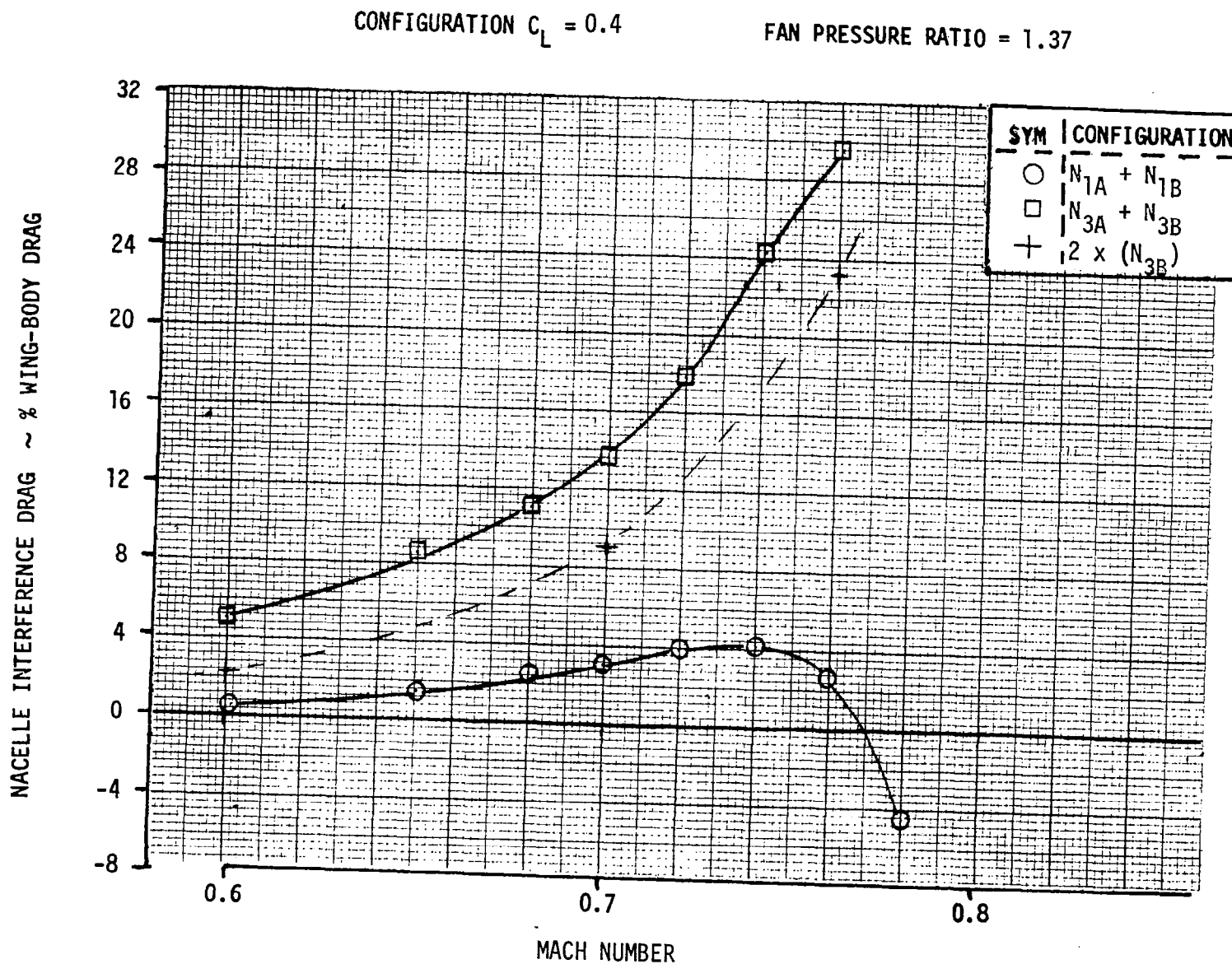
Figure 11.89. Comparison of Powered Interference Drags for $N_{1A} + N_{1B}$ and $N_{3A} + N_{3B}$ at $C_L = 0.4$.

ALPHA = 0.5°

13 PERCENT SEMI-SPAN
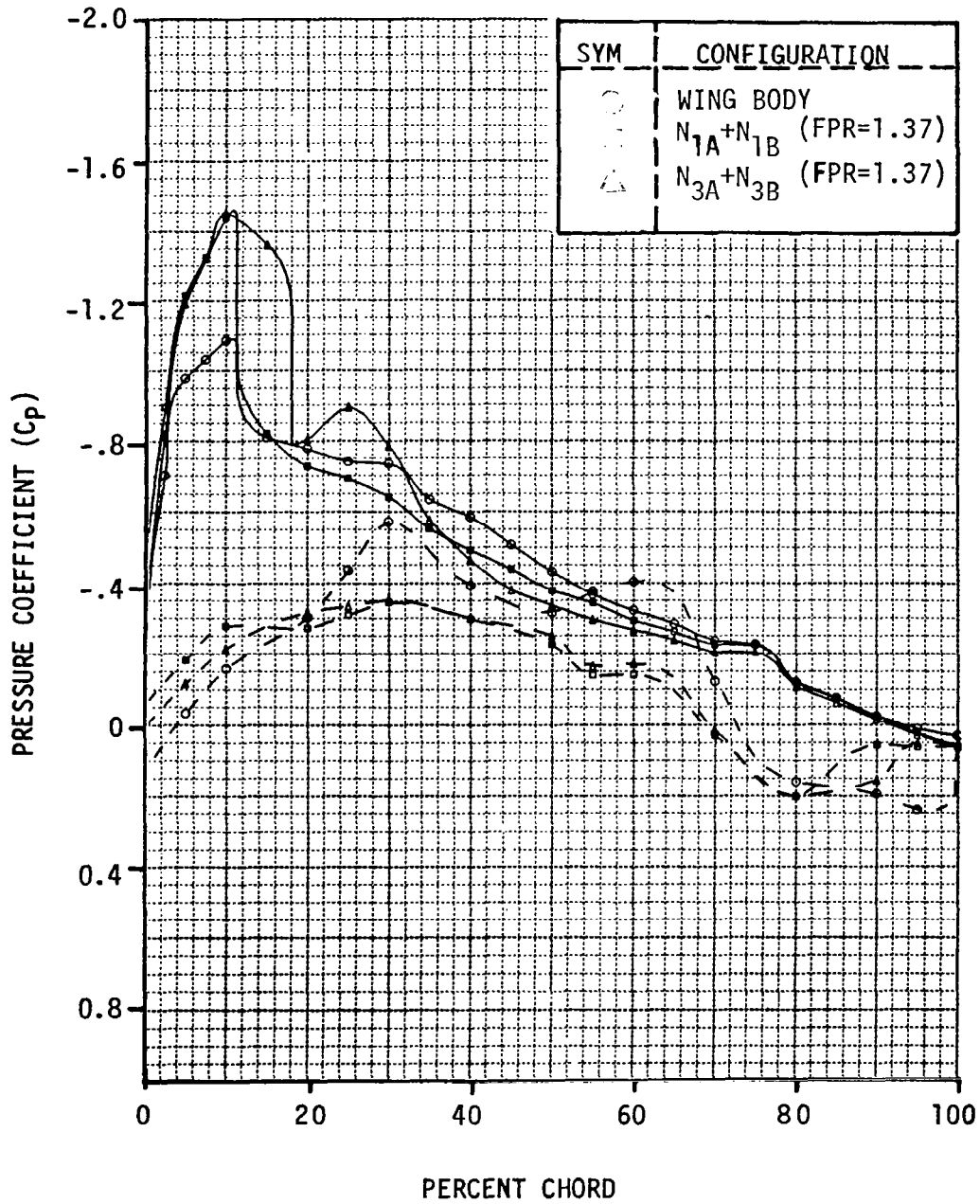
MACH NUMBER = 0.7

Figure 11.90. Wing Surface Pressure Distributions for the Wing-Body, $N_{1A} + N_{1B}$ and $N_{3A} + N_{3B}$ at 13% Semispan and M = 0.7

ALPHA = 0.5°

33 PERCENT SEMI-SPAN
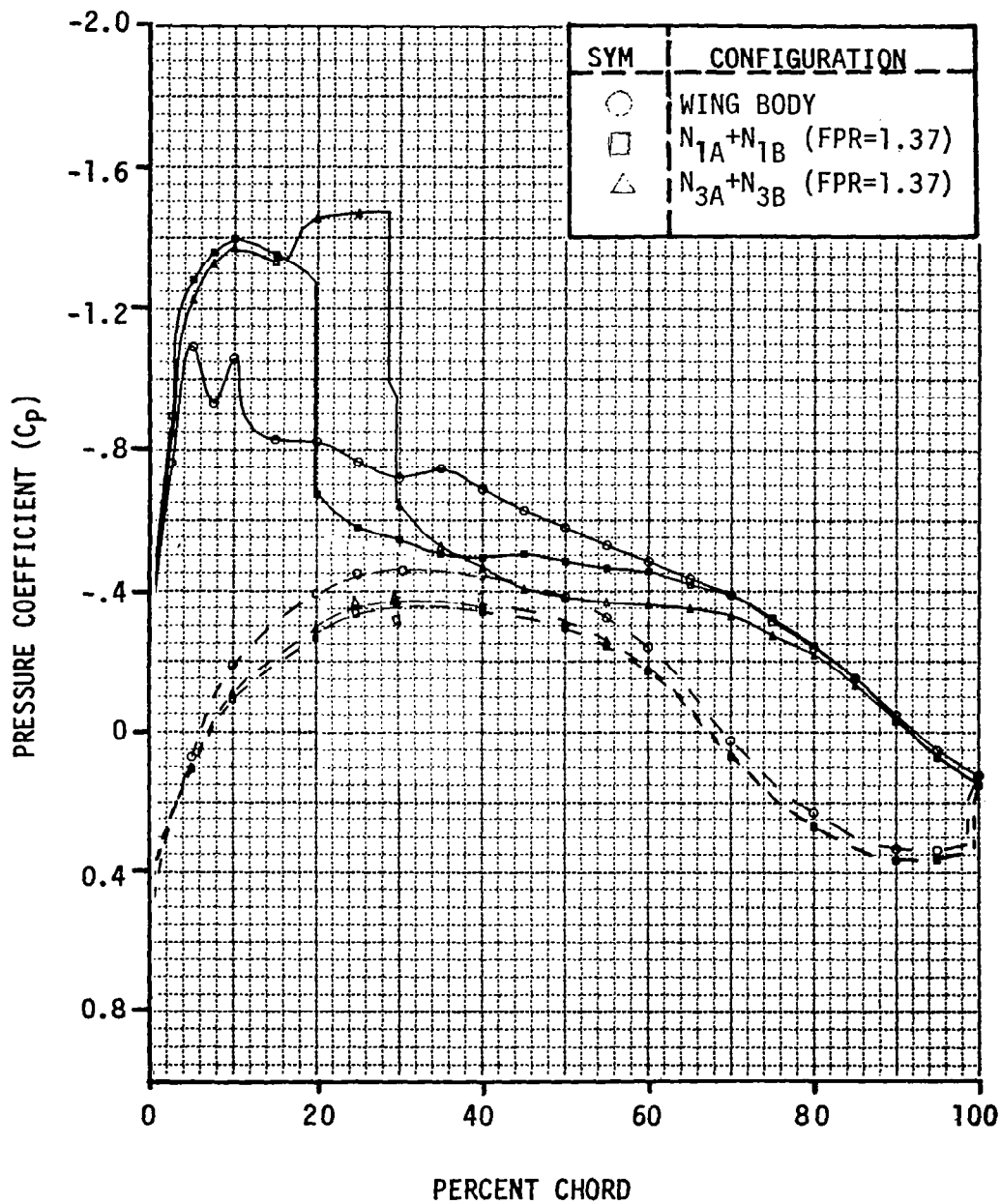
MACH NUMBER = 0.7

Figure 11.91. Wing Surface Pressure Distributions for the Wing-Body, $N_{1A} + N_{1B}$ and $N_{3A} + N_{3B}$ at 33% Semispan and M = 0.7

ALPHA = 0.5°

58 PERCENT SEMI-SPAN

MACH NUMBER = 0.7
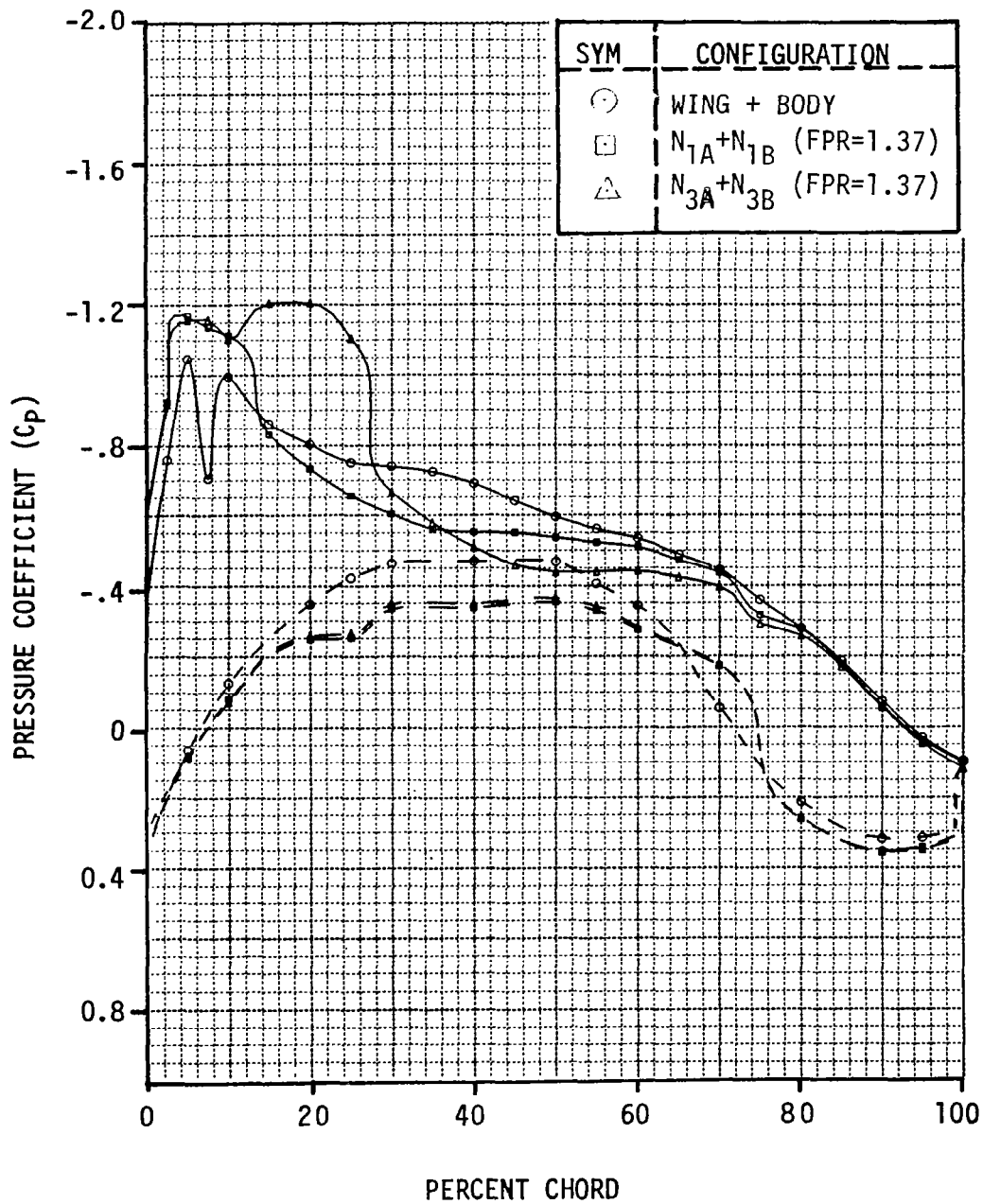
Figure 11.92. Wing Surface Pressure Distributions for the Wing-Body, $N_{1A} + N_{1B}$ and $N_{3A} + N_{3B}$ at 58% Semispan and M = 0.7

196
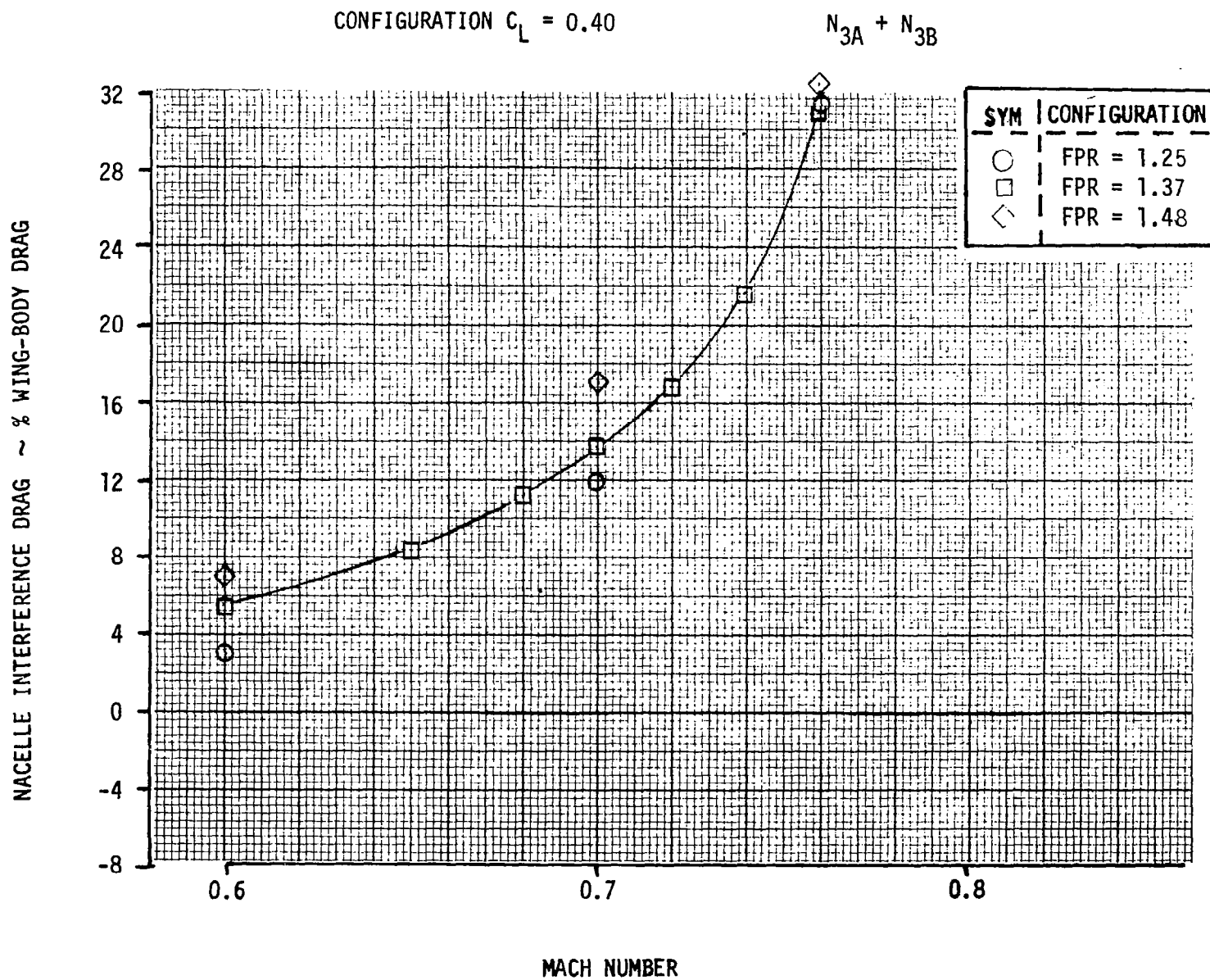
Figure 11.93. Variation of 4 Engine N_{3A} + N_{3B} Interference Drag with FPR
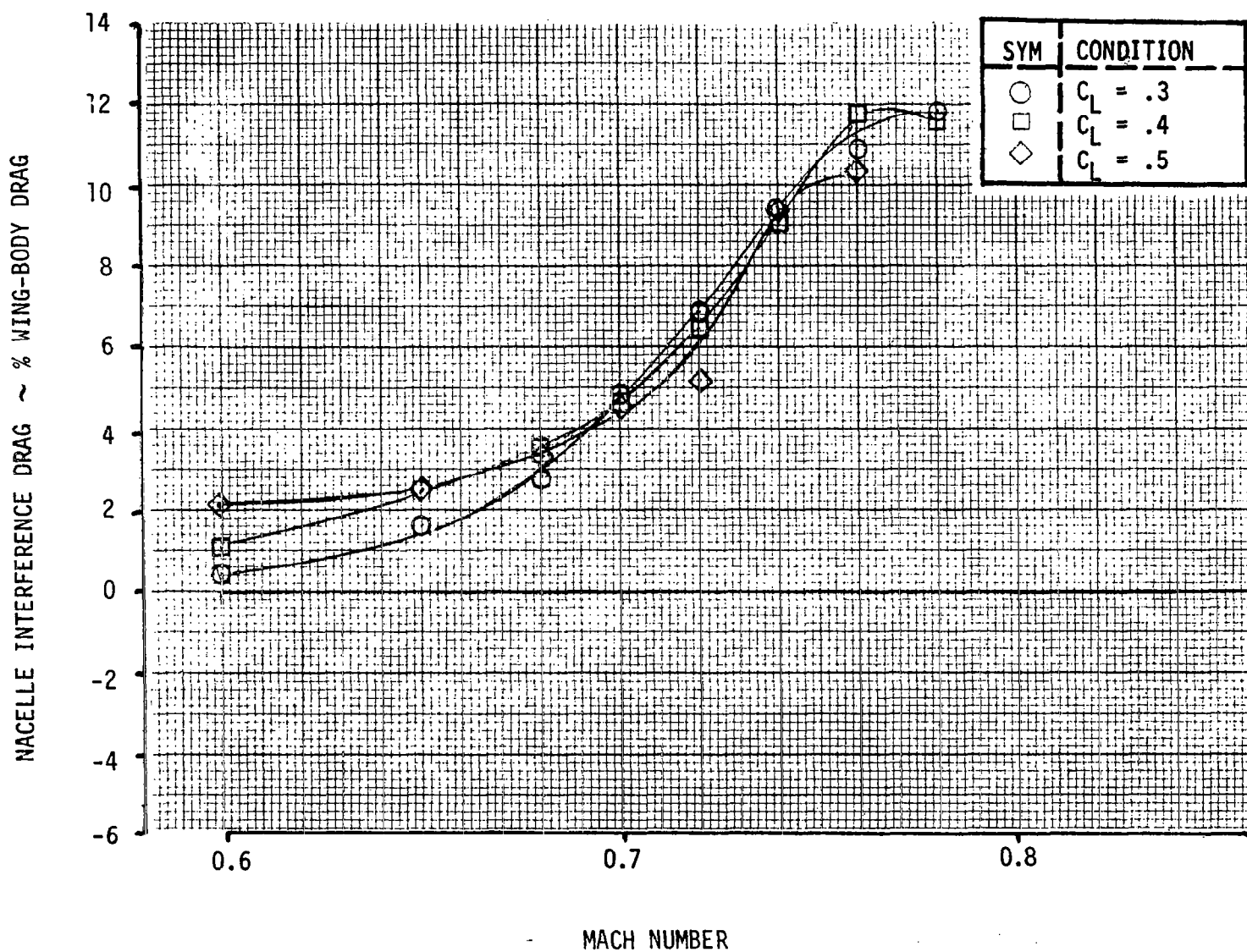
Figure 11.94.   Variation of N$_{3B}$ Nacelle Interference Drag with C$_L$.
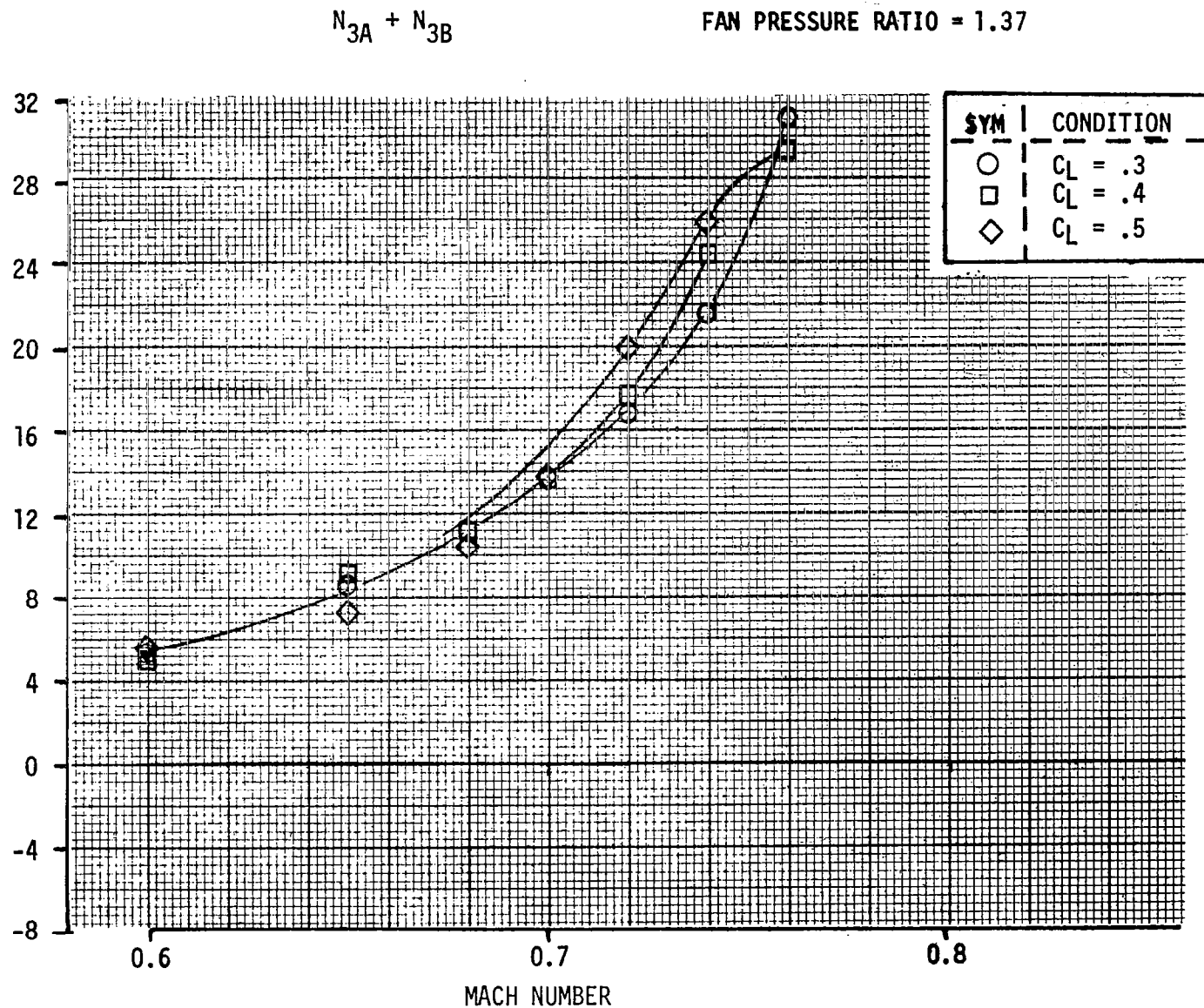
Figure 11.95.   Variation of Four-Engine N_{3A} + N_{3B} Interference Drag with C_L.
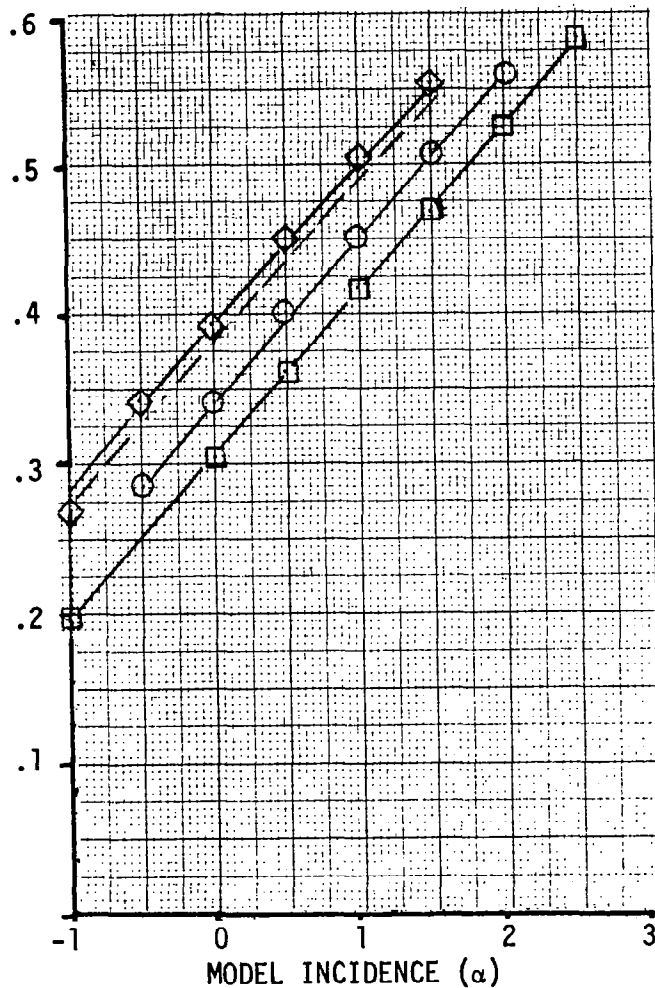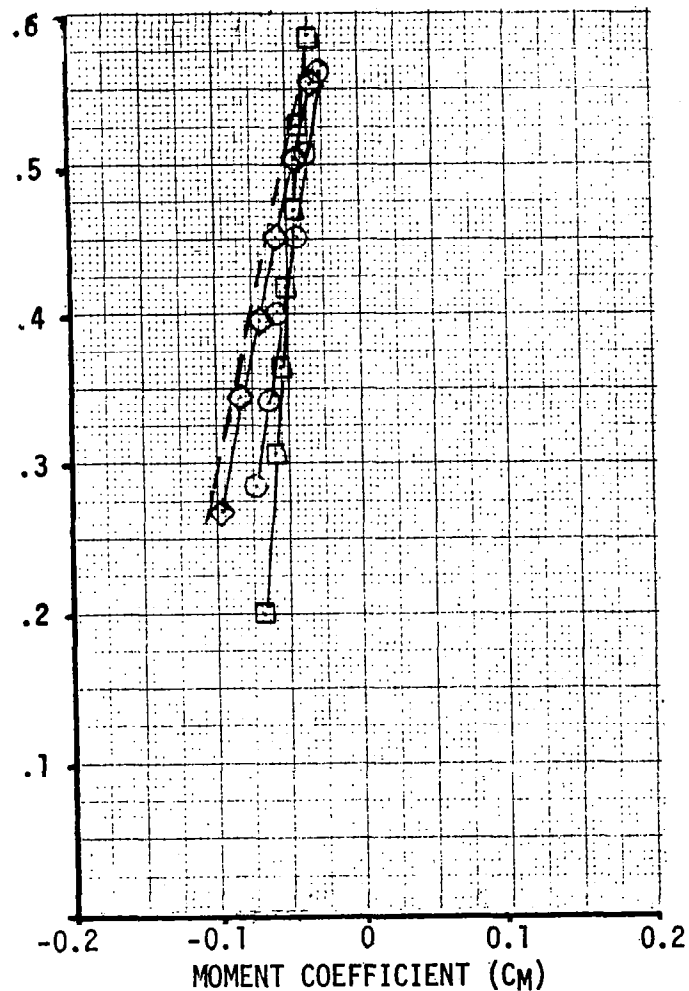
Figure 11.96. Lift and Pitching Moment for Powered N_{3B} and $N_{3A} + N_{3B}$ at M = 0.70.

SYMBOL	CONFIGURATION
◯	FPR = 1.25
▢	FPR = 1.37
◇	FPR = 1.48

MACH NUMBER = 0.7

N_{3A} + N_{3B} NACELLES
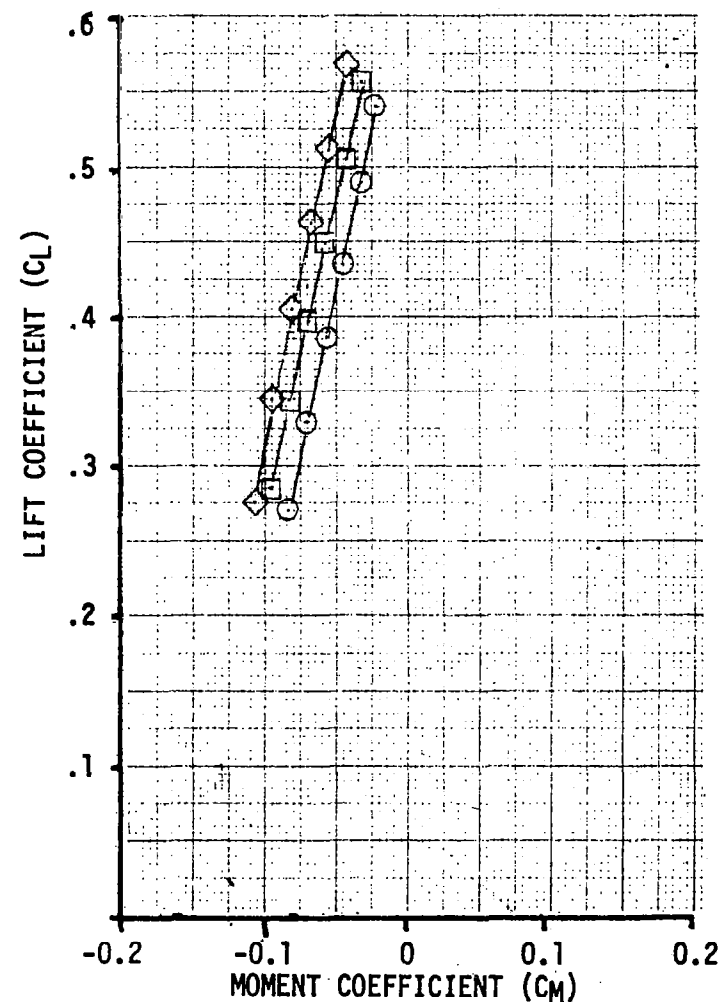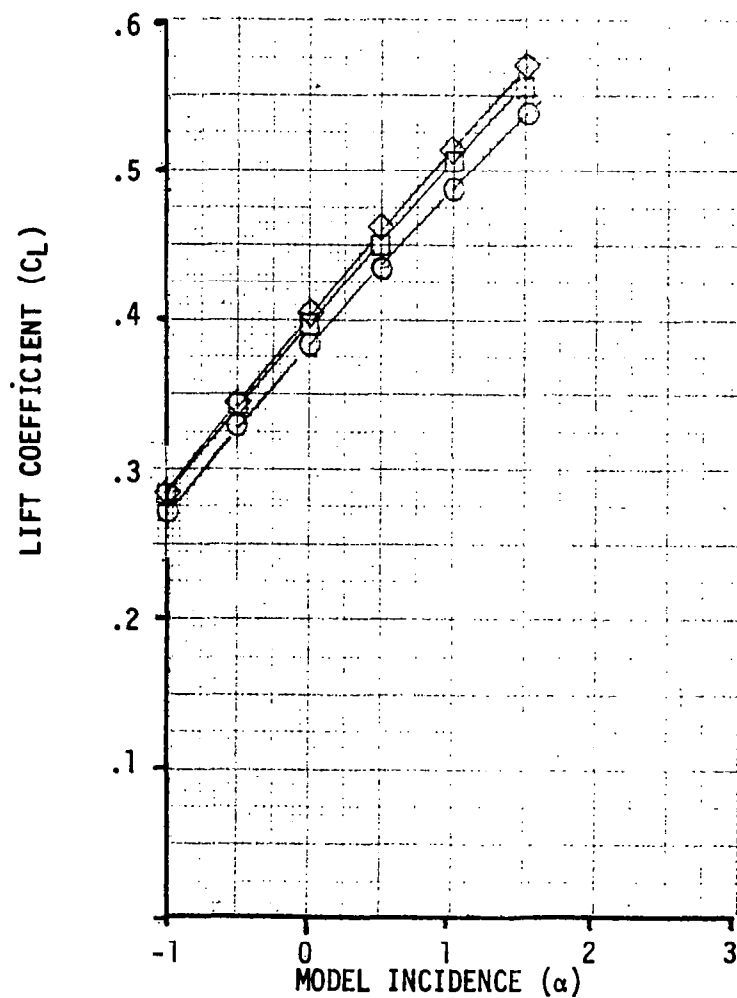
Figure 11.97. Lift and Pitching Moment for N_{3A} + N_{3B} at M = 0.70 and Several Power Settings.

FPR = 1.37   MACH NUMBER = 0.70   CONFIGURATION C_L = 0.40

SYM	CONFIGURATION
- - -	WING-BODY
◯	$N_{1A} + N_{1B}$
▢	$N_{3A} + N_{3B}$

LOCAL LIFT COEFFICIENT (C_l)
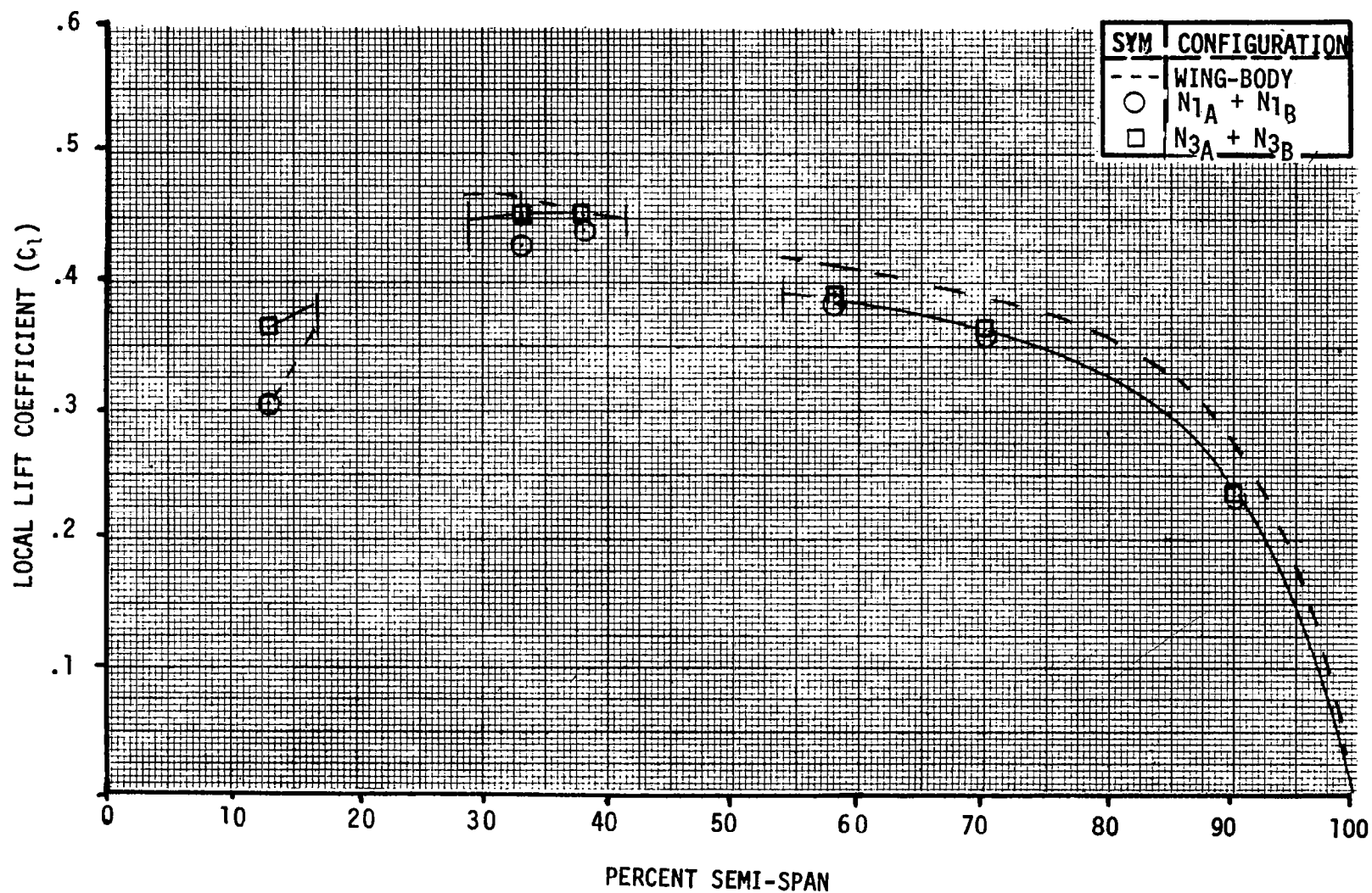
PERCENT SEMI-SPAN

Figure 11.98.   Spanwise Lift Distribution for Four Engine $N_{3A} + N_{3B}$ at M = 0.70.

CONFIGURATION C_L = 0.4   FAN PRESSURE RATIO = FLOW THROUGH
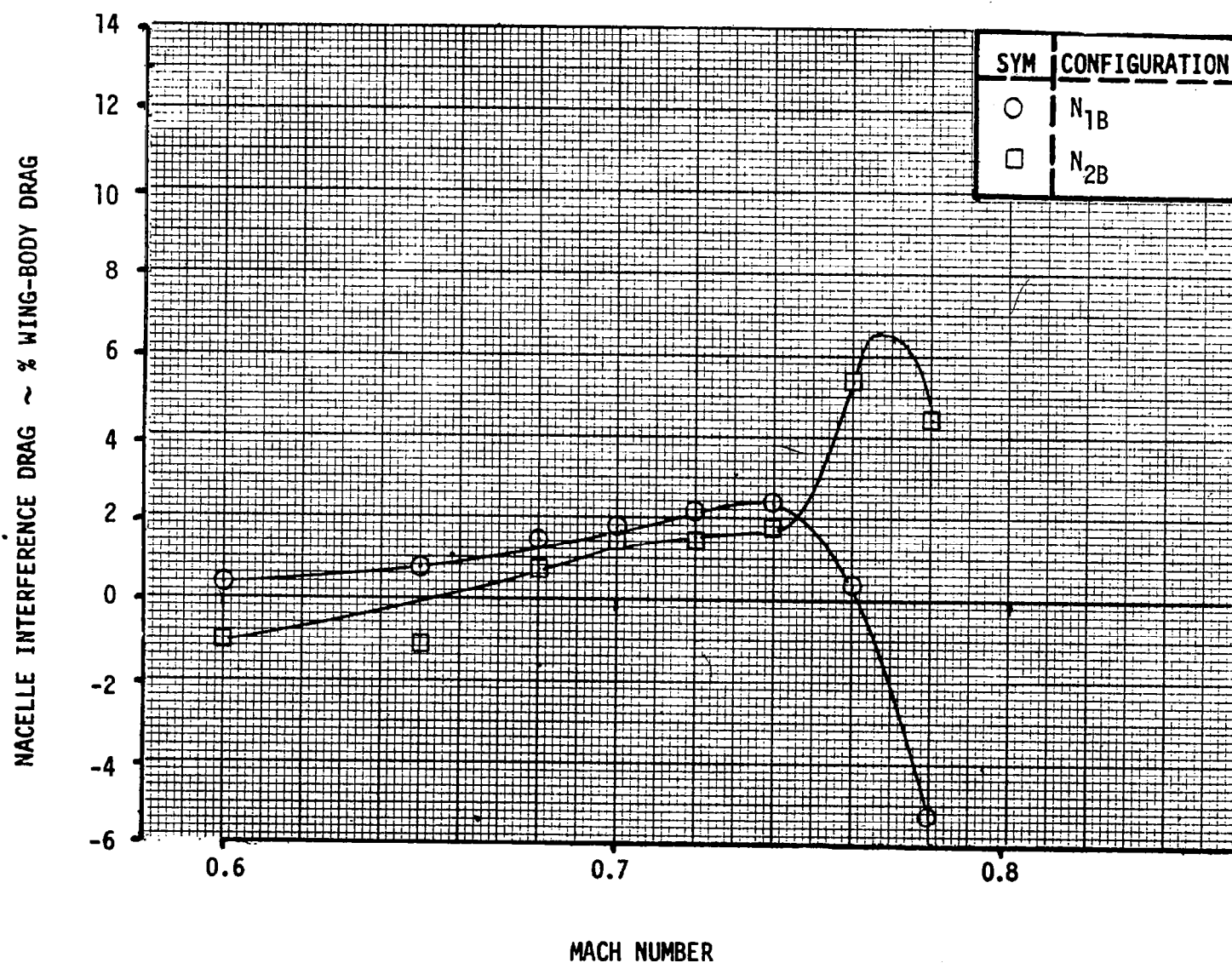
Figure 11.99. Comparison of Flow Through Nacelle Interference Drag - N_{1B} vs N_{2B}.

ALPHA = 0.5

33 PERCENT SEMI-SPAN
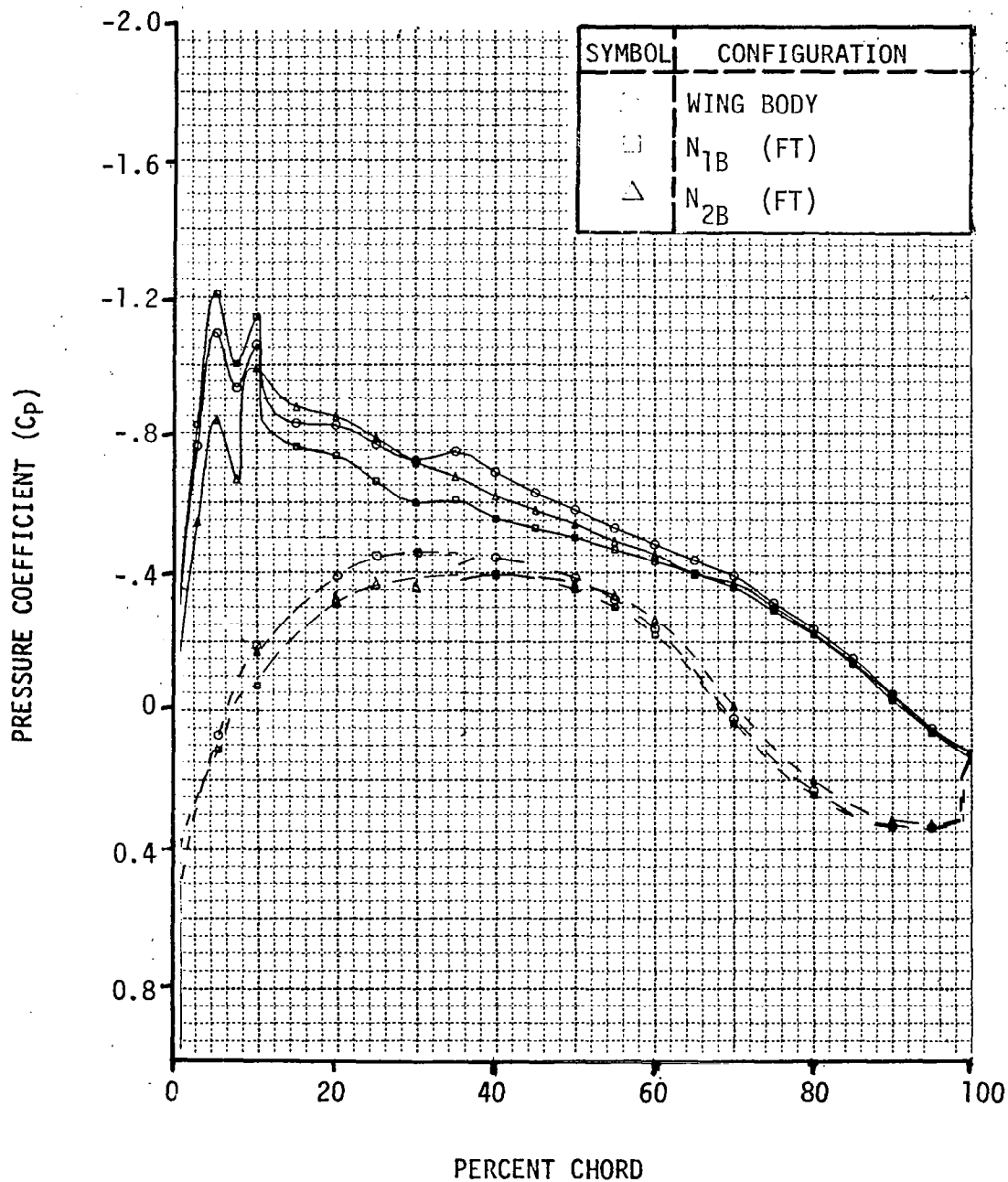
MACH NUMBER = 0.70

Figure 11.100. Wing Surface Pressure Distribution for Wing-Body, N_{1B} and N_{2B} at M = 0.70 and Flow Through Conditions.
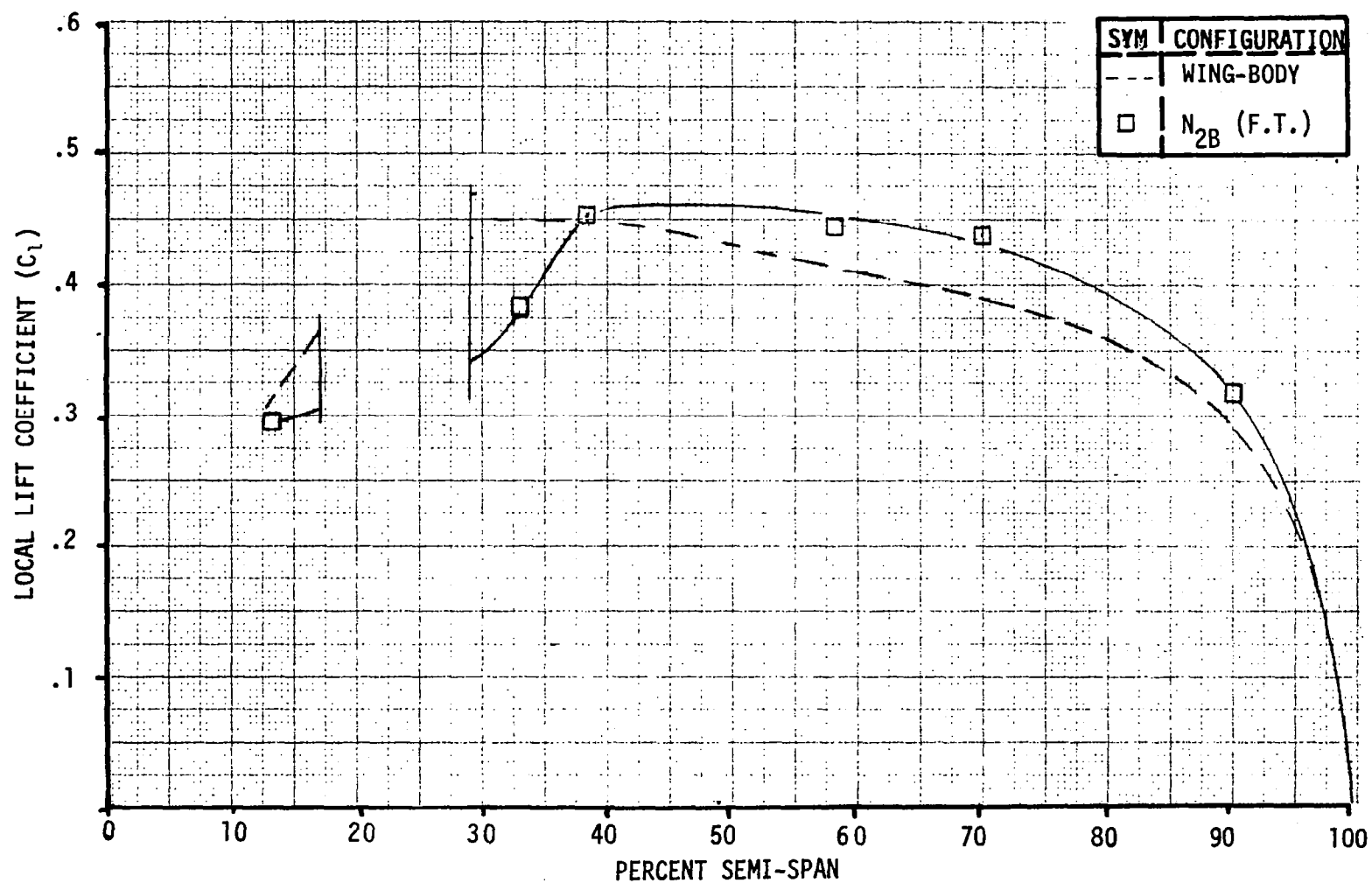
Figure 11.101. Effect of Flow-Through N_{2B} on Spanwise Lift Distribution at M = 0.70.
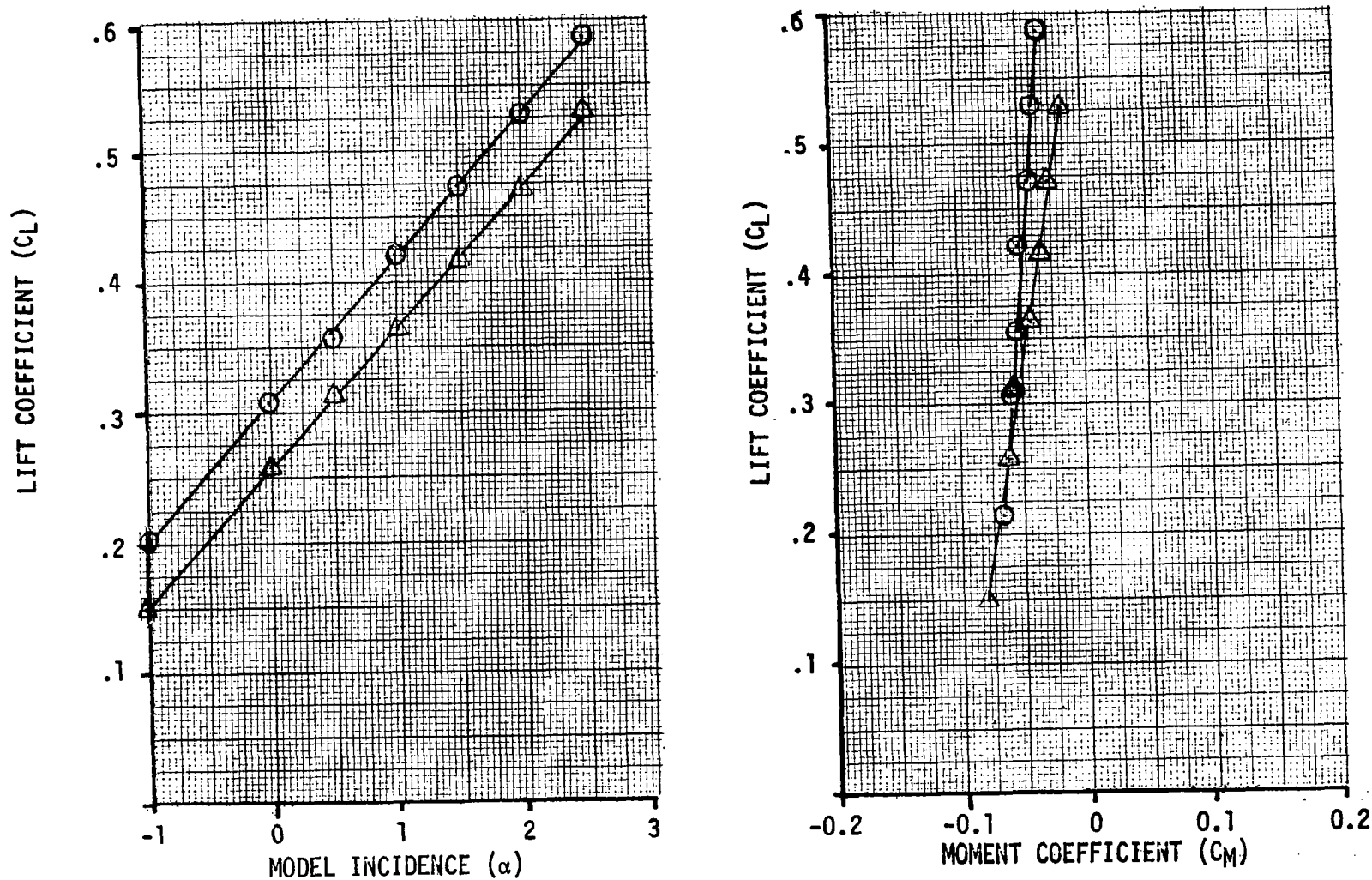
Figure 11.102. Lift and Pitching Moment for Flow Through N_{2B} at M = 0.70.

33 PERCENT SEMI-SPAN

MACH NUMBER = 0.76

FLOW-THROUGH
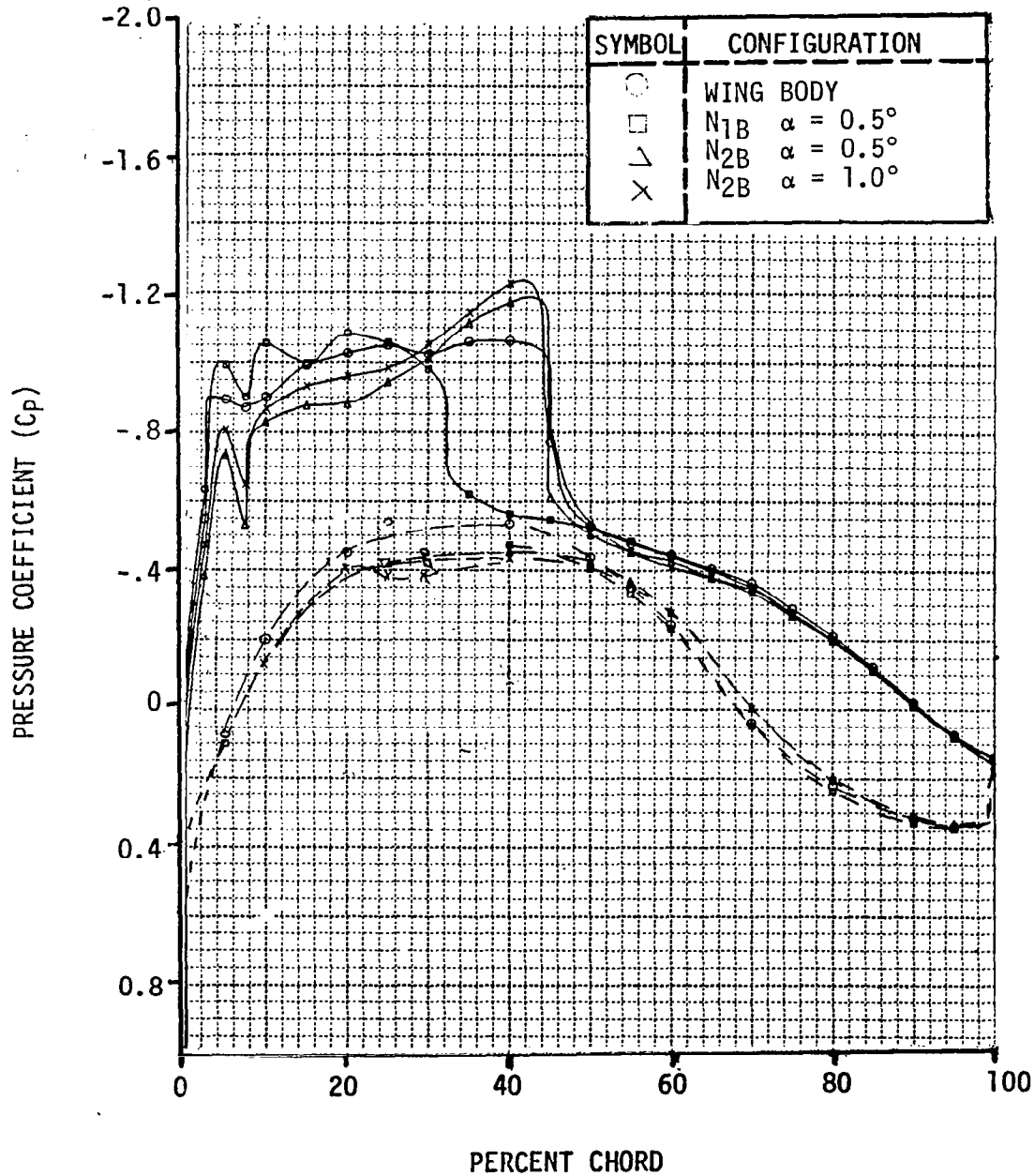
Figure 11.103. Effect of the Nacelle Contouring on Wing Surface Pressures at M = 0.76.
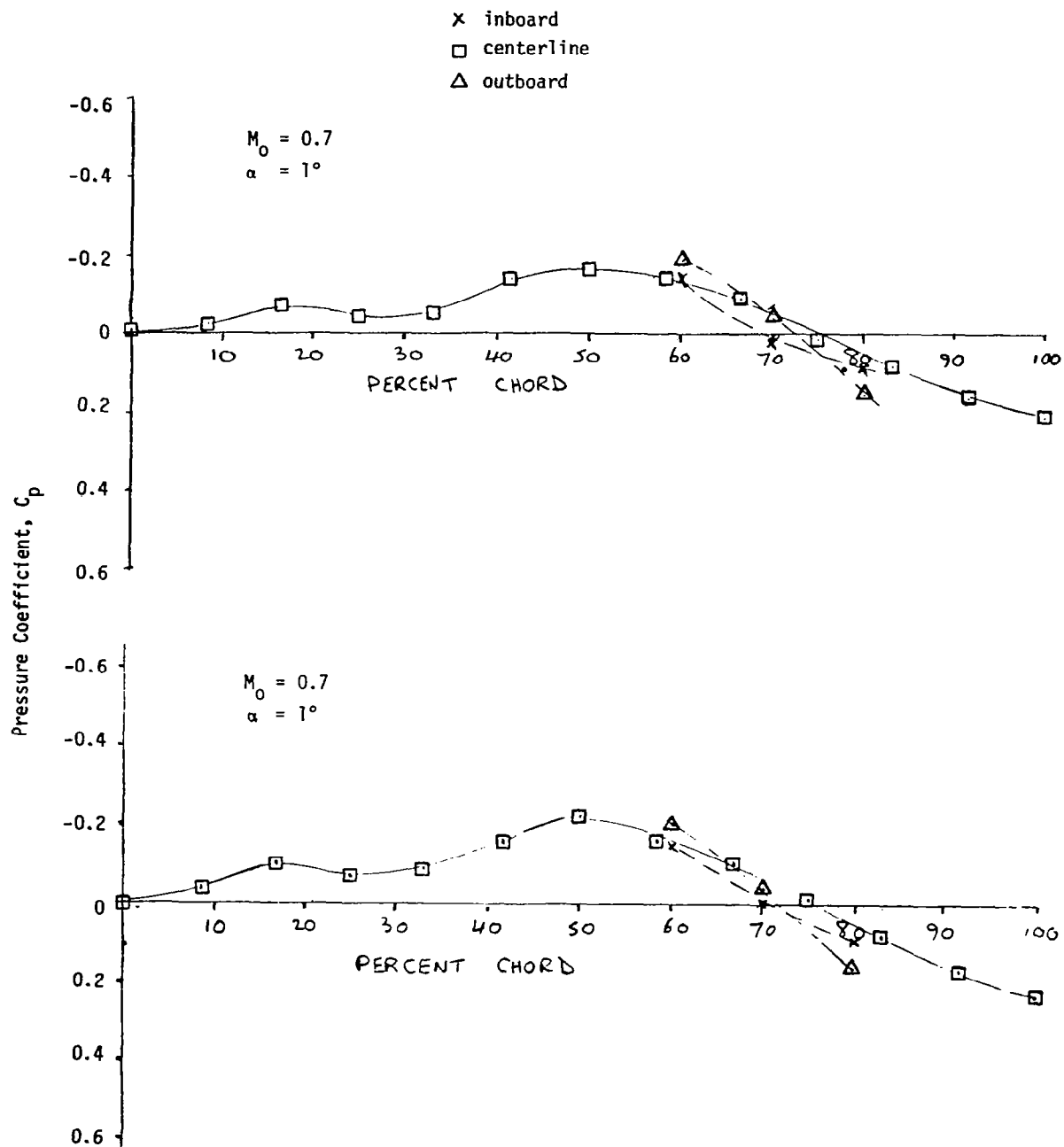
Figure 11.104. Lower Surface Fairing Pressures for N_{2B} (FT)
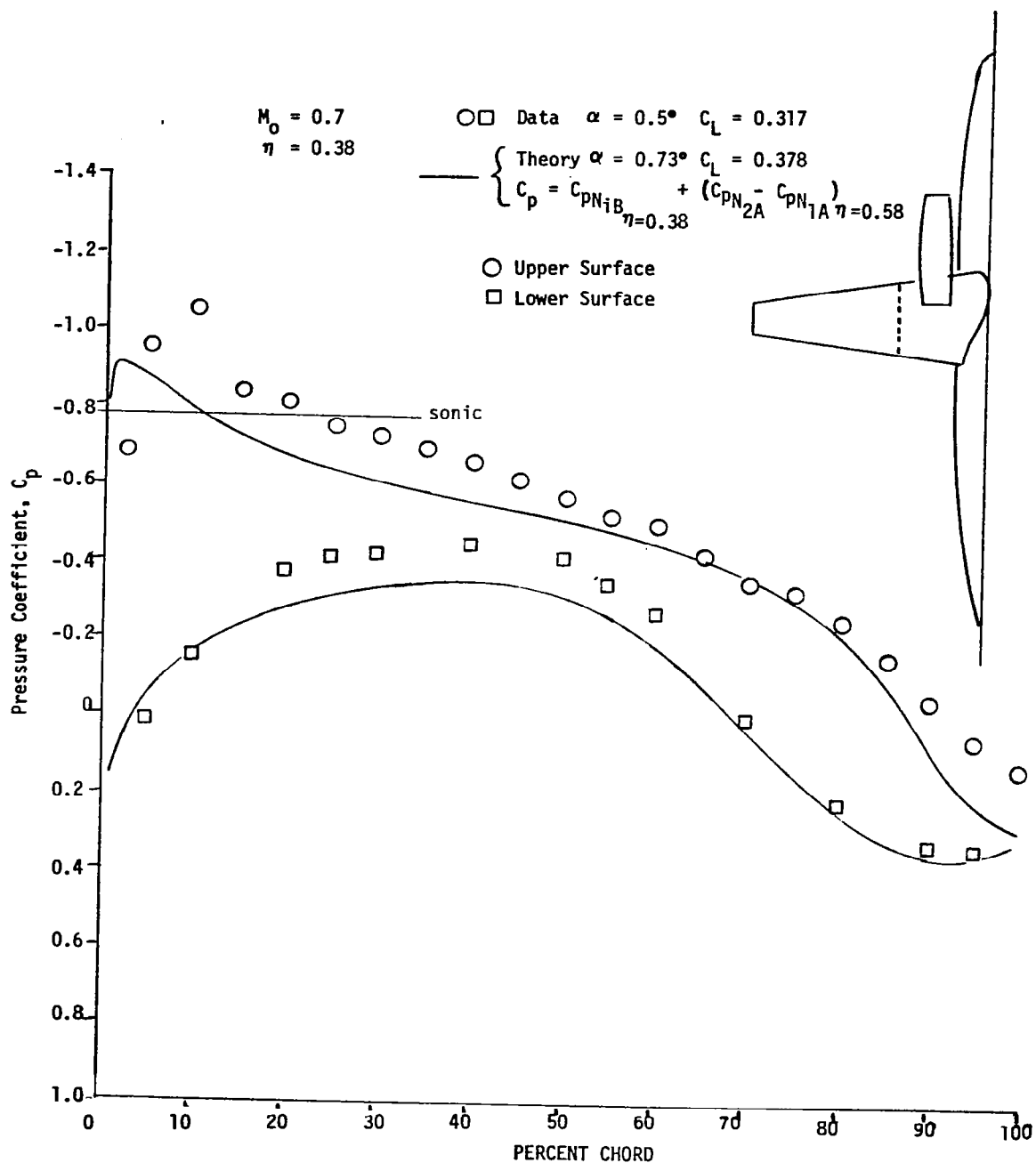
Figure 11.105. Comparison of Theory (Approximate) and Data for N_{2B}
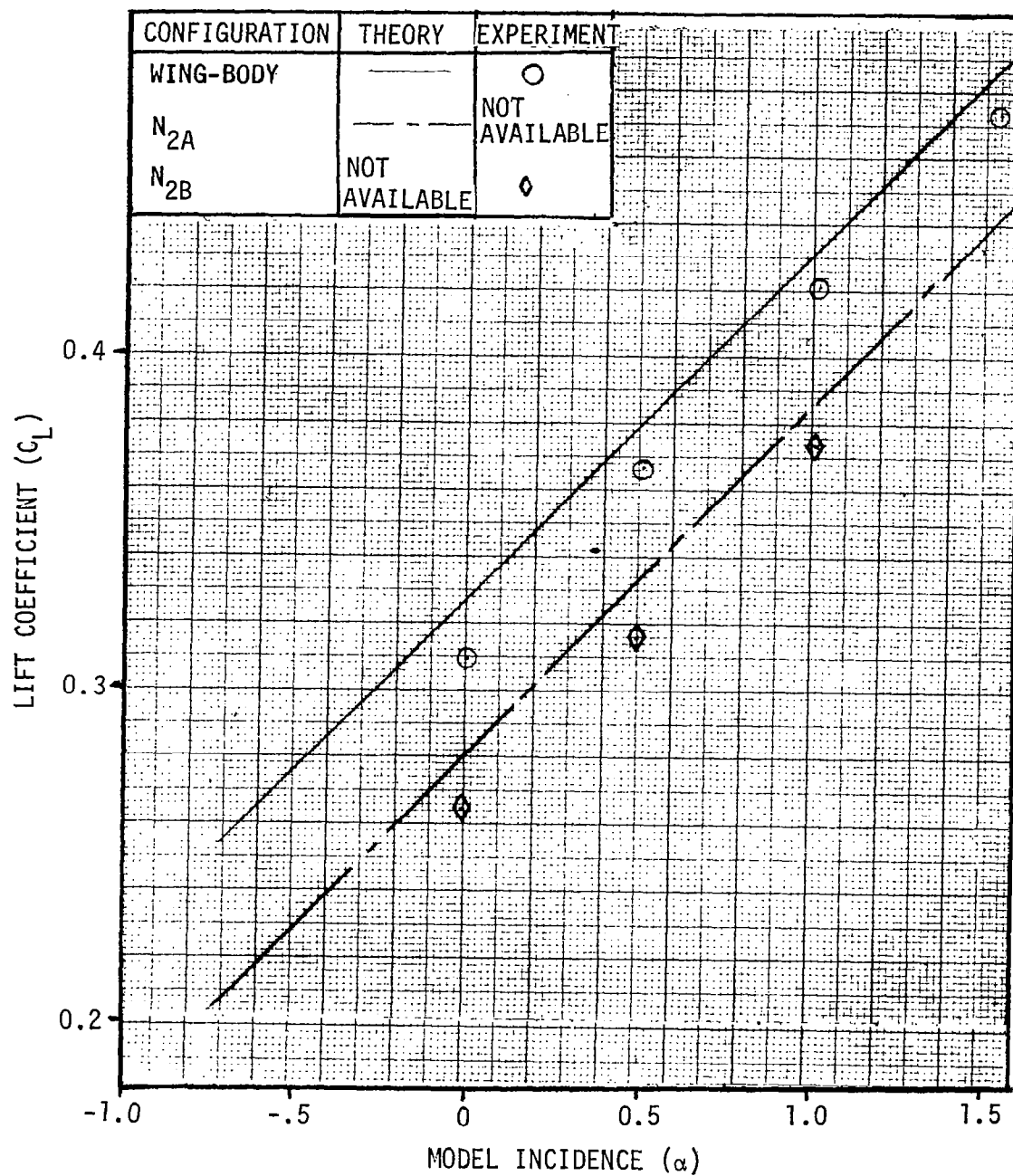
Figure 11.106. Comparison of Theoretical and Experimental
Lift Curves at M = 0.70 - N_2 Nacelles.

ALPHA = 0.5°

33 PERCENT SEMI-SPAN

MACH NUMBER = 0.7

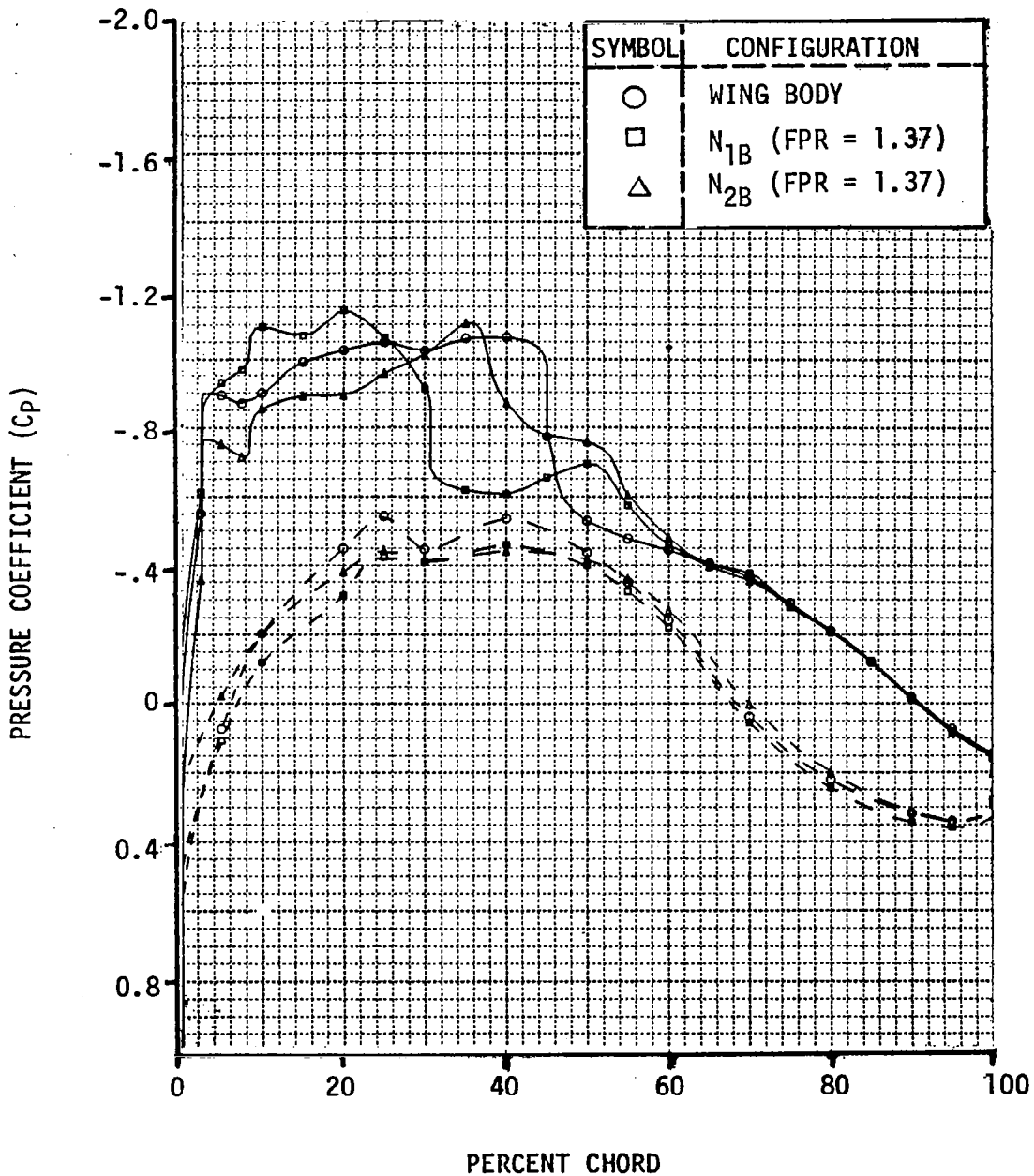| SYM	CONFIGURATION
⊙	WING + BODY
⊡	N_{1B} (FPR=1.37)
△	N_{2B} (FPR=1.37)
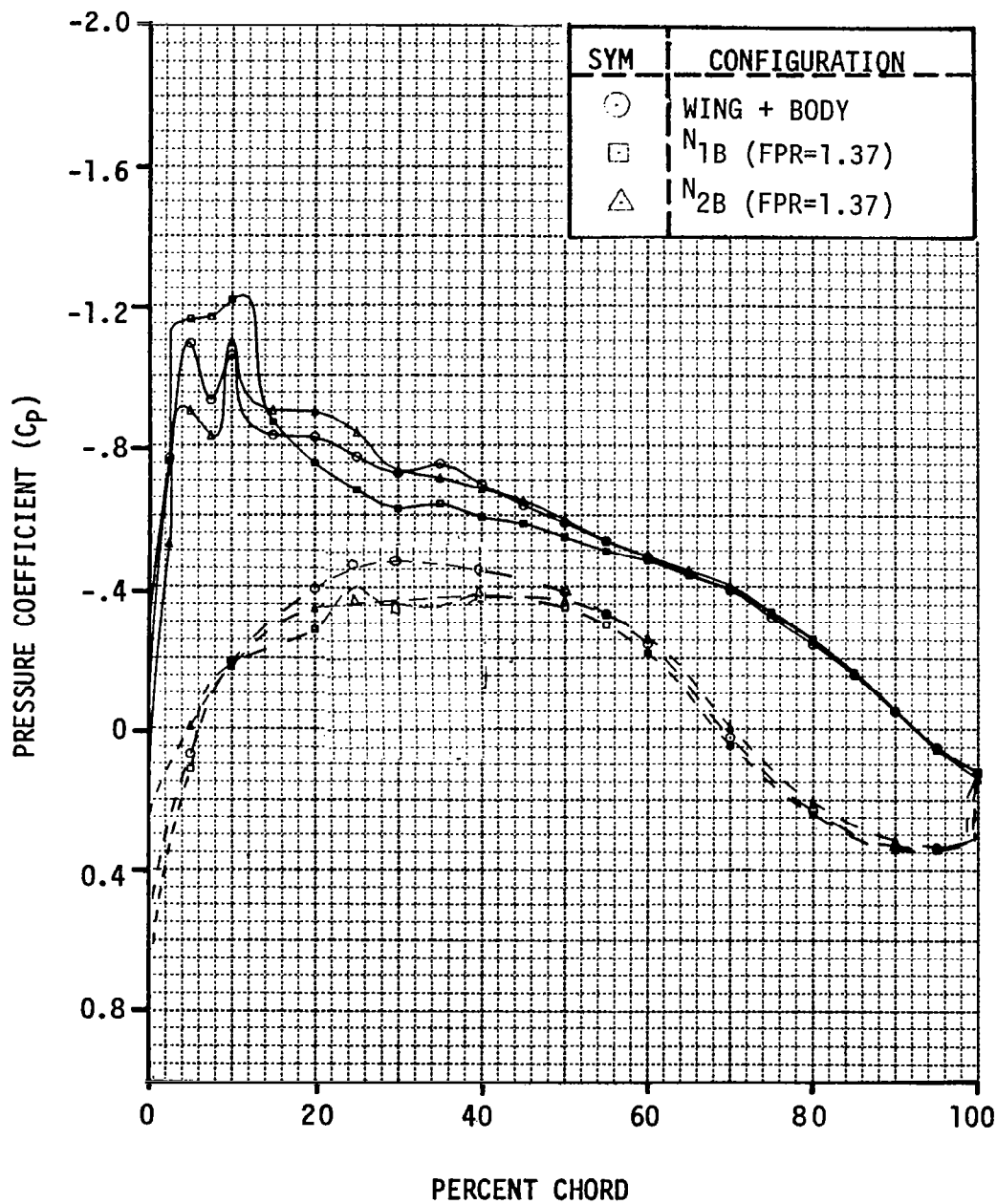
Figure 11.107. Wing Surface Pressure Distributions for the Wing-Body, N_{1B} and N_{2B} at 33% Semispan and M = 0.7
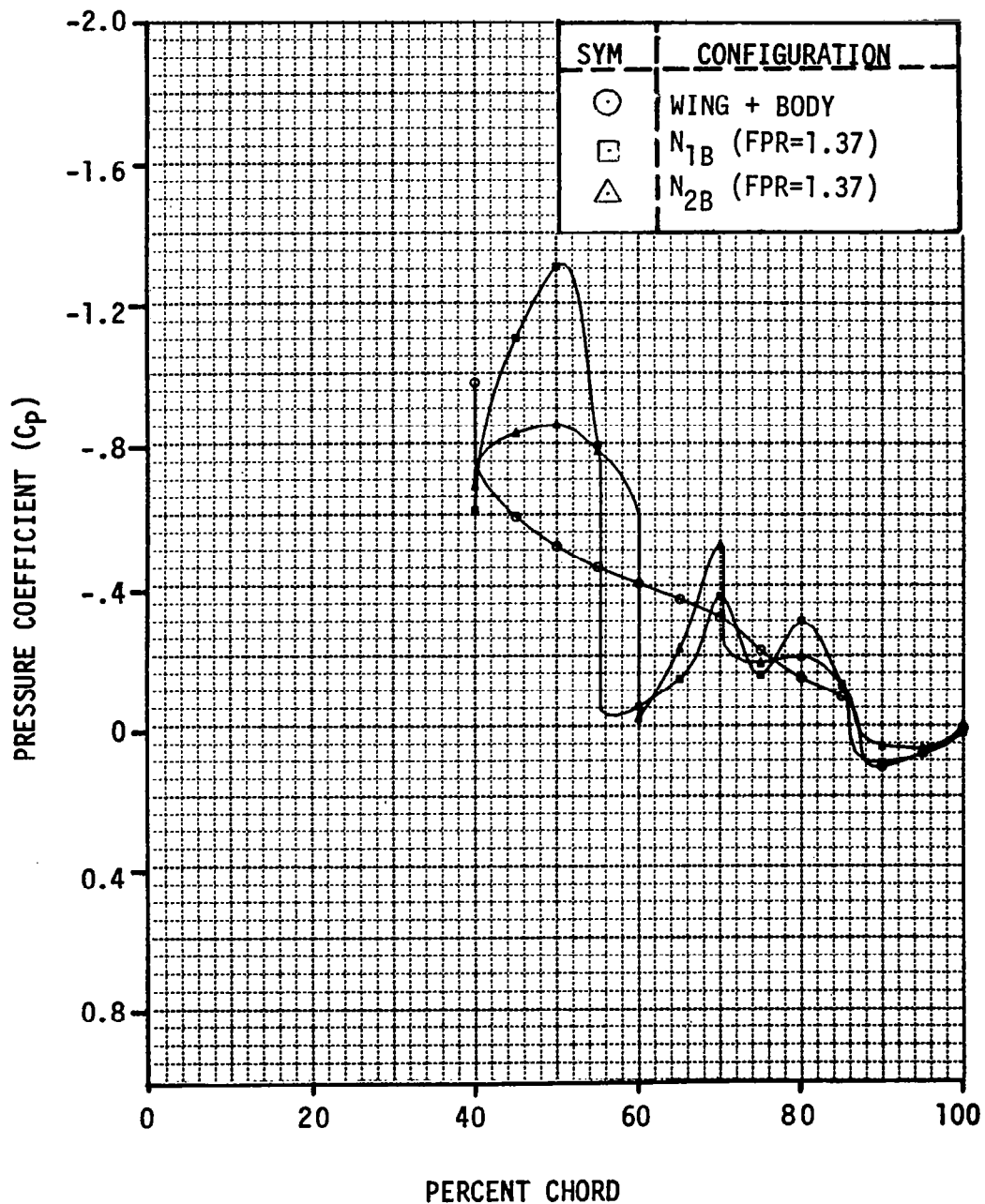
ALPHA = 0.5°

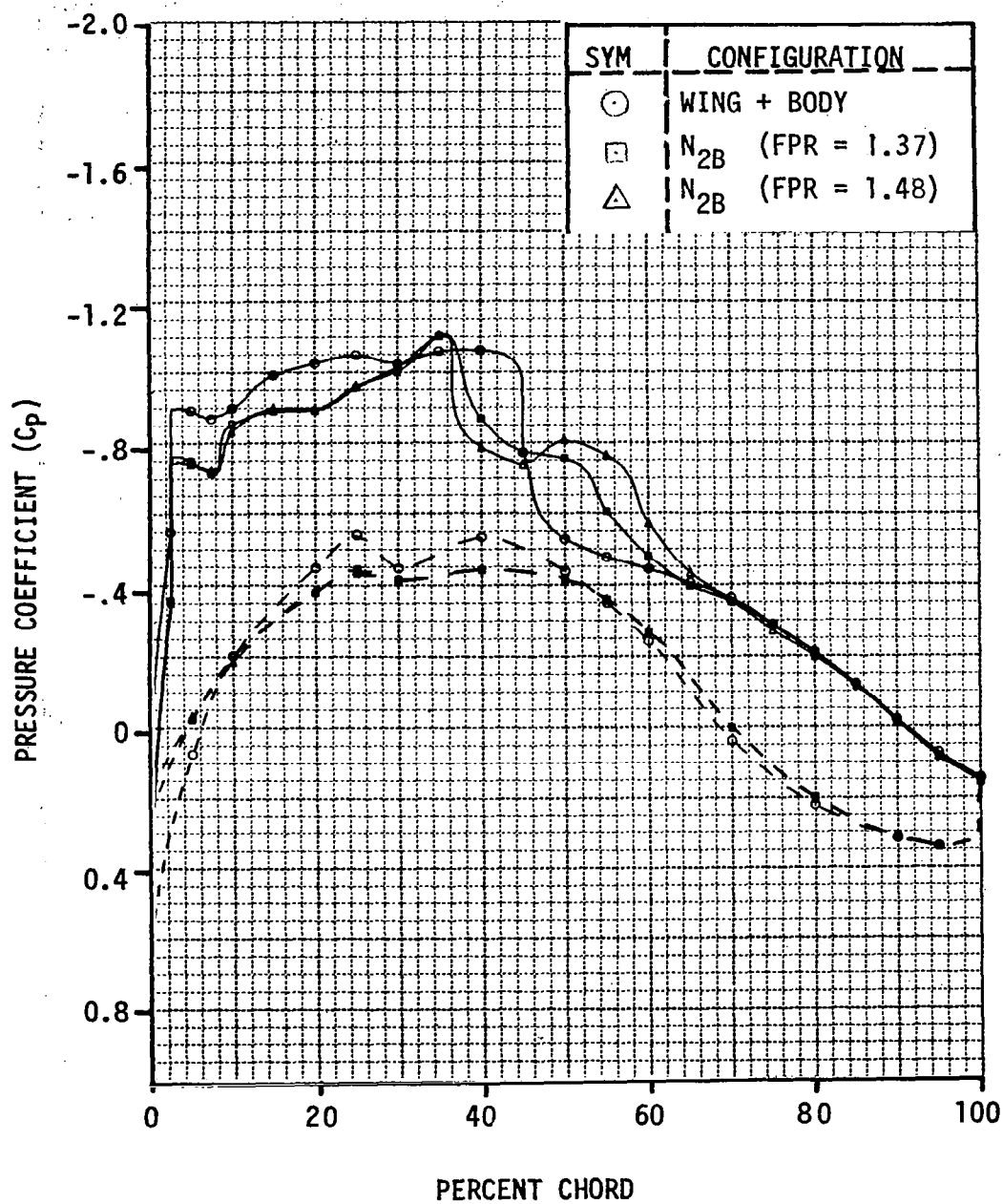23 PERCENT SEMI-SPAN

MACH NUMBER = 0.7

SYM	CONFIGURATION
⊙	WING + BODY
⊡	N_{1B} (FPR=1.37)
△	N_{2B} (FPR=1.37)
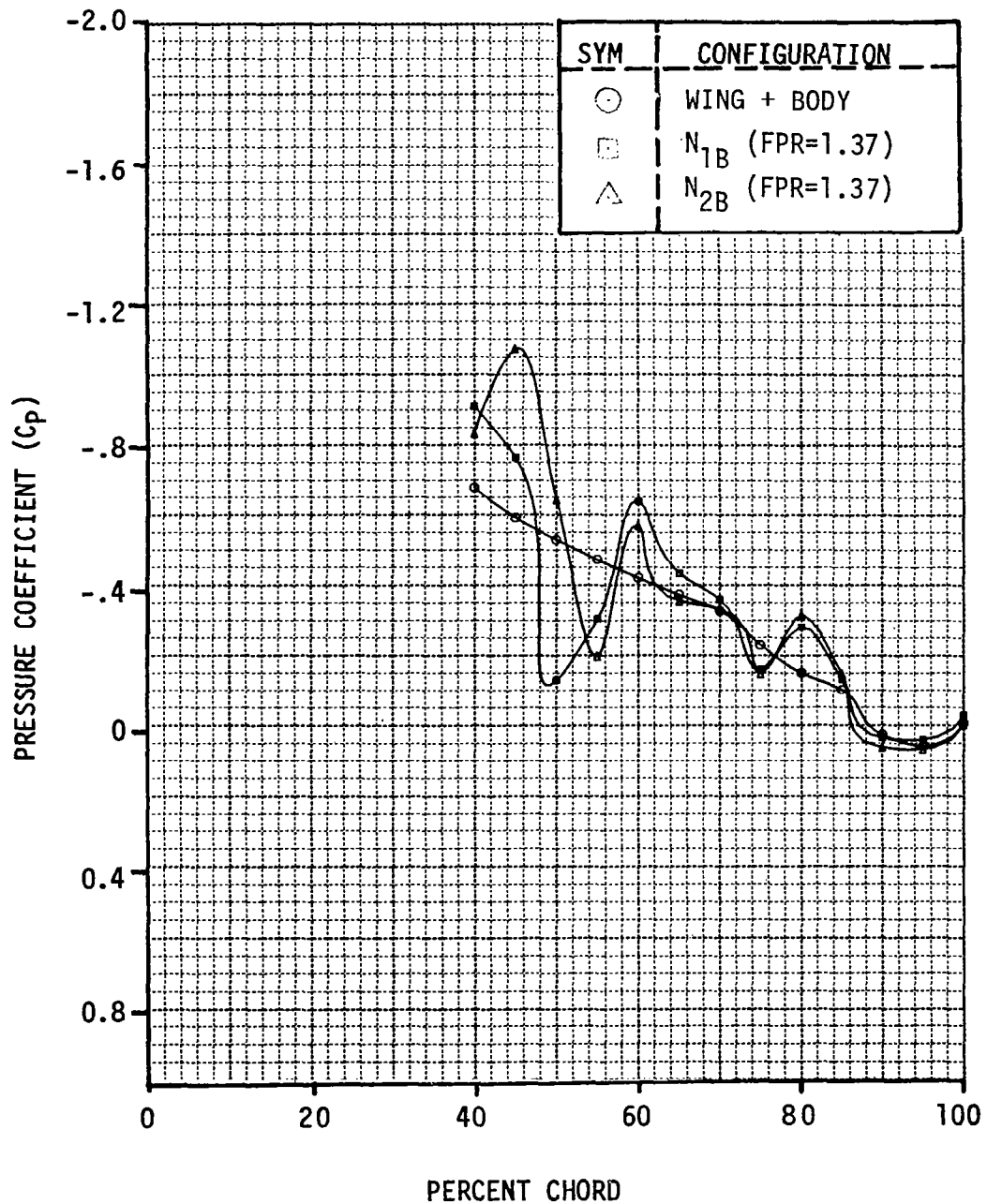
Figure 11.108. Wing Surface Pressures in the Jet for the Wing-Body, N_{1B} and N_{2B} at 23% Semispan and M = 0.7

CONFIGURATION C_L = 0.4   FAN PRESSURE RATIO = 1.37
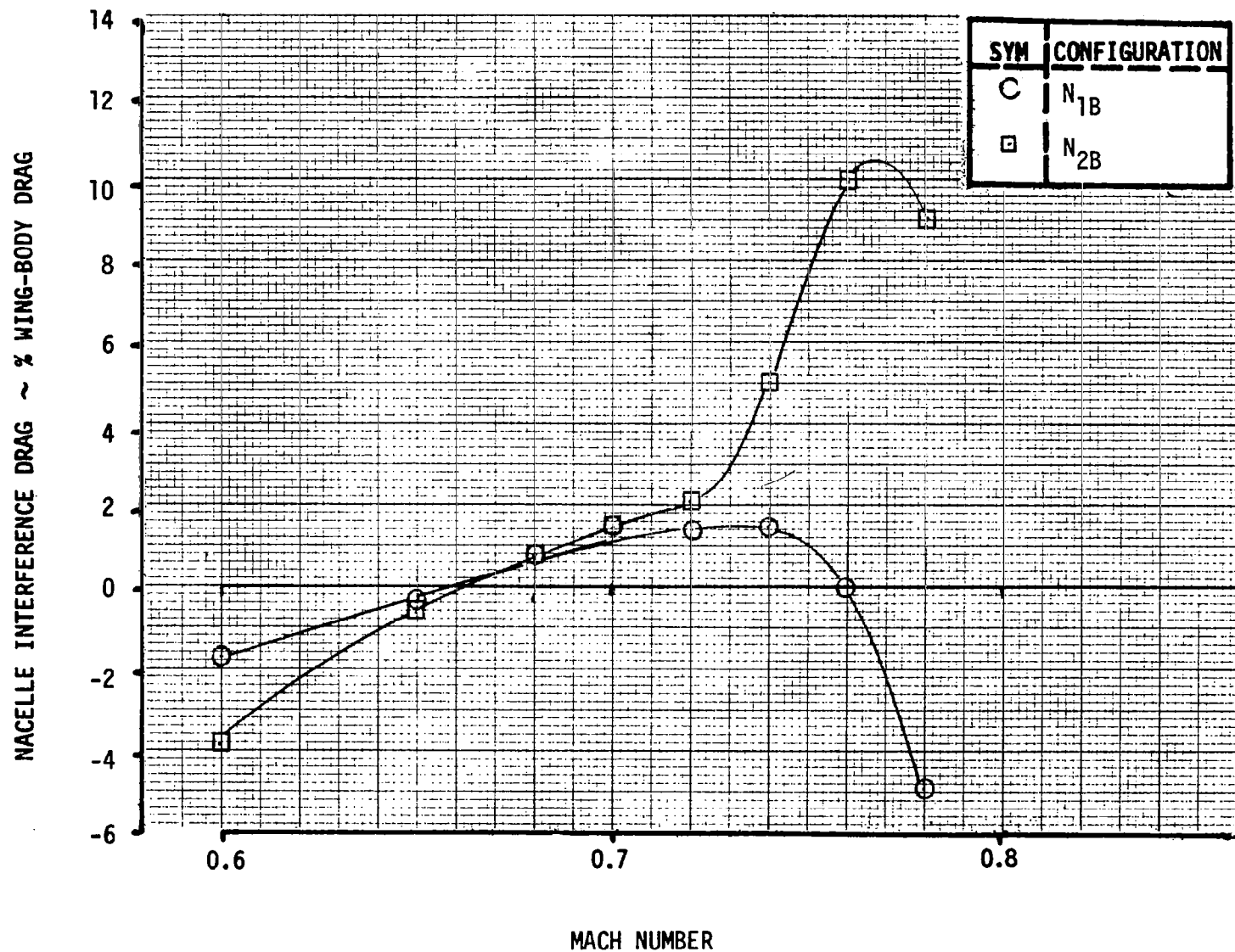
Figure 11.109.   Comparison of Powered Nacelle Interference Drag - N_{1B} vs N_{2B}

CONFIGURATION C_L = 0.40 N_{2B}
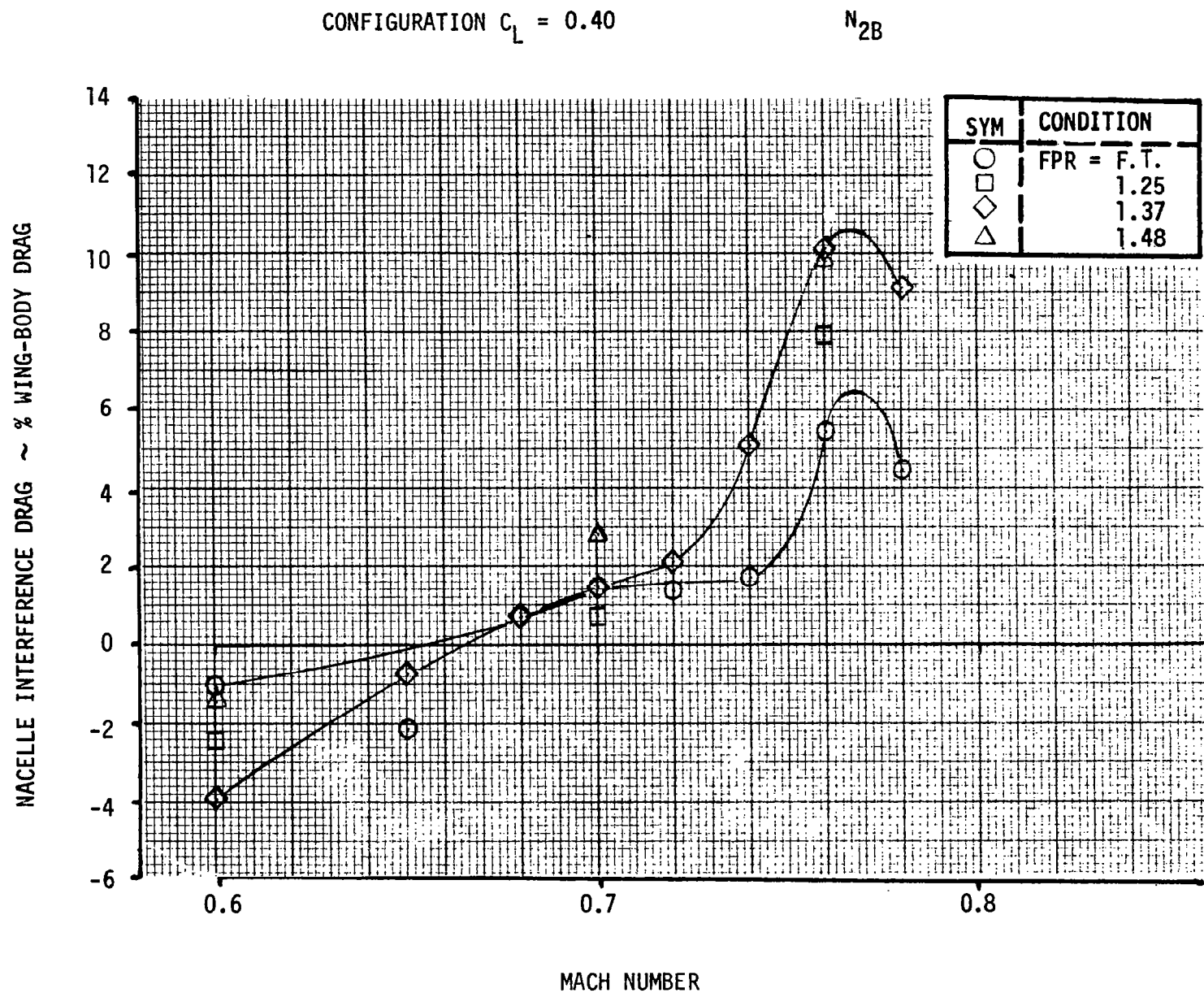
Figure 11.110.   Variation of N_{2B} Nacelle Interference Drag with FPR.

ALPHA = 0.5°

33 PERCENT SEMI-SPAN

MACH NUMBER = 0.76

SYMBOL	CONFIGURATION
○	WING BODY
□	N_{1B} (FPR = 1.37)
△	N_{2B} (FPR = 1.37)

PRESSURE COEFFICIENT (C_P)

PERCENT CHORD

Figure 11.111. Wing Surface Pressure Distributions for the Wing-Body, N_{1B} and N_{2B} at 33% Semispan and M = 0.76.

ALPHA = 0.5°

23 PERCENT SEMI-SPAN

MACH NUMBER = 0.76

Figure 11.112. Wing Surface Pressures in the Jet for the Wing-Body, N_{1B} and N_{2B} at 23% Semispan and M = 0.76

ALPHA = 0.5°

33 PERCENT SEMI-SPAN

MACH NUMBER = 0.76

SYM	CONFIGURATION
⊙	WING + BODY
⊡	N_{2B} (FPR = 1.37)
△	N_{2B} (FPR = 1.48)

Figure 11.113. Effect of Fan Pressure Ratio on the Wing Surface Pressures at 33% Semispan for N_{2B} at FPR = 1.32 and 1.48 and M = 0.76

217

ALPHA = 0.5°

23 PERCENT SEMI-SPAN
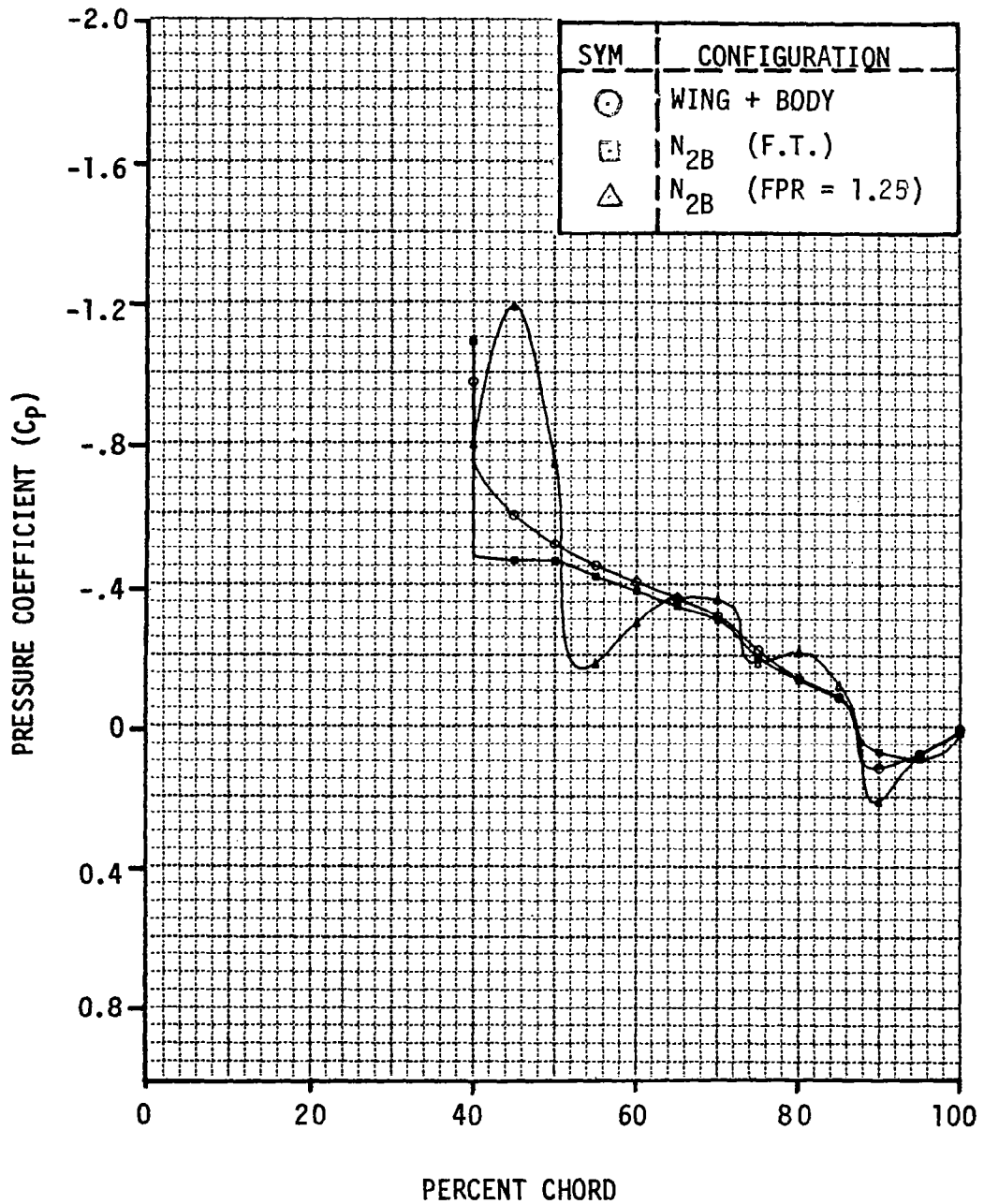
MACH NUMBER = 0.76

Figure 11.114. Wing Surface Pressures in the Jet for the Wing-Body and N_{2B} at a FPR of F.T. and 1.25 and M = 0.76

ALPHA = 0.5°

23 PERCENT SEMI-SPAN

MACH NUMBER = 0.76
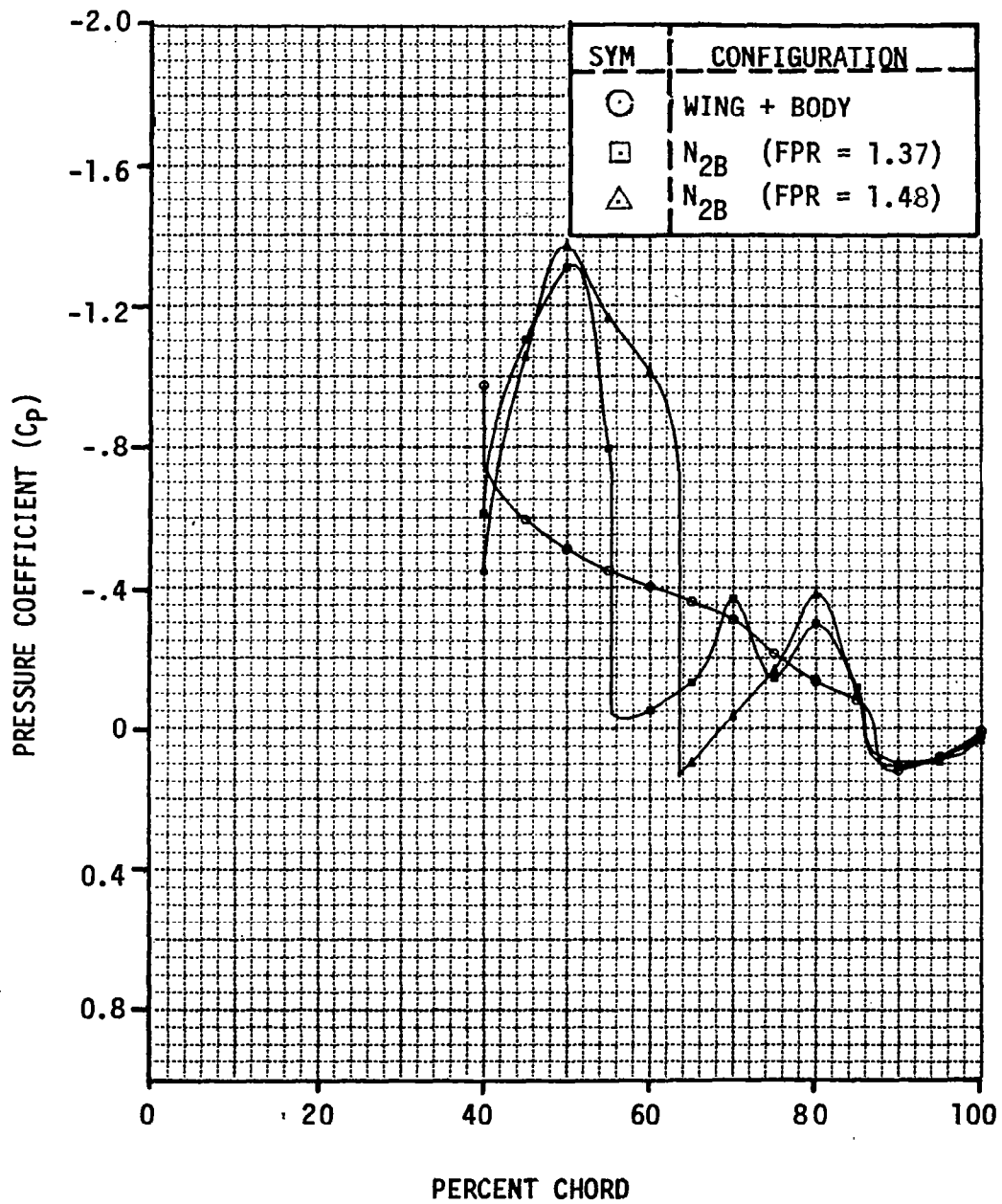
Figure 11.115. Wing Surface Pressures in the Jet for the Wing-Body and N_{2B} at a FPR of 1.32 and 1.48 and M = 0.76
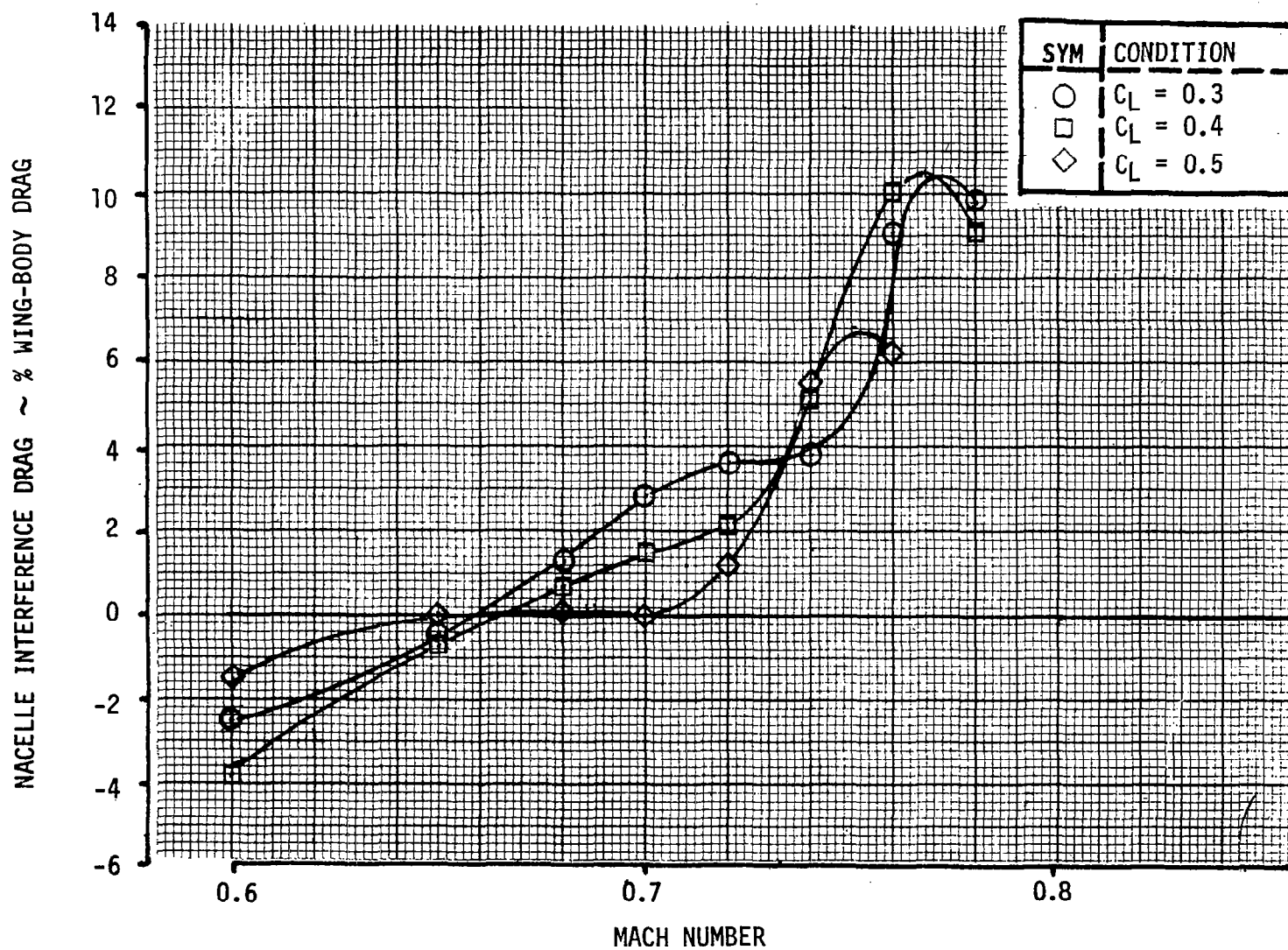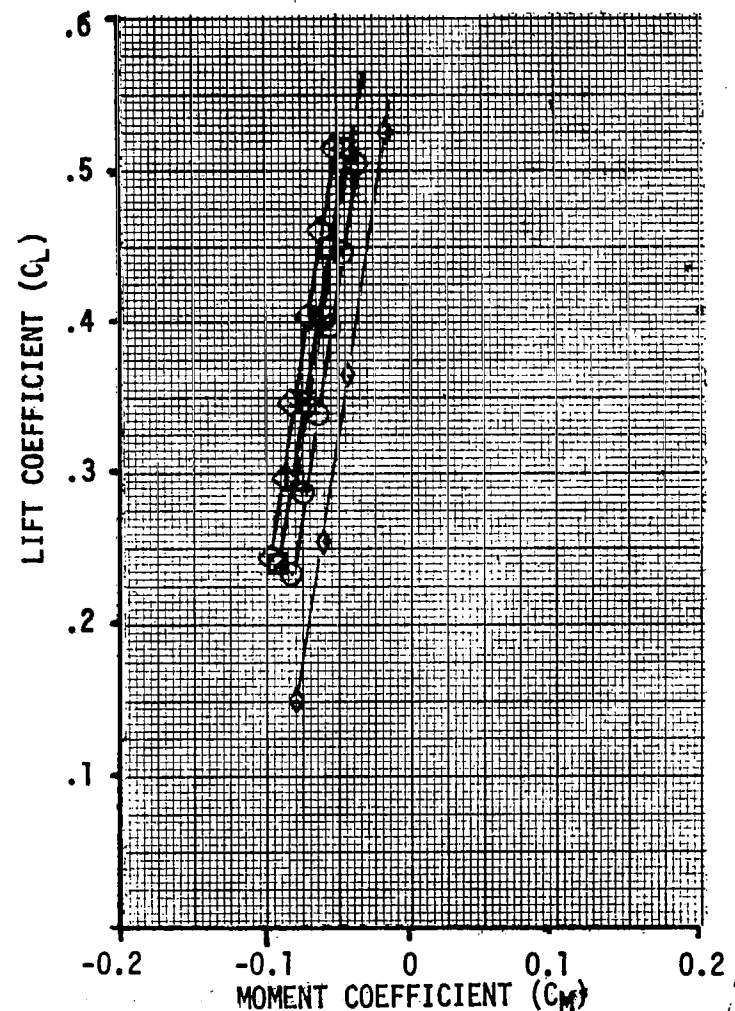
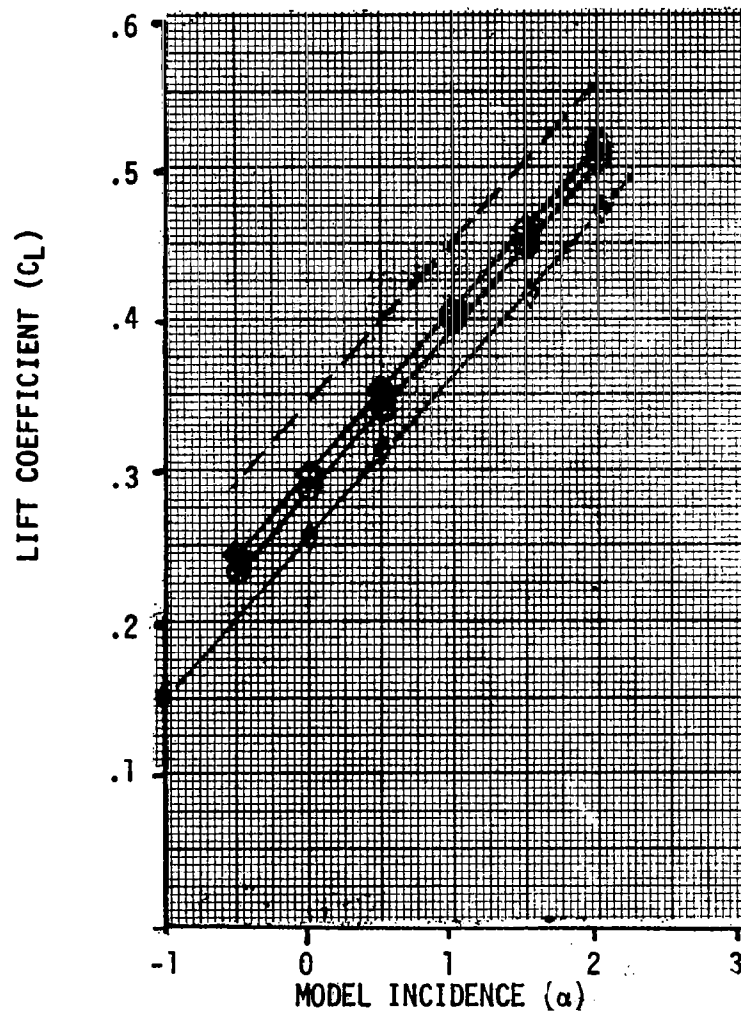Figure 11.116.   Variation of N$_{2B}$ Nacelle Interference with C$_L$.

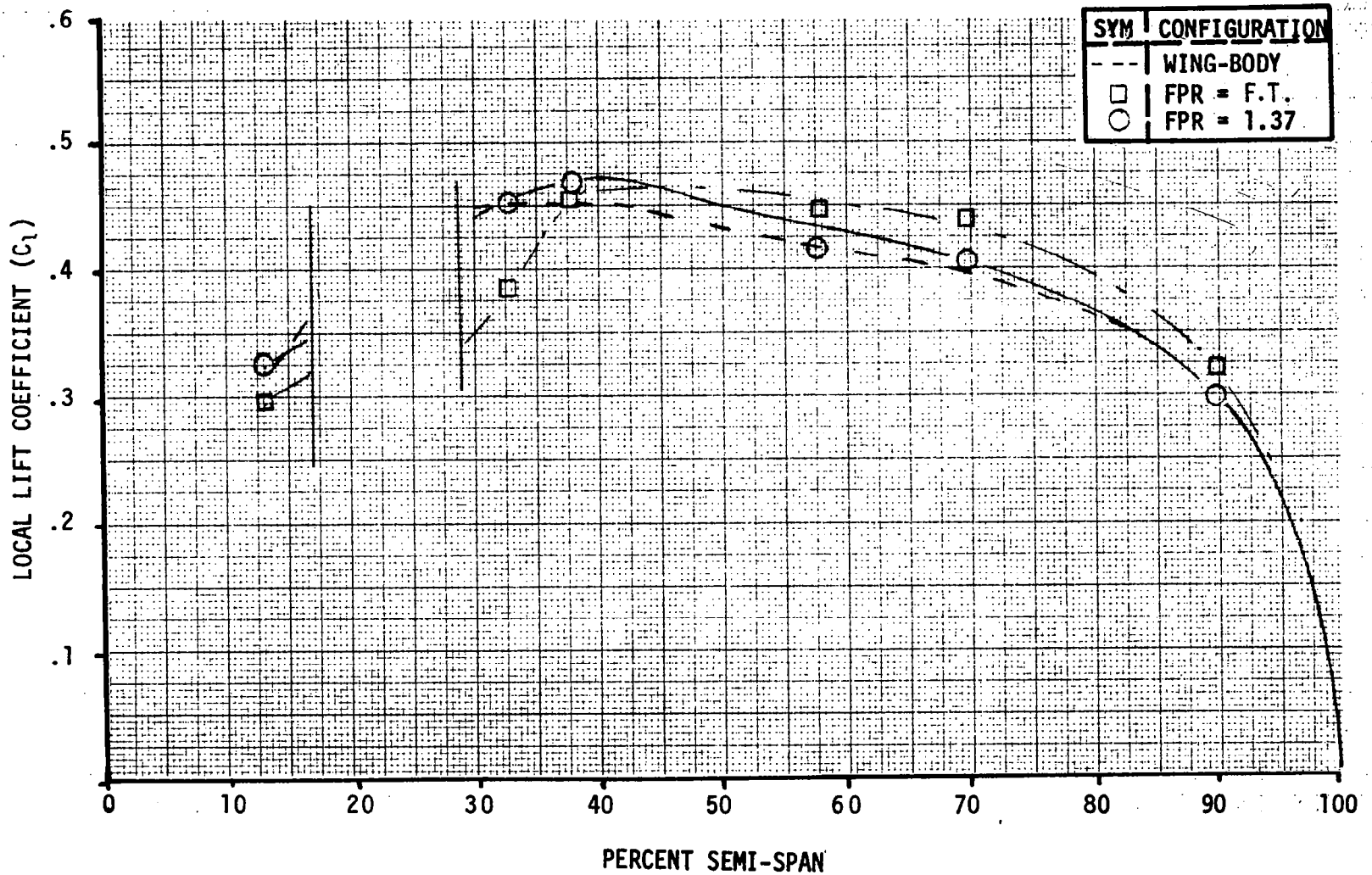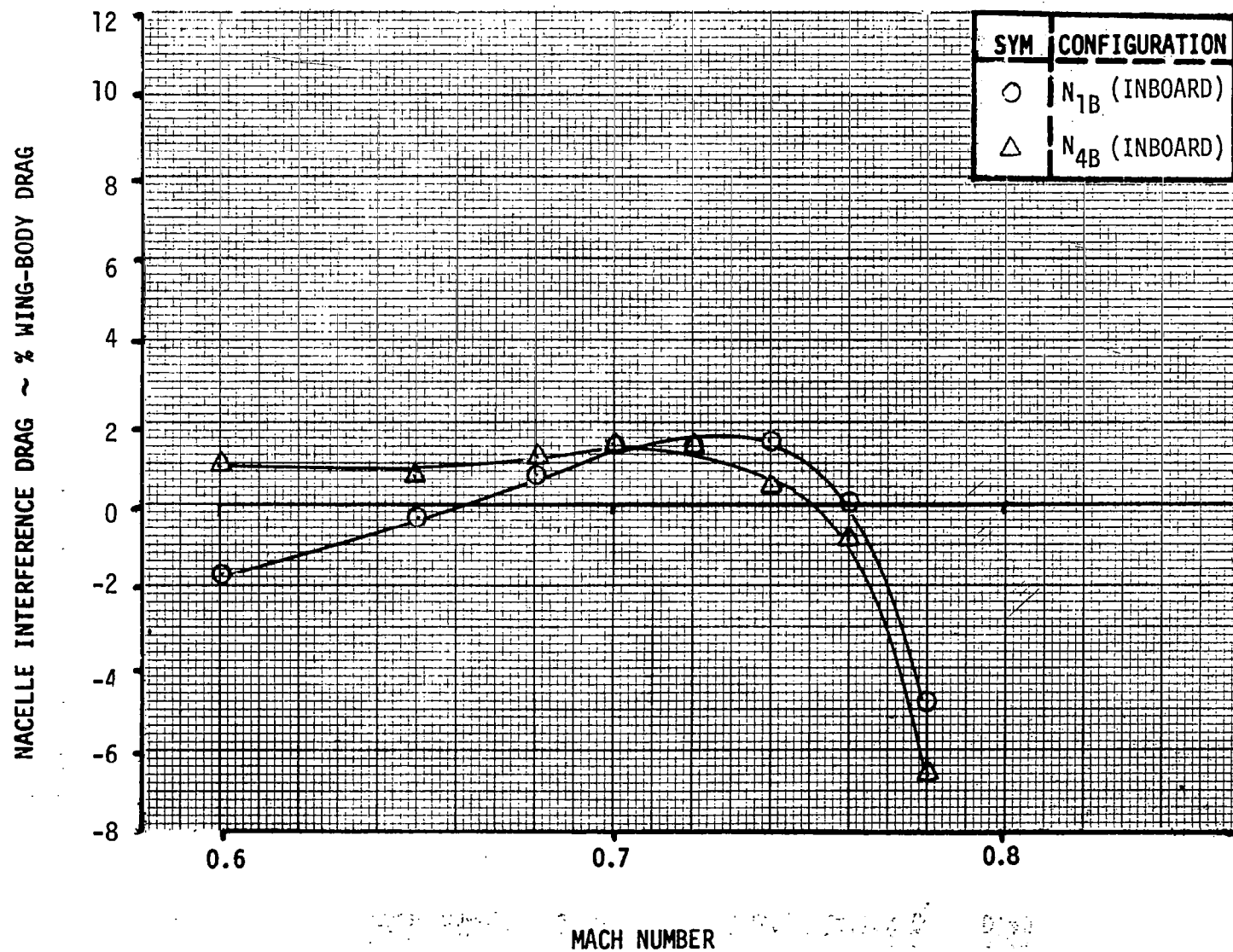Figure 11.117. Lift and Pitching Moment for N_{2B} at M = 0.70 and Several Power Settings.

222

Figure 11.118. Spanwise Lift Distribution for N_{2B} at M = 0.70.

CONFIGURATION C_L = 0.4   FAN PRESSURE RATIO = 1.37

SYM	CONFIGURATION
◯	N_{1B} (INBOARD)
△	N_{4B} (INBOARD)

Figure 11.119.   Comparison of Powered Nacelle Interference Drag for N_{1B} and N_{4B}.

CONFIGURATION C_L = 0.40 N_{4B}
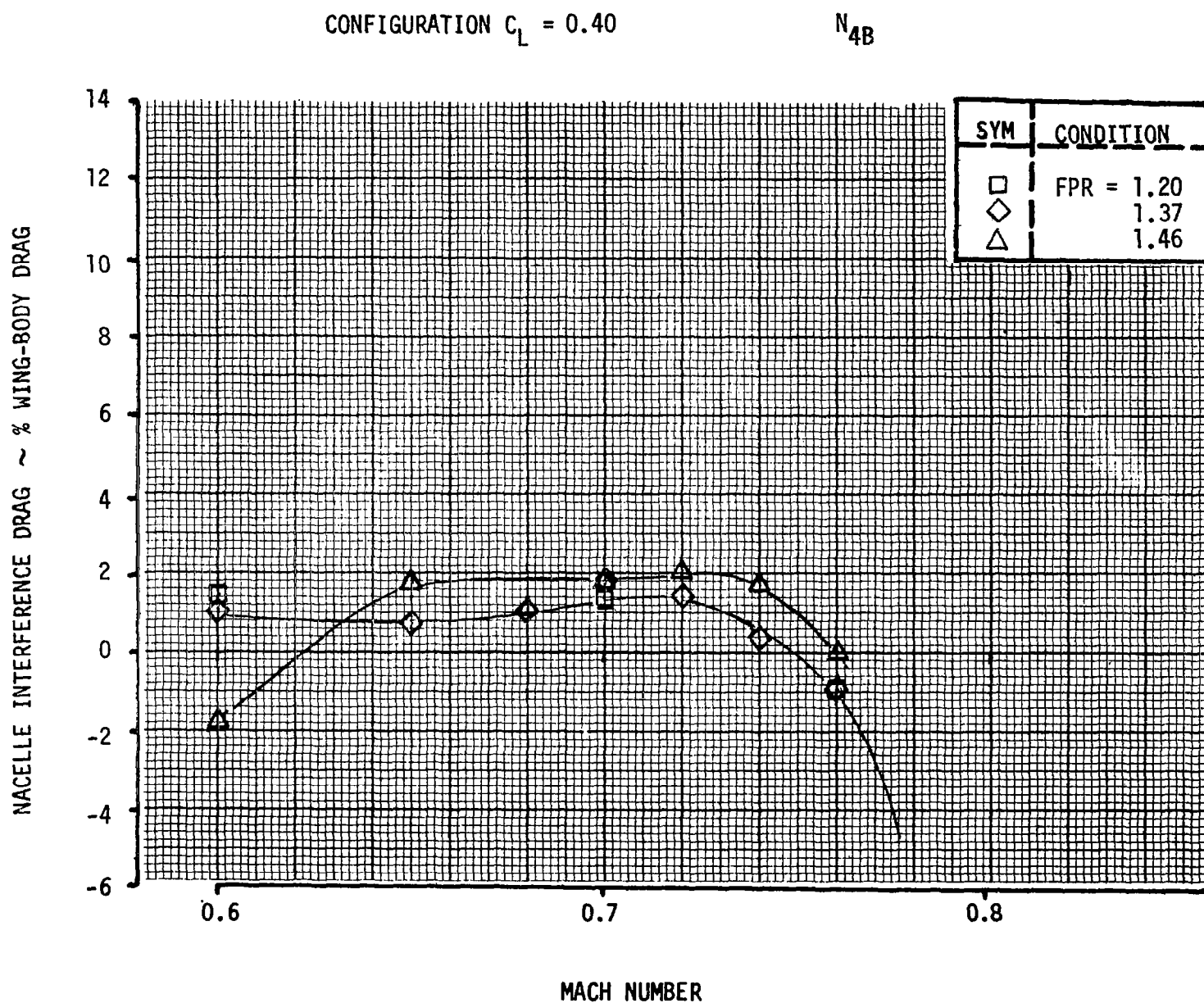

Figure 11.120.   Variation of N_{4B} Nacelle Interference Drag with FPR.

ALPHA = 0.5°

33 PERCENT SEMI-SPAN

MACH NUMBER = 0.7

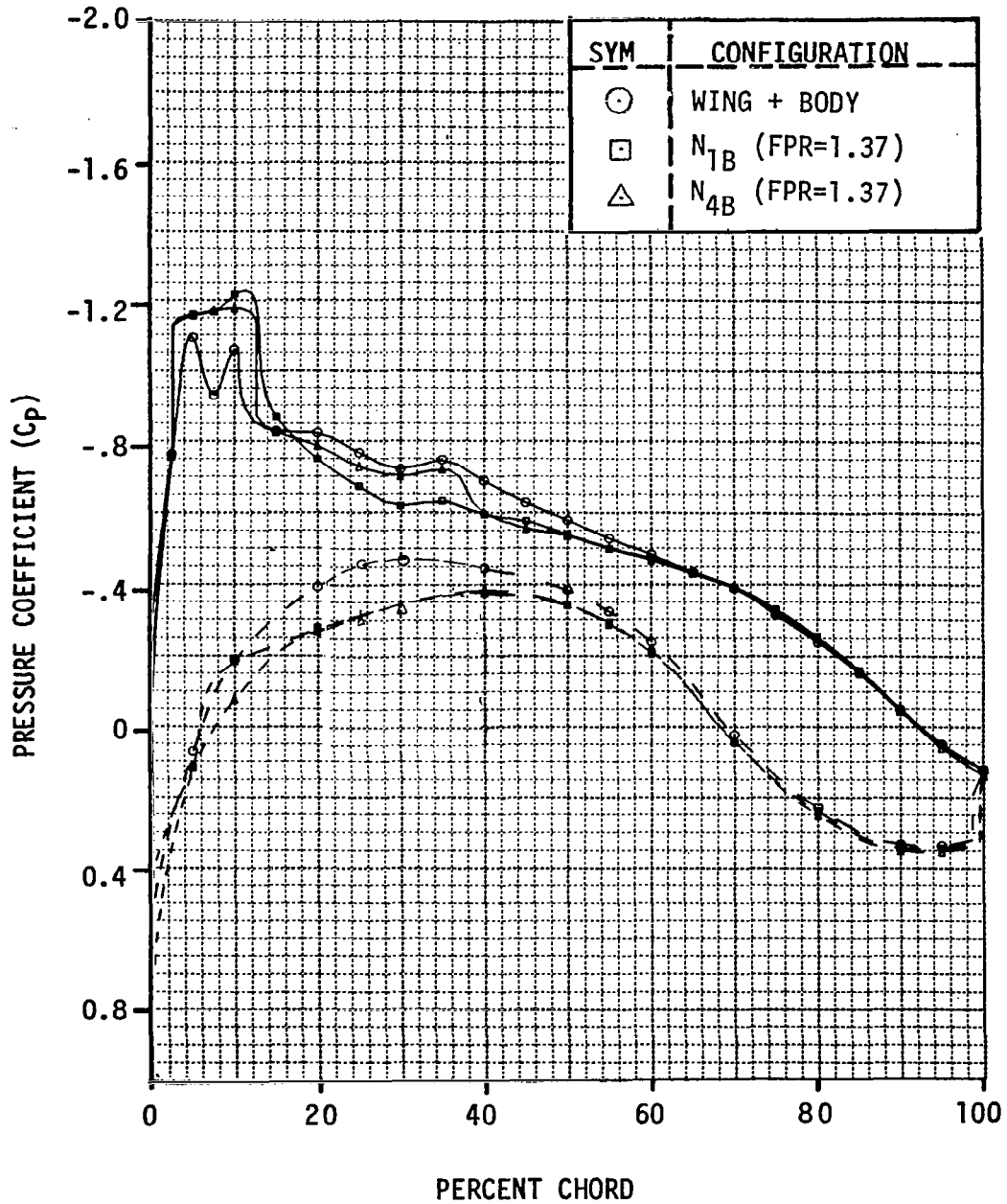| SYM	CONFIGURATION
⊙	WING + BODY
⊡	N_{1B} (FPR=1.37)
△	N_{4B} (FPR=1.37)

PERCENT CHORD

Figure 11.121. Wing Surface Pressure Distributions for the Wing-Body, N_{1B} and N_{4B} at 33% Semispan and M = 0.7

ALPHA = 0.5°

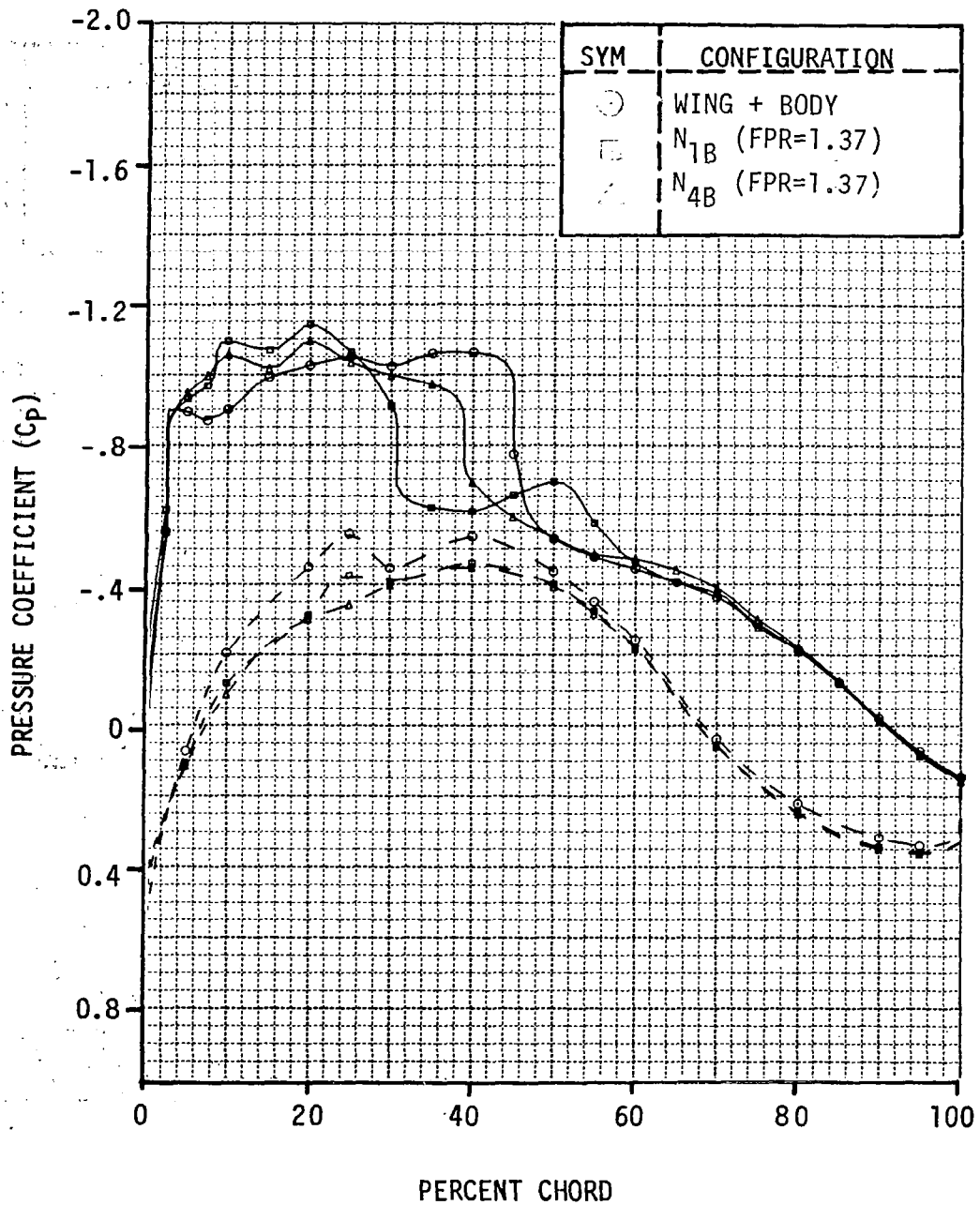33 PERCENT SEMI-SPAN

MACH NUMBER = 0.76

Figure 11.122. Wing Surface Pressure Distributions for the Wing-Body, N_{1B} and N_{4B} at 33% Semispan and M = 0.76

ALPHA = 0.5°

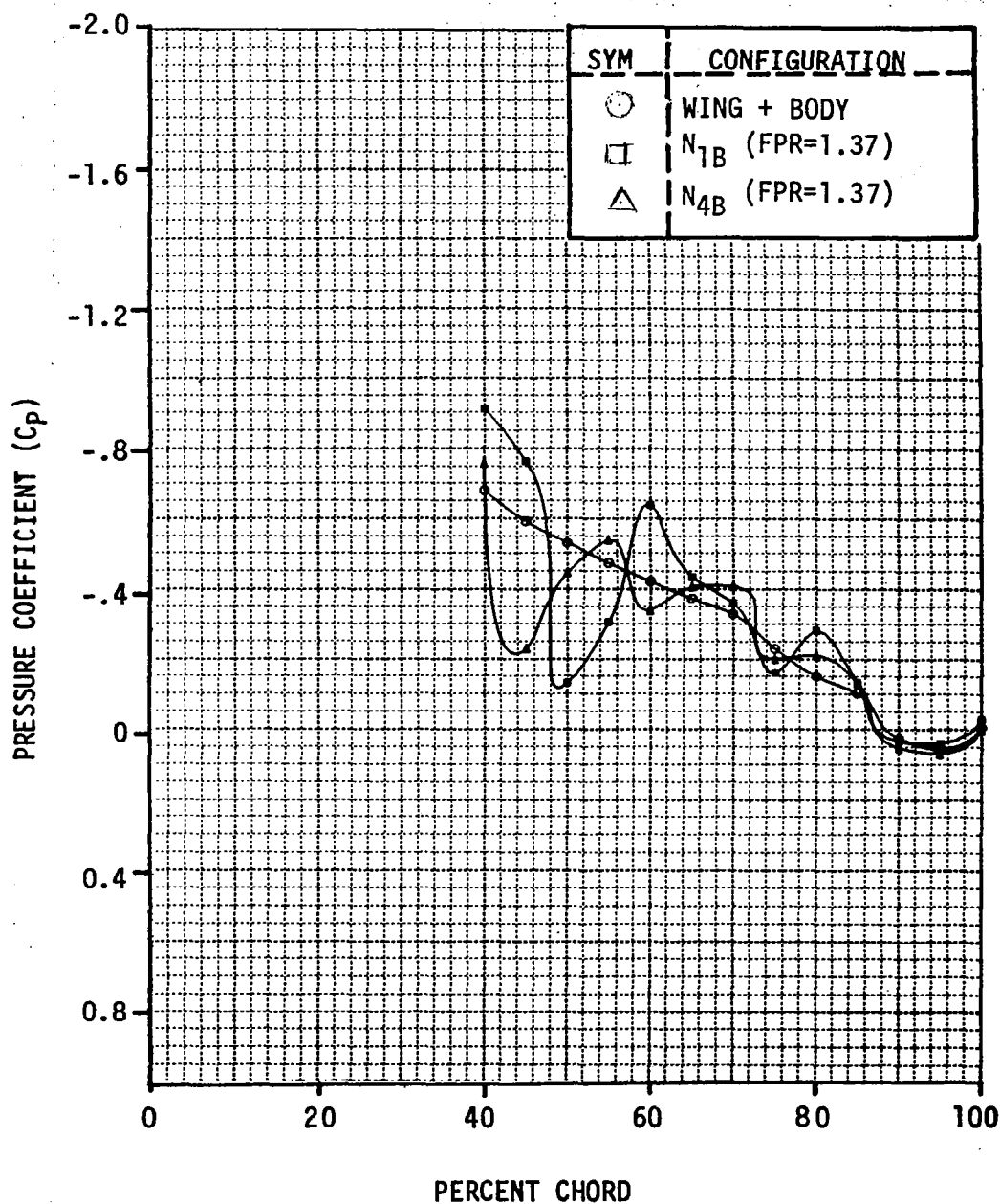23 PERCENT SEMI-SPAN

MACH NUMBER = 0.7

Figure 11.123. Wing Surface Pressures in the Jet for the Wing-Body, N_{1B} and N_{4B} at 23% Semispan and M = 0.7

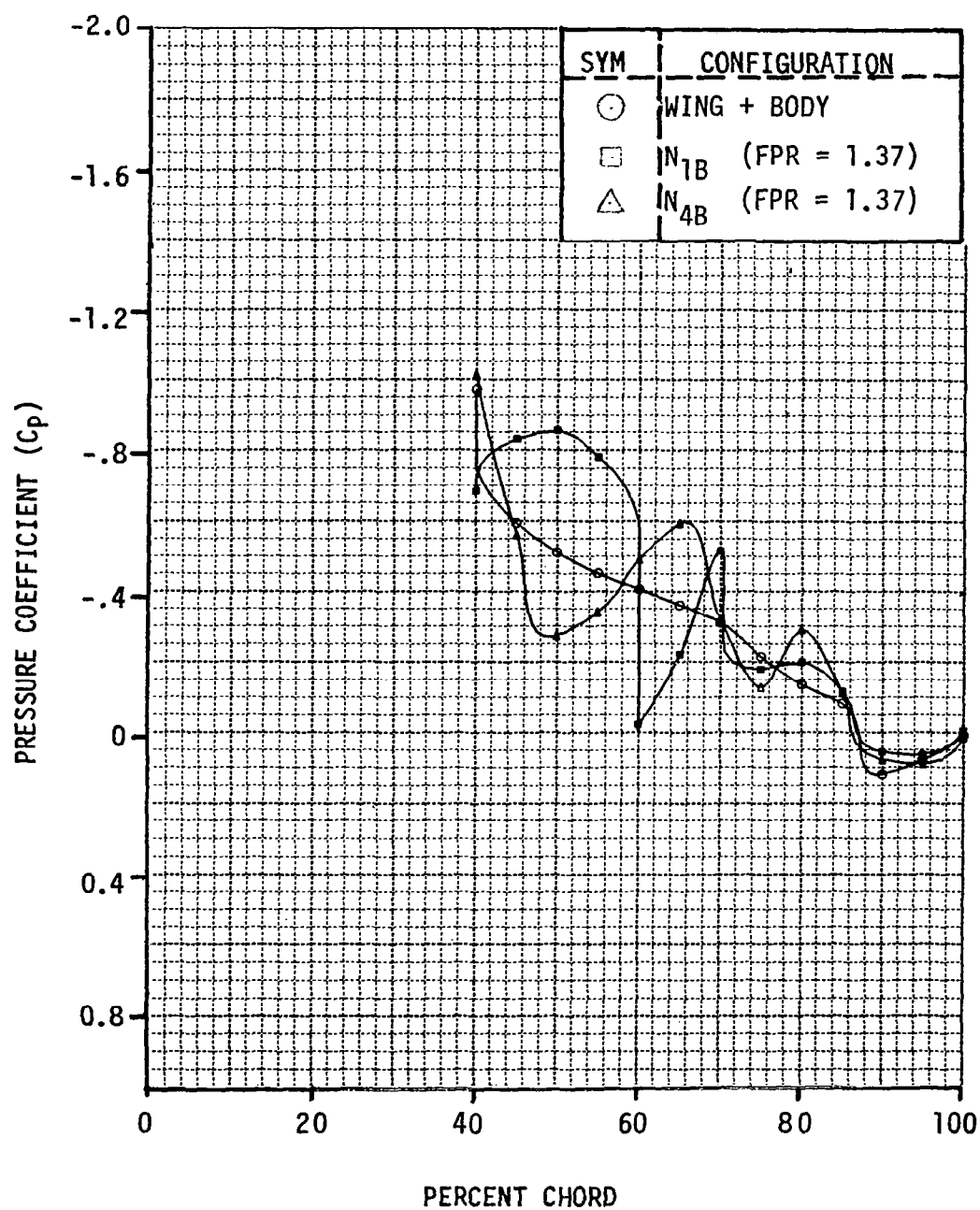ALPHA = 0.5°

23 PERCENT SEMI-SPAN

MACH NUMBER = 0.76

Figure 11.124. Wing Surface Pressures in the Jet for the Wing-Body, N_{1B} and N_{4B} at 23% Semispan and M = 0.76

ALPHA = 0.5°

23 PERCENT SEMI-SPAN
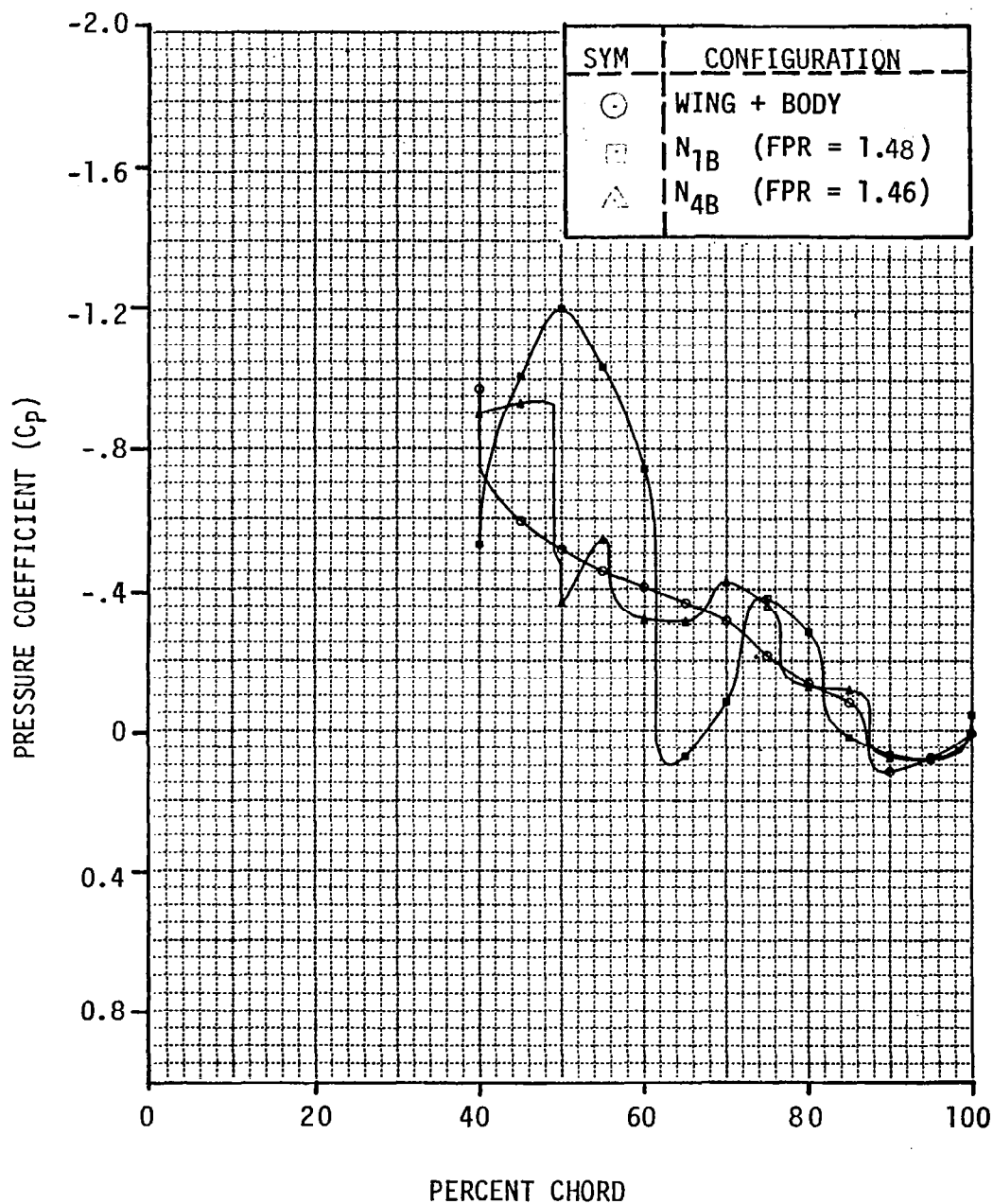
MACH NUMBER = 0.76

Figure 11.125. Wing Surface Pressures in the Jet at High FPR for the **Wing-Body,** N_{1B} and N_{4B} at 23% Semispan and M = 0.76
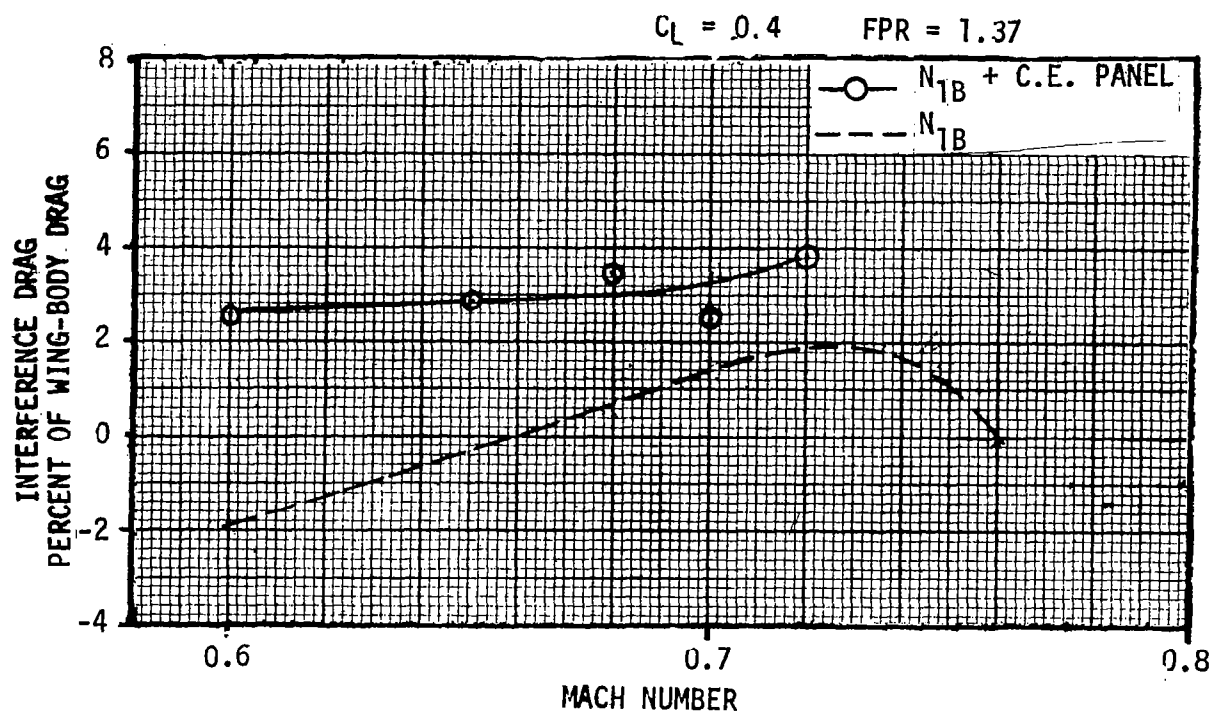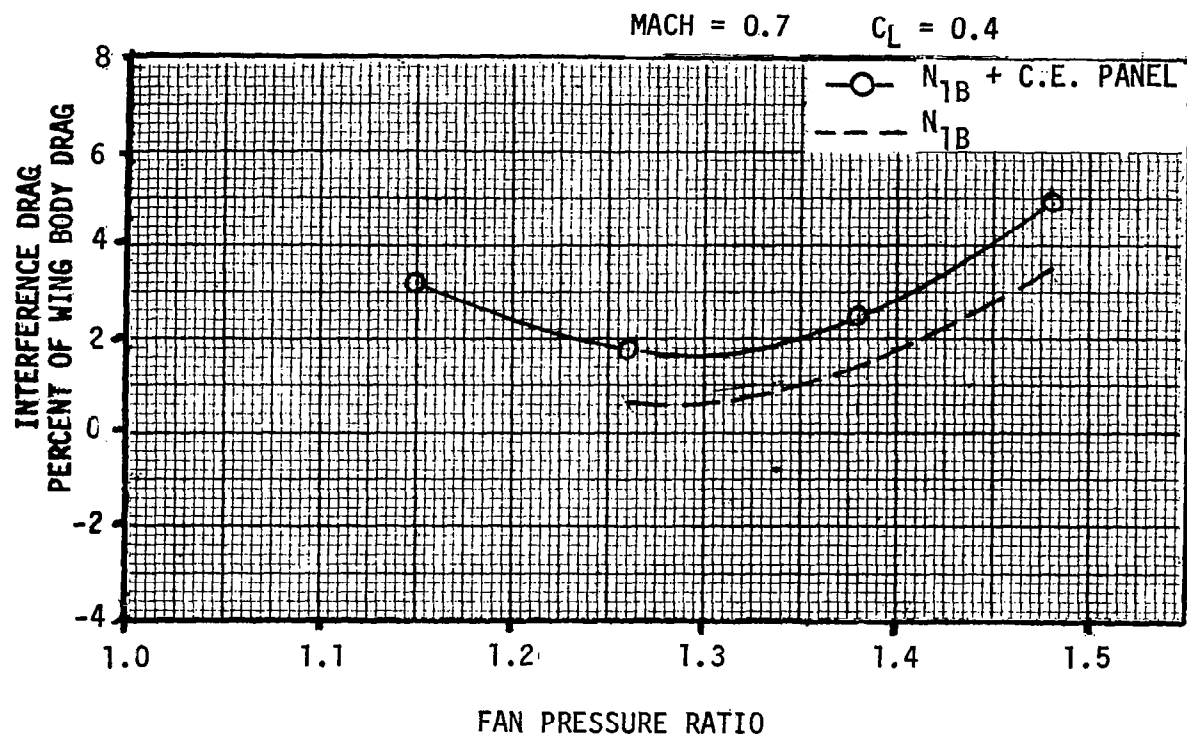
Figure 11.126.   Variation of Nacelle Interference Drag with Mach Number and Fan Pressure Ratio for N_{1B} Nacelle with Control Expansion Panel.
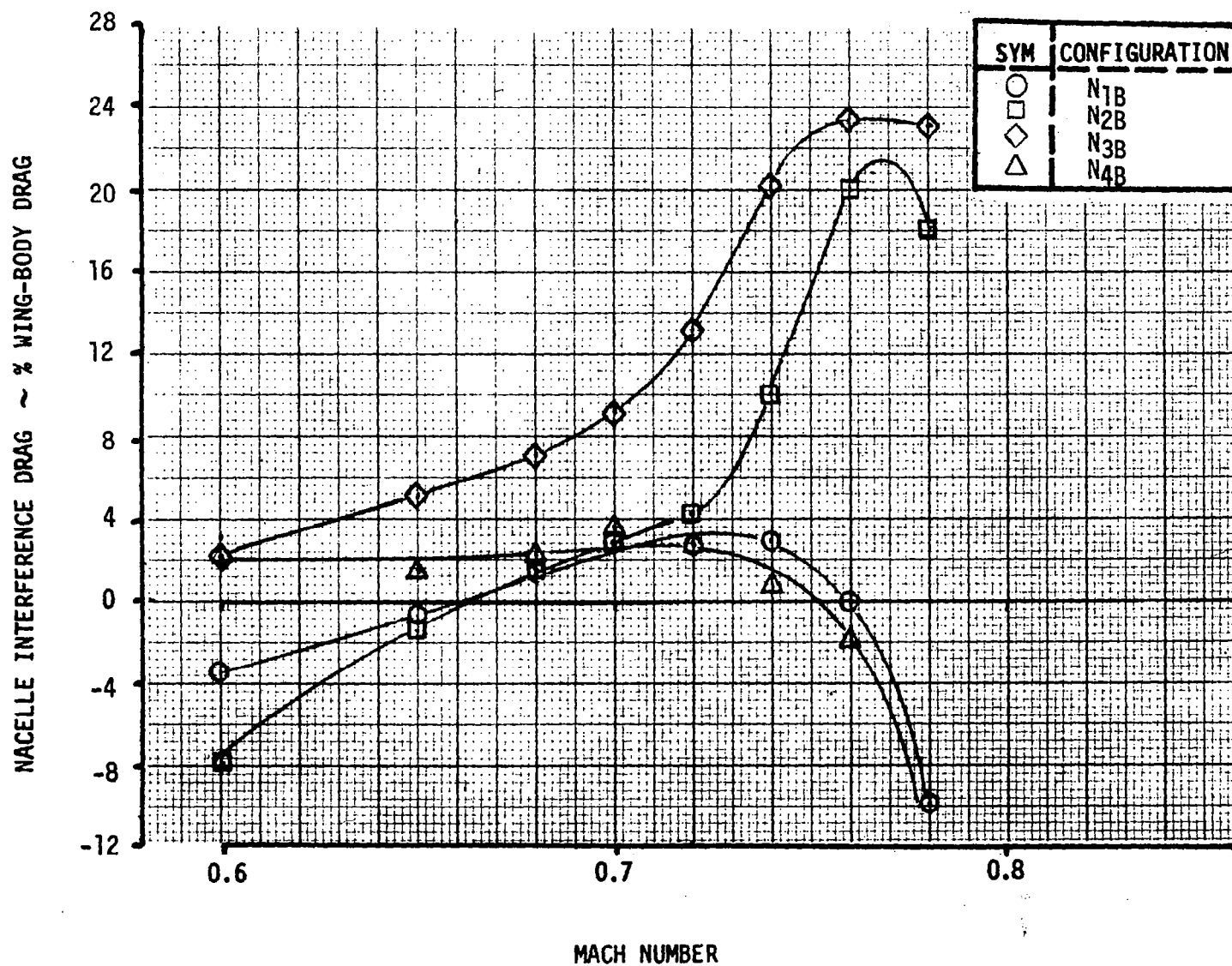
Figure 11.127.   Interference Drags for Various Two Inboard Engine Configurations.

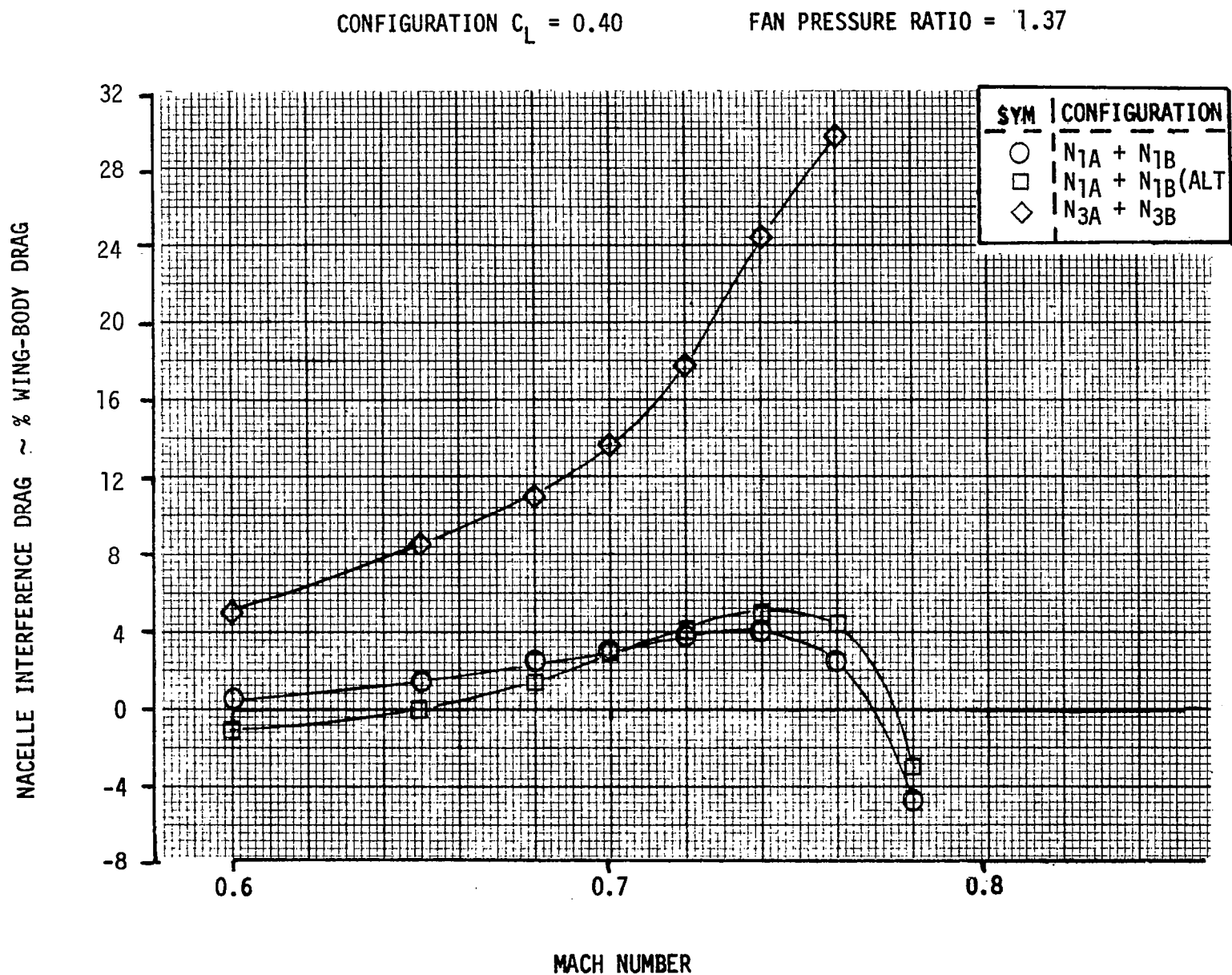CONFIGURATION C_L = 0.40   FAN PRESSURE RATIO = 1.37

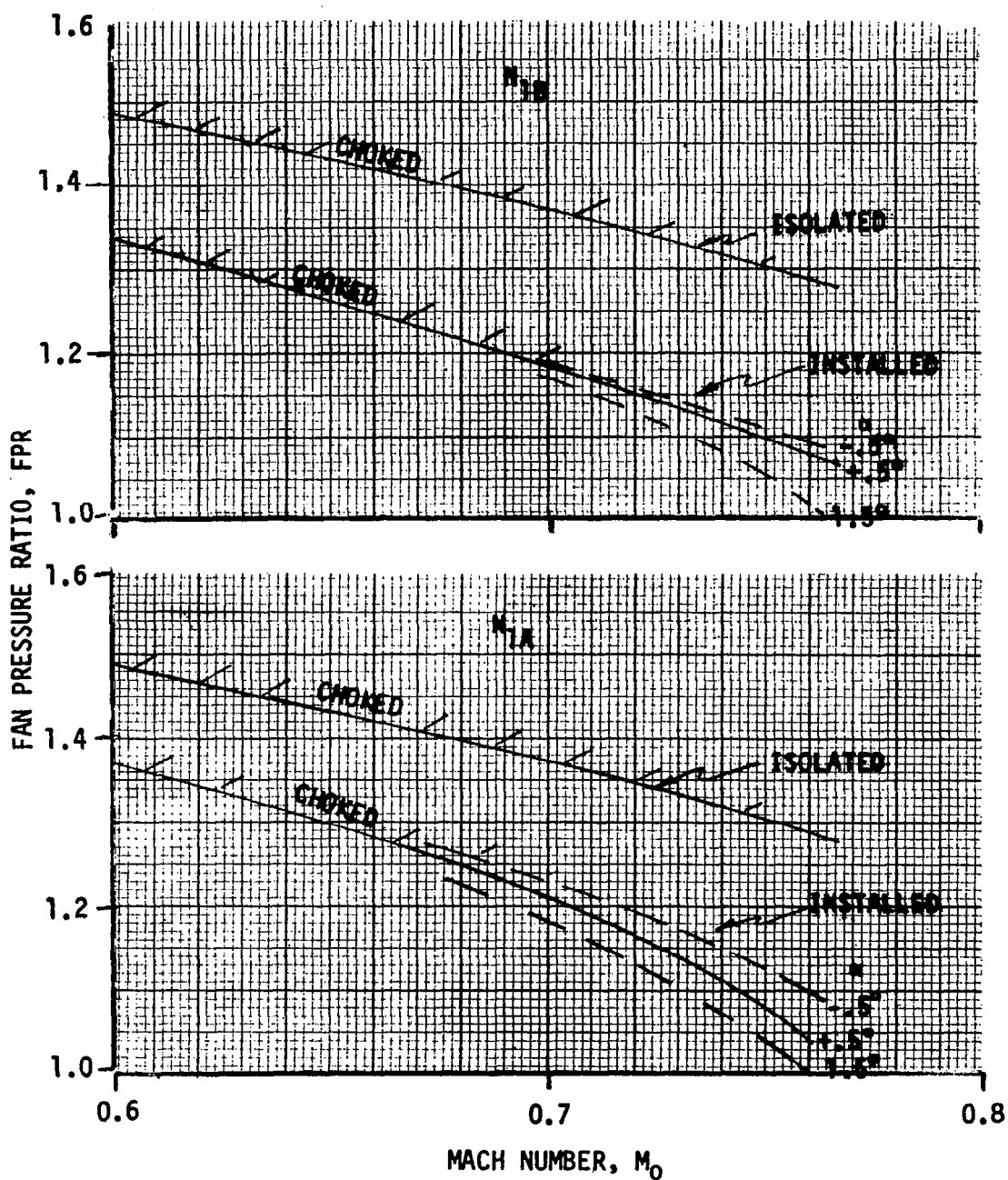Figure 11.128.   Interference Drags for Various Four Engine Configurations.

Figure 11.129. Effect of Installation on Nozzle Choking Characteristics.

12.0 CONCLUSIONS

The need to have accurate high speed aerodynamic/propulsion interferences grew out of configuration design studies on Over-the-Wing (OTW) STOL vehicles. This need led to a joint Douglas Aircraft/NASA wind tunnel test program conducted in the NASA Lewis 8-ft x 6-ft tunnel. The model consisted of a semispan supercritical wing-body that could be tested with various nacelle options. The nacelles could be tested in a flow through configuration or with powered simulators installed. The conclusions of the program follow.

Performance of Basic Nacelle Configurations

1. The interference drag of the outboard N_{1A} low boattail angle baseline nacelle configuration was about 1.5 percent of the basic wing-body drag level at the design condition of C_L=0.40, M_0=0.70, and FPR=1.37. The corresponding excess drag with both inboard and outboard nacelles was about 3.0 percent. The N_1 nacelles produce a favorable interference drag effect at M_0=0.76, where the basic wing shock wave appears to be moved forward and weakened by the presence of the nacelles. The spanwise locations of one N_1 flow through type nacelle was varied from 23-percent semispan to 48-percent semispan with only a small change in drag.

2. The contoured nacelle, N_2, did produce the desired effects on the wing flowfield by moving the wing shock and wing pressure distributions closer to the wing alone condition. The interference drag at the design point was little different than N_1, but higher drag was observed at M=0.76, caused by adverse nacelle interference at a given angle of attack and by configuration lift losses resulting from the nacelle installation. The effects of power at the design condition were small but larger adverse effects were observed at M=0.76. These adverse effects were caused by jet overexpansion losses into the low wing static pressure environment that was preserved by the nacelle contouring.

3. The N_3 high boattail configuration, with both inboard and outboard nacelles installed, exhibited an excess drag of about 14 percent of the basic wing-body configuration at the design point. This excess drag was associated with low pressures over the boattail and an enlarged region of supercritical flow on the wing as the wing shock moved aft from its clean wing position.

Effects Related to Power

1. The effects of power were dependent on configuration, C_L, M_0, and FPR, and were as much as 6.0 percent to 8.0 percent of the wing-body drag.

2. The C-D nozzle was effective in attenuating the first shock wave in the exhaust cyclic system, and probably would be effective in reducing the excess drag of the N_2 configuration at M_0=0.76.

3. The controlled expansion panel was not effective. The effectiveness of this device might be improved with nozzle sidewall extensions.

4. Analysis of the trimmer flap study indicates the probable presence of some induced drag due to exhaust stream jet flap action. It is possible that smooth local variations in wing trailing edge camber in the vicinity of the exhaust stream could minimize these induced losses without introducing the shock losses caused by the trimmer flaps.

Effectiveness of the Analysis Methods

1. The use of strip analysis techniques (2-D boundary solution at various spanwise stations) to synthesize a three-dimensional representation of the wing boundary layer on the three-dimensional potential flow mathematical model led to reasonably good agreement between the calculated and experimentally measured wing surface pressure distributions.

2. The streamline contouring technique was reasonably successful in that the treated (upper) portion of the nacelle, without power, produced little interference with the wing upper surface pressure distributions in the vicinity of the wing.

13.0 REFERENCES

1. Swan, W. C. and Sigalla, A.: The Problem of Installing a Modern High Bypass Engine on a Twin Jet Transport Aircraft. No. 17, AGARD Conference on Aerodynamic Drag, AGARD-CPP-124.

2. Kettle, D. J.; Kurn, A. G.; and Bagley, J. A.: Exploratory Tests on a Forward-Mounted Overwing Engine Installation. ARC CP No. 1207; 1972.

3. Douglas Aircraft Company: Study of Quiet Turbofan STOL Aircraft for Short Haul Transportation. NASA Vol. I, CR-2353; Vol. II, CR-114607; Vol. III, CR-114608; Vol. IV, CR-114609; Vol. V, CR-114610; Vol. VI, CR-114611; June 1973.

4. Douglas Aircraft Company: Parametric Study of STOL Short-Haul Transport Engine Cycles and Operational Techniques to Minimize Community Noise Impact. NASA CR-114759; June 1974.

5. Riebe, J. M. and Davenport, E. E.: Exploratory Wind-Tunnel Investigation to Determine the Lift Effects of Blowing Over Flaps from Nacelles Mounted Above the Wing. NACA TN 4298, 1958.

6. Turner, Th. R.; Davenport, E. E.; and Riebe, J. M.: Low Speed Investigation of Blowing from Nacelles Mounted Inboard and on the Upper Surface of an Aspect-Ratio 7.0, 35 Degree Swept Wing with Fuselage and Various Tail Arrangements. NASA Memo 5-1-59L; June, 1959.

7. Phelps, A. E.; Letko, W.; and Henderson, R. L.: Preliminary Low-Speed Wind Tunnel Investigation of a Semispan STOL Jet Transport Wing with an Upper-Surface Blown Jet Flap. NASA TN D-7183; May 1973.

8. Aoyagi, K; Falarski, M. D.; and Koenig, D. G.: Wind Tunnel Investigation of a Large-Scale Upper Surface Blown Flap Transport Model Having Two Engines. NASA TM X-62296; August, 1973.

9. Wimpress, J. K.: Upper Surface Blowing Technology as Applied to the YC-14 Airplane. SAE Paper 730916; October, 1973.

10. Skavdahl, H.; Wang, T.; and Hirt, W. J.: Nozzle Development for the Upper Surface-Blown Jet Flap on the YC-14 Airplane. SAE Paper 740469; April/May, 1974.

11. Johnson, J. L., Jr. and Phelps, A. E., III: Low-Speed Aerodynamics of the Upper-Surface Blown Jet Flap. SAE Paper 740470; April/May, 1974.

12. Gainer, T. G.: Low-Speed Wind-Tunnel Investigation to Determine the Aerodynamic Characteristics of a Rectangular Wing Equipped with a Full-Span and an Inboard Half-Span Jet-Augmented Flap Deflected 55 Degrees. NASA Memo 1-27-59L; 1959.

13. Williams, J.; Butler, S.F.J.; and Wood, M. N.: The Aerodynamics of Jet Flaps. R&M No. 3304; January, 1961.

236

14. Lopez, M. L. and Shen, C. C.: Recent Developments in Jet Flap Theory and Its Application to STOL Aerodynamic Analysis. AIAA Paper No. 71-578, AIAA 4th Fluid and Plasma Dynamics Conference; June, 1971. Also revised as Douglas Paper 5928, Douglas Aircraft Company, McDonnell Douglas Corporation; July, 1971.

15. Lopez, M. L.; Shen, C. C.; and Wasson, N. F.: A Theoretical Method for Calculating the Aerodynamic Characteristics of Arbitrary Jet-Flapped Wings. Volume I, The Elementary Vortex Distribution Jet-Wing Lifting Surface Theory. Douglas Aircraft Company Report MDC-J5519-01; May, 1973. Volume II, EVD Jet-Wing Computer Program User's Manual. Douglas Aircraft Company Report MDC-J5519-02, May, 1973.

16. Holmes, A. E.; Barnett, L.; and Jacobs, W. F.: Application of the Equivalent Mechanical Flap Concept to Jet Flapped Wing-Body Combinations, ARL 74-0136; November, 1974.

17. Ciepluch, C. C.: QCSEE Program, Aeronautical Propulsion. NASA SP-381, pp. 65-80; May, 1975.

18. Gillette, W. B.; Mohn, L. W.; Ridley, H. G.; and Nark, T. C.: Upper-Surface Blowing Nacelle Design Study for a Swept Wing at Cruise Conditions. NASA CR-2427; September, 1974.

19. Smith, C. C., Jr.; Phelps, A. E. III; Copeland, W. L.: Large-Scale Wind-Tunnel Investigation of a Semispan Wing with an Upper-Surface Blown Jet Flap. Langley Working Paper No. 1115; June 26, 1973.

20. Phelps, A. E. III and Smith, C. C. Jr.: Wind-Tunnel Investigation of an Upper Surface Blown Jet-Flap STOL Configuration. Langley Working Paper No. 1092; January 12, 1973.

21. General Electric Company: Quiet Clean Short-Haul Experimental Engine (QCSEE). NASA CR 134839, Vol. II - Preliminary Analyses and Design Report; October, 1974.

22. Friedman, D. M.: A Three-Dimensional Lifting Potential Flow Program. Douglas Aircraft Report MDC J6182; September, 1974. (Restricted Distribution)

23. Bauer, F.; Garabedian, P.; Korn, D.: Supercritical Wing Sections. Lecture Notes in Economics and Mathematical Systems #66, Springer Verlag; 1972.

24. Keller, H. B.; Cebeci, T.: Accurate Numerical Methods for Boundary Layer Flows. II Two-Dimensional Turbulent Flows, AIAA Paper 71-164; 1971.

25. Henne, P. A.: Unique Applications of the Method of Characteristics to Inlet and Nozzle Design Problems. AIAA Paper 75-1185; September, 1975.

26. Ciepluch, C. C.: Overview of the QCSEE Program. Powered Lift Aerodynamics and Acoustics, SP-406, 1976; NASA, pp. 325-333. (FEDD distribution).

27. Quiet Clean Short-Haul Experimental Engine (QCSEE) Over-the-Wing (OTW) Final Design Report. NASA CR-134848; 1977. (FEDD distribution).

28. Meleason, E. T.:   Effects of Nozzle Design and Power on Cruise Drag for Upper-Surface-Blowing Aircraft.   Powered Lift Aerodynamics and Acoustics, SP-406; 1976; NASA, pp. 183-196.   (FEDD distribution).

29. Pirrello, C. J.; Hardin, R. D.; Heckart, M. V.; and Brown, K. R.:   An Inventory of Aeronautical Ground Research Facilities, Volume I - Wind Tunnels, NASA CR-1874; November, 1971.

30. Braslow, A. L.; Knox, E. C.:   Simplified Method for Determination of Critical Height of Distributed Roughness Particals for Boundary-Layer Transition at Mach Numbers from 0 to 5.   NACA TN 4363; September, 1958.

31. Radkey, R. L.; Welge, H. R.; Felix, J. E.:   Aerodynamic Characteristics of a Mach 2.2 Advanced Supersonic Cruise Aircraft Configuration at Mach Numbers from 0.5 to 2.4.   NASA CR-145094; 1977.

32. Braden, J. A.; Bordges, K. P.; Hankock, J. P.:   Cruise Aerodynamics of USB Nacelle/Wing Geometric Variations.   Presented in NASA Langley Conference on Powered Lift Aerodynamics and Acoustics, Paper No. 11; May 24-26, 1976.